Methods to determine fast-ion distribution functions from multi-diagnostic measurements

Jacobsen, Asger Schou; Naulin, Volker; Salewski, Mirko

Publication date:
2015

Document Version
Publisher's PDF, also known as Version of record

Link back to DTU Orbit

Citation (APA):
Jacobsen, A. S., Naulin, V., & Salewski, M. (2015). Methods to determine fast-ion distribution functions from multi-diagnostic measurements. Department of Physics, Technical University of Denmark.

Methods to determine fast-ion distribution functions from multi-diagnostic measurements

PhD Thesis

Asger Schou Jacobsen

Abstract

Understanding the behaviour of fast ions in a fusion plasma is very important, since the fusion-born alpha particles are expected to be the main source of heating in a fusion power plant. Preferably, the entire fast-ion velocity-space distribution function would be measured. However, no fast-ion diagnostic is capable of measuring the entire distribution function. The velocity space sensitivity of a fast-ion diagnostic is given by so-called velocity-space weight functions. Here, the development of neutron emission spectrometry weight functions is presented. By combining measurements from several fast-ion diagnostic views, it is possible to infer the distribution function using a tomography approach. Several inversion methods for solving this tomography problem in velocity space are implemented and compared. It is found that the best quality it obtained when using inversion methods which penalise steep gradients in the velocity-space distribution function. The different inversion methods are used to study actual fast-ion measurements from the ASDEX Upgrade tokamak. By calculating tomographies of the distribution before and after a sawtooth crash, it is possible to identify the parts of velocity-space where the fast ions are affected the most. Finally, the first ever tomographies calculated using a combination of measurements from different types of fast-ion diagnostics are presented.

Dansk resume

Det er meget vigtigt at forstå opførslen af energirige ioner i et fusionsplasma, da det er forventet at energirige heliumkerner skabt i fusionsreaktionerne vil stå for hovedparten af opvarmningen af plasmaet i et fusionskraftværk. Det ville være at foretrække at måle hele hastighedsfordelingen af de hurtige ioner. Der er dog ingen hurtige ion måle-instrumenter der er i stand til at måle hele fordelingsfunktionen. Sensitiviteten i hastighedsrum for et hurtig ion måle-instrument er givet af såkaldte hastigheds-vægtfunktioner. Udviklingen af vægtfunktioner for neutron spektrometri er præsenteret her. Det er muligt at udregne hastighedfordelingen ved at kombinere målinger fra flere hurtige ion måle-instrumenter i en tomografi. En række inversionsmetoder er implementeret for at løse dette tomografiproblem i hastighedsrum, og deres resultater er sammenlignet. Det viser sig at de inversionsmetoder der minimerer stejle gradienter i hastighedsfordelingen giver de bedste resultater. De forskellige inversionsmetoder er anvendt på målinger af de hurtige ioner fra tokamaken ASDEX Upgrade. Ved at udregne tomografier af fordelingen før og efter et savtands-crash, er det muligt at identificere hvilke områder i hastighedsrum der bliver påvirket mest. De første tomografier udregnet for en kombination af målinger fra helt forskellige typer hurtige ion måle-instrumenter er præsenteret.

Acknowledgements

I have had the pleasure of working with many great people during my PhD project. First of all, I would like to thank my supervisors Volker Naulin and Mirko Salewski for guiding and supporting me throughout this project. A big thank you to the entire plasma physics section at DTU, you have been great colleagues and I have had a great time here. My fellow PhD students Michael, Alexander, Jeppe and Ning, it has been truly joyful sharing an office with you! I have also had the opportunity of working together with several very talented researchers from around the world. I would like to thank all of you, especially Ben Geiger from Max-Planck-Institute for plasma physics, Jacob Eriksson from Uppsala University and Luke Stagner and Bill Heidbrink from University of California, Irvine. Without your help, I would never have been able to achieve what I have done. I would like to thank Jakob Møller-Andersen, Pernille Nielsen, Alexander Simon Christensen and Rasmus Ellebæk Christiansen for proofreading this manuscript. Finally, I would like to thank all my friends and family for supporting me during this project.

Contents

Chapter 1

Introduction

The prospect of a stable, clean, CO_2-free source of energy with a practically unlimited supply of fuel has been driving fusion researchers for decades. Very fast fusion-born alpha particles are foreseen to be the main source of heating in a fusion power plant. Therefore, it is important to understand the behaviour of fast ions in a fusion plasma. Using a single fast-ion diagnostic, it is impossible to experimentally determine the full phase-space distribution function of the non-thermal ions present in a fusion plasma. Each such diagnostic measures only parts of the velocity-space distribution, given by the orientation of the instrument to the magnetic field and the type of diagnostic. Identifying which parts of velocity-space is measured by a given diagnostic contributes to the understanding of the measurements [1, 2]. This is made possible by the formulation of so-called fast-ion weight functions which determine the velocity-space sensitivity of a given part of a measured spectrum [1, 3–6]. The weight functions are used in the formulation of the following forward problem: how will my spectrum look given a fast-ion velocity distribution function. This is illustrated as going from left to right in figure 1.0.1. Solving the opposite problem, calculating the distribution which gives rise to a measured noisy spectrum is significantly harder. This type of problem is called an inverse problem. It corresponds to going from right to left in figure 1.0.1. A well-known example of an inverse problem is tomography. Solving the inverse problem sketched in figure 1.0.1 has similarities to conventional tomography. Thus it is dubbed velocity-space tomography.

During my PhD project I have been working on several aspects of improving and expanding the method of velocity-space tomography of the fast-ion velocity distribution function in a tokamak plasma. Specifically, my main focus has been divided into the following three branches of this subject:

- First, I derived velocity-space sensitivity functions, so-called weight functions, for neutron emission spectrometry. In principle this allows us to include measurements of neutron energy spectra in the tomographies. Furthermore, the weight functions allow an identification of the parts of velocity-space measured by a given diagnostic. These results are published in papers I and II.
- Secondly, I have been working on improving the quality of the tomographies by implementing a number of different inversion methods in order to determine which

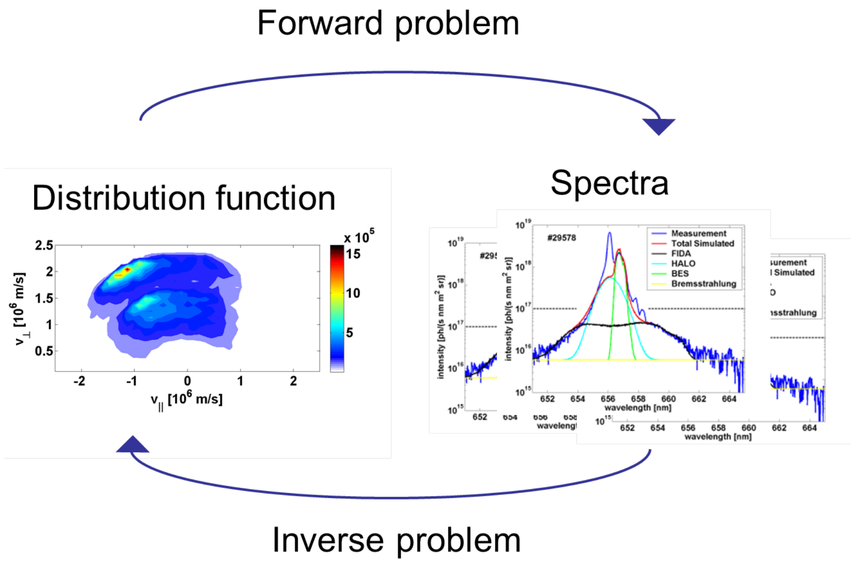

Figure 1.0.1: In the forward problem, synthetic spectra are calculated from a given fast-ion distribution function. The inverse problem is to find the distribution function which caused the measured noisy spectra. This is often a much harder problem to solve.

performs best for our specific problem. This is documented in paper III which has been submitted recently.

- Finally, I have calculated tomographies using real measurements obtained by the fast-ion D_α (FIDA) spectroscopy set-up at the ASDEX Upgrade tokamak in order to investigate the effect of a sawtooth crash on the fast-ion population and its dependence on velocity-space, see paper III and IV.

The above mentioned division of focus is reflected in this thesis, as I will present my work in the three different areas. The common theme is the expansion, improvement and application of the method of velocity-space tomography of the fast-ion distribution function. The thesis is organized as follows. Chapter 2 contains background information as well as a description of the status of velocity-space tomography before my project started. Thus chapter 2 does not contain results obtained by me, but is needed in order to make the rest of the thesis understandable and relate my work to the current status of the field. Chapter 3 describes my derivation of neutron emission spectrometry weight functions and gives examples of their applications. It also contains a description of how to calculate instrument-specific weight functions taking the instrumental response function of a specific instrument into account. Chapter 4 describes the work I have done on implementing various inversion methods. Chapter 5 contains my studies using experimentally measured fast-ion data. Conclusions are summarized in chapter 6 and chapter 7 describes the possible next steps for the field of velocity-space tomography.

Chapter 2

Background

2.1 Nuclear fusion

Fusion is a nuclear process where two nuclei fuse together and produce a heavier nucleus. If the sum of the two nuclei are lighter than iron, this process will release nuclear binding energy in the form of energy of the products. However, in order to get the nuclei to fuse, it is necessary to overcome the repulsive Coulomb force. This is done by heating the fuel components to enormous temperatures, to give them sufficient kinetic energy to overcome the energy-barrier and fuse together. If the two hydrogen isotopes deuterium and tritium are used as fuel, temperatures between 100 million K and 200 million K are needed. At such temperatures, all the fuel will be ionized forming a plasma. The plasma needs to be confined since touching the walls of a reactor chamber will cool down the plasma and potentially damage the wall. Currently, the most commonly used method of plasma confinement is to suspend the plasma midair in a magnetic field of several Tesla in a toroidally-shaped reactor chamber. Such magnetic fields are five orders of magnitude greater than the magnetic field of the Earth.

The most widespread machine design is the so-called tokamak[1] invented by Soviet scientists in the 1960'ies. A sketch of a tokamak is shown in figure 2.1.1. In a tokamak the magnetic field consists of a toroidal component created by external toroidal field coils and a poloidal component created by a strong toroidal current in the plasma. This creates a helically twisted magnetic field which confines the plasma. JET, the largest operating magnetic confinement fusion device today, as well as the next-generation device ITER, under construction in southern France, are both tokamaks.

2.2 ASDEX Upgrade

During my PhD, I have mainly been working with data from the tokamak ASDEX Upgrade[2] located in Garching near Munich. ASDEX Upgrade is a so-called medium sized

---

[1] The word tokamak is a Russian acronym meaning either toroidal chamber with magnetic coils or toroidal chamber with axial magnetic field.

[2] The name ASDEX is an abbreviation of "Axial Symmetrisches Divertor EXperiment".

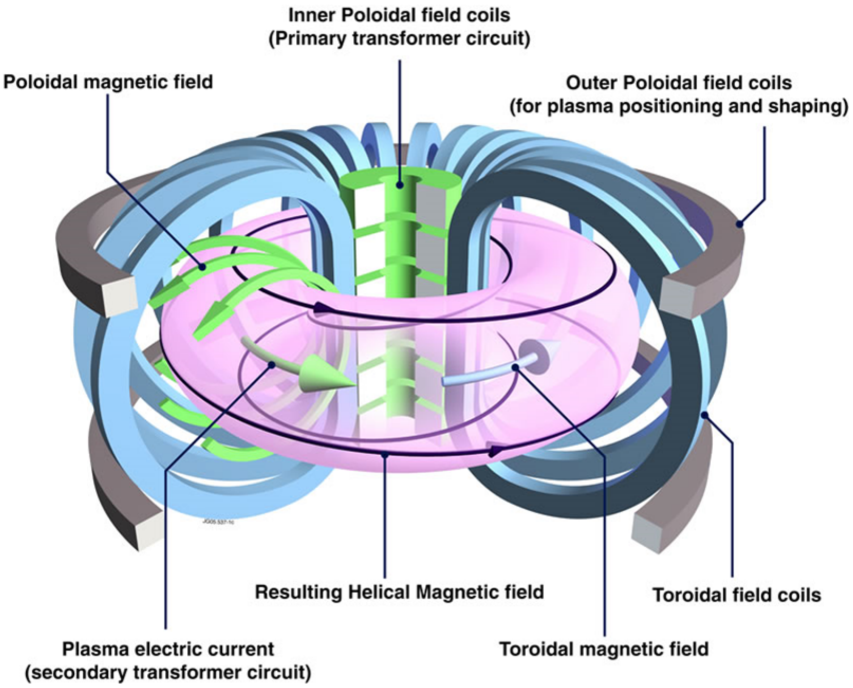

Figure 2.1.1: Sketch of a tokamak. Taken from www.euro-fusion.org.

fusion device, with a major radius of 1.65 m and a minor radius of 0.5 m [7]. The toroidal current producing the poloidal magnetic field component is of the order of 1 MA and the toroidal magnetic field is around 2.5 T. A single fusion experiment in ASDEX Upgrade usually lasts between 6 s and 10 s. Each such experiment is called a discharge. ASDEX Upgrade is very well suited for analysing the behaviour of fast ions due to the large number of fast-ion diagnostics installed. It also has several heating systems installed. These are neutral beam injection (NBI) and electron- and ion cyclotron resonance heating (ECRH) and (ICRH). For the work presented in this thesis, especially the NBI system is important. In NBI heating, ions are accelerated outside of the fusion reactor in a strong electric field. The high-energy beam of ions is neutralized and injected into the plasma where the neutral atoms are ionized in collisions or charge-exchange reactions. In subsequent collisions, the high-energy NBI ions will slow down on the bulk plasma, thereby delivering energy. ASDEX Upgrade has eight different NBI beams, each capable of delivering 2.5 MW of heating power to the plasma. The eight beams are named Q1-Q8 ("Quelle" is German for source). Q1-Q4 each have a maximum injection energy of 60 keV[3]. Q5-Q8 have a maximum injection energy of 93 keV. When accelerating deuterium ions in an NBI, also D_2 and D_3 molecules are accelerated. When these enter the plasma, they are split into single D ions, but with only half and third the energy each. Thus, a distribution of D ions injected with an NBI will have three peaks, called the full, half and third energy peaks. As will be explained later, the fast-ion diagnostic FIDA can only measures when an NBI beam is turned on. At ASDEX Upgrade, the beam needed for the FIDA system is the 60 keV beam Q3.

---

[3] In the fusion community, both energy and temperature are often given in eV. 1 eV equals around 11500 K.

2.3 Fast ions

The focus in my PhD project has been on very fast ions with energies of 10 keV or more. In general, the ion distribution in the plasma is considered as consisting of two components. The main component is distributed according to a Maxwellian distribution given by

$$f_t = n_t \left(\frac{m}{2\pi k_B T}\right)^{3/2} \exp\left(-\frac{m\mathbf{v}_t^2}{2k_B T}\right) , \tag{2.3.1}$$

where n_t is the density, m is the mass, $\mathbf{v}_t$ is the velocity, T is the temperature and k_B is Boltzmanns constant. This component makes up most of the plasma and is called the thermal or bulk ion distribution, and the ions are called the thermal ions. A typical thermal ion temperature in the centre of ASDEX Upgrade is of the order of 5 keV. The other component is the non-Maxwellian ions. These can have significantly higher energies. Understanding their behaviour is important as the energetic fusion-born alpha-particles are foreseen to be the main source of heating in a fusion power plant. Thus, if they are lost due to instabilities or poor confinement before they transfer their energy to the bulk plasma, it will be detrimental to the performance of the power plant. However, in current machines only few alpha-particles are produced and the main sources of energetic ions are NBI and ICRH.

2.3.1 Fast-ion instabilities

Several plasma instabilities have been observed to redistribute energetic ions both in position and velocity-space [8–10]. Here, the sawtooth instability is described.

The sawtooth instability

A sawtooth crash is a periodic change in the magnetic field topology in the centre of the plasma. It can occur when the central safety factor, q, drops below one [11]. q is a measure of the helicity of a magnetic field line and is given by the number of times the field line goes around the torus toroidally before it returns to a given position in the poloidal plane [11]. When q drops below one, a (1,1) kink mode can grow unstable which triggers the sawtooth crash [12]. A theory describing the process was proposed by Kadomtsev. According to the Kadomtsev model [11], the instability changes the magnetic field topology in the centre of the plasma. The magnetic field topology evolution is sketched in figure 2.3.1 taken from [13].

The drawings in figure 2.3.1 show poloidal cross sections of the plasma. The twisting magnetic field lines have been unwound such that the $q = 1$ magnetic field lines appear as coming straight out of the page, field lines with $q < 1$ go counter-clockwise and field lines with $q > 1$ go clockwise. At $t = 0$ only the centermost point has $q = 1$. Due to an increase in the toroidal current density, the q-value drops below one in the core as can be seen for $t = 16.5$. This creates a (1,1) kink mode which shifts the entire core to the right. In a small region, the magnetic flux surfaces are pressed together and the magnetic field lines reconnect. On the opposite side of the cross section, a magnetic island is formed

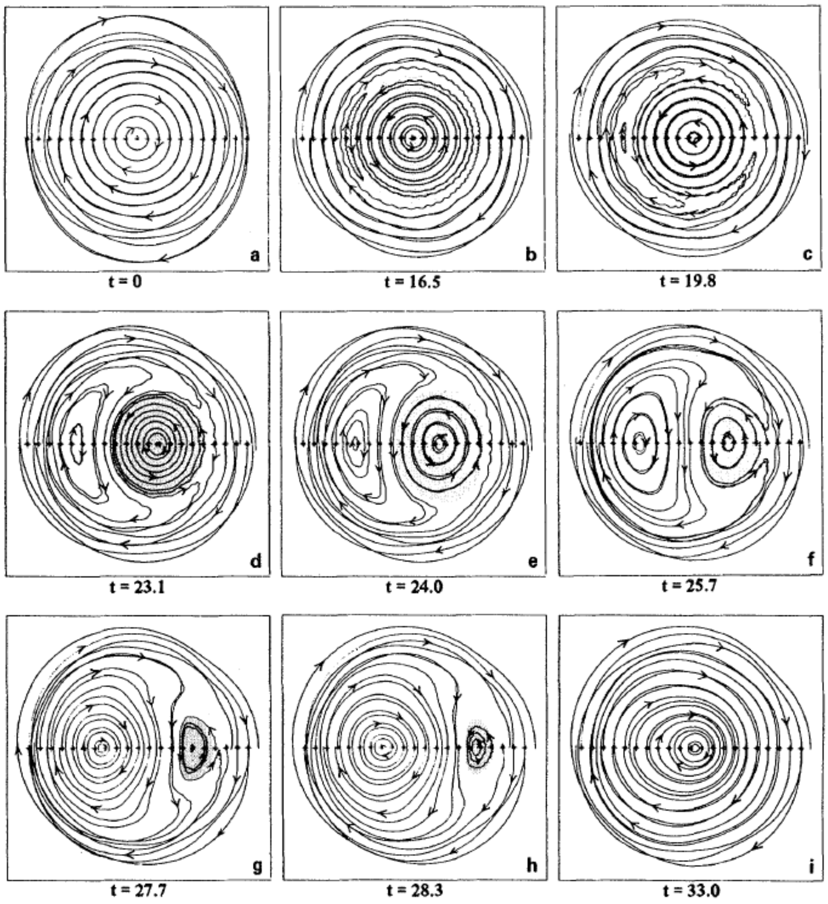

Figure 2.3.1: Poloidal cross sections of the magnetic field illustrating the princple of the magnetic field topology change during a sawtooth crash. Taken from [13]

and grows, assisting to push the core of the plasma into the reconnection region. After the sawtooth crash, the plasma has returned to a situation where $q > 1$ everywhere. The Kadomtsev model has been successful in explaining the sawtooth behaviour in small fusion devices. However, some experimental findings in larger devices cannot be explained by the model. According to the Kadomtsev model, a complete reconnection occurs, e.i. the q value is above one on axis after the crash. However, in large machines, sawtooth crashes with incomplete reconnection have been observed where the end result is a core with $q < 1$ [11]. This is not completely understood. Furthermore, the crash time predicted by the Kadomtsev model is longer than what is observed on larger devices.

After the crash, a lot of energy has been transported from the centre to the outer regions of the plasma. Thus, a measure of the central electron temperature and density will show sharp drops followed by a slower increase while the plasma recovers, followed by another crash. A plot of the central electron temperature or density as a function of time will look like sawteeth, hence the name of the instability. It has been observed that a sawtooth crash redistributes the energetic ions away from the centre. Experiments on several machines show that a sawtooth crash redistribute passing ions more compared to trapped ions [2, 14, 15].

2.3.2 Fast-ion diagnostics

Several different types of diagnostics exist for measuring the velocity of fast ions in a fusion plasma. However, none are capable of measuring the entire velocity-distribution function. It is only possible to deduce information of parts of the velocity-distribution function from each diagnostic view.

Collective Thomson scattering

Collective Thomson scattering (CTS) measures the scattering of an injected probe beam off fluctuations in, mainly, the electron density [2, 16–19]. The principle is sketched in figure 2.3.2 from [20].

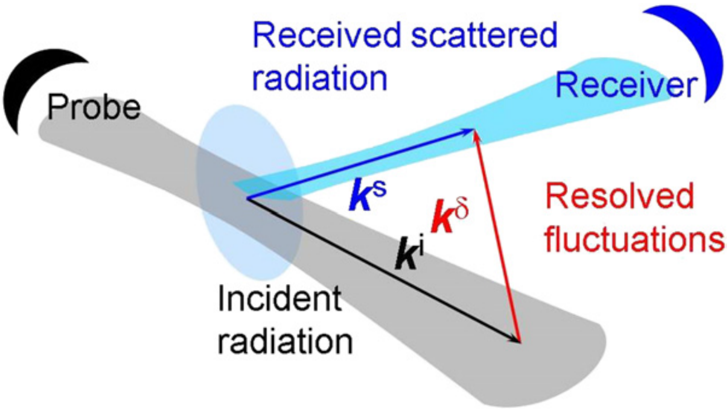

Figure 2.3.2: Sketch of the princple of a CTS diagnostic, from [20].

An injected probe wave with wave vector $\mathbf{k}^i$ is injected into the plasma. It interacts with collective fluctuations in the plasma which sets up a scattered wave with wave vector $\mathbf{k}^s$ given by

$$\mathbf{k}^s = \mathbf{k}^i + \mathbf{k}^\delta \,, \tag{2.3.2}$$

where $\mathbf{k}^\delta$ is the wave vector of the resolved plasma fluctuations. The scattered wave is then measured by a receiver. The angular frequency, ω^δ, of the plasma wave is given by

$$\omega^\delta = \mathbf{v} \cdot \mathbf{k}^\delta \,, \tag{2.3.3}$$

where $\mathbf{v}$ is the velocity of the fast ion setting up the fluctuation.

For very short injected wavelengths, the scattering will be determined by the properties of the electrons. This is called Thomson scattering. For longer wavelengths, the scattering is caused by the scattering off the collective motion of electrons moving under influence of the ions. This is called collective Thomson scattering. The wavelength required for the probe beam to work for CTS is given by the Salpeter parameter α_S [21].

$$\alpha_S = \frac{1}{k^\delta \lambda_D} > 1 \,, \tag{2.3.4}$$

where λ_D is the Debye length and k^δ is the magnitude of $\mathbf{k}^\delta$. The Debye length is a measure of the distance the electrostatic potential of a charged particle will affect the surrounding plasma before being screened. It is given by

$$\lambda_D = \sqrt{\frac{\epsilon_0 k_B T}{q^2 n}} \,, \tag{2.3.5}$$

where k_B is the Boltzmann constant, T is the temperature, q is the charge and n is the density.

At ASDEX Upgrade, the CTS system uses one of the ECRH gyrotrons as source for the probe beam. Most often this is done in a magnetic field configuration where the corresponding electron cyclotron emission (ECE) resonance is outside the plasma in order for the probe beam to affect the plasma as little as possible [22]. Recently, the CTS set-up at ASDEX Upgrade was upgraded with a second receiver. In the standard configuration, this receiver is oriented such that its field-of-view does not overlap the probe beam. Instead it measures the background as a function of time, which significantly improves the background subtraction capabilities [19].

Fast-ion D_α spectroscopy

Fast-ion D_α (FIDA) spectroscopy is a charge-exchange spectroscopic diagnostic on fast deuterium [23]. The same principle can be used for other species of ions [24]. Electrically neutral atoms are injected with a neutral beam injector, some of which undergo charge exchange with the fast ions in the plasma. The now neutral fast atom is no longer influenced by the magnetic field and will continue on a straight path. The fast neutral can be created in an excited state or become excited through collisions. It will shortly thereafter decay and emit a photon. If the decay transition is from the $n = 3$ to the $n = 2$ excited state, it is called a Balmer-α transition. The photon will have a wavelength around 656 nm and can be measured by the FIDA diagnostic, if it is emitted towards the detector. The emitted photon is Doppler shifted by the projection of the velocity of the emitting fast neutral along the direction towards the diagnostic. The principle of the FIDA diagnostic technique is sketched in figure 2.3.3 taken from [23]. FIDA diagnostic set-ups are installed in several fusion devices: five views at ASDEX Upgrade [25–27], three views at DIII-D [28, 29], two views at NSTX [30], two views at MAST [31, 32] and two views at LHD [24].

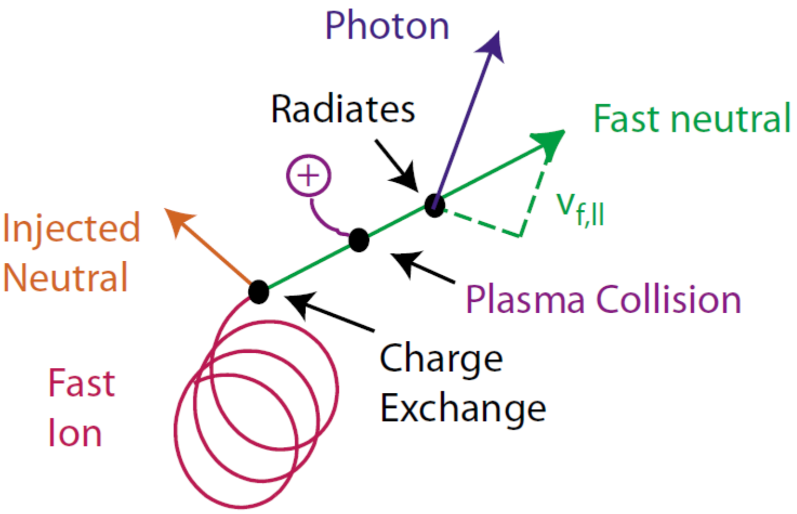

Figure 2.3.3: Sketch of the princple of a FIDA diagnostic, from [23].

Neutron emission spectrometry

The energy of a neutron created in a fusion reaction depends on the relative velocity of the reactants through conservation of momentum and energy. Neutrons are created in the following reactions:

$$\mathrm{D} + \mathrm{D} \rightarrow {}^{3}\mathrm{He} + \mathrm{n} \tag{2.3.6}$$

$$\mathrm{D} + \mathrm{T} \rightarrow {}^{4}\mathrm{He} + \mathrm{n} \tag{2.3.7}$$

where D is deuterium, T is tritium, n is a neutron and ^{3}He and ^{4}He denote helium-3 and helium-4, respectively.

Neutron emission spectrometry (NES) is a passive diagnostic method since it is not influencing the plasma itself. Several diagnostic principles exist for determining the energy of a neutron escaping the plasma. The detector with the best energy resolution is a time-of-flight spectrometer. A time-of-flight spectrometer consists of two sets of scintillator detectors placed at a given distance from each other. By correlating detections, it is possible to identify events caused by a neutron being detected in both. The flight time determines the neutron energy [33]. A second type of detector is a so-called compact spectrometer which consists of a single scintillator. By analysing the shape of the emitted light pulse, it is possible to extract information about the energy of the neutron [34]. NES is not a localized measurement. Instead the neutrons can potentially be created in any location in the plasma within the field-of-view of the instrument. Often, most neutrons are generated in so-called beam-target reactions between fast and thermal ions [35]. Hence the neutron rate scales linearly with the bulk ion and fast ion densities, and most neutrons will normally be generated in the centre of the plasma.

A commonly used reference of the neutron energy is from the 1973 paper by H. Brysk [36]. Here, Brysk derives an expression of the neutron energy, E_n, from conservation of energy and momentum in the center-of-mass frame

$$E_n = \frac{1}{2} m_n v_{cm}^2 + \frac{m_{He}}{m_n + m_{He}}(Q+K) + v_{cm}\cos(\theta)\sqrt{\frac{2 m_n m_{He}}{m_n + m_{He}}(Q+K)}\,, \tag{2.3.8}$$

where v_{cm} is the velocity of the center-of-mass frame, Q is the energy released in the fusion reaction (for a D-D reaction this is 3.27 MeV), K is the relative kinetic energy of the reacting nuclei, θ is the angle between the velocity of the center-of-mass frame and the velocity of the neutron in the center-of-mass frame and m_{He} and m_n are the Helium and neutron masses, respectively.

In this thesis, the focus is on neutrons from the D-D reaction and all examples are calculated using parameter values relevant for this reaction. Nevertheless, the neutron weight function derivation is valid for the D-T reaction or any other reaction directly producing neutrons, as long as appropriate values are used.

2.4 Velocity coordinates

A few words are needed about the velocity-space coordinate systems used throughout this thesis. The simplest is the $\left(v_\parallel, v_{\perp,1}, v_{\perp,2}\right)$-coordinate system, where $v_\parallel$ is the velocity parallel to the magnetic field and $v_{\perp,1}$ and $v_{\perp,2}$ are velocities perpendicular to the magnetic field. $v_{\perp,1}$ and $v_{\perp,2}$ are mutually perpendicular. Ions in a magnetic field are moving in a spiralling motion along the magnetic field. Their perpendicular velocities are given by

$$v_{\perp,1} = v_\perp \cos(\gamma)\,, \tag{2.4.1}$$

$$v_{\perp,2} = v_\perp \sin(\gamma),\,, \tag{2.4.2}$$

where $v_\perp$ is the total perpendicular velocity given by $v_\perp = \sqrt{v_{\perp,1}^2 + v_{\perp,2}^2}$ and γ is the gyro-angle. Assuming the gyro-motion of the ions occurs on a shorter time-scale compared to other important time scales, we can assume rotational symmetry around the magnetic field line. This rotational symmetry allows a reduction of the problem from three to two velocity dimensions by changing it to a cylindrical coordinate system and integrating out the gyro-angle. Thus, all the $\left(v_\parallel, v_\perp\right)$-figures are two-dimensional with no implied third direction. The Jacobian determinant for this transformation is $v_\perp$. The ion density, n, is given by

$$\begin{aligned} n &= \iiint f^{3D}\,\mathrm{d}v_{||}\mathrm{d}v_{\perp,1}\mathrm{d}v_{\perp,2} \\ &= \iint v_\perp f^{3D}\,\mathrm{d}v_{||}\mathrm{d}v_\perp \int \mathrm{d}\gamma \\ &= \iint 2\pi v_\perp f^{3D}\,\mathrm{d}v_{||}\mathrm{d}v_\perp = \iint f^{2D}\,\mathrm{d}v_{||}\mathrm{d}v_\perp\,. \end{aligned} \tag{2.4.3}$$

Here the assumption of rotational symmetry is used in order to move the distribution function outside the integral with respect to γ. The factor $2\pi v_\perp$ is included in the two-dimensional distribution function. From here on I will only be working with the two-dimensional distribution function, and therefore I will drop the 2D notation and simply write it as f. Throughout this thesis, $v_{||}$ and $v_\perp$ always refer to the velocities of the fast ions.

In the fast-ion community, a commonly used coordinate system is the (E, p)-coordinate system, where E is the kinetic energy of the ion and p is the pitch, defined as $p = \frac{v_{||}}{v}$ where v is the magnitude of the total ion velocity, $v = \sqrt{v_{||}^2 + v_\perp^2}$. This coordinate system is related to the $\left(v_{||}, v_\perp\right)$-coordinate system by the following simple relations

$$E = \frac{1}{2}m\left(v_{||}^2 + v_\perp^2\right)\,, \tag{2.4.4}$$

$$p = \frac{v_{||}}{\sqrt{v_{||}^2 + v_\perp^2}}\,, \tag{2.4.5}$$

$$\Updownarrow$$

$$v_{||} = p\sqrt{\frac{2E}{m}}\,, \tag{2.4.6}$$

$$v_\perp = \sqrt{1-p^2}\sqrt{\frac{2E}{m}}\,. \tag{2.4.7}$$

The Jacobian determinant for the transformation from $\left(v_{||}, v_\perp\right)$-coordinates to (E, p)-coordinates is

$$\begin{aligned} \det(J) &= \det\begin{bmatrix} \frac{\partial p}{\partial v_{||}} & \frac{\partial p}{\partial v_\perp} \\ \frac{\partial E}{\partial v_{||}} & \frac{\partial E}{\partial v_\perp} \end{bmatrix} \\ &= \det\begin{bmatrix} \frac{1}{\sqrt{v_{||}^2+v_\perp^2}} - \frac{v_{||}^2}{\left(v_{||}^2+v_\perp^2\right)^{3/2}} & -\frac{v_{||}v_\perp}{\left(v_{||}^2+v_\perp^2\right)^{3/2}} \\ m v_{||} & m v_\perp \end{bmatrix} \\ &= \frac{m v_\perp}{v} - \frac{m v_{||}^2 v_\perp}{v^3} + \frac{m v_{||}^2 v_\perp}{v^3} \\ &= \frac{m v_\perp}{v}\,. \end{aligned} \tag{2.4.8}$$

The energy-pitch coordinate system is popular because the energy of the ions can be read directly from the plot. The energy-pitch coordinate system is similar to the well-known polar coordinate system. Figure 2.4.1 shows how evenly distributed grid points in an (E, p)-coordinate system map to a $\left(v_{\|}, v_{\perp}\right)$-coordinate system. Lines of constant energies are semicircles in $\left(v_{\|}, v_{\perp}\right)$-coordinates and lines of constant pitch are straight lines going through origo. This uneven distribution of grid points in velocity-space is important to take into account when implementing inversion methods which penalize steep velocity-space gradients as explained in chapter 4.

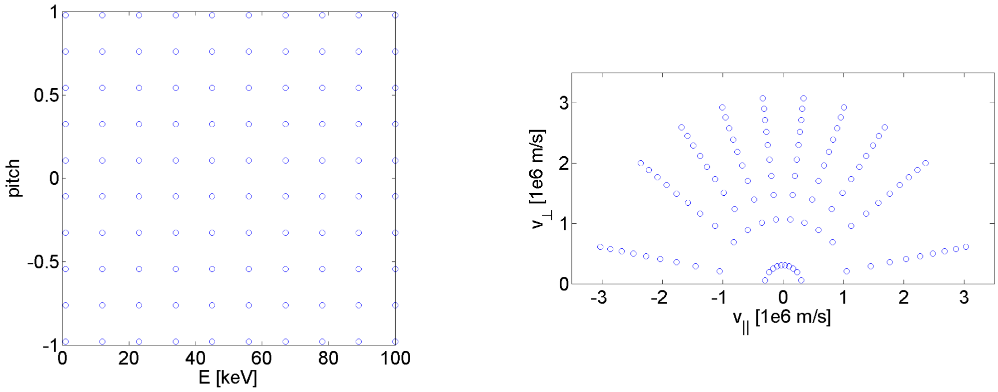

(a) (E, p)-coordinate system.

(b) $\left(v_{\|}, v_{\perp}\right)$-coordinate system.

Figure 2.4.1: Illustration of how grid points map from (E, p) to $\left(v_{\|}, v_{\perp}\right)$.

Because of its widespread use, the tomographies calculated in this thesis are in energy-pitch coordinates. However, the analytic derivations of the velocity-space sensitivity functions take on the most simple form in $\left(v_{\|}, v_{\perp}\right)$-coordinates.

2.5 Velocity-space weight functions

The all-important starting point of any attempt to solve an inverse problem is a well-defined forward problem. This goes for any inverse problem in any field of science. The fast-ion velocity-space sensitivity functions, or weight functions, are just this; a formulation of the forward problem. It is the function, w, which relates a part of a measured spectrum, $s\left(x_1, x_2, \phi\right)$, to the fast-ion distribution function, $f(E, p)$ [1]:

$$s\left(x_1, x_2, \phi\right)=\iint w\left(x_1, x_2, \phi, E, p\right) f(E, p) \,\mathrm{d} E \,\mathrm{d} p\,. \tag{2.5.1}$$

x_1 and x_2 denote what part of the spectrum this weight functions corresponds to, i.e. for a neutron energy spectrum, $x_1=E_{n,1}$ and $x_2=E_{n,2}$ and $s\left(E_{n,1}, E_{n,2}, \phi\right)$ is the number of neutrons with energies between $E_{n,1}$ and $E_{n,2}$. ϕ is the angle between the resolved direction and the magnetic field.

The integrals in equation (2.5.1) are approximated with sums:

$$S_k=\sum_i \sum_j \mathbf{W}_{i,j,k} \mathbf{F}_{i,j}\, \Delta E \Delta p\,. \tag{2.5.2}$$

i and j are summation indices of energy and pitch and k denotes the k'th measurement variable bin. Reshaping $\mathbf{W}$ to a $(1 \times n)$ row matrix and $\mathbf{F}$ to a $(n \times 1)$ column matrix and including $\Delta E \Delta p$ in $\mathbf{W}$ reduces equation (2.5.2) to

$$S_k = \mathbf{W}_k \mathbf{F} \,. \tag{2.5.3}$$

Given m data points in a spectrum, all m equations on the form of equation (2.5.3) can be combined into a single linear algebra problem

$$\mathbf{S} = \mathbf{W}\mathbf{F} \,, \tag{2.5.4}$$

where $\mathbf{S}$ is a $(m \times 1)$ column matrix containing every measurement and $\mathbf{W}$ is a $(m \times n)$ matrix dubbed the transfer matrix.

2.5.1 CTS weight functions

Prior to my PhD project, analytic weight functions had been derived for CTS [3]. In [3], the main focus was on a derivation of differential weight functions which are valid for a single Doppler shifted frequency. However, a real measurement will always be associated with a range in the projected velocity according to the spectral resolution of the instrument. Therefore, the derivation of CTS weight functions in the form they are most often used today is sketched here. This derivation is very similar to that of the Doppler-shifted part of the FIDA weight functions derived in [6]. CTS measures a frequency spectrum, from which the projected ion velocity along $\mathbf{k}^\delta$ can be inferred [37]. The projected velocity is denoted u and the one-dimensional velocity-distribution along $\mathbf{k}^\delta$ is denoted $g(u)$. This velocity-space projection is illustrated in figure 2.5.1, a modified version of figure 2 in [3]. The left figure shows the gyro-motion in the $(v_{\perp,1}, v_{\perp,2})$ plane.

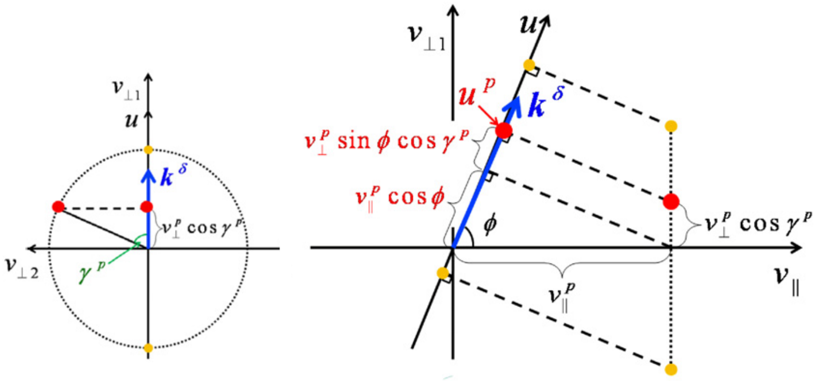

Figure 2.5.1: Sketch of the projection of ion velocity along $\mathbf{k}^\delta$. Modified version of a figure from [3].

Because of the rotational symmetry, the $v_{\perp,1}$- and $v_{\perp,2}$-axes can be oriented freely. The $v_{\perp,1}$ axis is placed such that $\mathbf{k}^\delta$ lies in the $\left(v_\parallel, v_{\perp,1}\right)$ plane. The gyro-angle is defined such that $v_{\perp,1} = v_\perp \cos(\gamma)$ and $v_{\perp,2} = v_\perp \sin(\gamma)$. The right part of figure 2.5.1 shows the $\left(v_\parallel, v_{\perp,1}\right)$-plane. The angle ϕ between the projection direction and the magnetic field line is the resolved angle or projection angle. This is the angle that determines the shape of the weight functions. In this coordinate system the gyrating ion moves up and down the vertical dashed line to the right. The yellow dots correspond to the extreme velocity-coordinates the ion reaches during its gyro-orbit. The p index stands for point and corresponds to the velocities of the ion illustrated by the red point. The projection along $\mathbf{k}^\delta$ is also shown. The projection equation is

$$u = v_\parallel \cos(\phi) + v_\perp \sin(\phi)\cos(\gamma)\,. \tag{2.5.5}$$

If a certain γ solves equation (2.5.5) for given $v_\parallel$, $v_\perp$ and u, so too does $2\pi - \gamma$. From equation (2.5.5) it is clear that a population of ions at a given position in velocity-space will give rise to an entire spectrum in u due to the gyro-motion [3]. The CTS velocity-space sensitivity for a projected velocity between u_1 and u_2 as a function of $v_\parallel$, $v_\perp$ and ϕ is written as $w\left(u_1, u_2, v_\parallel, v_\perp, \phi\right)$. It is defined as

$$w\left(u_1, u_2, v_\parallel, v_\perp, \phi\right) = \frac{1}{u_2 - u_1}\int_{u_1}^{u_2} \mathrm{pdf}_u \,\mathrm{d}u\,, \tag{2.5.6}$$

where pdf_u is the probability distribution function that an ion has a certain projected velocity. The factor in front ensures that the weight function is per unit velocity. For a given set of $v_\parallel$, $v_\perp$ and ϕ, pdf_u depends only on the gyro angle γ. Thus, pdf_u can be written as

$$\mathrm{pdf}_u = \mathrm{pdf}_\gamma \left|\frac{\mathrm{d}\gamma}{\mathrm{d}u}\right|\,, \tag{2.5.7}$$

where $\left|\frac{\mathrm{d}\gamma}{\mathrm{d}u}\right|$ denotes the absolute value of the derivative of γ with respect to u. pdf_γ is the probability density function of the gyro-angle. An ion is equally likely to have any given gyro angle, thus

$$\mathrm{pdf}_\gamma = \frac{1}{2\pi}\,. \tag{2.5.8}$$

γ is isolated in equation (2.5.5):

$$\gamma = \arccos\left(\frac{u - v_\parallel \cos(\phi)}{v_\perp \sin(\phi)}\right)\,. \tag{2.5.9}$$

The derivative of γ with respect to u is

$$\begin{aligned}\frac{\mathrm{d}\gamma}{\mathrm{d}u} &= -\frac{1}{v_\perp \sin(\phi)}\frac{1}{\sqrt{1 - \left(\frac{u - v_\parallel}{v_\perp \sin(\phi)}\right)^2}} \\ &= -\frac{1}{v_\perp \sin(\phi)}\frac{1}{\sin(\gamma)}\,. \end{aligned} \tag{2.5.10}$$

Changing the integration variable in equation (2.5.6) from u to γ' gives

$$w\left(u_1, u_2, v_\parallel, v_\perp, \phi\right) = \frac{1}{u_2 - u_1}\left(\int_{\gamma(u_1)}^{\gamma(u_2)} \frac{1}{2\pi}\frac{\left|\frac{\mathrm{d}\gamma'}{\mathrm{d}u}\right|}{\frac{\mathrm{d}\gamma'}{\mathrm{d}u}}\,\mathrm{d}\gamma' + \int_{2\pi-\gamma(u_1)}^{2\pi-\gamma(u_2)} \frac{1}{2\pi}\frac{\left|\frac{\mathrm{d}\gamma'}{\mathrm{d}u}\right|}{\frac{\mathrm{d}\gamma'}{\mathrm{d}u}}\,\mathrm{d}\gamma'\right)\,, \tag{2.5.11}$$

where the second integral arises because equation (2.5.5) is fulfilled for both γ and $2\pi-\gamma$ as mentioned earlier. The signs of the integrands in equation (2.5.11) depend only on γ since ϕ is only defined between 0 and π. For $\gamma<\pi$ equation (2.5.11) reduces to

$$\begin{aligned} w\left(u_1,u_2,v_\parallel,v_\perp,\phi\right) &= \frac{1}{(u_2-u_1)}\frac{1}{2\pi}\left(\int_{\gamma(u_1)}^{\gamma(u_2)}(-1)\,\mathrm{d}\gamma' + \int_{2\pi-\gamma(u_1)}^{2\pi-\gamma(u_2)}\mathrm{d}\gamma'\right) \\ &= \frac{1}{(u_2-u_1)}\frac{1}{2\pi}\left(\gamma(u_1)-\gamma(u_2)+2\pi-\gamma(u_2)-2\pi+\gamma(u_1)\right) \\ &= \frac{1}{(u_2-u_1)}\frac{\gamma(u_1)-\gamma(u_2)}{\pi}\,. \end{aligned} \tag{2.5.12}$$

Equation (2.5.12) can be understood as the fraction of the gyro-orbit which produces a certain Doppler-shift along $\mathbf{k}^\delta$ divided by the velocity bin width u_2-u_1. Inserting equation (2.5.9) in equation (2.5.12) gives the complete expression for CTS weight functions derived for a u-interval.

$$w\left(u_1,u_2,v_\parallel,v_\perp,\phi\right) = \frac{\arccos\left(\frac{u_1-v_\parallel\cos(\phi)}{v_\perp\sin(\phi)}\right)-\arccos\left(\frac{u_2-v_\parallel\cos(\phi)}{v_\perp\sin(\phi)}\right)}{\pi\left(u_2-u_1\right)}\,. \tag{2.5.13}$$

In (E,p)-coordinates, equation (2.5.13) becomes

$$w\left(u_1,u_2,E,p,\phi\right) = \frac{\arccos\left(\frac{u_1\sqrt{\frac{m}{2E}}-p\cos(\phi)}{\sqrt{1-p^2}\sin(\phi)}\right)-\arccos\left(\frac{u_2\sqrt{\frac{m}{2E}}-p\cos(\phi)}{\sqrt{1-p^2}\sin(\phi)}\right)}{\pi\left(u_2-u_1\right)}\,. \tag{2.5.14}$$

An important note is that equation (2.5.14) is derived using the pitch definition $p=\frac{v_\parallel}{v}$. At several fusion devices, pitch is defined positive in the co-current direction. At some machines, including ASDEX Upgrade, the toroidal current and the toroidal magnetic field are positive in opposite directions. At these machines the pitch is defined as $p=-\frac{v_\parallel}{v}$ and equation (2.5.14) becomes

$$w\left(u_1,u_2,E,p,\phi\right) = \frac{\arccos\left(\frac{u_1\sqrt{\frac{m}{2E}}+p\cos(\phi)}{\sqrt{1-p^2}\sin(\phi)}\right)-\arccos\left(\frac{u_2\sqrt{\frac{m}{2E}}+p\cos(\phi)}{\sqrt{1-p^2}\sin(\phi)}\right)}{\pi\left(u_2-u_1\right)}\,. \tag{2.5.15}$$

Figure 2.5.2 shows CTS weight functions calculated for various values of u and ϕ. The distinct triangular shape of CTS weight functions is evident for all but $\phi=90°$ which contains no information on the parallel velocity. Figure 2.5.3 shows examples of CTS weight functions calculated in (E,p)-coordinates. The weight functions in both figures 2.5.2 and 2.5.3 are plotted on a logarithmic scale. They are all calculated with $\Delta u = 0.5\times10^5$ m/s. It is evident how different parts of a given $g(u)$ spectrum are sensitive to different regions in velocity-space. When increasing values of the projected velocity u, a CTS diagnostic is sensitive to ions with increasing energy. A toroidally oriented view with a small angle to the magnetic field is sensitive to a rather narrow interval in $v_\parallel$ and pitch, whereas a radially oriented view with ϕ close to 90° is selective in $v_\perp$ and energy. This is the reason why it is beneficial to have multiple views with different angles to the magnetic field. Finally it is shown that the weight functions for $\phi'>90°$ are mirrored versions of the weight functions for $\phi<90°$ with $\phi'=180°-\phi$. This is also evident from equation (2.5.13), which is symmetric for $\phi\rightarrow180°-\phi$, $v_\parallel\rightarrow-v_\parallel$.

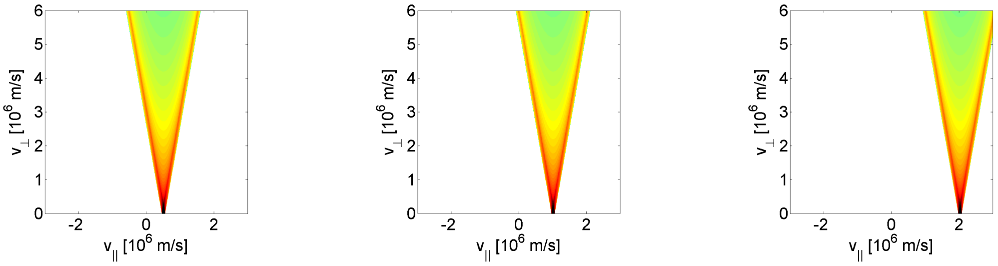

(a) $u = 0.5 \times 10^6$ m/s, $\phi = 10°$ (b) $u = 1 \times 10^6$ m/s, $\phi = 10°$ (c) $u = 2 \times 10^6$ m/s, $\phi = 10°$

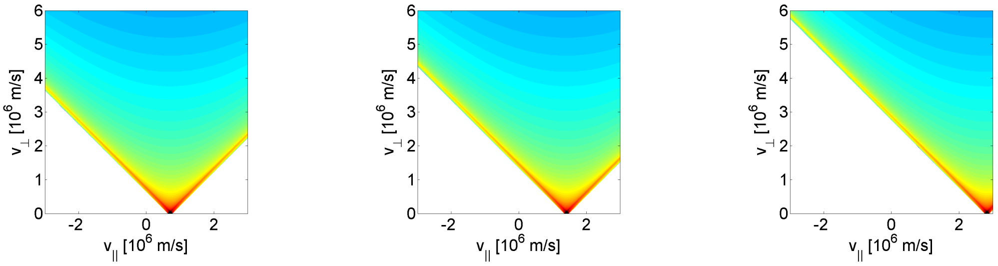

(d) $u = 0.5 \times 10^6$ m/s, $\phi = 45°$ (e) $u = 1 \times 10^6$ m/s, $\phi = 45°$ (f) $u = 2 \times 10^6$ m/s, $\phi = 45°$

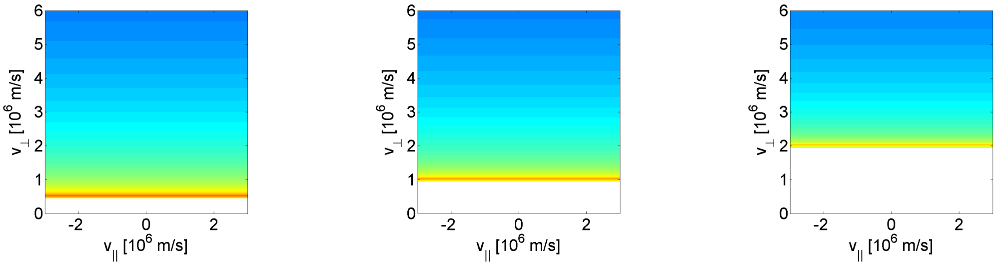

(g) $u = 0.5 \times 10^6$ m/s, $\phi = 90°$ (h) $u = 1 \times 10^6$ m/s, $\phi = 90°$ (i) $u = 2 \times 10^6$ m/s, $\phi = 90°$

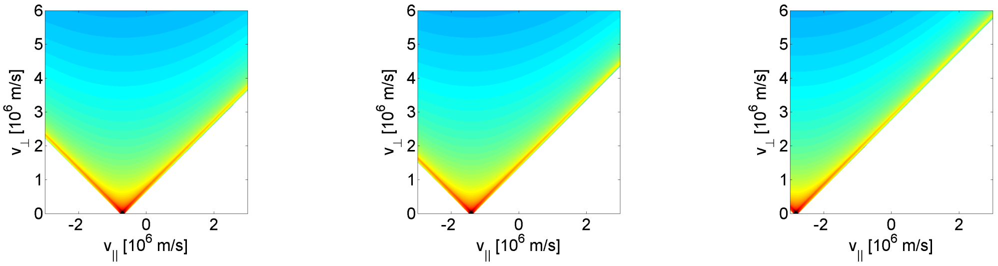

(j) $u = 0.5 \times 10^6$ m/s, $\phi = 135°$ (k) $u = 1 \times 10^6$ m/s, $\phi = 135°$ (l) $u = 2 \times 10^6$ m/s, $\phi = 135°$

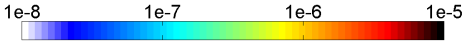

Figure 2.5.2: Examples of CTS weight functions calculated in $\left(v_{\|}, v_{\perp}\right)$-coordinates for different values of u and ϕ. The units of the CTS weight functions are [1/(m/s)].

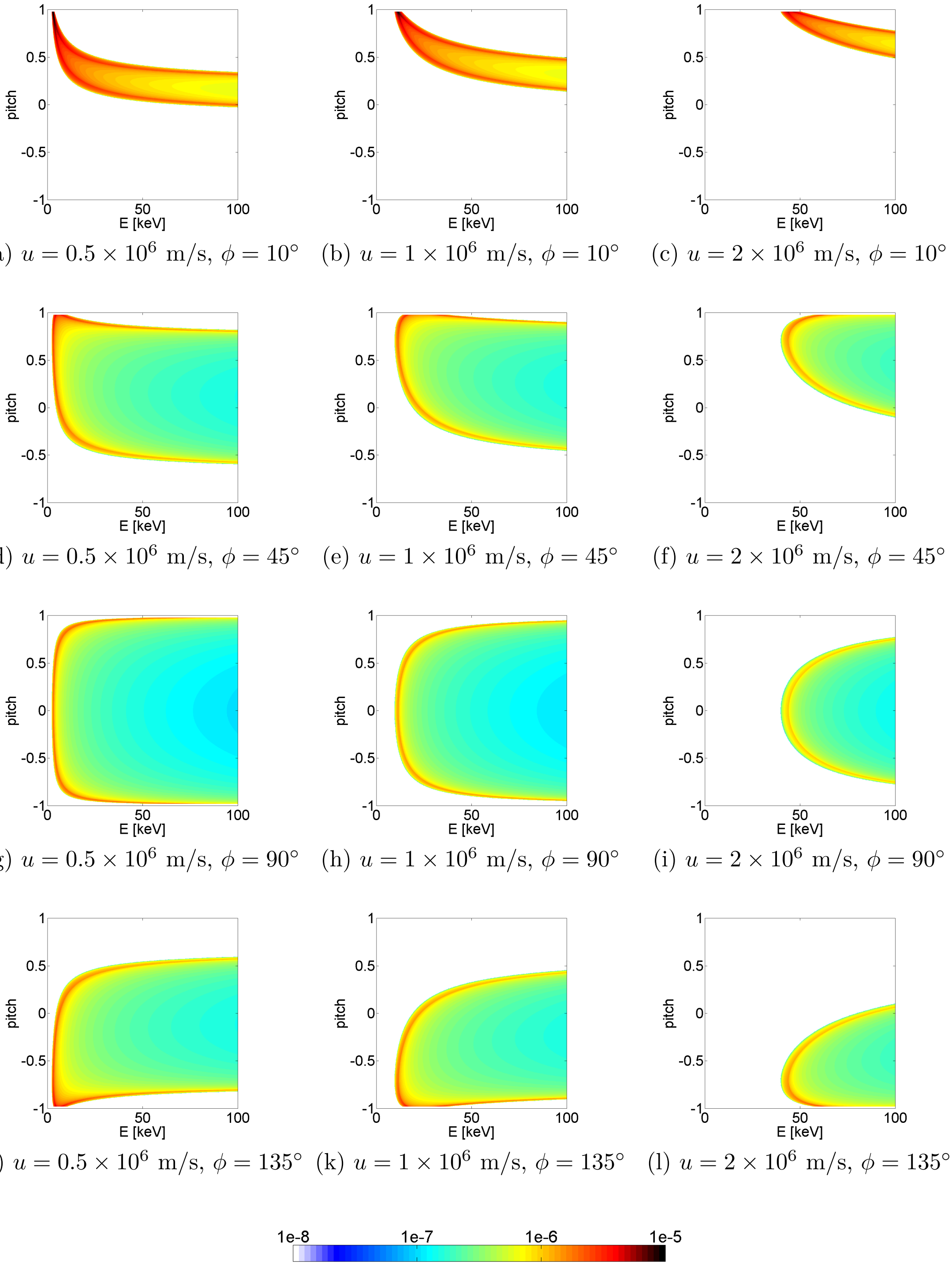

(a) $u = 0.5 \times 10^6$ m/s, $\phi = 10°$ (b) $u = 1 \times 10^6$ m/s, $\phi = 10°$ (c) $u = 2 \times 10^6$ m/s, $\phi = 10°$

(d) $u = 0.5 \times 10^6$ m/s, $\phi = 45°$ (e) $u = 1 \times 10^6$ m/s, $\phi = 45°$ (f) $u = 2 \times 10^6$ m/s, $\phi = 45°$

(g) $u = 0.5 \times 10^6$ m/s, $\phi = 90°$ (h) $u = 1 \times 10^6$ m/s, $\phi = 90°$ (i) $u = 2 \times 10^6$ m/s, $\phi = 90°$

(j) $u = 0.5 \times 10^6$ m/s, $\phi = 135°$ (k) $u = 1 \times 10^6$ m/s, $\phi = 135°$ (l) $u = 2 \times 10^6$ m/s, $\phi = 135°$

Figure 2.5.3: Examples of CTS weight functions calculated in (E, p)-coordinates for different values of u and ϕ. The units of the CTS weight functions are [1/(m/s)].

2.5.2 FIDA weight functions

Numeric FIDA weight functions have been calculated since 2007 [1]. Recently, analytic FIDA weight functions were formulated [4]. The FIDA weight functions are comprised of two factors.

$$w\left(\lambda_1, \lambda_2 \middle| v_\parallel, v_\perp, \phi\right) = R\left(v_\parallel, v_\perp\right) \operatorname{prob}\left(\lambda_1 < \lambda < \lambda_2 \middle| v_\parallel, v_\perp, \phi\right) , \tag{2.5.16}$$

where $R\left(v_\parallel, v_\perp\right)$ is the total FIDA intensity per fast ion irrespective of wavelength. It is a measure of the number of photons emitted due to the charge-exchange reaction and detected in the FIDA instrument as a function of the velocity of the fast ion. $\operatorname{prob}\left(\lambda_1 < \lambda < \lambda_2 \middle| v_\parallel, v_\perp, \phi\right)$ is the probability that an emitted photon will have a wavelength between λ_1 and λ_2 given the velocity of the fast ion and the angle between the line-of-sight of the detector and the magnetic field in the measurement volume. The probability part is influenced by three different physical effects. The first is a Doppler-shift factor identical to the one for CTS derived in section 2.5.1. The second effect is Stark splitting. This effect splits the spectral lines of an atom when it is placed in a strong electric field. Here it is caused by the $\mathbf{v} \times \mathbf{B}$ electric field seen by the atom in its own reference frame [25], where $\mathbf{B}$ is the magnetic field. The last effect arises because of the charge exchange probability and the probability for the specific relaxation to occur [4]. Examples of numeric FIDA weight functions are shown in figure 2.5.4 in both $\left(v_\parallel, v_\perp\right)$- and (E, p)-coordinates, for different wavelengths and ϕ-angles. The weight function are calculated in (E, p)-coordinates and transformed onto $(v_\parallel, v_\perp)$-coordinates. The shaded regions correspond to parts of velocity-space not included in the simulation of the weight functions. An approximate overall shape of the weight functions are determined by the Doppler-shift effect which is identical to the CTS weight functions. Therefore, the FIDA weight functions in general resemble those for CTS. The triangular shape of the FIDA weight functions in $\left(v_\parallel, v_\perp\right)$-space is evident in figures 2.5.4a-2.5.4c. The effect of the Stark splitting is especially evident in figures 2.5.4a and 2.5.4g. It can be seen as the spreading of the maxima in the weight functions. When comparing figures 2.5.4a-2.5.4c to figure 2.5.2a-2.5.2c it is seen that the FIDA weight functions are not symmetric like the CTS weight functions. This is caused by the charge-exchange probability which favours parts of the gyro-orbit since it depends on the relative velocity [4].

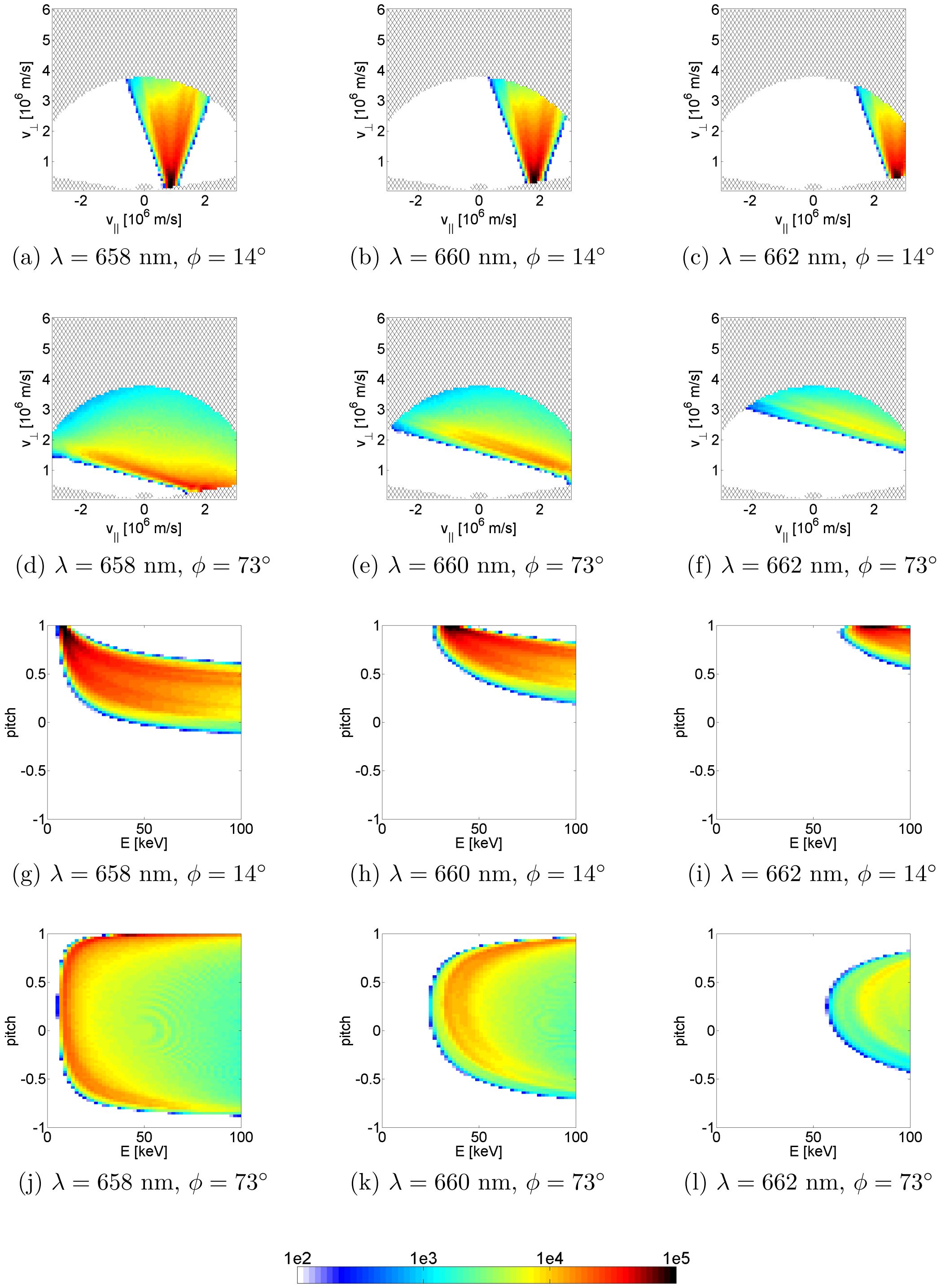

(a) $\lambda = 658$ nm, $\phi = 14°$ (b) $\lambda = 660$ nm, $\phi = 14°$ (c) $\lambda = 662$ nm, $\phi = 14°$

(d) $\lambda = 658$ nm, $\phi = 73°$ (e) $\lambda = 660$ nm, $\phi = 73°$ (f) $\lambda = 662$ nm, $\phi = 73°$

(g) $\lambda = 658$ nm, $\phi = 14°$ (h) $\lambda = 660$ nm, $\phi = 14°$ (i) $\lambda = 662$ nm, $\phi = 14°$

(j) $\lambda = 658$ nm, $\phi = 73°$ (k) $\lambda = 660$ nm, $\phi = 73°$ (l) $\lambda = 662$ nm, $\phi = 73°$

Figure 2.5.4: Examples of FIDA weight functions calculated in both $\left(v_{\|}, v_{\perp}\right)$- and (E, p)-coordinates in units of FIDA intensity per fast ion.

2.5.3 Neutron count detector weight functions

In reference [1], a weight function for the neutron diagnostic at the DIII-D tokamak in San Diego is shown. This weight function describes a neutron count detector which simply counts the number of neutrons irrespective of their energy. In paper I, I show how these neutron count weight functions arise as the limiting case when the NES weight function include all neutron energies.

2.5.4 Applications of velocity-space weight functions

The weight functions have additional applications besides velocity-space tomography. So far, weight functions have been used in analyses in four different ways. The most simple use is in an identification of the part of velocity space measured by a given diagnostic [1,3–6,14,19,23,25–28,30,31,38–50]. The second use is together with an assumed fast-ion distribution function. By plotting the product of a weight function and the distribution function, i.e. the integrand of equation (2.5.1) it is possible to identify the ions which produced a signal in a certain part of a measured spectrum [1,2,5,6,14,23,25,28,44–50]. The third use is to evaluate equation (2.5.4) as a very quick way to generate synthetic spectra [3,5,6,51–53]. Often, synthetic spectra are generated using a Monte Carlo code which can be time-consuming. The final use is in an inversion of equation (2.5.4) in fast-ion velocity-space tomography [3,15,27,51–55].

2.6 Velocity-space tomography

Solving equation (2.5.4) is a mathematically ill-posed inverse problem. Ill-posed inverse problems are encountered in many different fields of science. A problem is defined as well-posed if its solution fulfils the three requirements of existence, uniqueness and continuity with respect to the data [56]. The solution must exist, it should be unique and not change drastically for small changes in the data. If the solution does not fulfil all three conditions, it is ill-posed. Inverse problems are very often ill-posed [57]. To solve an ill-posed inverse problem, it is necessary to regularize the problem or include some additional assumptions. This will be explained further in chapter 4. A tomography problem is an example of an inverse ill-posed problem. The most well-known use of tomography is in medical imaging where an electromagnetic wave is sent through a patient. By rotating the source around the patient, many different lines-of-sight are obtained. Measuring the transmitted fraction of the radiation, it is possible to determine the internal structures. Thereby, an internal cross sectional image can be produced.

In velocity-space tomography, it is not in the same way possible to rotate source and detector around a stationary target. Instead, multiple measurements are performed simultaneously using several different lines-of-sight. Because of the gyro-motion of the ions around the magnetic field lines, ions with many different velocities can give rise to a given measured signal in a diagnostic. Thus, each individual data point in the measurements is sensitive to a larger region of velocity-space compared to the simple straight lines of conventional tomography. This makes it possible to cover the entire velocity-space using significantly fewer lines-of-sight compared to conventional tomography. On the other hand, the broadly covering weight functions make it more difficult to resolve fine details in the velocity-space distribution function. Before I started my project, velocity-space tomography was calculated using a method called truncated singular value decomposition [51] which is a method that expands the solution in basis functions with increasing frequency. To reduce the effect of noise, the expansion is truncated such that the highest frequency functions are not included, as these are dominated by the noise. Only tomographies using synthetic data had been calculated. Synthetic data is here defined as self-generated artificial data which is useful for method development and testing.

Chapter 3

Neutron emission spectrometry weight functions

The energy of a neutron created in a fusion reaction between a fast ion and a thermal ion depends on the relative velocity of the reactants. Thus neutron emission spectrometry (NES) can be used to diagnose fast ions in a fusion plasma. To determine the velocity-space sensitivity of the NES measurements, I derived NES weight functions analytically and verified the results numerically. These results are valid for the often dominating neutron contribution coming from reactions involving a fast and a thermal ion. Other possible sources of neutrons are reactions involving two fast ions or two thermal ions.

3.1 NES weight functions

The analytic derivation of the NES weight functions are explained in detail in paper I. As for the FIDA weight functions, the NES weight functions are written as the product of a rate part, R, and a probability part, prob:

$$w\left(v_{n,1}, v_{n,2}, \phi, v_{\|}, v_{\perp}, \mathbf{r}\right) = R\left(\phi, v_{\|}, v_{\perp}, \mathbf{r}\right) \mathrm{prob}\left(v_{n,1} < v_n < v_{n,2} \middle| \phi, v_{\|}, v_{\perp}\right) , \tag{3.1.1}$$

where v_n is the magnitude of the neutron velocity, and ϕ is the angle between the line-of-sight of the detector and the magnetic field. The rate part determines the total number of neutrons sent towards the detector per fast ion per second irrespective of the neutron energy. The probability part determines the probability that the neutron has a velocity between $v_{n,1}$ and $v_{n,2}$. The neutron rate per fast ion is defined as

$$R\left(\phi, v_{\|}, v_{\perp}, \mathbf{r}\right) = \frac{\Omega(\mathbf{r})}{4\pi} \iint f_t\left(v_{t,\|}, v_{t,\perp}, \mathbf{r}\right) \sigma\left(\phi, v_{rel}\right) v_{rel} \, \mathrm{d}v_{t,\|} \mathrm{d}v_{t,v_{\perp}} , \tag{3.1.2}$$

where $\Omega(\mathbf{r})$ is the solid angle of the detector seen from the plasma, f_t is the thermal ion distribution and $v_{t,\|}$ and $v_{t,\perp}$ are the parallel and perpendicular thermal velocities, respectively. v_{rel} is the magnitude of the relative velocity of the fast and the thermal ions and σ is the fusion reaction cross section. Figure 3.1.1 shows examples of the rate part of NES weight functions calculated assuming stationary thermal ions and disregarding the angle-dependence in σ. See paper I for more details. If the bulk plasma drifts toroidally around the torus, it will affect the rate part through the relative velocity. This effect is shown in figure 3.1.1b. The value of the co-current bulk ion drift velocity of 2.1×10^5 m/s is chosen in order to be able to compare these results with the neutron count measurement weight function described in [1]. As expected, the rate function increases with energy since both the relative velocity and the fusion cross section increase with energy in the energy range shown here.

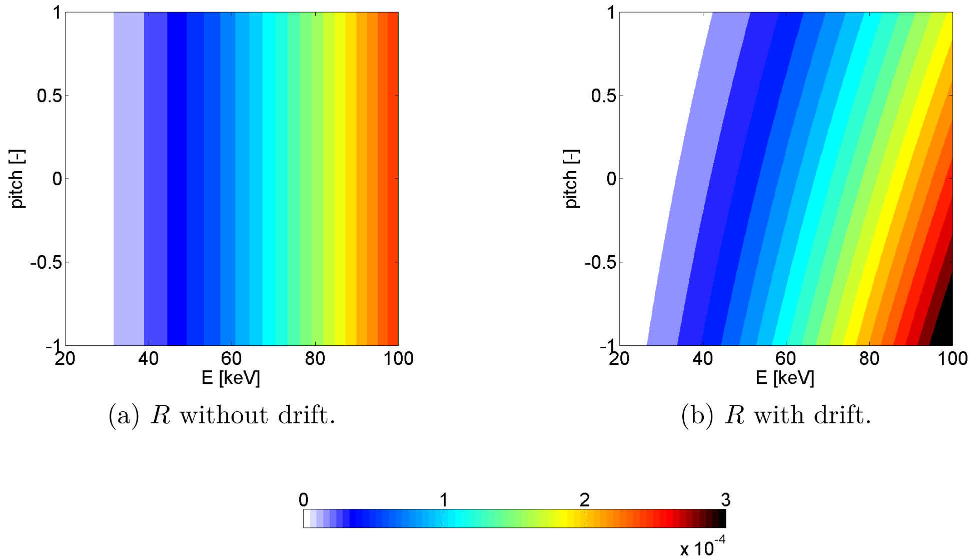

(a) R without drift.

(b) R with drift.

Figure 3.1.1: Rate functions with and without a toroidal drift of the thermal ions in units of neutrons per fast ion per second. The co-current drift velocity is $2.1 \times 10^5\ \frac{\mathrm{m}}{\mathrm{s}}$. The thermal ion density is $5 \times 10^{19}\ \mathrm{m}^{-3}$.

In analogy to the derivation of the CTS weight functions in section 2.5.1, the probability part of the NES weight function is defined as

$$\mathrm{prob}\left(v_{n,1} < v_n < v_{n,2} \middle| \phi, v_\parallel, v_\perp\right) = \int_{v_{n,1}}^{v_{n,2}} \mathrm{pdf}_{v_n}\, \mathrm{d}v_n \,, \tag{3.1.3}$$

where pdf_{v_n} is the neutron velocity probability density function. Assuming stationary target ions, the neutron velocity only depends on the gyro-angle of the fast ion, if the parallel and perpendicular velocities of the fast ion and the angle between the magnetic field and the detector are all given. Like for the CTS weight function, pdf_{v_n} is written as

$$\mathrm{pdf}_{v_n} = \mathrm{pdf}_\gamma \left| \frac{\mathrm{d}\gamma}{\mathrm{d}v_n} \right| \,, \tag{3.1.4}$$

Since an ion is equally likely to have any given gyro angle, pdf_γ is

$$\mathrm{pdf}_\gamma = \frac{1}{2\pi} \,. \tag{3.1.5}$$

The task is now to derive a relation between v_n and γ expressed only in known quantities. The full derivation including all the intermediate results can be found in paper I. Here, selected necessary steps are sketched. The relation is derived from conservation of energy and momentum in the D-D fusion reaction described in equation (2.3.6), neglecting the energy and momentum of the thermal ions. Conservation of momentum gives

$$m_f \mathbf{v}_f = m_{He} \mathbf{v}_{He} + m_n \mathbf{v}_n \,. \tag{3.1.6}$$

Conservation of energy gives

$$\frac{1}{2} m_f v_f^2 + Q = \frac{1}{2} m_{He} v_{He}^2 + \frac{1}{2} m_n v_n^2 \,. \tag{3.1.7}$$

Here m_f and $\mathbf{v}_f$ are the mass and velocity of the fast ion, m_{He} and $\mathbf{v}_{He}$ are the mass and velocity of the helium-3 ion and m_n and $\mathbf{v}_n$ are the mass and velocity of the neutron. Q is the energy released in the fusion reaction. For this reaction it is 3.27 MeV. $\mathbf{v}_{He}$ is isolated in equation (3.1.6) and the result is squared giving

$$v_{He}^2 = \frac{1}{m_{He}^2} \left(m_f^2 v_f^2 + m_n^2 v_n^2 - 2 m_f m_n \mathbf{v}_f \cdot \mathbf{v}_n \right) \,. \tag{3.1.8}$$

Inserting equation (3.1.8) in equation (3.1.7) and rearranging gives the following equation

$$\mathbf{v}_f \cdot \hat{\mathbf{v}}_n = \frac{1}{2} \frac{(m_{He} + m_n)}{m_f} v_n - \frac{1}{2} \frac{(m_{He} - m_f)}{m_n} \frac{v_f^2}{v_n} - \frac{m_{He}}{m_f m_n} \frac{Q}{v_n} \,, \tag{3.1.9}$$

where $\hat{\mathbf{v}}_n$ is the unit vector in the direction of the neutron velocity. $\mathbf{v}_f \cdot \hat{\mathbf{v}}_n$ can also be written as

$$\mathbf{v}_f \cdot \hat{\mathbf{v}}_n = v_\parallel \cos(\phi) + v_\perp \sin(\phi) \cos(\gamma) \,, \tag{3.1.10}$$

where ϕ is the angle between the magnetic field and the line-of-sight of the detector. Combining equations (3.1.9) and (3.1.10) a relation between v_n and γ is obtained which depends only on known quantities:

$$\gamma = \arccos \left(\frac{1}{v_\perp \sin(\phi)} \left(\frac{1}{2} \frac{(m_{He} + m_n)}{m_f} v_n - \frac{1}{2} \frac{(m_{He} - m_f)}{m_n} \frac{v_f^2}{v_n} - \frac{m_{He}}{m_f m_n} \frac{Q}{v_n} - v_\parallel \cos(\phi) \right) \right) \,. \tag{3.1.11}$$

Inserting equation (3.1.4) in equation (3.1.3) and changing the integration variable to γ gives

$$\mathrm{prob} \left(v_{n,1} < v_n < v_{n,2} \middle| \phi, v_\parallel, v_\perp \right) = \frac{1}{2\pi} \left(\int_{\gamma(v_{n,1})}^{\gamma(v_{n,2})} \frac{\left| \frac{\mathrm{d}\gamma}{\mathrm{d}v_n} \right|}{\frac{\mathrm{d}\gamma}{\mathrm{d}v_n}} \mathrm{d}\gamma + \int_{2\pi - \gamma(v_{n,1})}^{2\pi - \gamma(v_{n,2})} \frac{\left| \frac{\mathrm{d}\gamma}{\mathrm{d}v_n} \right|}{\frac{\mathrm{d}\gamma}{\mathrm{d}v_n}} \mathrm{d}\gamma \right) \,, \tag{3.1.12}$$

where the second integral arises since equation (3.1.10) is fulfilled for both γ and $2\pi - \gamma$. Equation (3.1.11) is differentiated with respect to v_n

$$\frac{\mathrm{d}\gamma}{\mathrm{d}v_n} = - \frac{1}{\sin(\gamma)} \left(\frac{1}{v_\perp \sin(\phi)} \left(\frac{1}{2} \frac{(m_{He} + m_n)}{m_f} + \frac{1}{2} \frac{(m_{He} - m_f)}{m_n} \frac{v_f^2}{v_n^2} + \frac{m_{He}}{m_f m_n} \frac{Q}{v_n^2} \right) \right) \,. \tag{3.1.13}$$

The outer parenthesis in equation (3.1.13) is always positive, and therefore the sign of $\frac{\mathrm{d}\gamma}{\mathrm{d}v_n}$ depends only on γ. For $\gamma < \pi$, $\frac{\mathrm{d}\gamma}{\mathrm{d}v_n}$ is negative and for $\gamma > \pi$ it is positive. Thus equation (3.1.12) becomes

$$\text{prob}\left(v_{n,1} < v_n < v_{n,2} \middle| \phi, v_\parallel, v_\perp\right) = \frac{\gamma\left(v_{n,1}\right) - \gamma\left(v_{n,2}\right)}{\pi}\,. \tag{3.1.14}$$

Equation (3.1.14) can be evaluated using equation (3.1.11) for given values of $v_\parallel$, $v_\perp$ and ϕ. Figure 3.1.2 shows examples of the probability part of the NES weight functions in $\left(v_\parallel, v_\perp\right)$-coordinates for different neutron energies and ϕ-angles. The probability part of NES weight functions has a distinct circular shape in velocity-space. In (E, p)-coordinates, equation (3.1.11) becomes

$$\begin{aligned}\gamma \;=\; & \arccos\left(\frac{1}{\sqrt{1-p^2}}\frac{1}{\sin(\phi)}\left(\frac{1}{2}\frac{(m_{He}+m_n)}{\sqrt{m_f m_n}}\sqrt{\frac{E_n}{E}} - \frac{1}{2}\frac{(m_{He}-m_f)}{\sqrt{m_f m_n}}\sqrt{\frac{E}{E_n}}\right.\right. \\ & \left.\left. -\frac{1}{2}\frac{m_{He}}{\sqrt{m_f m_n}}\frac{Q}{\sqrt{E E_n}} - p\cos(\phi)\right)\right)\,, \end{aligned} \tag{3.1.15}$$

where E_n is the neutron energy. Figure 3.1.3 shows examples of the probability part of NES weight functions in (E, p)-coordinates.

I calculated the numerical NES weight functions in paper I using a PYTHON code written and used by the team of scientists responsible for the daily operation of the neutron detectors at JET [58, 59]. In order to be applicable for calculating numeric NES weight functions, a code must be able to calculate a neutron energy spectrum based on any given fast-ion distribution function. The procedure can be visualized using a 3D grid, see figure 3.1.4. The axes are (E, p, E_n), where E_n is the neutron energy. A delta function-like fast ion distribution is made by placing ions in a single cell in the (E, p)-plane. The resulting neutron energy spectrum is placed along the E_n axis at the relevant (E, p)-grid point, see figure 3.1.4a. This is repeated for every grid point in the (E, p)-plane, see figure 3.1.4b. Afterwards, 2D slices for a given E_n define the weight functions, see figure 3.1.4c. A formal exposition of this idea can be found in paper I.

Figure 3.1.5 shows a comparison of the probability part of the NES weight function calculated analytically and numerically demonstrating the excellent agreement between the two approaches. The numerically calculated weight functions contain Monte Carlo noise, and are calculated on a coarser grid than the analytically calculated weight functions.

In the numerical code, it is possible to have the thermal ions distributed according to a Maxwellian distribution with a given finite temperature. The effect of a finite temperature of the thermal ions is a smearing of the finer features of the probability part as shown in paper I.

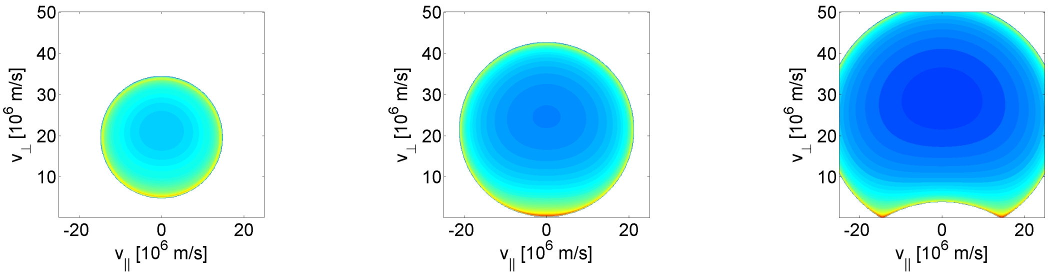

(a) $E_n = 2$ MeV, $\phi = 90°$ (b) $E_n = 2.4$ MeV, $\phi = 90°$ (c) $E_n = 3$ MeV, $\phi = 90°$

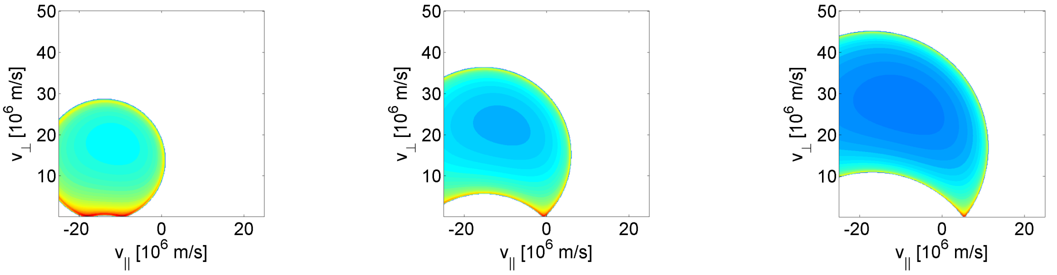

(d) $E_n = 2$ MeV, $\phi = 45°$ (e) $E_n = 2.4$ MeV, $\phi = 45°$ (f) $E_n = 3$ MeV, $\phi = 45°$

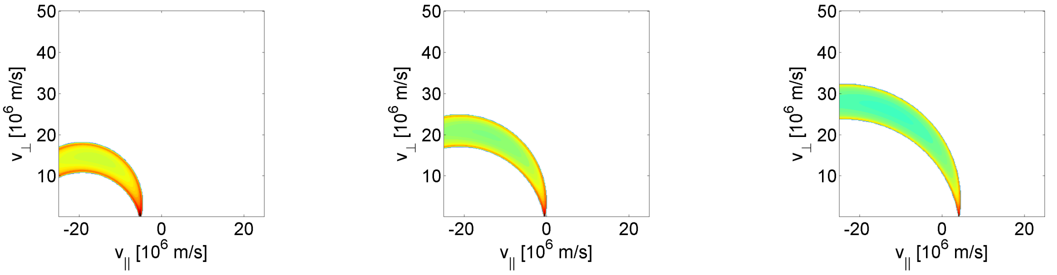

(g) $E_n = 2$ MeV, $\phi = 10°$ (h) $E_n = 2.4$ MeV, $\phi = 10°$ (i) $E_n = 3$ MeV, $\phi = 10°$

Figure 3.1.2: Examples of the probability part of NES weight functions calculated in $\left(v_{\|}, v_{\perp}\right)$-coordinates.

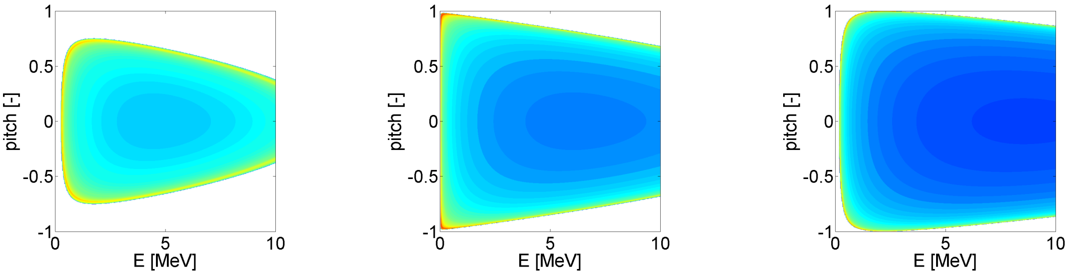

(a) $E_n = 2$ MeV, $\phi = 90°$ (b) $E_n = 2.4$ MeV, $\phi = 90°$ (c) $E_n = 3$ MeV, $\phi = 90°$

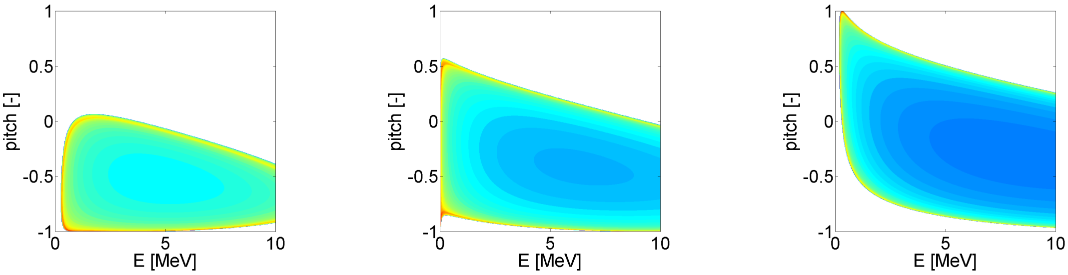

(d) $E_n = 2$ MeV, $\phi = 45°$ (e) $E_n = 2.4$ MeV, $\phi = 45°$ (f) $E_n = 3$ MeV, $\phi = 45°$

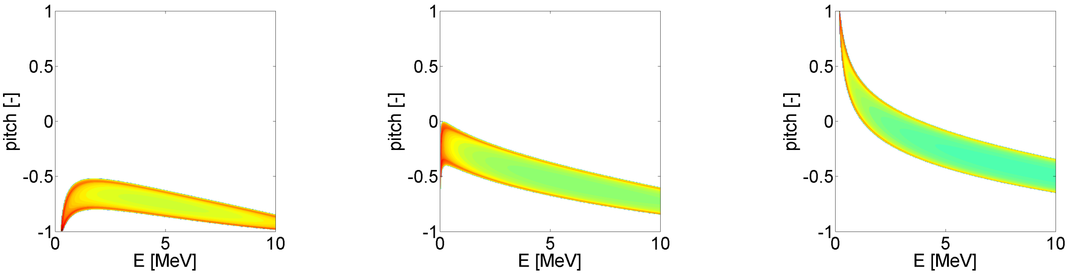

(g) $E_n = 2$ MeV, $\phi = 10°$ (h) $E_n = 2.4$ MeV, $\phi = 10°$ (i) $E_n = 3$ MeV, $\phi = 10°$

Figure 3.1.3: Examples of NES weight functions calculated in (E, p)-coordinates.

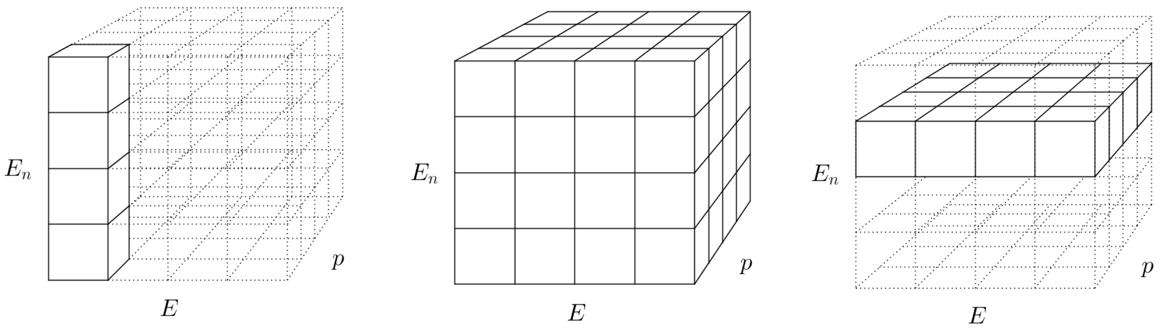

(a) A spectrum is calculated.

(b) This is repeated for every (E, p)-coordinate.

(c) Single slice showing weight function.

Figure 3.1.4: Illustration of how weight functions can be extracted from the output of a numerical code capable of calculating a neutron energy spectrum given a point-like fast-ion distribution.

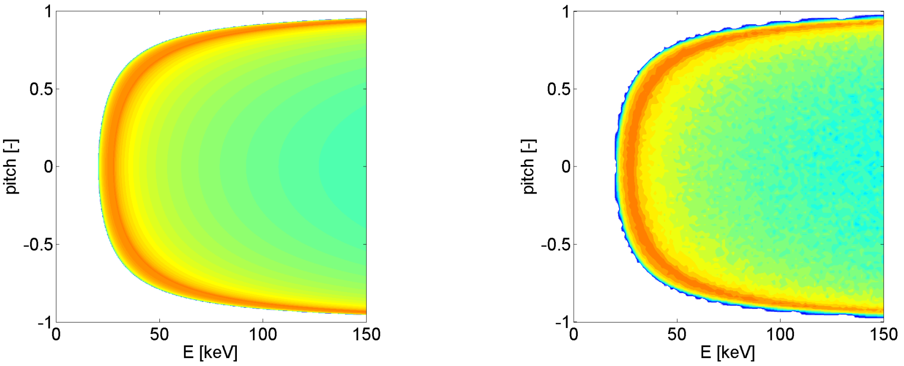

(a) $\phi = 90°$, analytical

(b) $\phi = 90°$, numerical

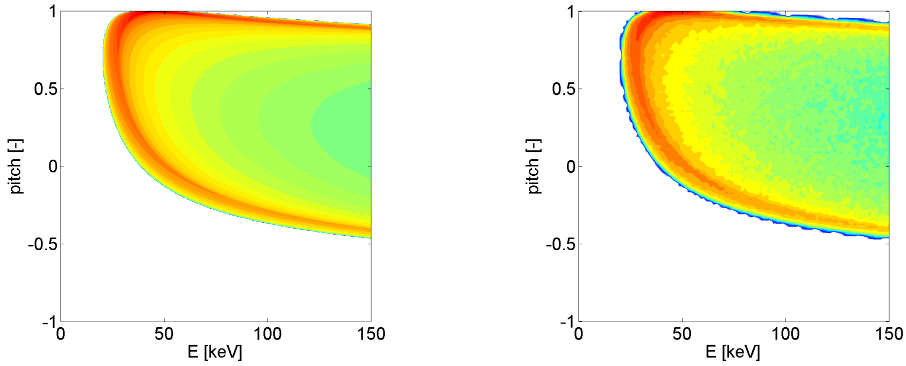

(c) $\phi = 45°$, analytical

(d) $\phi = 45°$, numerical

Figure 3.1.5: Examples of the probability part of NES weight functions calculated analytically and numerically for $\phi = 45°$ and $\phi = 90°$.

3.1.1 Using NES weight functions in a forward model

As explained in section 6 in paper I, it is possible to use the weight functions in a forward model by solving equation (2.5.4). Since it only consists of a matrix multiplication, it is very fast. The NES weight function depends on the thermal ion temperature and density. The density dependence is only through the rate part of the weight function. The neutron rate scales linearly with the thermal ion density as can be seen by inserting equation (2.3.1) in equation (3.1.2). A neutron rate per thermal ion can be calculated by normalizing the neutron rate with the thermal ion density. This makes it possible for a rate part calculated for any given thermal ion density to be scaled appropriately as needed. The probability part of the weight function depends on the thermal ion temperature if the thermal species in the energy and momentum equations are not neglected. This is easily implemented for the numerical weight functions. The effect is shown in section 4 in paper I. This makes it necessary to calculate numerical weight functions for every thermal ion temperature. To use the weight functions in a fast forward model, a database of weight functions can be created, each calculated for different temperatures and scaled using the appropriate thermal ion density as needed. Figure 3.1.6a shows the comparison of synthetic neutron spectra calculated using the weight functions and the conventional Monte Carlo based forward model used for calculating neutron energy spectra for the time-of-flight neutron spectrometer TOFOR at JET [60]. Figure 3.1.6b shows the measured thermal ion temperature as a function of position in the TOFOR field-of-view for this discharge. The conventional forward model splits the TOFOR field-of-view in cubes with a volume of 1 cm^3 each, for a total of 128000 cubes. The needed plasma conditions are then interpolated for each cube and assumed constant over the cube volume. For the neutron spectrum calculated using weight functions, the field-of-view is split in 10 volumes. Despite the much coarser spatial resolution, it is possible to recreate the conventional spectrum to a very good approximation, as seen in figure 3.1.6a.

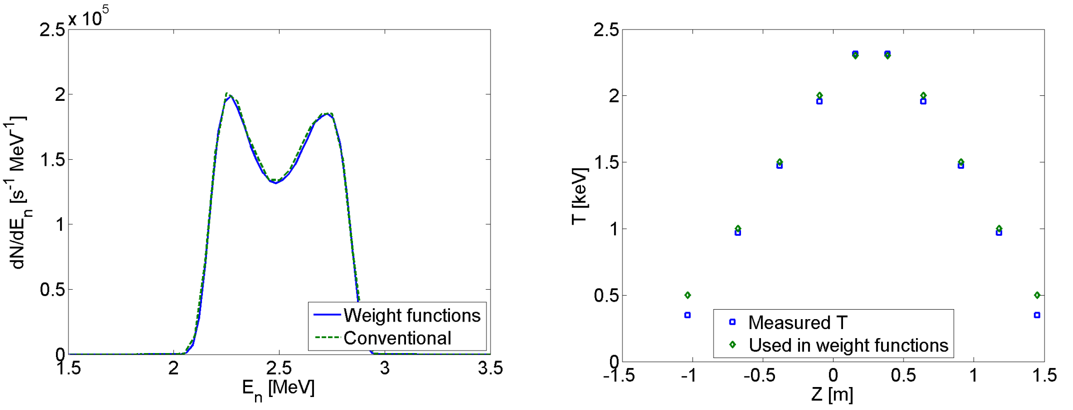

(a) Neutron spectra.

(b) Measured temperature profile and temperatures used in calculations of the weight functions.

Figure 3.1.6: Synthetic neutron spectrum calculated using the NES weight functions compared to a synthetic spectrum calculated using the conventional Monte Carlo based forward model.

3.1.2 Deriving NES weight functions in center-of-mass frame

In paper I, I derive an analytic expression for the probability part of the NES weight function in the lab frame. In the NES community, the common reference for the neutron energy as a function of the velocity of the reacting atoms is equation (2.3.8) [36]. Here, the derivation of weight functions starting from equation (2.3.8) is outlined. I will show that both approaches to derive weight functions encouragingly lead to the same result, as they should. However, since quite a lot of algebra is involved, the complete derivation including all intermediate results are placed in appendix A. The starting point is the often cited equation in [36] which describes the energy of a neutron, E_n, produced in a fusion reaction:

$$E_n = \frac{1}{2}m_n v_{cm}^2 + \frac{m_{He}}{m_n + m_{He}}(Q+K) + v_{cm}\cos(\theta)\sqrt{\frac{2m_n m_{He}}{m_n + m_{He}}(Q+K)}\,. \qquad (3.1.16)$$

v_{cm} is the velocity of the centre-of-mass frame, K is the relative kinetic energy and θ is the angle between the neutron velocity in the centre-of-mass frame and the centre-of-mass velocity. Assuming a D-D reaction, $m_f = 2m_n$ and $m_{He} = 3m_n$. It is assumed that the thermal target ion is stationary. Using this, $\mathbf{v}_{cm}$ and K become

$$\mathbf{v}_{cm} = \frac{\mathbf{v}_f}{2} \qquad (3.1.17)$$

$$K = \frac{1}{2}m_n v_f^2\,. \qquad (3.1.18)$$

θ is the angle between the velocity of the center-of-mass frame and the velocity of the neutron in the center-of-mass frame. As shown in appendix A, $\cos(\theta)$ can be written as

$$\cos(\theta) = \frac{\frac{1}{2}\mathbf{v}_f\cdot\mathbf{v}_n - \frac{1}{4}v_f^2}{\frac{1}{2}v_f\sqrt{v_n^2 + \frac{1}{4}v_f^2 - \mathbf{v}_f\cdot\mathbf{v}_n}}\,. \qquad (3.1.19)$$

Inserting equations (3.1.17) - (3.1.19) in equation (3.1.16) gives

$$\frac{1}{2}m_n v_n^2 = \frac{3}{4}Q + \frac{1}{2}m_n v_f^2 + \frac{\frac{1}{2}\mathbf{v}_f\cdot\mathbf{v}_n - \frac{1}{4}v_f^2}{\sqrt{v_n^2 + \frac{1}{4}v_f^2 - \mathbf{v}_f\cdot\mathbf{v}_n}}\sqrt{\frac{3}{2}m_n\left(Q + \frac{1}{2}m_n v_f^2\right)}\,. \qquad (3.1.20)$$

Rewriting and squaring equation (3.1.20), it can be written as a quadratic equation in $\mathbf{v}_f\cdot\mathbf{v}_n$:

$$\begin{aligned}&\left(\frac{3}{2}m_n Q + \frac{3}{4}m_n^2 v_f^2\right)(\mathbf{v}_f\cdot\mathbf{v}_n)^2\\ &+\left(\frac{3}{2}m_n v_f^2 Q + \frac{1}{4}m_n^2 v_f^4 + m_n^2 v_n^4 + \frac{9}{4}Q^2 - 3m_n v_n^2 Q - 2m_n^2 v_n^2 v_f^2\right)(\mathbf{v}_f\cdot\mathbf{v}_n)\\ &-m_n^2 v_n^6 - \frac{1}{16}m_n^2 v_f^6 + \frac{7}{4}m_n^2 v_n^4 v_f^2 + 3m_n v_n^4 Q - \frac{1}{2}m_n^2 v_n^2 v_f^4\\ &-\frac{9}{4}m_n v_n^2 v_f^2 Q - \frac{9}{4}v_n^2 Q^2 - \frac{9}{16}v_f^2 Q^2 - \frac{3}{8}m_n v_f^4 Q = 0\,. \end{aligned} \qquad (3.1.21)$$

The two solutions to equation (3.1.21) are

$$\begin{aligned}\mathbf{v}_f\cdot\mathbf{v}_n \;=\;& \frac{1}{3m_nQ+\frac{3}{2}m_n^2v_f^2}\left(-\frac{3}{2}m_nv_f^2Q-\frac{1}{4}m_n^2v_f^4-m_n^2v_n^4-\frac{9}{4}Q^2+3m_nv_n^2Q\right.\\ &\left.+\,2m_n^2v_n^2v_f^2\pm\left(\frac{9}{4}Q^2+\frac{9}{4}m_nv_f^2Q+\frac{1}{2}m_n^2v_n^2v_f^2+\frac{1}{2}m_n^2v_f^4-m_n^2v_n^4\right)\right)\end{aligned} \tag{3.1.22}$$

The "-" solution reduces to

$$\begin{aligned}\mathbf{v}_f\cdot\hat{\mathbf{v}}_n \;&=\; \frac{1}{6v_n\left(Q+\frac{1}{2}m_nv_f^2\right)}\left(-9\frac{Q^2}{m_n}-\frac{15}{2}v_f^2Q+3m_nv_n^2v_f^2-\frac{3}{2}m_nv_f^4+6v_n^2Q\right)\\ &=\; \frac{1}{6v_n\left(Q+\frac{1}{2}m_nv_f^2\right)}\left(-9\frac{Q}{m_n}-3v_f^2+6v_n^2\right)\left(Q+\frac{1}{2}m_nv_f^2\right)\\ &=\; -\frac{3}{2}\frac{Q}{m_nv_n}-\frac{1}{2}\frac{v_f^2}{v_n}+v_n\,,\end{aligned} \tag{3.1.23}$$

which is identical to equation (3.1.9) for $m_f = 2m_n$ and $m_{He} = 3m_n$.

3.2 Instrument-specific NES weight functions

It is possible to calculate instrument-specific NES weight functions, which directly relate the measured quantity to the fast-ion distribution function. To do this, a well-defined instrumental response function of the given detector is needed. The instrument specific weight function is given by

$$w_{\text{instrument},ijl} = \sum_k R_{kl} w_{E_n,ijk} \, , \tag{3.2.1}$$

where R is the instrumental response function and W_{E_n} is the neutron energy weight function. i, j, k and l are indices of fast ion energy and pitch, neutron energy and the instrumental measurement variable. Thus, an instrument-specific weight function for given values of the ion energy, pitch and instrumental measurement variable, is given by summing all the neutron energy weight functions for these values of energy and pitch, weighted by the instrumental response function for the given value of the instrumental measurement variable.

Figure 3.2.1 illustrates the idea of instrument-specific weight functions. Using the relevant instrumental response function, it is possible to relate a neutron energy spectrum to the measured spectrum of the detector, in this example a neutron time-of-flight spectrum. The energy spectrum can then be related to the fast-ion velocity-space distribution function using NES weight functions. By using instrument-specific weight functions it is possible to directly relate the velocity-space distribution function with the measured spectrum.

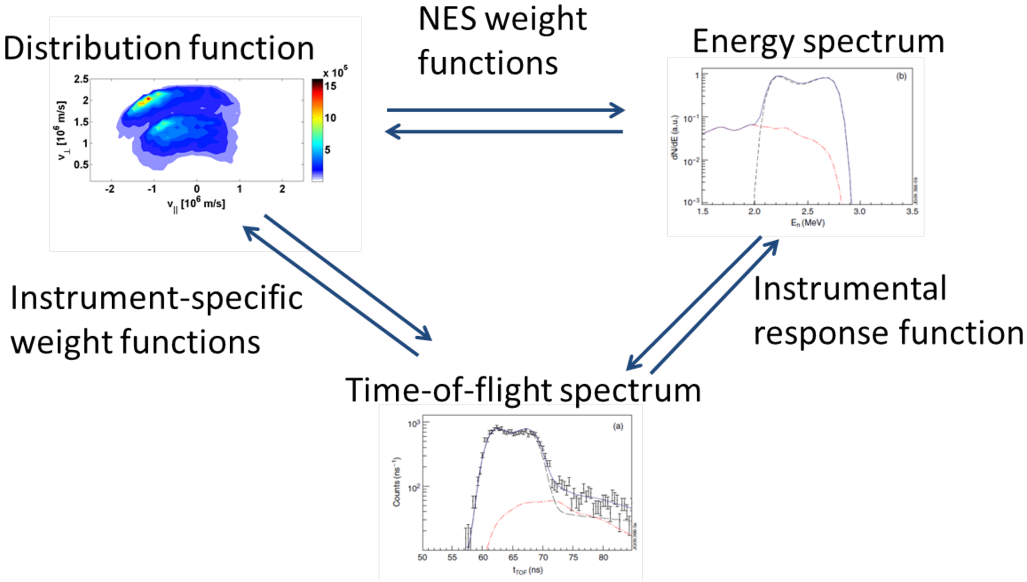

Figure 3.2.1: Illustrating the idea of instrument-specific weight functions.

3.2.1 TOFOR time-of-flight weight functions

Instrument-specific time-of-flight weight functions are calculated for the time-of-flight neutron spectrometer TOFOR installed at JET [60]. TOFOR consists of two sets of scintillator detectors. By correlating detections in the two sets, it is possible to determine the flight time of neutrons detected in both. As the distance is known, the neutron energy can be deduced. A sketch of the location of TOFOR relative to the JET plasma is shown in figure 3.2.2. The distance between the plasma and TOFOR is not to scale.

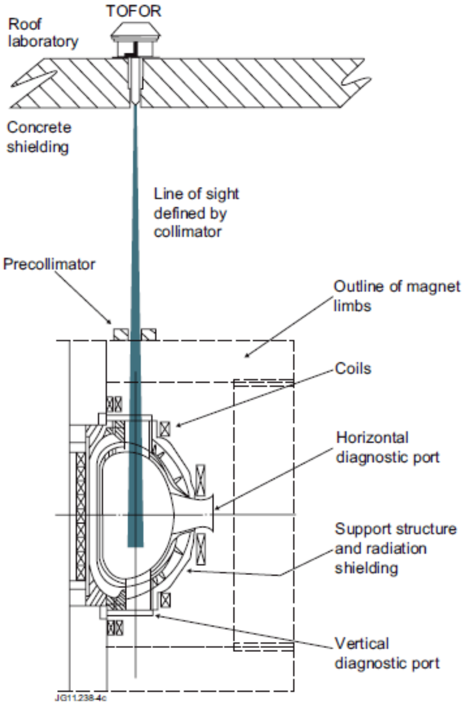

Figure 3.2.2: Sketch of the location of TOFOR. The distance from the plasma centre to TOFOR is 19 metres and not shown to scale in this figure. The figure is from [61].

Paper II describes how to calculate instrument specific weight functions in general and shows examples of TOFOR time-of-flight weight functions. TOFOR has a very fine energy resolution, which is evident from its instrumental response function shown in figure 3.2.3a. The instrumental response function has been calculated using a 3D Monte Carlo model which takes into account the specific geometry and thickness of the spectrometer [60]. It accounts for the possibility of multiple-scattering events to take place in the scintillators. The narrow peaking of the response function causes the time-of-flight weight functions to be slightly smeared-out versions of the NES weight functions.

3.2.2 NE213 spectrometer weight function

Several neutron spectrometers are installed at JET [62]. Figure 3.2.3b shows the response function of a compact neutron spectrometer located at JET. This spectrometer uses a liquid organic scintillator called NE213 to determine the energies of the neutrons. An incoming neutron can excite the organic scintillator through neutron-hydrogen elastic scattering [63]. The scintillator emits light in the subsequent relaxation. The amount of light emitted will depend on the neutron energy [63, 64]. The units of the light output of the NE213 spectrometer are MeVee (megaelectronvolts electron equivalents). This is

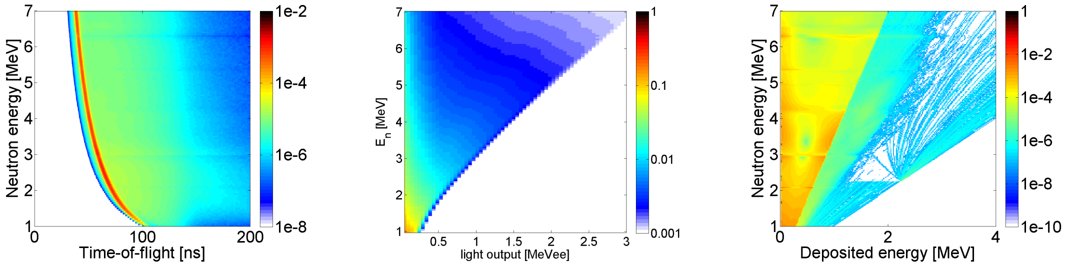

(a) TOFOR. (b) NE213. (c) Diamond.

Figure 3.2.3: Instrumental response functions for three neutron spectrometers at JET. The three detectors are the time-of-flight detector TOFOR and two compact scintillator spectrometers. The scintillating materials are an organic material named NE213 and synthetic diamond crystal, respectively.

the light which would be produced by an electron with that energy. This unit is chosen since the light output response to incoming electrons is linear [63]. The active scintillator material in the NE213 neutron spectrometer at JET is placed in a cylinder with a diameter of 12.3 mm and a length of 8.4 mm [64].

The instrumental response function for this instrument looks entirely different from the one for TOFOR. A large range of neutron energies can potentially give rise to the signal for a given light output. This degrades the energy resolution of the instrument. However, the weight functions are still confined to parts of velocity-space especially for large light output values. Figure 3.2.4 shows examples of instrument specific weight functions calculated for the NE213 spectrometer. They are generated using analytically calculated probability functions and numerically calculated rate functions. The angle used is 45° as this is the approximate angle between the magnetic field and the line-of-sight of this detector in the plasma centre.

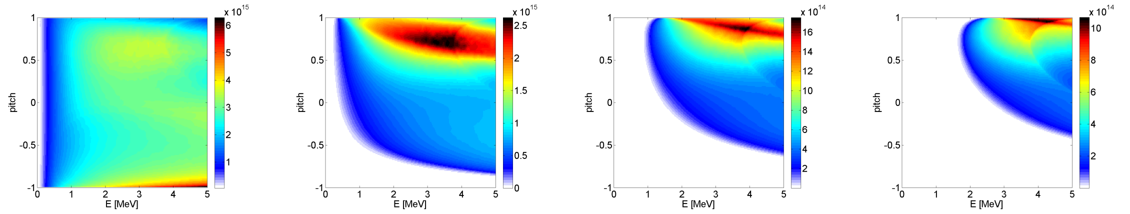

(a) 0.48±0.025 MeVee. (b) 1.02±0.025 MeVee. (c) 1.50±0.025 MeVee. (d) 1.98±0.025 MeVee.

Figure 3.2.4: Instrument specific weight functions calculated for the NE213 neutron spectrometer at JET for different light output values.

It is clear from figure 3.2.4 that the poor energy resolution of this detector makes it difficult to identify the measured parts of velocity space for values of the light output below 1 MeVee. However, for larger values, the weight functions become more localized both in energy and pitch. Thus, weight functions can be used to determine which parts of velocity-space were probed for the high light output tail of a measured NE213 spectrum.

3.2.3 Diamond detector weight function

There is another compact neutron spectrometer at JET. The scintillator material in this spectrometer is a synthetic single-crystal diamond. The diamond detector can be excited by an incoming neutron through neutron-carbon elastic scattering [65]. This detector is placed right in front of the NE213 spectrometer and therefore also has an angle to magnetic field on axis of around 45° [62]. The diamond scintillator has an area of 4.7 mm × 4.7 mm and a thickness of 0.5 mm [65]. The instrumental response function of this detector is shown in figure 3.2.3c. It shows the relation between the energy of the neutrons and the possible deposited energy in the detector. For a given neutron energy, the response function is almost flat up to a deposited energy of $E_{dep} = 0.284E_n$, where E_{dep} is the deposited energy. Above this energy, the response function drops about two orders of magnitude. Deposited energies above $0.284E_n$ are caused by neutrons scattering twice in the detector. Instrument specific weight functions for the diamond detector are calculated for a specific deposited energy. From figure 3.2.3c it is evident that an instrument specific weight function for the diamond detector will be an almost equally weighted sum of neutron weight functions calculated for neutron energies above $3.52E_{dep}$. This makes the internal features of the weight functions almost completely flat. However, since the lower energy bound of NES weight functions increases with E_n, these instrument specific weight functions will still be restricted to a certain region of velocity space. The lower energy bound is given by the $E_n = 3.52E_{dep}$ weight function. Examples of instrument specific weight functions for the diamond detector are shown in figure 3.2.5.

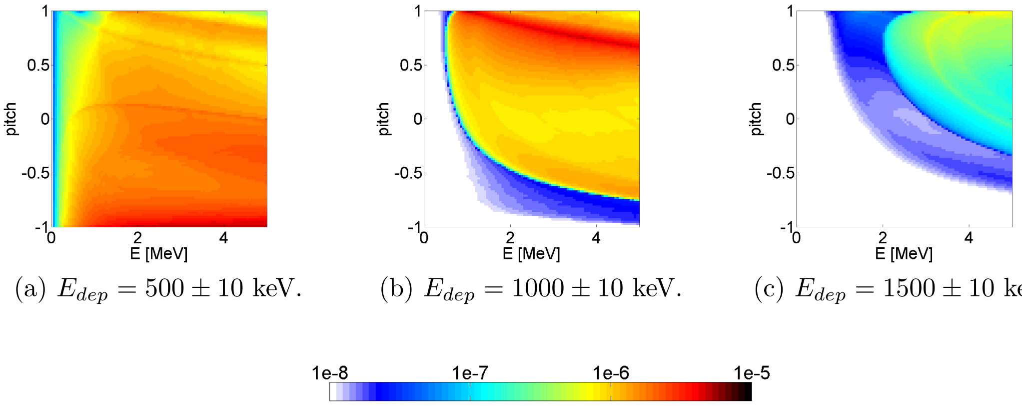

(a) $E_{dep} = 500 \pm 10$ keV. (b) $E_{dep} = 1000 \pm 10$ keV. (c) $E_{dep} = 1500 \pm 10$ keV.

Figure 3.2.5: Instrument specific weight functions calculated for the diamond neutron spectrometer for different deposited energies E_{dep}.

3.3 Using NES weight functions

Using velocity-space tomography, it is possible to combine measurements from different fast-ion diagnostics in a combined tomography. In principle, NES can be included in such a tomography. However, NES is not a localized measurement in position space. This needs to be accounted for. One way is simply to assume that most neutrons are produced in reactions in the plasma centre where the ion temperature and density are largest. If this assumption is valid, a central mean fast-ion velocity distribution function can be obtained. Otherwise, a four dimensional phase-space tomography is needed. The four dimensions would be $v_\parallel$, $v_\perp$, R and z, assuming toroidal symmetry, where R and z are the radius and height, respectively. These coordinates are often used to describe position in a poloidal cross section of a tokamak. To formulate a four dimensional phase-space tomography problem, a transfer matrix which takes into account the possible correlation between different measurement volumes needs to be formulated.

The NES and instrument specific weight functions have other applications as well. Figure 3.3.1 from [62] shows measured and modelled time-of-flight spectra from JET discharge #86459 (left). The right figure shows the corresponding fitted neutron energy spectrum. The neutron energy spectrum is split into two components. The main component is from neutrons created in fusion reactions between a fast and a thermal ion. The second component is from neutrons which scatter in the machine, thereby losing energy, before they are detected. The scattered component dominates the neutron energy spectrum for neutron energies below 2 MeV, but is otherwise negligible.

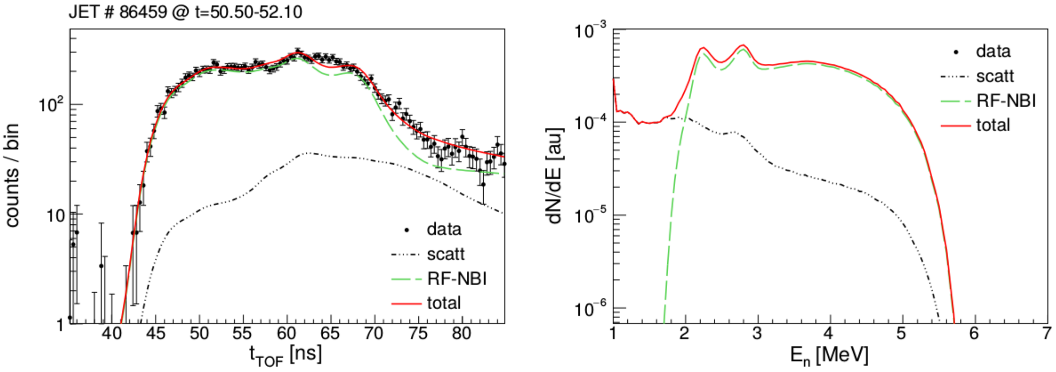

Figure 3.3.1: Measured and modelled time-of-flight spectra (left) and the corresponding neutron energy spectrum (right). The modelled spectra are split into two components. One from the fast ions and one from scattered neutrons. Figure is from [62].

Figure 3.3.2 from [62] shows a measured and simulated spectra from the NE213 compact neutron spectrometer from discharge #86459. The right figure shows the corresponding simulated neutron energy spectrum. The two measured spectra in figures 3.3.1 and 3.3.2 are measured at the same time, however, TOFOR measures neutrons with around 0.5 MeV higher energy compared to the compact spectrometer. Since the diamond spectrometer is located right in front of the NE213 spectrometer, it measures the same neutrons. Using either NES or instrument specific weight functions, null-measurement weight functions can

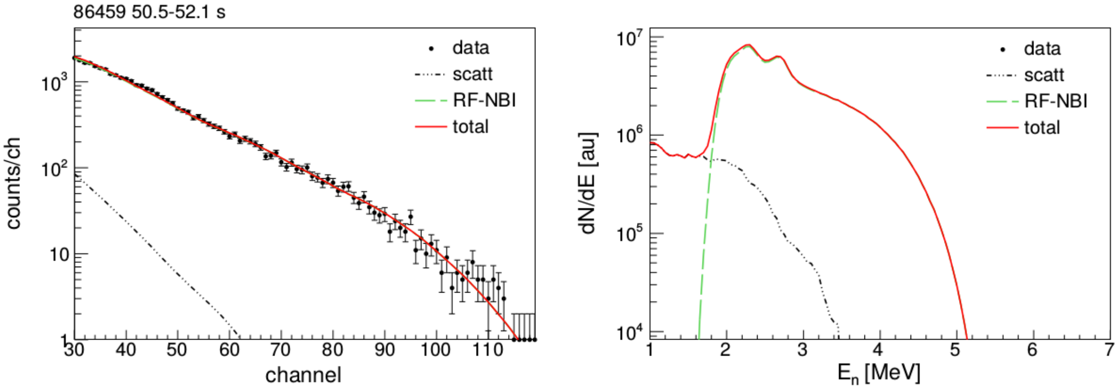

Figure 3.3.2: Measured and modelled spectra from the NE213 compact neutron spectrometer (left). The corresponding neutron energy spectrum, again split in two components (right). The figure is from [62].

be calculated. Null-measurement weight functions are defined as the weight functions calculated for the part of a spectrum where no signal is measured. For the neutron spectrum in figure 3.3.1 this corresponds to neutrons with energies above 5.7 MeV. Null-measurement weight functions cannot be used to determine any internal features in a fast-ion distribution function. However, they can limit the region in velocity-space where the fast-ions can exist for a given spectrum. Figure 3.3.3 shows NES null-measurement weight functions for TOFOR and the diamond spectrometer calculated from the neutron energy limits in figures 3.3.1 and 3.3.2. The TOFOR null-measurement weight function is shown in double lines and the null-measurement weight function for the two compact spectrometers is shown in single lines. Here, I only show the weight functions as hatched regions since the internal features of the weight functions are not as important. Because of the different viewing geometries ($\phi = 90°$ for TOFOR and $\phi = 45°$ for the compact spectrometers), the weight functions cover different regions in velocity-space. During this time in discharge #86459 the plasma was heated using ICRH which creates a strongly anisotropic distribution with ions at pitch close to zero having significantly higher energy than ions with pitch close to ±1 [11]. The null-measurement weight functions can be used to limit the possible fast-ion distribution both in maximum energy (here around 2.4 MeV) and its width in pitch. This is particularly useful for fast-ion distribution functions due to ICRH that are not as well established as beam ion distribution functions. For example, in reference [62] ICRH distribution functions in two pitch ranges ([-0.1;0.1], [-0.2,0.2]) were considered. It was found that the broader pitch range gave a better match to dual sightline NES measurements. Null-measurement weight functions directly reveal the maximum pitch range.

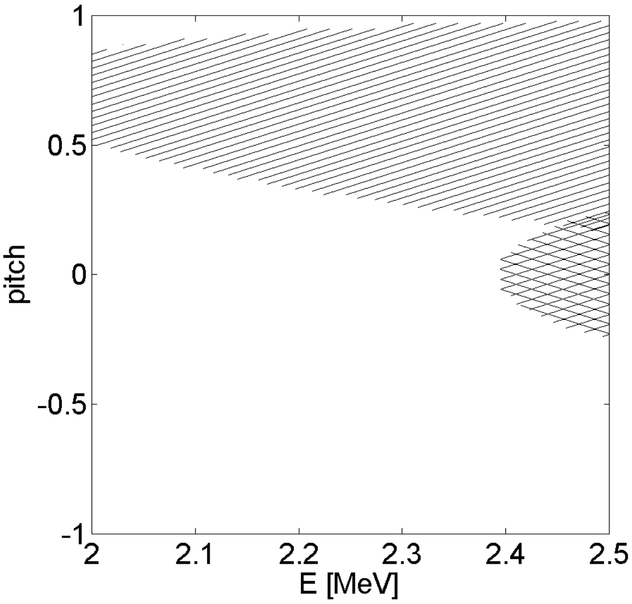

Figure 3.3.3: Null-measurement weight functions for TOFOR and the diamond/NE213 spectrometer.

Chapter 4

Inversion methods

In velocity-space tomography, the aim is to find the velocity-distribution, $\mathbf{F}$, from

$$\mathbf{W}\mathbf{F} = \mathbf{S}\,. \tag{4.0.1}$$

Equation (4.0.1) is normalized with the measurement uncertainties in order to give most credibility to data points with a large signal-to-noise ratio [52]. If $\mathbf{W}$ was invertible, the solution would simply be

$$\mathbf{F} = \mathbf{W}^{-1}\mathbf{S}\,. \tag{4.0.2}$$

However, that is not the case. As explained in section 2.6, finding $\mathbf{F}$ from equation (4.0.1) is an ill-posed problem. In the realistic situation of noisy measurements, it is necessary to regularize the problem [57]. As mentioned in chapter 2, many different methods and algorithms exist for calculating an estimate of the inverse of $\mathbf{W}$. In paper III we investigate the performance of several different inversion methods for velocity-space tomography. In this chapter, the different inversion methods are described and compared. Systematic methods to choose the regularization strength are presented and an estimate of the uncertainty of a tomography is presented.

4.1 Truncated singular value decomposition

Truncated singular value decomposition (SVD) is the regularization method used so far to calculate velocity-space tomographies in fusion plasmas [51–53]. In generel, an $m \times n$ matrix, $\mathbf{W}$, can be written as the product of three matrices[1]:

$$\mathbf{W} = \mathbf{A}\mathbf{\Sigma}\mathbf{B}^T\,, \tag{4.1.1}$$

where $\mathbf{B}^T$ is the transpose of $\mathbf{B}$. The columns of $\mathbf{A}$ ($m \times m$) are the eigenvectors of the matrix $\mathbf{W}\mathbf{W}^T$, and the columns of $\mathbf{B}$ ($n \times n$) are the eigenvectors of the matrix $\mathbf{W}^T\mathbf{W}$. $\mathbf{A}$ and $\mathbf{B}$ are orthogonal. $\mathbf{\Sigma}$ is a diagonal $m \times n$ rectangular matrix. The values in

---

[1] Often, $\mathbf{U}$ and $\mathbf{V}$ are used as symbols for the two orthogonal matrices. Here, I use $\mathbf{A}$ and $\mathbf{B}$ instead in order to distinguish these matrices from the ion and neutron velocities.

the diagonal are called the singular values. They are the square roots of the non-zero eigenvalues of both $\mathbf{W}\mathbf{W}^T$ and $\mathbf{W}^T\mathbf{W}$ [66]. The values in the diagonal of $\mathbf{\Sigma}$ are ordered in a decreasing manner. Using the singular value decomposition, it is possible to define a pseudoinverse of any matrix [66]:

$$\mathbf{W}^+ = \mathbf{B}\mathbf{\Sigma}^+\mathbf{A}^T\,, \tag{4.1.2}$$

where $\mathbf{\Sigma}^+$ is a rectangular diagonal matrix with the reciprocal of the diagonal elements of $\mathbf{\Sigma}$ in the diagonal.

The SVD solution to equation (2.5.4) is

$$\mathbf{F}_{SVD} = \mathbf{B}\mathbf{\Sigma}^+\mathbf{A}^T\mathbf{S}\,. \tag{4.1.3}$$

Equation (4.1.3) can be written as a sum:

$$\mathbf{F}_{SVD} = \sum_i \frac{\mathbf{a}_i^T\mathbf{S}}{\sigma_i}\mathbf{b}_i\,, \tag{4.1.4}$$

where $\mathbf{a}_i$ and $\mathbf{b}_i$ are the i'th column of $\mathbf{A}$ and $\mathbf{B}$, respectively. σ_i is the i'th singular value. Equation (4.1.4) can be seen as an expansion in basis functions, $\mathbf{b}_i$, each weighted by the factor $\frac{\mathbf{a}_i^T\mathbf{S}}{\sigma_i}$. Figure 4.1.1 shows examples of columns of $\mathbf{B}$ reshaped into two dimensions as function of energy and pitch. The complexity of the functions increases for higher values of i.

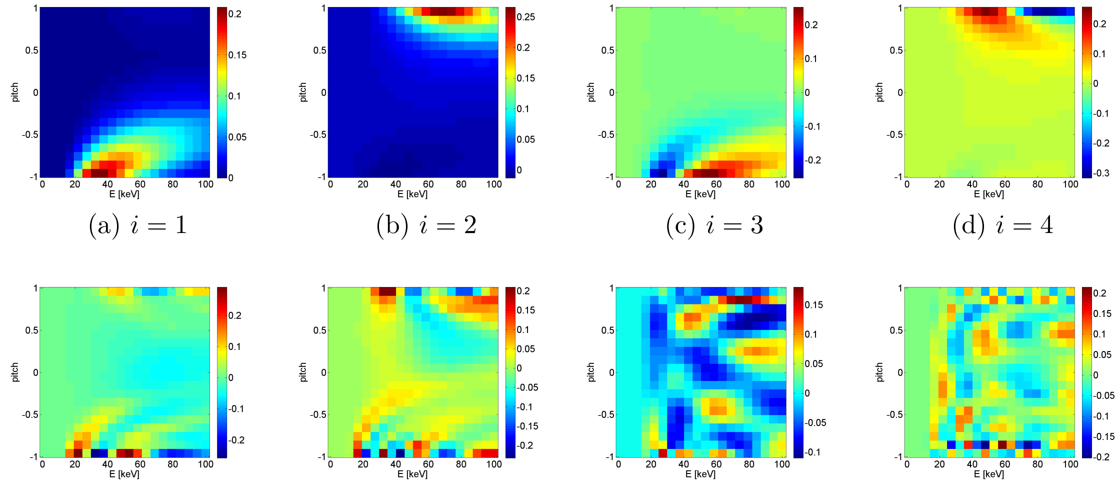

(a) $i = 1$ (b) $i = 2$ (c) $i = 3$ (d) $i = 4$

(e) $i = 8$ (f) $i = 16$ (g) $i = 30$ (h) $i = 50$

Figure 4.1.1: Examples of columns of $\mathbf{B}$. Higher index terms in the sum have increasingly complicated basis functions.

Experimental data always contains some form of measurement noise

$$\mathbf{S} = \mathbf{S}_{exact} + \mathbf{e}\,, \tag{4.1.5}$$

where $\mathbf{S}_{exact}$ is the idealized measurements without measurement noise and $\mathbf{e}$ is the noise. Inserting equation (4.1.5) in equation (4.1.4) I get

$$\mathbf{F}_{SVD} = \sum_i \frac{\mathbf{a}_i^T \mathbf{S}_{exact}}{\sigma_i}\mathbf{b}_i + \sum_i \frac{\mathbf{a}_i^T \mathbf{e}}{\sigma_i}\mathbf{b}_i = \mathbf{F}_{exact} + \sum_i \frac{\mathbf{a}_i^T \mathbf{e}}{\sigma_i}\mathbf{b}_j\,, \tag{4.1.6}$$

where $\mathbf{F}_{exact}$ is the exact solution. If the singular values get very small, the SVD solution can be completely dominated by the last sum in equation (4.1.6). It is possible to reduce the influence of the noise in equation (4.1.6) by not including all the terms in the sum. Keeping only the k first terms, corresponding to the k largest singular values, regularizes the problem by reducing the influence of the noise, but at the same time makes it impossible to recreate $\mathbf{F}_{exact}$ completely. This method is called truncated SVD. Truncated SVD introduces the problem of choosing the stopping parameter, k. This will be discussed in section 4.4.

4.1.1 Example of SVD tomography

Here is shown an example of an SVD tomography including the different steps to illustrate the procedure. Figure 4.1.2 shows a Gaussian distribution in (E, p)-coordinates on a 20x20 grid and a 12x12 grid.

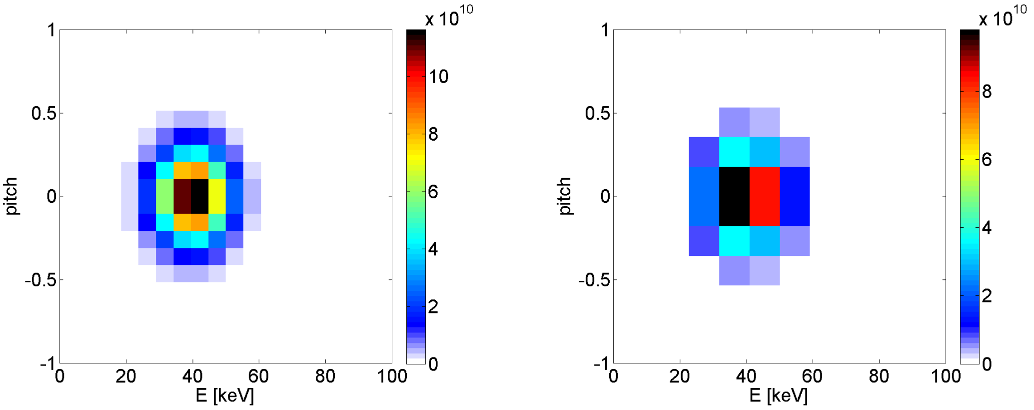

(a) 20x20 (b) 12x12

Figure 4.1.2: Gaussian test distribution on a 20x20 grid and a 12x12 grid in units of [ions/keV/cm^3].

An artificial CTS diagnostic set-up with three different views is defined. The angles between their respective $\mathbf{k}^\delta$ and the magnetic field in the measurement volume are 10°, 45° and 80°. It is assumed, that it is possible to determine $g(u)$ for projected velocities from -5×10^6 m/s to -0.5×10^6 m/s and from 0.5×10^6 m/s to 5×10^6 m/s. The interval from -0.5×10^6 m/s to 0.5×10^6 m/s is assumed to be experimentally inaccessible due to the contribution from thermal ions dominating this part of the spectrum [37]. A resolution in projected velocity of 0.1×10^6 m/s is assumed. This results in 82 measurement points for each view. Synthetic spectra are calculated using equation (2.5.4). To illustrate the

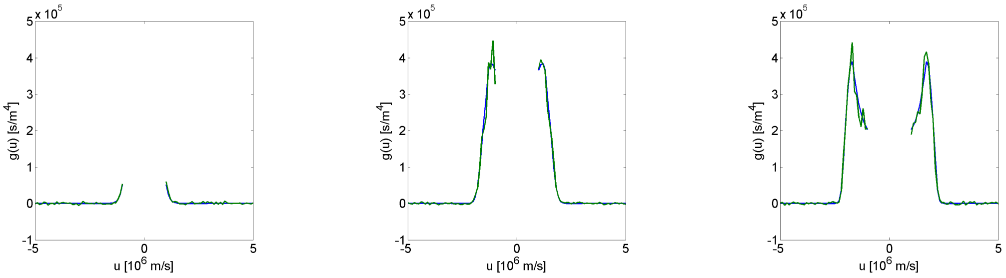

(a) $\phi = 10°$ (b) $\phi = 45°$ (c) $\phi = 80°$

Figure 4.1.3: Synthetic spectra without noise (blue) and with Gaussian noise (green).

effect of noise in the measurements, 10% Gaussian noise is added to the synthetic spectra. The spectra for the three views are shown in figure 4.1.3.

The view with $\phi = 10°$ measures mainly ions with pitch-values close to ±1. This is the explanation for the much smaller values in figure 4.1.3a.

12x12 grid - An overdetermined system

First, tomographies are calculated on the 12x12 grid. In this case, there are more measurements than grid points and the problem is overdetermined. For an overdetermined system, the least squares solution which minimizes

$$\min_{\mathbf{F}} \left(||\mathbf{WF} - \mathbf{S}|| \right) , \tag{4.1.7}$$

is sought. The singular values of the SVD of the transfer matrix are shown in figure 4.1.4.

The singular values are gradually decreasing until around the 120'th singular value. Afterwards, they drop by about 12 orders of magnitude. Figure 4.1.5 shows tomographies calculated using synthetic data without noise for an increasing truncation level. By comparing figures 4.1.2b and 4.1.5k it is seen that when 120 terms in the sum in equation (4.1.4) are included, it is almost possible to reconstruct the true distribution completely. However, when including 130 terms in the solution, the very small singular values seen in figure 4.1.4 cause the solution to blow up due to numerical round-off errors. Furthermore, it is observed that the tomographies can contain negative values which is an unphysical result. Such negative values typically occur for the other inversion methods as well. Negative values are disregarded in the following. Figure 4.1.6 shows tomographies calculated using noisy data. When noise is added to the measurements, it is no longer possible to reconstruct the true distribution completely. The solution explodes for a truncation level of 120. The noise makes it necessary to truncate the sum earlier to suppress the effect of the noise. In this case it is not possible to reconstruct the true distribution function, as explained previously.

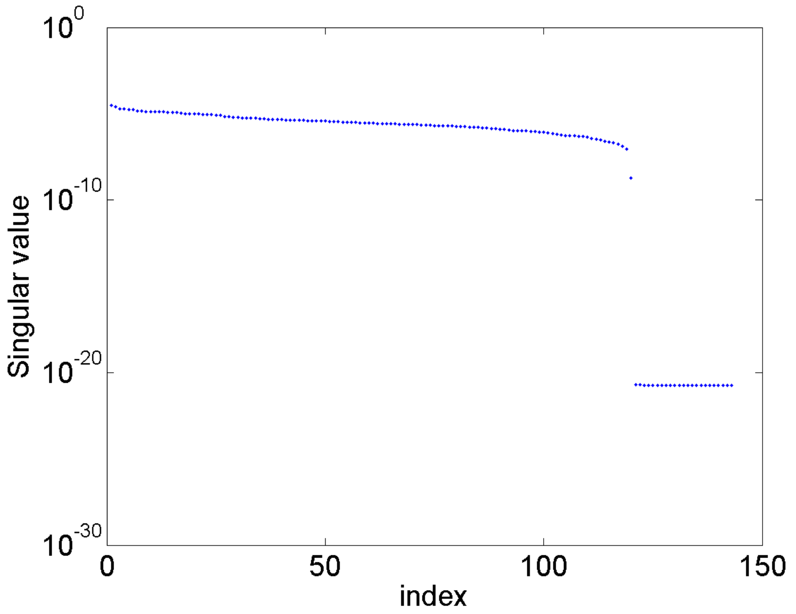

Figure 4.1.4: Singular values of the SVD of the transfer matrix in the 12x12 example.

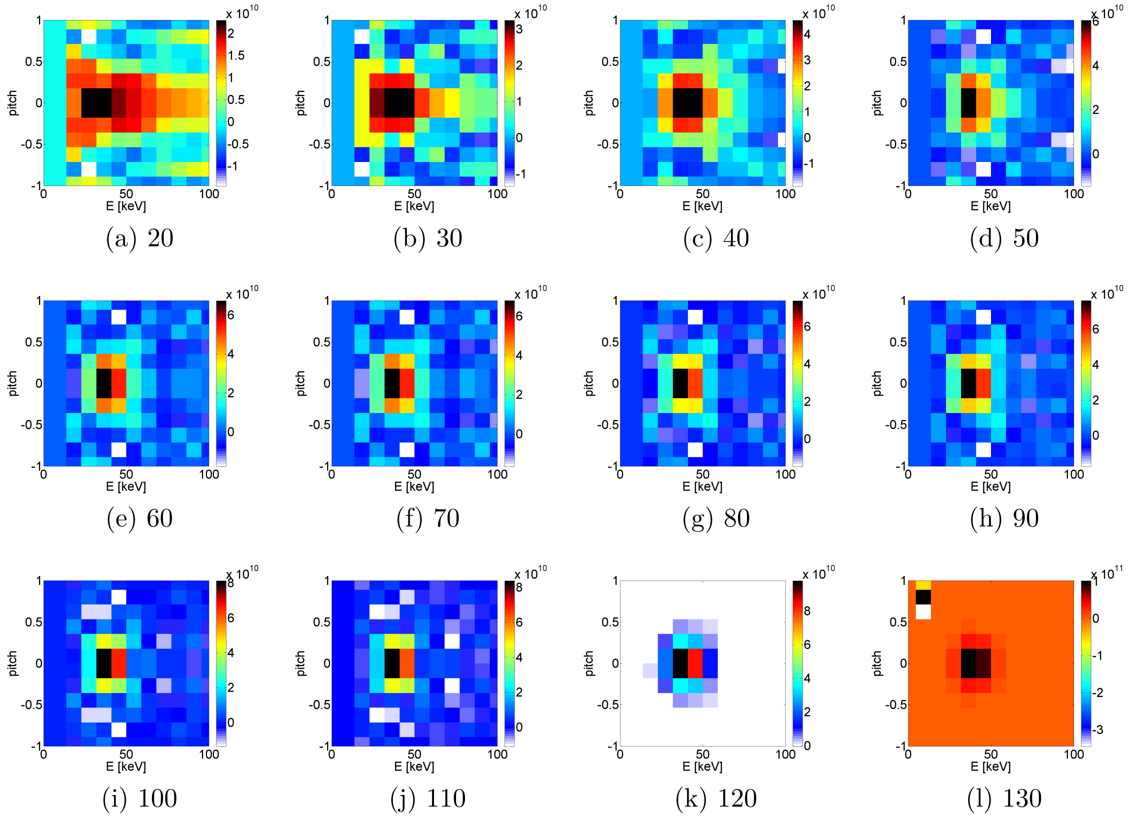

(a) 20 (b) 30 (c) 40 (d) 50

(e) 60 (f) 70 (g) 80 (h) 90

(i) 100 (j) 110 (k) 120 (l) 130

Figure 4.1.5: Tomographies of synthetic data without noise for an increasing truncation level on a 12x12 grid in units of [ions/keV/cm^3].

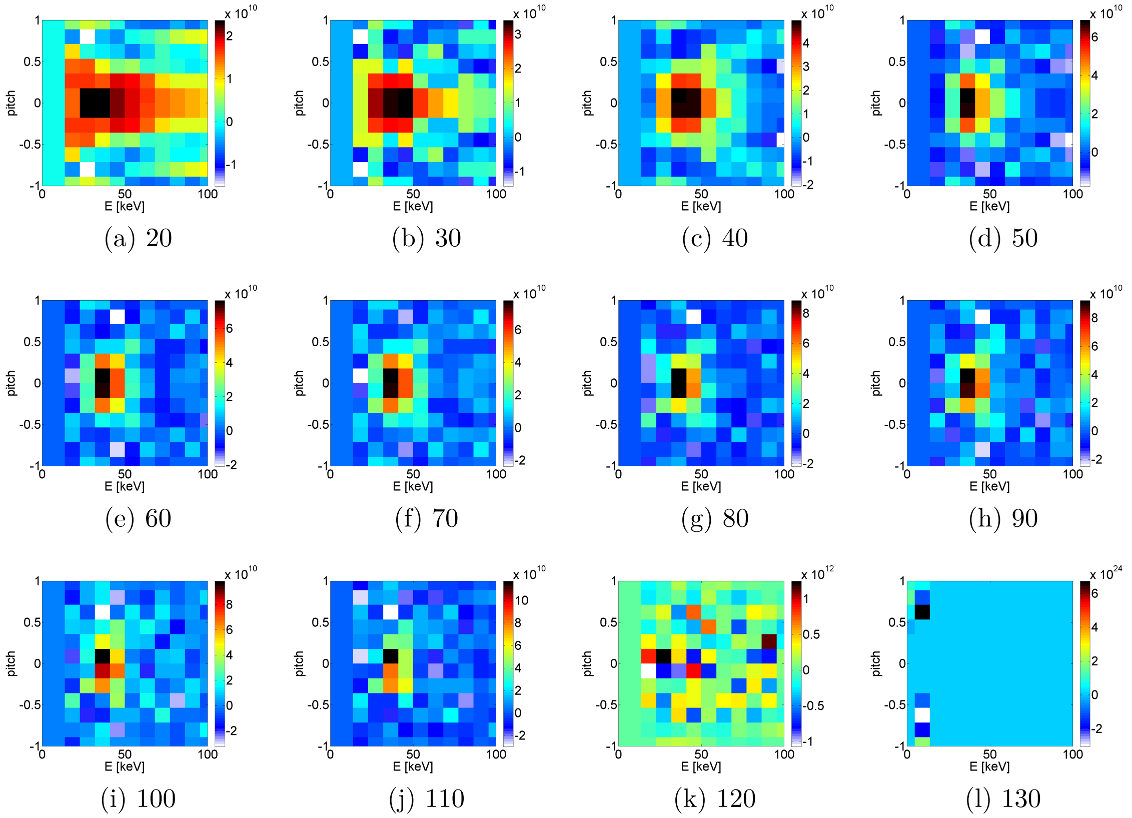

(a) 20 (b) 30 (c) 40 (d) 50

(e) 60 (f) 70 (g) 80 (h) 90

(i) 100 (j) 110 (k) 120 (l) 130

Figure 4.1.6: Tomographies of synthetic data with noise for an increasing truncation level on a 12x12 grid in units of [ions/keV/cm^3].

20x20 grid - An underdetermined system

For the 20x20 grid, the system of equations is underdetermined since it contains more unknowns (grid points) than equations (measurements). In this case, the sought solution is the minimum norm solution.

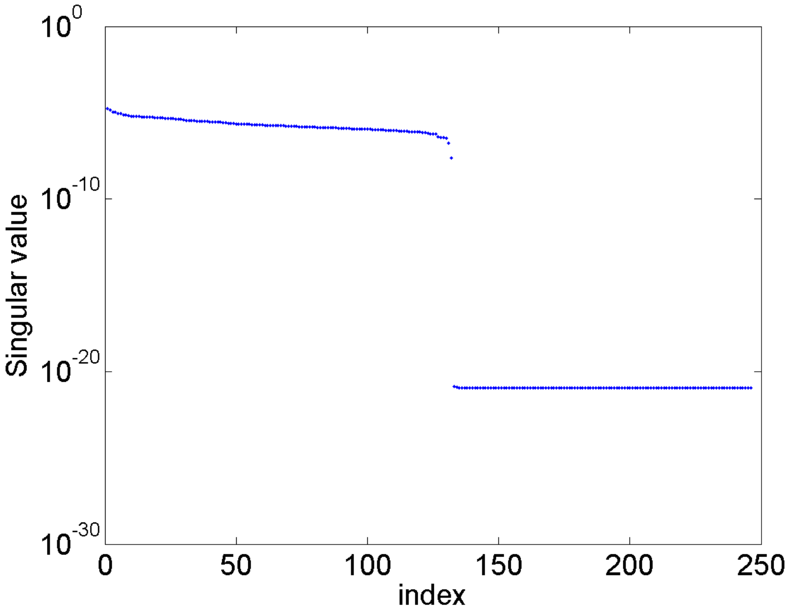

Figure 4.1.7: Singular values of the SVD of the transfer matrix in the 20x20 example.

Figure 4.1.7 shows the singular values from the SVD of the transfer matrix constructed using weight functions calculated on the 20x20 grid. For this transfer matrix, the sudden drop happens at the 132'nd singular value.

Figure 4.1.8 shows tomographies calculated on the 20x20 grid from synthetic measurements without noise. In the underdetermined case, it is no longer possible to recreate the true distribution even in the case without noise. Very distinct features emerge in the tomographies at velocities where there should be no distribution. The shape of these artefacts are created by the shapes of the weight functions themselves. Figure 4.1.9 shows the tomographies on the 20x20 grid calculated using synthetic data with noise. As expected, the solution blows up when any of the very small singular value terms are included in the sum. Here, this happens for a truncation level above 130.

In the remainder of the thesis, only overdetermined systems are examined.

4.2 Tikhonov regularization

Another regularization method is known as linear regularization [67] or Tikhonov regularization [56]. The idea is to replace the ill-posed inverse problem with a closely related well-posed problem. Instead of finding **F** that minimizes

$$\min_{\mathbf{F}} \left(||\mathbf{W}\mathbf{F} - \mathbf{S}|| \right) , \tag{4.2.1}$$

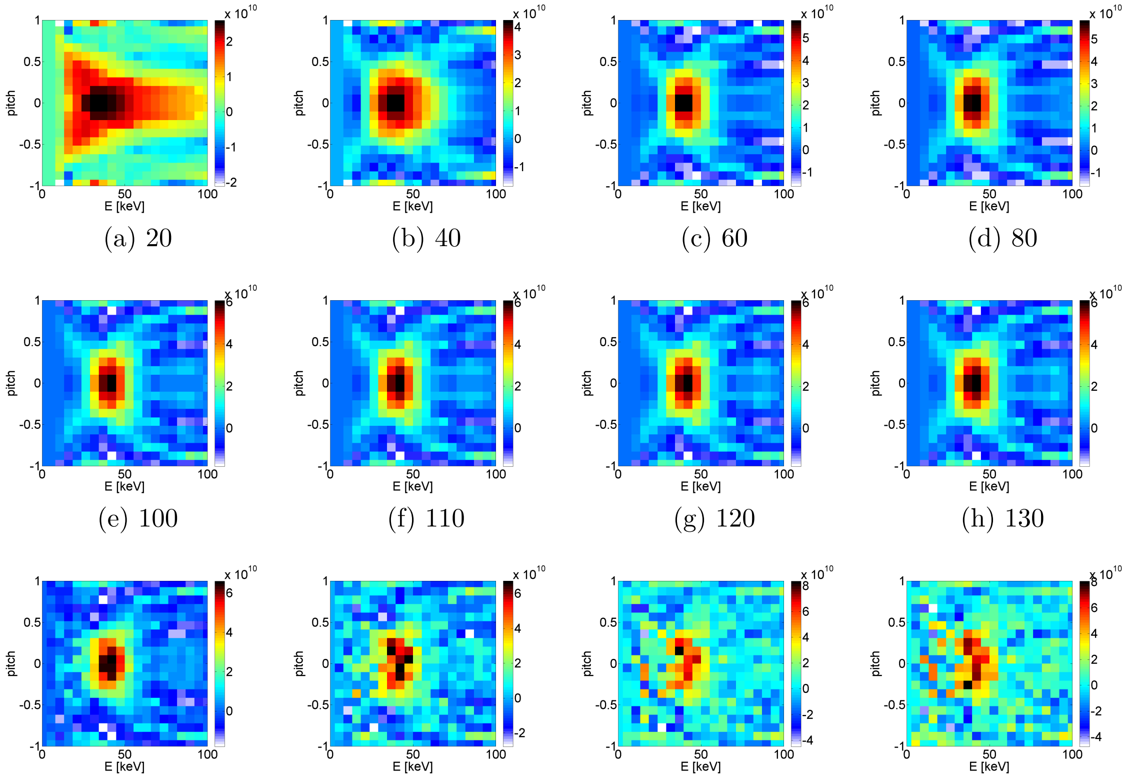

(a) 20 (b) 40 (c) 60 (d) 80

(e) 100 (f) 110 (g) 120 (h) 130

(i) 140 (j) 160 (k) 180 (l) 200

Figure 4.1.8: Tomographies of synthetic data without noise for an increasing truncation level on a 20x20 grid in units of [ions/keV/cm^3].

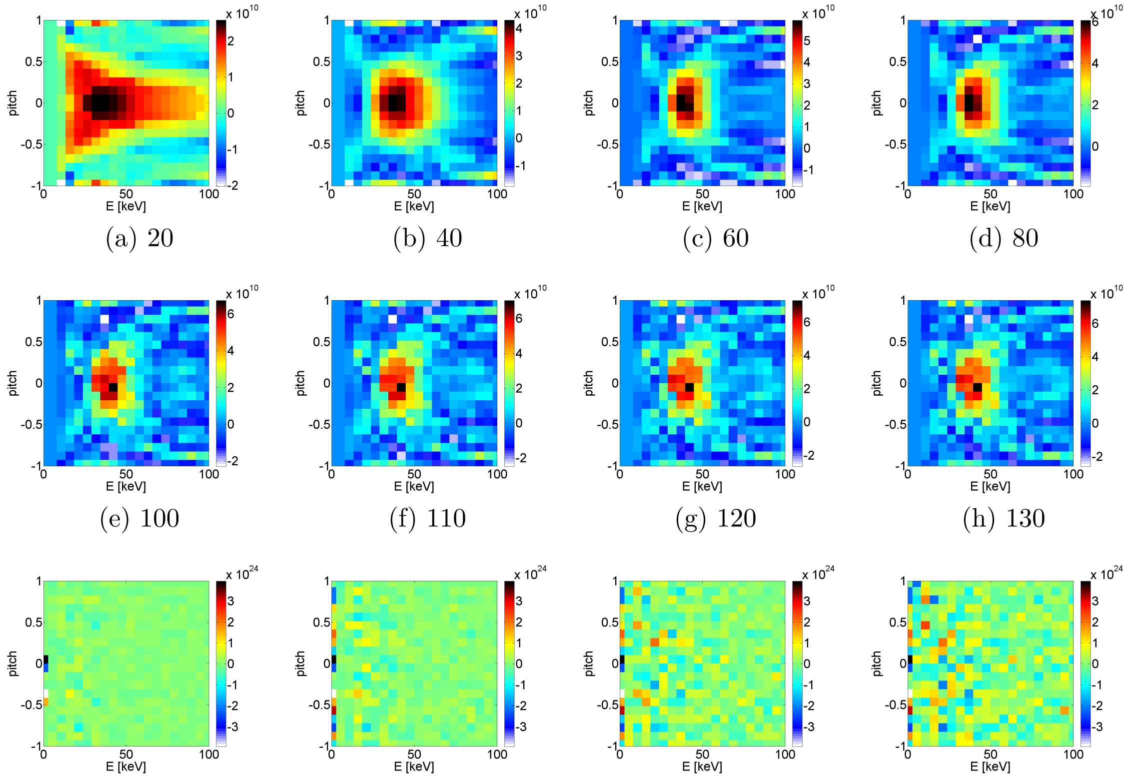

(a) 20 (b) 40 (c) 60 (d) 80

(e) 100 (f) 110 (g) 120 (h) 130

(i) 140 (j) 160 (k) 180 (l) 200

Figure 4.1.9: Tomographies of synthetic data with noise for an increasing truncation level on a 20x20 grid in units of [ions/keV/cm^3].

the **F** that minimizes

$$\min_{\mathbf{F}}\left(||\mathbf{WF}-\mathbf{S}||+\alpha||\mathbf{LF}||\right)\,, \tag{4.2.2}$$

is sought. where α is a positive scalar which determines the relative importance of the two terms and **L** is known as the penalty function. The solution to equation (4.2.2) can be written schematically by the normal equation [57]

$$\mathbf{F}_\alpha=\left(\mathbf{W}^T\mathbf{W}+\alpha\mathbf{L}^T\mathbf{L}\right)^{-1}\mathbf{W}^T\mathbf{S}\,, \tag{4.2.3}$$

where $\mathbf{F}_\alpha$ denotes the Tikhonov solution. In my project I solve equation (4.2.3) using a QR solver implemented in MatLab. How to choose α is discussed in section 4.4.

Zeroth order Tikhonov regularization

The choice of the penalty function **L** has a strong influence on the solution, and preferably it should be based on assumptions about the true solution. The simplest possible penalty function is

$$\mathbf{L}=\mathbf{I}\,, \tag{4.2.4}$$

where **I** is the identity matrix. Solving equation (4.2.2) with $\mathbf{L}=\mathbf{I}$ will yield a solution which fits the data as best as possible while avoiding large absolute values in **F** by penalizing them. This choice of penalty function is called zeroth order Tikhonov regularization or zeroth order linear regularization. Introducing the SVD of **W**, writing $\mathbf{I}=\mathbf{B}\mathbf{B}^T$ and remembering that $(\mathbf{XYZ})^T=\mathbf{Z}^T\mathbf{Y}^T\mathbf{X}^T$ gives [57]

$$\begin{aligned}\mathbf{W}^T\mathbf{W}+\alpha\mathbf{I} &= \mathbf{B}\boldsymbol{\Sigma}^T\mathbf{A}^T\mathbf{A}\boldsymbol{\Sigma}\mathbf{B}^T+\alpha\mathbf{B}\mathbf{B}^T\\ &= \mathbf{B}\boldsymbol{\Sigma}^T\boldsymbol{\Sigma}\mathbf{B}^T+\alpha\mathbf{B}\mathbf{B}^T\\ &= \mathbf{B}\left(\boldsymbol{\Sigma}^T\boldsymbol{\Sigma}+\alpha\mathbf{I}\right)\mathbf{B}^T\,. \end{aligned}\tag{4.2.5}$$

Using equation (4.2.5), $\mathbf{F}_\alpha$ can be written as

$$\begin{aligned}\mathbf{F}_\alpha &= \left(\mathbf{B}\left(\boldsymbol{\Sigma}^T\boldsymbol{\Sigma}+\alpha\mathbf{I}\right)\mathbf{B}^T\right)^{-1}\mathbf{B}\boldsymbol{\Sigma}^T\mathbf{A}^T\mathbf{S}\\ &= \mathbf{B}\left(\boldsymbol{\Sigma}^T\boldsymbol{\Sigma}+\alpha\mathbf{I}\right)^{-1}\mathbf{B}^T\mathbf{B}\boldsymbol{\Sigma}^T\mathbf{A}^T\mathbf{S}\\ &= \mathbf{B}\left(\boldsymbol{\Sigma}^T\boldsymbol{\Sigma}+\alpha\mathbf{I}\right)^{-1}\boldsymbol{\Sigma}^T\mathbf{A}^T\mathbf{S}\,. \end{aligned}\tag{4.2.6}$$

Writing equation (4.2.6) as a sum analogously to equation (4.1.4) gives

$$\mathbf{F}_\alpha=\sum_i\frac{\sigma_i\mathbf{u}_i^T\mathbf{S}}{\sigma_i^2+\alpha}\mathbf{b}_i\,. \tag{4.2.7}$$

For $\alpha\ll\sigma_j^2$ equation (4.2.7) reduces to equation (4.1.4). For $\alpha\gg\sigma_j^2$, the terms in the sum are effectively suppressed by a factor $\frac{\sigma_j^2}{\alpha}$. If α is chosen sufficiently large, it will prevent that the solution blows up.

First order Tikhonov regularization

First order Tikhonov regularization penalizes the gradients of the solution [67]. The velocity-space gradient penalty function is

$$\mathbf{L}^T\mathbf{L} = \boldsymbol{\nabla}_{v_\|}^T\boldsymbol{\nabla}_{v_\|} + \boldsymbol{\nabla}_{v_\perp}^T\boldsymbol{\nabla}_{v_\perp} \, , \tag{4.2.8}$$

where $\boldsymbol{\nabla}_{v_\|}$ and $\boldsymbol{\nabla}_{v_\perp}$ are first order finite-difference approximations of the partial derivatives with respect to $v_\|$ and $v_\perp$, respectively. Because of how the discretized 2D distribution function is reshaped as a column vector, the $\boldsymbol{\nabla}_{v_\|}$ and $\boldsymbol{\nabla}_{v_\perp}$ matrices are not trivial. To illustrate this, the matrices in the case of a 3x3 distribution function, $\mathbf{F}^{2D}$, are shown below.

$$\mathbf{F}^{2D} = \begin{bmatrix} f_{1,1} & f_{1,2} & f_{1,3} \\ f_{2,1} & f_{2,2} & f_{2,3} \\ f_{3,1} & f_{3,2} & f_{3,3} \end{bmatrix} . \tag{4.2.9}$$

This matrix is now reshaped as a 9x1 column matrix, $\mathbf{F}$:

$$\mathbf{F} = \begin{bmatrix} f_{1,1} \\ f_{2,1} \\ f_{3,1} \\ f_{1,2} \\ f_{2,2} \\ f_{3,2} \\ f_{1,3} \\ f_{2,3} \\ f_{3,3} \end{bmatrix} . \tag{4.2.10}$$

First, the derivative with respect to $v_\perp$ is considered. In this example, a backwards finite difference approximation where $\frac{\partial \mathbf{F}_{i,j}}{\partial v_\perp} \simeq \frac{\mathbf{F}_{i,j} - \mathbf{F}_{(i-1),j}}{\Delta v}$ is used. At the boundary, the entire row is set equal to 0 [68].

$$\nabla_{v_\perp} = \frac{1}{\Delta v}\begin{bmatrix} 0 & 0 & 0 & 0 & 0 & 0 & 0 & 0 & 0 \\ -1 & 1 & 0 & 0 & 0 & 0 & 0 & 0 & 0 \\ 0 & -1 & 1 & 0 & 0 & 0 & 0 & 0 & 0 \\ 0 & 0 & 0 & 0 & 0 & 0 & 0 & 0 & 0 \\ 0 & 0 & 0 & -1 & 1 & 0 & 0 & 0 & 0 \\ 0 & 0 & 0 & 0 & -1 & 1 & 0 & 0 & 0 \\ 0 & 0 & 0 & 0 & 0 & 0 & 0 & 0 & 0 \\ 0 & 0 & 0 & 0 & 0 & 0 & -1 & 1 & 0 \\ 0 & 0 & 0 & 0 & 0 & 0 & 0 & -1 & 1 \end{bmatrix} \tag{4.2.11}$$

$$\Rightarrow \nabla_{v_\perp}\mathbf{F} = \frac{1}{\Delta v}\begin{bmatrix} 0 \\ f_{2,1} - f_{1,1} \\ f_{3,1} - f_{2,1} \\ 0 \\ f_{2,2} - f_{1,2} \\ f_{3,2} - f_{2,2} \\ 0 \\ f_{2,3} - f_{1,3} \\ f_{3,3} - f_{2,3} \end{bmatrix}. \tag{4.2.12}$$

In the same way, $\nabla_{v_\parallel}$ can be formulated:

$$\nabla_{v_\parallel} = \frac{1}{\Delta v}\begin{bmatrix} 0 & 0 & 0 & 0 & 0 & 0 & 0 & 0 & 0 \\ 0 & 0 & 0 & 0 & 0 & 0 & 0 & 0 & 0 \\ 0 & 0 & 0 & 0 & 0 & 0 & 0 & 0 & 0 \\ -1 & 0 & 0 & 1 & 0 & 0 & 0 & 0 & 0 \\ 0 & -1 & 0 & 0 & 1 & 0 & 0 & 0 & 0 \\ 0 & 0 & -1 & 0 & 0 & 1 & 0 & 0 & 0 \\ 0 & 0 & 0 & -1 & 0 & 0 & 1 & 0 & 0 \\ 0 & 0 & 0 & 0 & -1 & 0 & 0 & 1 & 0 \\ 0 & 0 & 0 & 0 & 0 & -1 & 0 & 0 & 1 \end{bmatrix} \tag{4.2.13}$$

$$\Rightarrow \nabla_{v_\parallel}\mathbf{F} = \frac{1}{\Delta v}\begin{bmatrix} 0 \\ 0 \\ 0 \\ f_{1,2} - f_{1,1} \\ f_{2,2} - f_{2,1} \\ f_{3,2} - f_{3,1} \\ f_{1,3} - f_{1,2} \\ f_{2,3} - f_{2,2} \\ f_{3,3} - f_{3,2} \end{bmatrix}. \tag{4.2.14}$$

For any $\mathbf{F}$ of size $(n \times 1)$, analogous $(n \times n)$ gradient matrices can be formulated.

It is possible to formulate a first order Tikhonov scheme in energy-pitch coordinates. To do this correctly, the velocity-space gradient in (E, p)-coordinates must be derived. The (E, p)-coordinates have some resemblance to the well-known polar coordinate system.

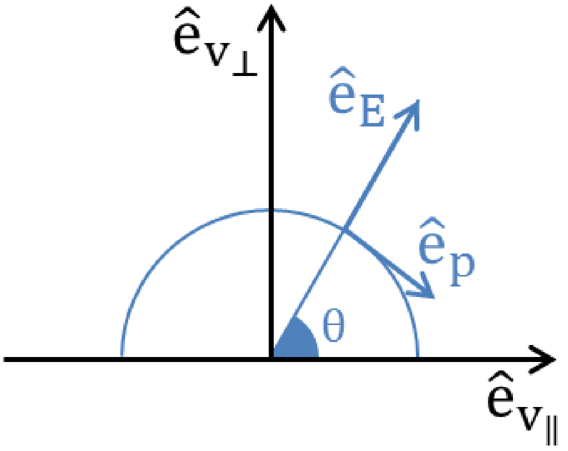

Figure 4.2.1: The relations between $\hat{\mathbf{e}}_{v_\parallel}, \hat{\mathbf{e}}_{v_\perp}, \hat{\mathbf{e}}_E$ and $\hat{\mathbf{e}}_p$.

Figure 4.2.1 shows the relations between the unit vectors $\hat{\mathbf{e}}_{v_\parallel}, \hat{\mathbf{e}}_{v_\perp}, \hat{\mathbf{e}}_E$ and $\hat{\mathbf{e}}_p$. The velocity-space gradient of f is

$$\nabla f = \left(\nabla_{v_\parallel} f\right) \hat{\mathbf{e}}_{v_\parallel} + \left(\nabla_{v_\perp} f\right) \hat{\mathbf{e}}_{v_\perp} = a \left(\nabla_E f\right) \hat{\mathbf{e}}_E + b \left(\nabla_p f\right) \hat{\mathbf{e}}_p \,, \tag{4.2.15}$$

where a and b are unknowns that must be calculated from the Jacobian. ∇_E and ∇_p are velocity-gradients along $\hat{\mathbf{e}}_E$ and $\hat{\mathbf{e}}_p$ respectively. Writing $\hat{\mathbf{e}}_E$ and $\hat{\mathbf{e}}_p$ as functions of $\hat{\mathbf{e}}_{v_\parallel}$ and $\hat{\mathbf{e}}_{v_\perp}$ gives

$$\hat{\mathbf{e}}_E = \cos(\theta)\, \hat{\mathbf{e}}_{v_\parallel} + \sin(\theta)\, \hat{\mathbf{e}}_{v_\perp} = p\, \hat{\mathbf{e}}_{v_\parallel} + \sqrt{1-p^2}\, \hat{\mathbf{e}}_{v_\perp} \,, \tag{4.2.16}$$

$$\hat{\mathbf{e}}_p = \sin(\theta)\, \hat{\mathbf{e}}_{v_\parallel} - \cos(\theta)\, \hat{\mathbf{e}}_{v_\perp} = \sqrt{1-p^2}\, \hat{\mathbf{e}}_{v_\parallel} - p\, \hat{\mathbf{e}}_{v_\perp} \,, \tag{4.2.17}$$

where the relation $p = \cos(\theta)$ has been used. The gradient in energy is now found by dotting equation (4.2.15) with $\hat{\mathbf{e}}_E$:

$$\begin{aligned} (\nabla f) \cdot \hat{\mathbf{e}}_E \quad &\Rightarrow \quad \left(\nabla_{v_\parallel} f\right) p + \left(\nabla_{v_\perp} f\right) \sqrt{1-p^2} = a \left(\nabla_E f\right) \\ &= \quad a \left(\left(\nabla_{v_\parallel} f\right) \frac{\partial v_\parallel}{\partial E} + \left(\nabla_{v_\perp} f\right) \frac{\partial v_\perp}{\partial E} \right) \,, \end{aligned} \tag{4.2.18}$$

To calculate the partial derivatives, the relations between $v_\parallel, v_\perp, E$ and p are needed:

$$v_\parallel = p \sqrt{\frac{2E}{m}} \tag{4.2.19}$$

$$v_\perp = \sqrt{1-p^2} \sqrt{\frac{2E}{m}} \,, \tag{4.2.20}$$

where m is the ion mass. The partial derivatives are:

$$\frac{\partial v_\parallel}{\partial E} = \frac{p}{\sqrt{2mE}} \tag{4.2.21}$$

$$\frac{\partial v_\perp}{\partial E} = \frac{\sqrt{1-p^2}}{\sqrt{2mE}} \,. \tag{4.2.22}$$

Inserting equations (4.2.21) and (4.2.22) in equation (4.2.18) gives

$$\left(\nabla_{v_\parallel} f\right) p + \left(\nabla_{v_\perp} f\right) \sqrt{1-p^2} = a\left(\left(\nabla_{v_\parallel} f\right) \frac{p}{\sqrt{2mE}} + \left(\nabla_{v_\perp} f\right) \frac{\sqrt{1-p^2}}{\sqrt{2mE}}\right). \tag{4.2.23}$$

Equation (4.2.23) is fulfilled for

$$a = \sqrt{2mE}\,. \tag{4.2.24}$$

Similarly, b can be found by dotting equation (4.2.15) with $\hat{\mathbf{e}}_p$:

$$\begin{aligned}(\nabla f)\cdot\hat{\mathbf{e}}_p \;&\Rightarrow\; \left(\nabla_{v_\parallel} f\right)\sqrt{1-p^2} - \left(\nabla_{v_\perp} f\right) p = b\left(\nabla_p f\right) \\ &= \; b\left(\left(\nabla_{v_\parallel} f\right)\frac{\partial v_\parallel}{\partial p} + \left(\nabla_{v_\perp} f\right)\frac{\partial v_\perp}{\partial p}\right).\end{aligned} \tag{4.2.25}$$

The partial derivatives are:

$$\frac{\partial v_\parallel}{\partial p} = \sqrt{\frac{2E}{m}}\,, \tag{4.2.26}$$

$$\frac{\partial v_\perp}{\partial p} = -\frac{p}{\sqrt{1-p^2}}\sqrt{\frac{2E}{m}}\,. \tag{4.2.27}$$

Inserting equations (4.2.26) and (4.2.27) in equation (4.2.25) gives

$$\left(\nabla_{v_\parallel} f\right)\sqrt{1-p^2} - \left(\nabla_{v_\perp} f\right) p = b\left(\left(\nabla_{v_\parallel} f\right)\sqrt{\frac{2E}{m}} - \left(\nabla_{v_\perp} f\right)\frac{p}{\sqrt{1-p^2}}\sqrt{\frac{2E}{m}}\right). \tag{4.2.28}$$

Equation (4.2.28) is fulfilled for

$$b = \sqrt{\frac{m}{2E}}\sqrt{1-p^2}\,. \tag{4.2.29}$$

Thus, the velocity-space gradient in energy-pitch coordinates becomes

$$\nabla f = \sqrt{2mE}\left(\nabla_E f\right)\,\hat{\mathbf{e}}_E + \sqrt{\frac{m}{2E}}\sqrt{1-p^2}\left(\nabla_p f\right)\,\hat{\mathbf{e}}_p\,. \tag{4.2.30}$$

where ∇_E and ∇_p are finite difference approximations to the partial derivatives. ∇_E has units of [1/energy] and ∇_p is unitless. The penalty function for first order Tikhonov regularization in (E,p)-coordinates becomes

$$\mathbf{L}^T\mathbf{L} = 2mE\boldsymbol{\nabla}_E^T\boldsymbol{\nabla}_E + \frac{m}{2E}\left(1-p^2\right)\boldsymbol{\nabla}_p^T\boldsymbol{\nabla}_p\,. \tag{4.2.31}$$

4.3 Minimum Fisher information

Position space tomography in plasma physics using regularization based on the principle of minimum Fisher information was first suggested by M. Anton and co-workers in 1996 [67]. In the implementation by M. Anton, the Fisher information principle is effectively built in as a Tikhonov penalty function. It can therefore be seen as a variant or expansion of the general Tikhonov regularisation method.

The minimum Fisher algorithm from M. Anton is an iterative algorithm that works as follows: a solution is found using Tikhonov regularization with a first-order linear penalty function. Let's call that solution $\mathbf{F}^{(1)}$. In the subsequent iterations, the penalty function in $\left(v_\parallel, v_\perp\right)$-coordinates becomes

$$\mathbf{L}^T\mathbf{L} \;=\; \boldsymbol{\nabla}_{v_\parallel}^T \mathbf{M}^{(n)} \boldsymbol{\nabla}_{v_\parallel} + \boldsymbol{\nabla}_{v_\perp}^T \mathbf{M}^{(n)} \boldsymbol{\nabla}_{v_\perp} \,, \tag{4.3.1}$$

where

$$\mathbf{M}_{i,j}^{(n)} \;=\; \begin{cases} \frac{1}{\mathbf{F}_i^{(n-1)}}\,\delta_{i,j} & \text{if } \mathbf{F}_i^{(n-1)} > 0 \\ M_{max}^{(n)}\,\delta_{i,j} & \text{if } \mathbf{F}_i^{(n-1)} \leq 0 \end{cases} \,, \tag{4.3.2}$$

where $M_{max}^{(n)}$ is one divided with the smallest positive value in $\mathbf{F}$. In (E,p)-coordinates, the minimum Fisher information penalty function becomes

$$\mathbf{L}^T\mathbf{L} = 2mE\boldsymbol{\nabla}_E^T \mathbf{M}^{(n)} \boldsymbol{\nabla}_E + \frac{m}{2E}\left(1-p^2\right)\boldsymbol{\nabla}_p^T \mathbf{M}^{(n)} \boldsymbol{\nabla}_p \,. \tag{4.3.3}$$

The solution converges after a few iterations. Figure 4.3.1 shows minimum Fisher information tomographies of the Gaussian distribution shown in figure 4.1.2a using noisy data. An increasing number of minimum Fisher information iterations are used in the tomographies. The tomography is already recreating the main features of the distribution after a single iteration. Including a few more iterations makes the tomography slightly more spiked. After three or four iterations, the tomography has converged. Figure 4.3.2 shows the same analysis for tomographies of an NBI distribution function. Again it is seen that the second and third iteration make the tomography slightly more peaked but additional iterations do not change the results much.

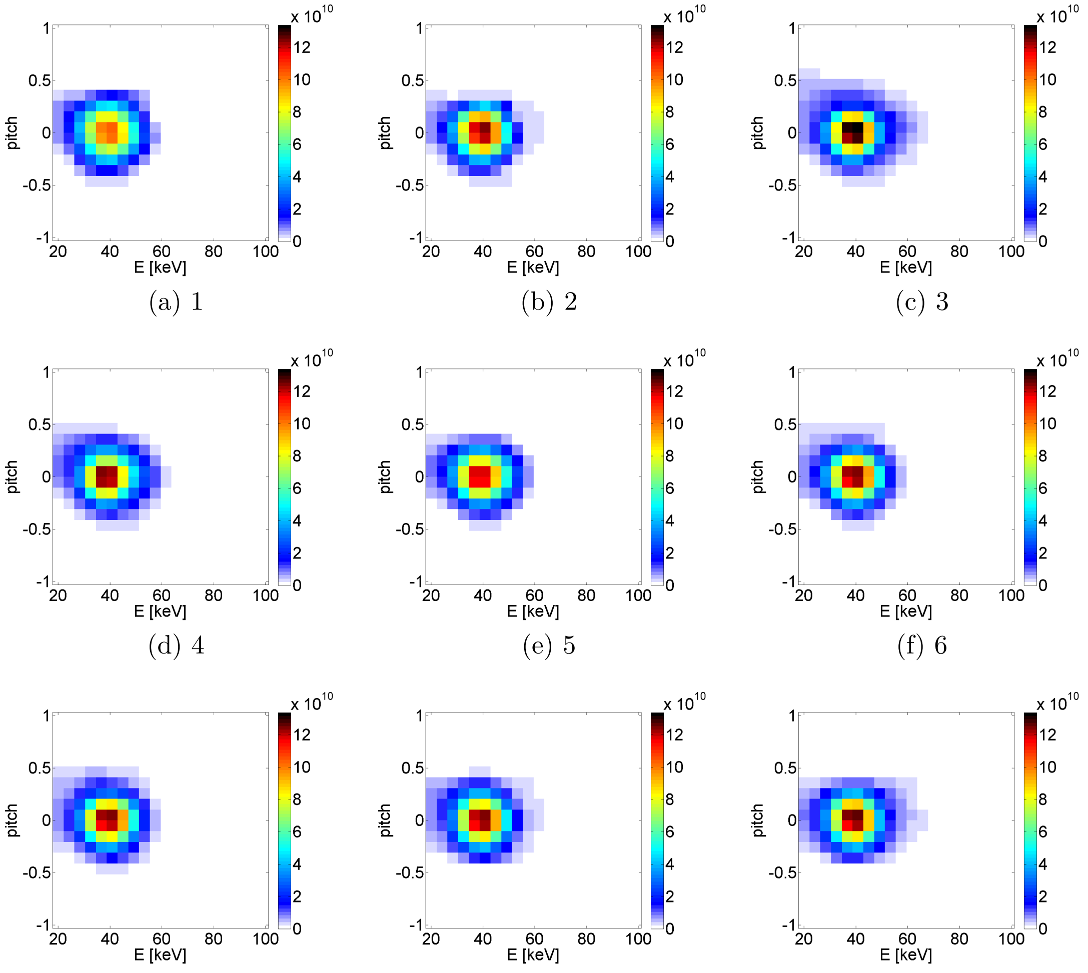

(a) 1 (b) 2 (c) 3

(d) 4 (e) 5 (f) 6

(g) 10 (h) 15 (i) 20

Figure 4.3.1: Tomographies of a Gaussian distribution function calculated using an increasing number of minimum Fisher information iterations in units of [ions/keV/cm^3].

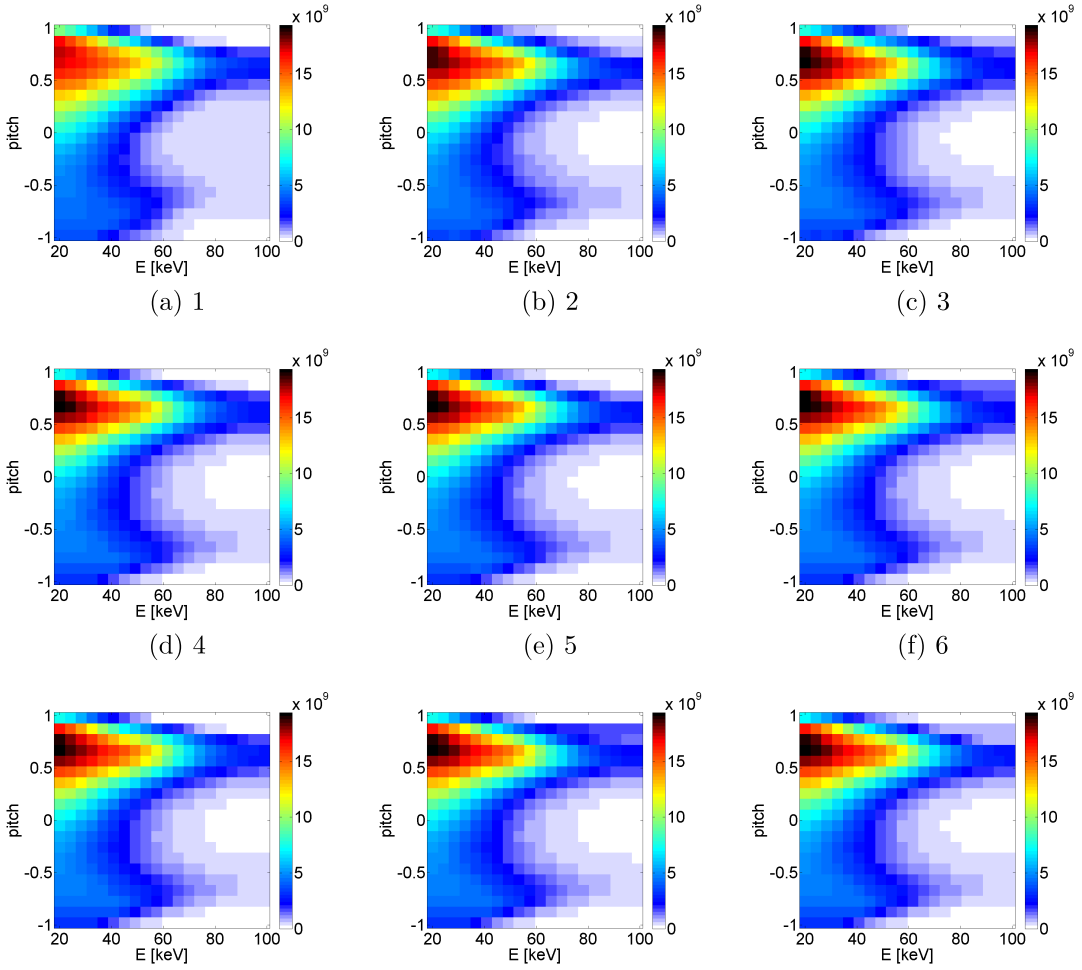

(a) 1 (b) 2 (c) 3

(d) 4 (e) 5 (f) 6

(g) 10 (h) 15 (i) 20

Figure 4.3.2: Tomographies of an NBI distribution function calculated using an increasing number of minimum Fisher information iterations in units of [ions/keV/cm^3].

4.4 Determining the regularization strength

When regularizing an inverse problem, a free parameter is introduced which determines the strength of regularization. In the case of truncated SVD, the free parameter is the number of singular values included when calculating the pseudo-inverse. For Tikhonov and the related minimum Fisher information regularization methods, the parameter α determines the balance between fitting the data and minimizing the regularizing term. Here, two different systematic methods for choosing the regularization strength are presented and compared.

4.4.1 Discrepancy method

One method to determine the value of the regularizing strength is the discrepancy principle which states that it should be chosen such that the residual norm is comparable to the norm of the error in the measurements [57]. The discrepancy principle is an intuitive method. However, it requires a good estimate of the noise level in the data. It can be shown that the residual norm is a monotonically increasing function of α. Writing the SVD of the transfer matrix $\mathbf{W}$ as a sum, using equation (4.2.7) and expanding the measurements, $\mathbf{S}$ in the basis of $\mathbf{u}_j$ from the SVD allows for writing the residual of a zeroth order Tikhonov solution as

$$\begin{aligned}\mathbf{WF}-\mathbf{S} &= \sum_j \left(\frac{\sigma_j \left(\mathbf{a}_j^T \mathbf{S}\right)}{\sigma_j^2+\alpha} \mathbf{a}_j \sigma_j \mathbf{b}_j^T \mathbf{b}_j - \left(\mathbf{a}_j^T \mathbf{S}\right) \mathbf{a}_j \right) \\ &= \sum_j \left(\frac{\sigma_j^2}{\sigma_j+\alpha} - 1 \right) \left(\mathbf{a}_j^T \mathbf{S}\right) \mathbf{a}_j \, . \qquad (4.4.1)\end{aligned}$$

The squared residual norm becomes

$$\begin{aligned}||\mathbf{WF}-\mathbf{S}||^2 &= \sum_j \left(\frac{\sigma_j^2}{\sigma_j+\alpha} - 1 \right)^2 \left(\mathbf{a}_j^T \mathbf{S}\right)^2 \mathbf{a}_j \mathbf{a}_j^T \\ &= \sum_j \left(\frac{\sigma_j^2}{\sigma_j+\alpha} - 1 \right)^2 \left(\mathbf{a}_j^T \mathbf{S}\right)^2 . \qquad (4.4.2)\end{aligned}$$

The derivative of the squared residual norm with respect to α is

$$\begin{aligned}\frac{\partial}{\partial \alpha} ||\mathbf{WF}-\mathbf{S}||^2 &= \sum_j 2 \left(\frac{\sigma_j^2}{\sigma_j^2+\alpha} - 1 \right) \left(\mathbf{a}_j^T \mathbf{S}\right)^2 (-1) \sigma_j^2 \frac{1}{\left(\sigma_j^2+\alpha\right)^2} \\ &= \sum_j \frac{2\sigma_j^2 \left(\mathbf{a}_j^T \mathbf{S}\right)^2}{\left(\sigma_j^2+\alpha\right)^2} \left(1 - \frac{\sigma_j^2}{\sigma_j^2+\alpha} \right) . \qquad (4.4.3)\end{aligned}$$

From equation (4.4.3) it is seen that $\frac{\partial}{\partial \alpha}||\mathbf{WF}-\mathbf{S}||^2 > 0$ since $\alpha > 0$. Using this result the discrepancy principle can be implemented in an iterative algorithm. A lower and upper bound on α is chosen and α is found in between. The geometric or arithmetic mean can be used. If the residual norm of the new solution is much smaller than the norm of the noise in the measurements, the new α is too small and it becomes the new lower bound. If the residual norm is much larger than the norm of the noise α becomes the new upper bound. This is repeated until the residual norm is close to the norm of the noise.

4.4.2 L-curve method

Another method is the L-curve method [57,69]. Figure 4.4.1 shows an L-curve for 0'th order Tikhonov inversions of a Gaussian distribution. For each value of α the corresponding Tikhonov solution which minimizes

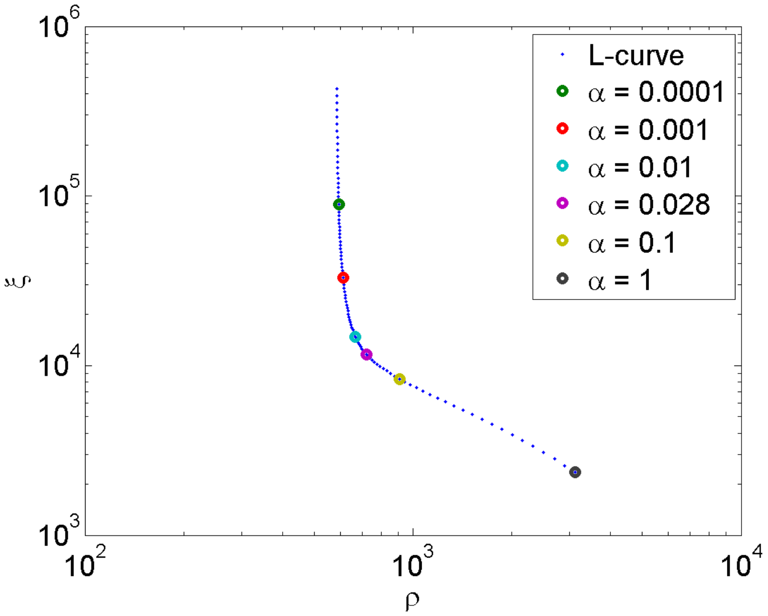

Figure 4.4.1: Example of an L-curve.

$$\min_{\mathbf{F}} \left(||\mathbf{WF} - \mathbf{S}|| + \alpha ||\mathbf{F}|| \right) \tag{4.4.4}$$

is found. The norm squared of the solution and the residual norm squared are calculated and plotted as a single point in a loglog plot. ρ is the squared residual norm and ξ is the squared norm of $\mathbf{F}$. When changing α many orders of magnitude, a curve in the shape of an L is obtained. The L-curve plot can be split in different regimes as a function of α. For very low values of α (top left vertical part of the L-curve) the norm of the solution is large but the residual norm is very small. This means that the solution fits the (noisy) data very well. This corresponds to the unregularized solution which is useless in the realistic case of noisy measurements. When increasing α, at some point the L-curve becomes almost horizontal. At this point, increasing α even further does not lead to a much more regularized solution. However, the solutions found will fit the data less and less. The idea is now that the optimal value of α is the one which corresponds to the corner in the L-curve. In this example the optimal value is found to be $\alpha = 0.028$. The Tikhonov solutions calculated for the α-values shown in figure 4.4.1 are shown in figure 4.4.2.

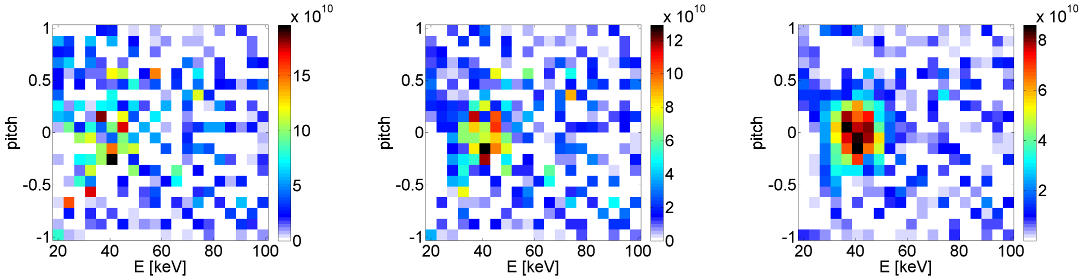

(a) $\alpha = 0.0001$. (b) $\alpha = 0.001$. (c) $\alpha = 0.01$.

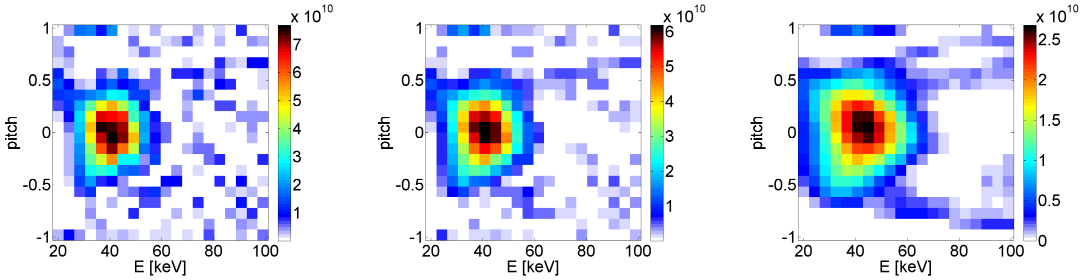

(d) $\alpha = 0.028$. (e) $\alpha = 0.1$. (f) $\alpha = 1$.

Figure 4.4.2: Tomographies of the Gaussian distribution for different α-values in units of [ions/keV/cm^3].

The curvature of the L-curve

The curvature of the L-curve is maximized in the corner. Therefore, the curvature of the L-curve is a parameter which can be used for choosing the value of the regularization parameter [70]. First, $\lambda = \sqrt{\alpha}$ is introduced. The squared norms are:

$$\rho = ||\mathbf{WF} - \mathbf{S}||^2 , \tag{4.4.5}$$
$$\xi = ||\mathbf{F}||^2 . \tag{4.4.6}$$

It can be shown that

$$\rho' = \frac{d\rho}{d\lambda} = -\lambda^2 \xi' , \tag{4.4.7}$$

where $\xi' = \frac{d\xi}{d\lambda}$ [70]. The logarithm of the squared norms are

$$\hat{\xi} = \log(\xi) , \tag{4.4.8}$$
$$\hat{\rho} = \log(\rho) . \tag{4.4.9}$$

The derivatives of the logarithm of the squared norms with respect to λ become

$$\frac{d}{d\lambda}\left\{\hat{\xi}\right\} = \frac{\xi'}{\xi} = \hat{\xi}' , \tag{4.4.10}$$
$$\frac{d}{d\lambda}\left\{\hat{\rho}\right\} = \frac{\rho'}{\rho} = \hat{\rho}' . \tag{4.4.11}$$

The second derivatives of the logarithm of the squared norms are

$$\frac{d}{d\lambda}\left\{\hat{\xi}'\right\} = \frac{\xi\xi'' - (\xi')^2}{\xi^2} = \hat{\xi}'' \,, \tag{4.4.12}$$

$$\frac{d}{d\lambda}\left\{\hat{\rho}'\right\} = \frac{\rho\rho'' - (\rho')^2}{\rho^2} = \hat{\rho}'' \,. \tag{4.4.13}$$

The second derivative of ρ is

$$\rho'' = \frac{d}{d\lambda}\left\{\rho'\right\} = \frac{d}{d\lambda}\left\{-\lambda^2\xi'\right\} = -2\lambda\xi' - \lambda^2\xi'' \,, \tag{4.4.14}$$

where the relation between ρ' and ξ' from equation (4.4.7) is used. The curvature, κ, is given by

$$\begin{aligned}
\kappa &= \frac{\hat{\rho}'\hat{\xi}'' - \hat{\rho}''\hat{\xi}'}{\left((\hat{\rho}')^2 + \left(\hat{\xi}'\right)^2\right)^{3/2}} \\
&= \frac{\frac{-\lambda^2\xi'}{\rho}\left(\frac{\xi\xi''-(\xi')^2}{\xi^2}\right) - \frac{\xi'}{\xi}\left(\frac{\rho\rho''-(\rho')^2}{\rho^2}\right)}{\left(\left(\frac{-\lambda^2\xi'}{\rho}\right)^2 + \left(\frac{\xi'}{\xi}\right)^2\right)^{3/2}} \\
&= -\frac{-\frac{\lambda^2\xi\xi'\xi''}{\rho\xi^2} + \frac{\lambda^2(\xi')^3}{\rho\xi^2} - \frac{\xi'}{\xi}\left(\frac{\rho\left(-2\lambda\xi'-\lambda^2\xi''\right)-\left(-\lambda^2\xi'\right)^2}{\rho^2}\right)}{(\xi')^3\left(\frac{\lambda^4}{\rho^2} + \frac{1}{\xi^2}\right)^{3/2}} \,.
\end{aligned} \tag{4.4.15}$$

The minus sign arises because ξ' i negative. This can be deduced from figure 4.4.1.

$$\begin{aligned}
\kappa &= -\frac{-\frac{\lambda^2\xi'\xi''}{\xi\rho} + \frac{\lambda^2(\xi')^3}{\xi^2\rho} + \frac{2\lambda(\xi')^2}{\xi\rho} + \frac{\lambda^2\xi'\xi''}{\xi\rho} + \frac{\lambda^4(\xi')^3}{\xi\rho^2}}{(\xi')^3\left(\frac{\lambda^4\xi^2+\rho^2}{\xi^2\rho^2}\right)^{3/2}} \\
&= -\frac{\frac{\lambda^2(\xi')^3}{\xi^2\rho} + \frac{2\lambda(\xi')^2}{\xi\rho} + \frac{\lambda^4(\xi')^3}{\xi\rho^2}}{\left(\frac{\xi'}{\xi\rho}\right)^3\left(\lambda^4\xi^2 + \rho^2\right)^{3/2}} \\
&= -\frac{\lambda^2\xi\rho^2 + \frac{2\lambda\xi^2\rho^2}{\xi'} + \lambda^4\xi^2\rho}{\left(\lambda^4\xi^2 + \rho^2\right)^{3/2}} \,.
\end{aligned} \tag{4.4.16}$$

κ is shown as a function of α in figure 4.4.3.

L-curve method applied to 1st order Tikhonov and minimum Fisher information regularization

The L-curve method can also be applied to higher order Tikhonov regularization as well as the minimum Fisher information regularization method implemented as an iterative Tikhonov variant. The only difference is in the definition of ξ. For the first order Tikhonov regularization, ξ is

$$\xi = ||\boldsymbol{\nabla}_E\mathbf{F}||^2 + ||\boldsymbol{\nabla}_p\mathbf{F}||^2 \,. \tag{4.4.17}$$

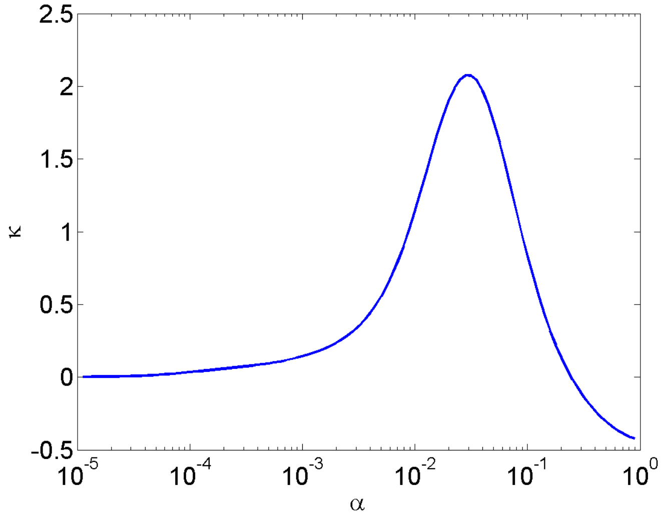

Figure 4.4.3: Example of the behaviour of the curvature.

For minimum Fisher information regularization, ξ is

$$\xi = ||\sqrt{\mathbf{M}}\boldsymbol{\nabla}_E\mathbf{F}||^2 + ||\sqrt{\mathbf{M}}\boldsymbol{\nabla}_p\mathbf{F}||^2 \, , \tag{4.4.18}$$

where $\mathbf{M}$ is given by equation (4.3.2).

L-curve method applied to truncated SVD

It is also possible to apply the principle behind the L-curve to truncated SVD. The problem is slightly different as the truncation level, k, to be determined is not a continuous variable. When calculating the L-curve for SVD, the norm of the solution is used as for zeroth order Tikhonov. In my implementation of the L-curve method for SVD in MatLab, I am using a function written by P.C. Hansen available in the MatLab repository called regtools[2]. It is based on an adaptive pruning algorithm [71].

4.4.3 Comparison of L-curve and discrepancy methods

The two methods for choosing the regularization strength are compared. Synthetic noisy measurements are calculated using the following equation

$$\mathbf{S}_{noisy} = \mathbf{S}_{exact} + c\left\langle\sqrt{\mathbf{S}_{exact}}\right\rangle \mathcal{N}\left(0, \max\left(e_{min}, \sqrt{\mathbf{S}_{exact}}\right)\right) \, , \tag{4.4.19}$$

where $\left\langle\sqrt{\mathbf{S}_{exact}}\right\rangle$ is the mean of the square root of the noise-free signal. $\mathcal{N}\left(0, \max\left(e_{min}, \sqrt{\mathbf{S}_{exact}}\right)\right)$ is a Gaussian distribution with mean 0 and standard deviation the square root of the noise-free signal or a constant e_{min}. e_{min} mimics the noise contribution from the background, which dominates when the noise-free signal goes to zero. c is a scaling factor between 0 and 1 which allows for controlling the noise level in the synthetic measurements.

---

[2] Available at http://www.mathworks.com/matlabcentral/fileexchange/52-regtools

Figure 4.4.4 shows a bi-Maxwellian distribution function used as a test distribution in this comparison of methods to choose the regularization strength.

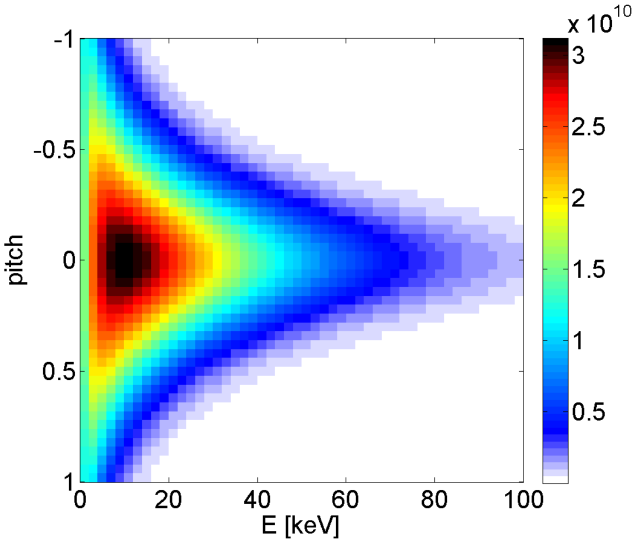

Figure 4.4.4: Bi-Maxwellian distribution function in units of [ions/keV/cm^3].

Figures 4.4.5 and 4.4.6 show tomographies of the bi-Maxwellian test distribution calculated using the zeroth order Tikhonov and minimum Fisher information regularization methods for increasing noise levels. For very small noise levels ($c = 0.1$), the discrepancy principle and L-curve method produce almost the same results. When increasing the noise level it is seen that the discrepancy principle over-regulates the problem as is evident in the top row in both figure 4.4.5 and 4.4.6.

Figure 4.4.7 shows the absolute value of the difference between the true distribution shown in figure 4.4.4 and the tomographies as a function of the noise level, c, in the synthetic data. The difference between the true distribution and the tomographies increase as a function of noise level for both methods, as expected. However, choosing the regularization strength using the L-curve method clearly produce better results in these examples.

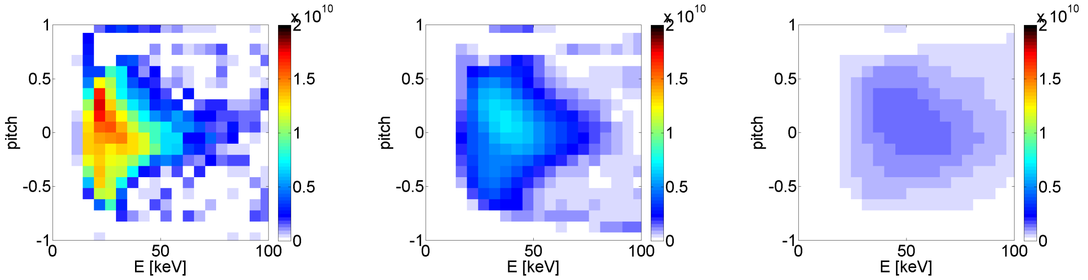

(a) Discrepancy, $c = 0.1$ (b) Discrepancy, $c = 0.5$ (c) Discrepancy, $c = 0.9$

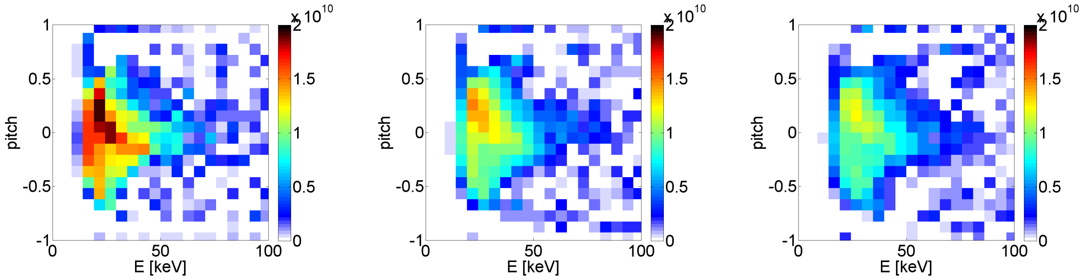

(d) L-curve, $c = 0.1$ (e) L-curve, $c = 0.5$ (f) L-curve, $c = 0.9$

Figure 4.4.5: Tomographies of the bi-Maxwellian test distribution calculated using zeroth order Tikhonov regularization and synthetic data with increasing noise level. The top row shows the result when the discrepancy principle is used for choosing α, the bottom row shows the result when the L-curve method is used. All in units of [ions/keV/cm^3]

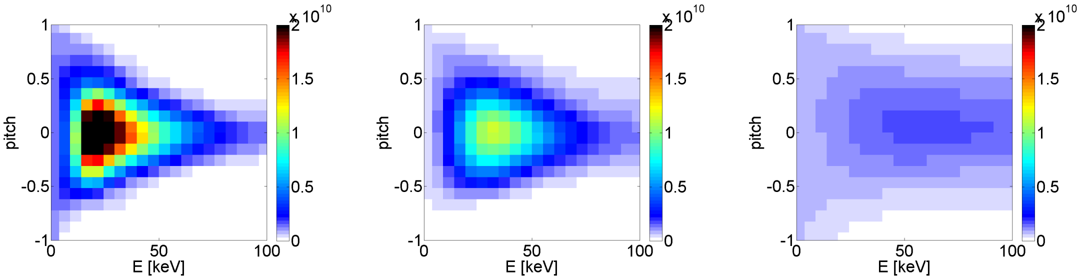

(a) Discrepancy, $k = 0.1$ (b) Discrepancy, $k = 0.5$ (c) Discrepancy, $k = 0.9$

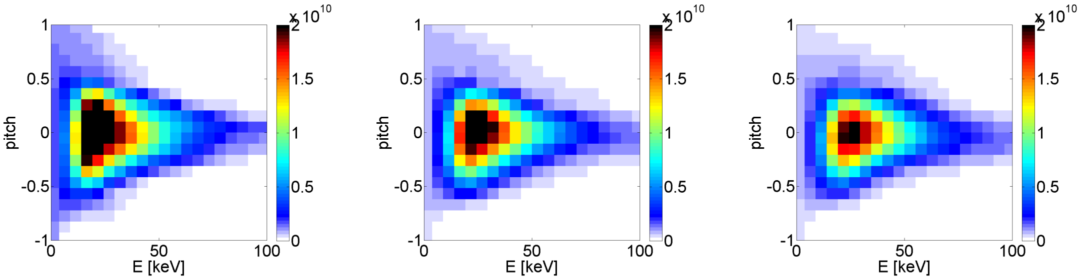

(d) L-curve, $k = 0.1$ (e) L-curve, $k = 0.5$ (f) L-curve, $k = 0.9$

Figure 4.4.6: Tomographies of the bi-Maxwellian test distribution calculated using minimum Fisher information regularization and synthetic data with increasing noise level. The top row shows the result when the discrepancy principle is used for choosing α, the bottom row shows the result when the L-curve method is used. All in units of [ions/keV/cm^3]

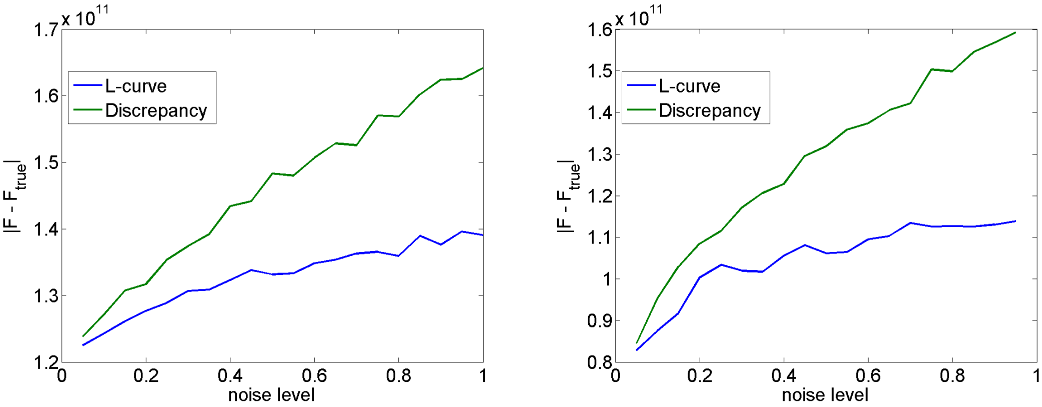

(a) T0 (b) MFI

Figure 4.4.7: Difference between the true distribution and the tomographies as a function of noise level.

4.5 Uncertainties of a tomography

It is possible to estimate the uncertainties in a tomography. Here, the uncertainties due to noise in the measurements, due to uncertainties in the forward model and uncertainties introduced by the regularization methods themselves are considered.

If the forward model contains uncertainties, these will propagate through to the tomographies. For velocity-space tomography, the forward model is described by the weight functions. The numerical FIDA weight functions are calculated using a code called FIDASIM [72]. It takes several measured plasma parameters at input. The radial profiles of these plasma parameters are measured during a plasma discharge and are associated with given uncertainties. The weight functions are most sensitive to the ion temperature and drift velocity, the electron temperature and density and the effective charge Z_{eff}. The uncertainties in these, and in principle any other nuisance parameter, lead to uncertainties in the weight functions, $\delta\mathbf{W}$. Assuming a Gaussian error distribution of the bulk plasma parameters, the uncertainty in the forward model is calculated by sampling a population of weight functions calculated by varying one nuisance plasma parameter at a time and keeping the other parameters fixed. The total variance of the weight function is then obtained by summing the variances obtained from each plasma parameter. The corresponding uncertainty in the spectrum, $\mathbf{e}_m$, can be calculated from $\delta\mathbf{W}$

$$\begin{aligned} \mathbf{S}_{exact} + \mathbf{e}_m &= (\mathbf{W} + \delta\mathbf{W})\,\mathbf{F}_{true} \\ \Rightarrow \mathbf{e}_m &= \delta\mathbf{W}\mathbf{F}_{true}\,. \end{aligned} \tag{4.5.1}$$

$\delta\mathbf{W}$ is the square root of the total weight function variance. $\mathbf{e}_m$ depends on the (often unknown) true distribution function. However, if an estimate of $\mathbf{F}_{true}$ can be obtained, $\mathbf{e}_m$ can be estimated. Assuming that the measurement and forward model uncertainties are uncorrelated, the combined uncertainty is

$$\mathbf{e}_{data} = \sqrt{\mathbf{e}_S^2 + \mathbf{e}_m^2}\,, \tag{4.5.2}$$

where $\mathbf{e}_S$ is the measurement uncertainty in the measured spectrum from the fast-ion diagnostic. For FIDA it is the photon noise. $\mathbf{e}_{data}$ is then used to normalize the measurements and transfer matrix as explained in the beginning of chapter 4.

The covariance matrix of the tomography due to uncertainty in the spectra, $\mathbf{C}_e^F$, is [52, 68, 73]

$$\mathbf{C}_e^F = \mathbf{W}^{\dagger}\mathbf{C}_e^S\left(\mathbf{W}^{\dagger}\right)^T\,, \tag{4.5.3}$$

where $\mathbf{C}_e^S$ is the covariance matrix of the uncertainty in the spectra and $\mathbf{W}^{\dagger}$ denotes the regularized inverse. For uncorrelated uncertainties, the variance in the tomography is then given by the diagonal elements of the covariance matrix. For SVD, $\mathbf{W}^{\dagger} = \mathbf{W}^{+}$; the pseudoinverse of $\mathbf{W}$. For Tikhonov and minimum Fisher information regularization the regularized inverse is

$$\mathbf{W}^{\dagger} = \left(\mathbf{W}^T\mathbf{W} + \alpha\mathbf{L}^T\mathbf{L}\right)^{-1}\mathbf{W}^T\,, \tag{4.5.4}$$

where the relevant $\mathbf{L}$ operator is used for the given inversion method.

As $\mathbf{W}^\dagger$ depends on the regularization, $\mathbf{C}_e^F$ depends both on the choice of regularization method and the level of regularization. In fact, the purpose of the regularization is to suppress the effect of noise in the spectra. The price one pays by regularizing the problem is to introduce a regularization error or bias. This error makes it impossible to recreate the true distribution, even if the measurements were noise free. This is illustrated by the so-called resolution matrix, $\mathbf{R}_m$ [68, 74]. It is defined as

$$\mathbf{R}_m = \mathbf{W}^\dagger \mathbf{W}\,, \tag{4.5.5}$$

In the case that $\mathbf{W}^\dagger = \mathbf{W}^{-1}$, $\mathbf{R}_m$ is the identity matrix. The more different $\mathbf{R}_m$ is from the identity matrix, the poorer $\mathbf{W}^\dagger$ is as an estimate of the inverse of $\mathbf{W}$.

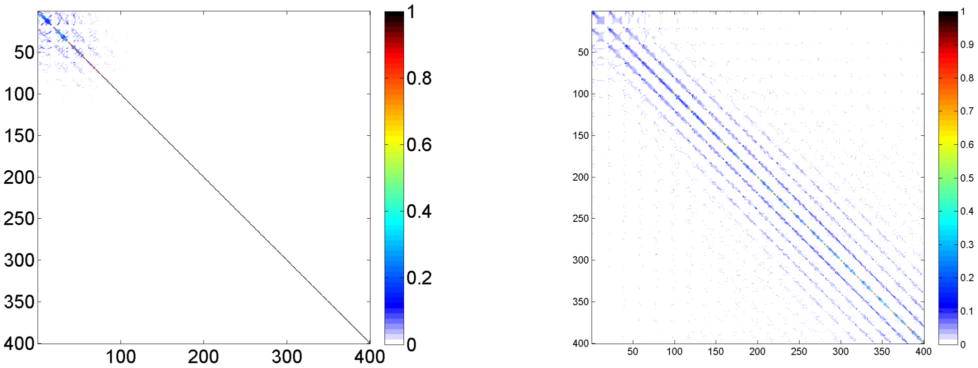

(a) $\alpha = 10^{-5}$ (b) $\alpha = 0.028$

Figure 4.5.1: Examples of resolution matrices calculated using zeroth order Tikhonov for different α values.

Figure 4.5.1 shows two examples of resolution matrices calculated using zeroth order Tikhonov regularization for different α-values. $\alpha = 0.028$ correspond to the optimal value found using the L-curve method. $\alpha = 10^{-5}$ correspond to the case with very low regularization.

The regularization error, $\mathbf{e}_{reg}$, is defined as [68, 74]

$$\begin{aligned} \mathbf{e}_{reg} &= \mathbf{F}_{true} - \mathbf{F}_{tomography,0} \\ &= \mathbf{F}_{true} - \mathbf{W}^\dagger \mathbf{S}_{exact} \\ &= \mathbf{F}_{trye} - \mathbf{W}^\dagger \mathbf{W} \mathbf{F}_{true} \\ &= \left(\mathbf{I} - \mathbf{W}^\dagger \mathbf{W}\right) \mathbf{F}_{true}\,, \end{aligned} \tag{4.5.6}$$

where $\mathbf{I}$ is the $n \times n$ identity matrix and $\mathbf{F}_{tomography,0}$ is the tomography that would be obtained with noise free measurements. $\mathbf{e}_{reg}$, as $\mathbf{e}_m$, depends on $\mathbf{F}_{true}$.

A measure of the total uncertainty of the tomographic inversion as is defined as

$$\mathbf{e}_{tot} = \sqrt{\left(\operatorname{diag}\left(\mathbf{C}_e^F\right)\right)^2 + \mathbf{e}_{reg}^2}\,. \tag{4.5.7}$$

However, it should be noted that the regularization error has a different character than the data uncertainty which represents an assumed Gaussian distribution of values in many realizations of the experiment. Instead, the regularization error characterizes a systematic bias introduced by the method. Nevertheless, the combination of these uncertainties can be used as a figure of merit of the total uncertainty of the tomographic inversion.

In paper III we used a slightly different approach to calculate the uncertainties. Instead of using equation (4.5.3) to calculate the covariance matrix due to noise in the spectra, many synthetic spectra were generated and an inversion were calculated for each. The resulting variance in the tomography was used as a measure of $\operatorname{diag}\left(\mathbf{C}_e^F\right)$. The bias introduced by the regularization method was calculated as the difference between the true distribution and the mean of all the calculated tomographies. This is very similar to the first equality in equation (4.5.6).

4.6 Comparing inversion methods

If paper III, the different inversion methods are compared in how well they reconstruct known test distributions for various amount of noise in the synthetic data. It is found that the minimum Fisher information method performs better than the rest of the methods, except for the NBI beam distribution where the first order Tikhonov regularization method performs equally well. These two methods which both regularize by penalizing steep gradients are in general very good at reconstructing the overall shape of a distribution function. However, due to the way they regulate, the results are often smoother than the true distribution. On the other hand, the truncated SVD and zeroth order Tikhonov regularization methods can resolve finer details, but if the data is noisy, the details might be lost in jitter in the tomographies.

Chapter 5

Tomographies of real data

Calculating inversions using synthetic spectra (artificially generated data) is usable for method development and testing as well as for gaining insight into the behaviour of the inversion methods. The application of tomography to real measurements taken in situations where the physics is poorly understood may contribute significant new knowledge.

Most tomographies in this chapter are calculated from FIDA measurements at ASDEX Upgrade. In addition, the first tomographies based on the combination of FIDA and CTS measurements are presented. Figure 5.0.1 shows an example of a measured FIDA spectrum. This specific spectrum is measured during discharge #30815. It shows the measured intensity as a function of wavelength.

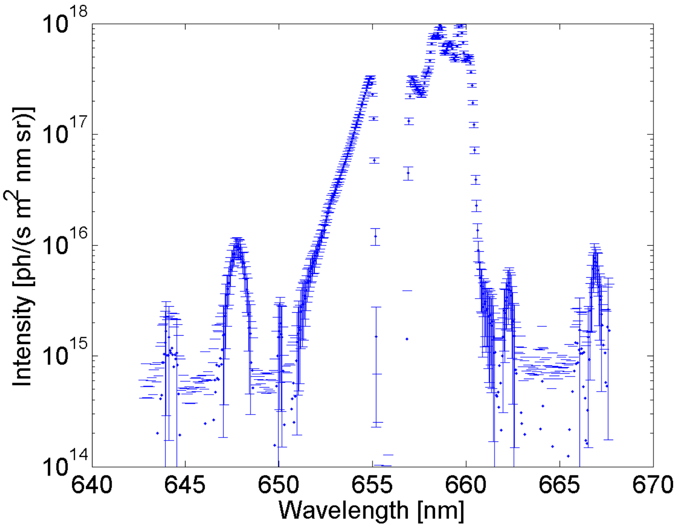

Figure 5.0.1: FIDA spectrum measured during discharge #30815.

The unshifted D_α light, named the cold D_α line, has a wavelength of 656.1 nm. To prevent saturation of the spectrometer from cold D_α light originating from the edge of the plasma, this part of the spectrum is blocked. This is evident as the large drop in intensity in this wavelength range in figure 5.0.1. Several other important features are visible in this spectrum. The radiation emitted by the injected neutral D atoms is here redshifted to wavelengths between 657 nm and 661 nm. The narrow peaks at large red- and blueshifts are caused by impurities in the plasma [25].

In order to identify the parts of a FIDA spectrum which can be used for tomography, the measured spectrum is compared with a synthetic spectrum. Using the numerical code FIDASIM [72], it is possible to simulate the different components in a measured spectrum. Figure 5.0.2 shows a simulation of the measured FIDA spectrum from figure 5.0.1. The beam emission contribution completely dominates the part of the spectrum between 657 nm and 661 nm. The two other components in the simulated spectrum are the halo component and the FIDA component [25]. The halo component is caused by charge exchange reactions between injected NBI neutrals and thermal ions. The halo component dominates the spectrum for small Doppler-shifts at wavelengths near 656.1 nm. The FIDA component is emitted by fast neutrals created in charge exchange reactions between an injected NBI neutral and a fast ion. Impurity emission lines, the cold D_α peak and the flat bremsstrahlung background are not included in the FIDASIM simulation. Bremsstrahlung is radiation emitted by the electrons in the plasma being slowed down in collisions with the ions [25]. Using the simulated FIDASIM components, I determine the usable parts of the spectrum by excluding the wavelength ranges dominated by beam and impurity emission as well as the part closest to the cold D_α line. For the spectrum in figure 5.0.1, the usable parts are shown in green in figure 5.0.3.

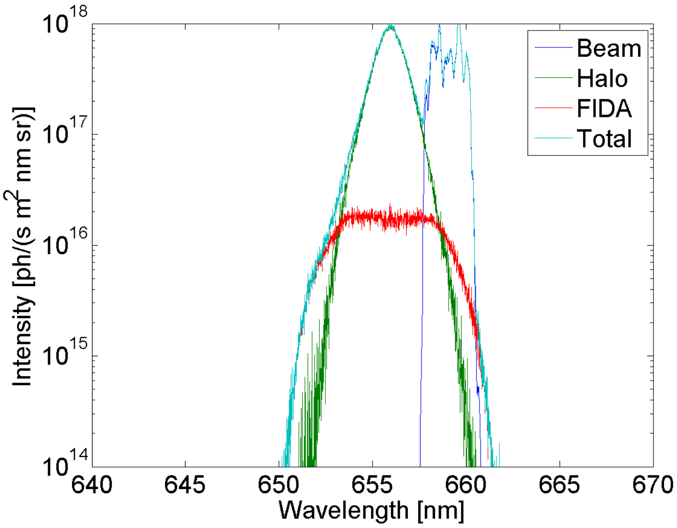

Figure 5.0.2: Simulation of the FIDA spectrum shown in figure 5.0.1.

Each data point in the spectrum in figure 5.0.3 has an associated weight function. Given a certain grid in velocity-space, it is investigated whether each weight function has non-zero values on this grid. Furthermore, to include as much data as possible while at the same time not have the result dominated too much by the thermal ions, a lower energy limit is defined, typically 10 keV. A data point is omitted if the corresponding weight function has non-zero values below this energy limit.

As explained in the beginning of chapter 4, the measurements are normalized with their measurement uncertainty in order to give most emphasis to data points with a high

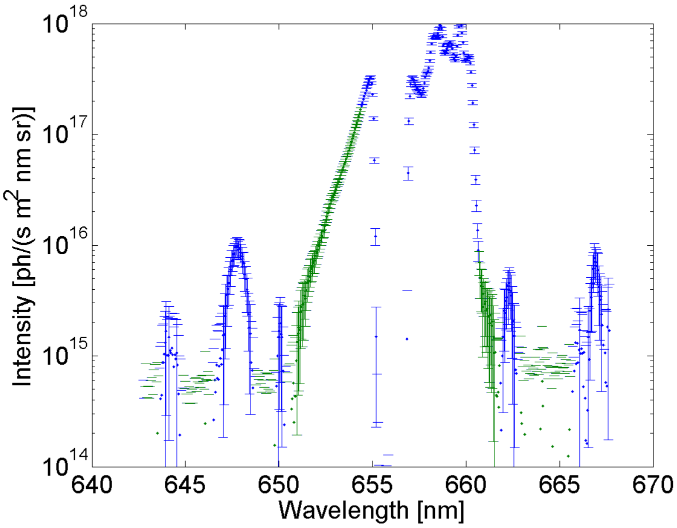

Figure 5.0.3: FIDA spectrum measured during discharge #30815. The usable parts of the spectrum are shown in green.

signal-to-noise ratio. Each individual data point in figure 5.0.3 is related to the fast-ion distribution function by a weight function calculated for that specific wavelength

$$S_k = \mathbf{W}_k \mathbf{F} \,. \tag{5.0.1}$$

S_k is the k'th data point and $\mathbf{W}_k$ is the corresponding weight function. As explained in section 2.6, each equation on the form of equation (5.0.1) is combined in a single linear algebra problem

$$\mathbf{S} = \mathbf{W}\mathbf{F} \,. \tag{5.0.2}$$

Figure 5.0.4a shows **S** for the usable data points from figure 5.0.3 normalized with their respective measurement uncertainty. **S** is a function of wavelength, however, as seen in figure 5.0.3, two neighbouring usable data points can correspond to wavelengths several nm apart. This is the reason that **S** is shown as a function of index number instead. The wavelength information is contained in the corresponding weight functions. This way, a combined **S** can be defined containing usable measurement points from several different views, as shown in figure 5.0.4b, which contains data from four different FIDA views.

5.1 FIDA set-up at ASDEX Upgrade

ASDEX Upgrade is very well equipped for diagnosing fast ions. The FIDA set-up is currently comprised of five different so-called views. Each view is a single plug in the tokamak wall, but each is made up of several lines-of-sight. A sketch of the different lines-of-sight is shown in figure 5.1.1 from [27]. Each view is shown with a different color. The single grey line is the 60 keV NBI beam named Q3. Every FIDA line-of-sight intersects this NBI beam. The FIDA system can only measure when this beam is turned

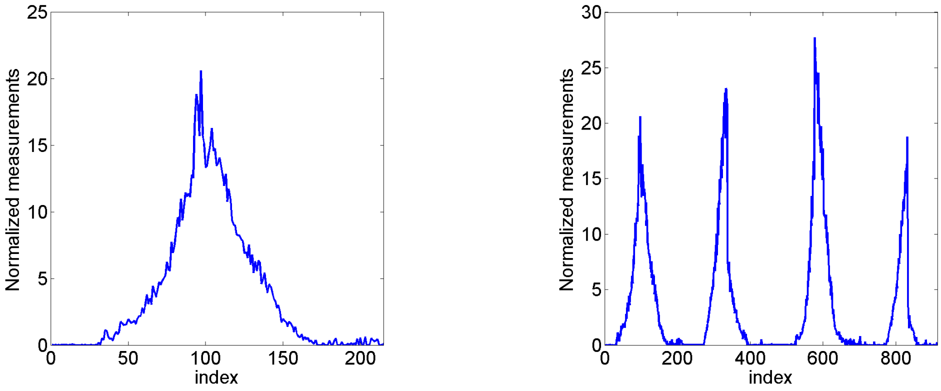

(a) **S** from one view (b) **S** from four views

Figure 5.0.4: FIDA data points normalized with their respective measurement uncertainty.

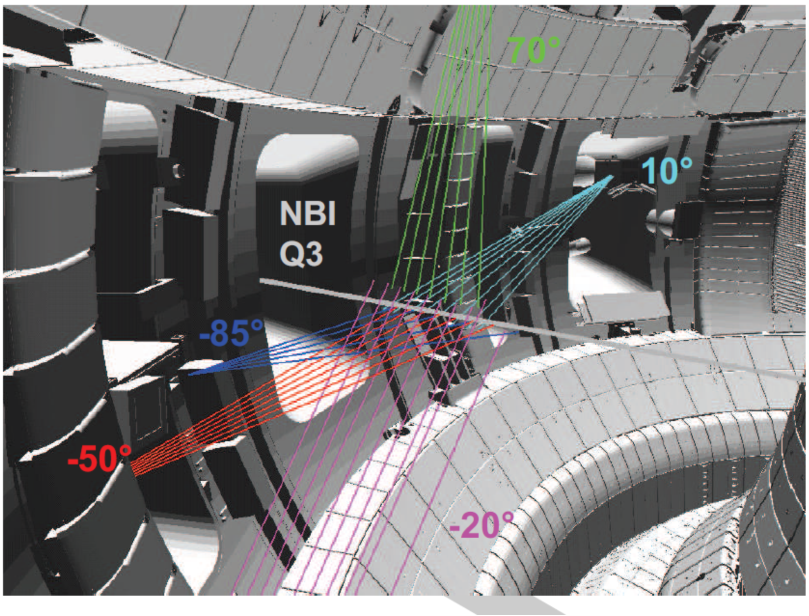

Figure 5.1.1: Illustration of the five FIDA views at ASDEX Upgrade. This figure is from [27].

on. The lines-of-sight for a single view are oriented in a fan-like formation along the NBI beam such that a radial profile of FIDA measurements is possible. For each view, the approximate angle between the central line-of-sight and the magnetic field is shown.

Two of the five views were installed recently with the specific purpose of optimizing the diagnostic for velocity-space tomography. Before that, the FIDA system was comprised of two dedicated and one borrowed view. The first dedicated view is a toroidal view composed of 15 radially distributed lines-of-sight. The angles between the toroidal view and the local magnetic field are about 10°. The other is a radial view composed of 12 lines-of-sight with angles to the local magnetic field of about 70°. A third line-of-sight with an angle to the magnetic field of about 160° (-20°) originally installed for the motional Stark effect (MSE) diagnostic is now used for the FIDA diagnostic as well. Measurements using this three-view set-up was used to calculate a fast-ion distribution function by tomographic inversion of the three FIDA spectra [53]. Using the method of velocity-space tomography, I determined the optimal angles for the new FIDA views. Synthetic measurements are calculated using the weight functions and a TRANSP simulated fast-ion velocity-space distribution of Q3, in a forward model for the three existing views. In addition to this, synthetic FIDA measurements are calculated for a wide range of other angles for additional two views. For each such 5 view FIDA set-up, an error parameter of the reconstruction is calculated. The error parameter is defined as

$$e_{rr} = \frac{\iint \left(\mathbf{F}_{true} - \mathbf{F}_{tomography}\right)^2 \,\mathrm{d}E\mathrm{d}p}{\iint \mathbf{F}_{true}\,\mathrm{d}E\mathrm{d}p}\,. \tag{5.1.1}$$

By repeating this for a large number of different viewing angles, a 2D grid is created showing the error parameter of a reconstruction of a hypothetical 5-view FIDA set-up as a function of the viewing angles of the two additional views. Figure 5.1.2 shows a contour plot of the error parameter as a function of the viewing angles of the two additional views. Several features are evident from figure 5.1.2. A clear diagonal line for $\phi_4 = \phi_5$ can be

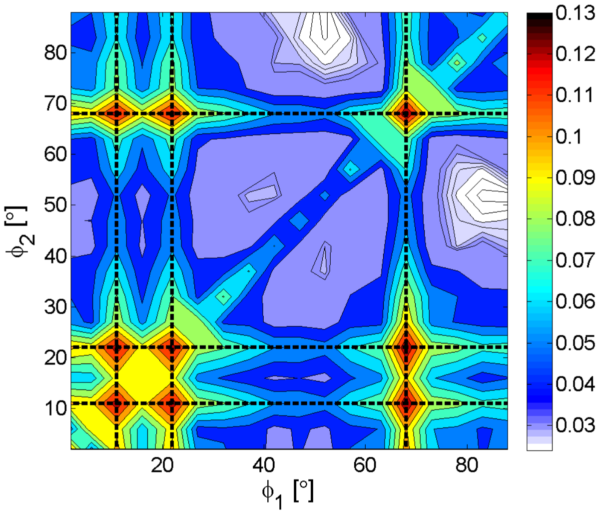

Figure 5.1.2: Contourplot of the error parameter, e_{rr} calculated using equation (5.1.1). It is shown as a function of the viewing angles of two additional FIDA views.

seen. Different viewing angles resolve different regions in velocity space, and thus the best inversion is possible when the views have different resolved angles. Therefore, the error parameter is larger on the diagonal. For the same reason the error parameter has local maxima at the angles of the existing views, at 10°, 20° and 70°. The error parameter map is mirrored along the diagonal since the two views are interchangeable. The lowest values of the error parameters are found away from the existing views, between 40° and 60° and between 80° and 90°. Finally, it is evident that the global minimum is found when one of the new views has a resolved angle around 50° and the other has a resolved angle around 85°. The angles of the views which were installed are around 95° and 130° (-85° and -50°).

5.2 Tomographies of one beam vs several beams

Here, tomographies of a velocity distribution consisting of a single NBI beam and a distribution with several beams are shown. This is done in order to test whether the tomograhy method is capable of distinguishing between the two cases.

5.2.1 One beam vs three beams

In ASDEX Upgrade discharge #30950 the FIDA measurements were performed during a phase of one beam heating at 60 keV, as well as a phase with three NBI beams heating the plasma, one at 60 keV and two at 93 keV.

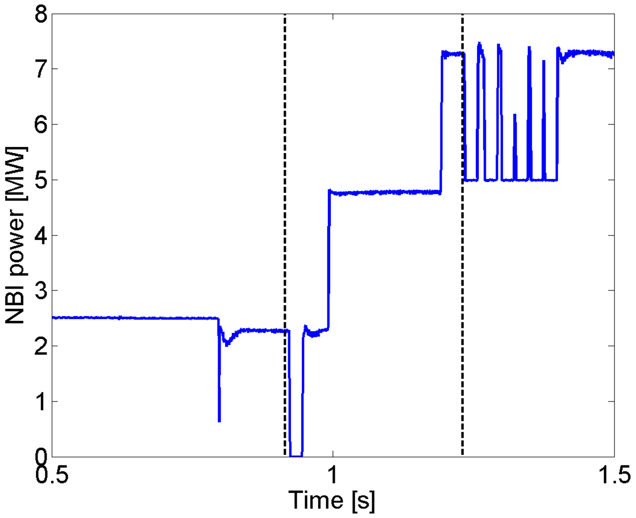

Figure 5.2.1: Injected NBI power as a function of time. The two dashed lines represent the times where tomographies are calculated.

Figure 5.2.1 shows the injected NBI power as a function of time during the beginning of discharge #30950. The two vertical lines represent the times where tomographies are calculated using measured FIDA data.

The simulated velocity-distribution functions from TRANSP are shown in figure 5.2.2. Figure 5.2.2a shows the one-beam distribution function. The full and half energy peaks at 60 keV and 30 keV are clearly visible. Figure 5.2.2b shows the simulated velocity distribution function for the three beam phase. The two additional beams are Q5 and Q8, both with injection energies of 93 keV.

Figure 5.2.3 show tomographies calculated for the one-beam phase and the three-beam phase using the different inversion methods. The tomographies of the three-beam phase clearly contain more fast ions compared to the one-beam phase. Furthermore, the calculated tomographies extend to higher energies in the three-beam phase. However, since the full energy peak at 93 keV is relatively weak compared to the large peak between 20 keV and 60 keV, none of the inversion methods are able to recreate it. Similar conclusions are drawn in [27] using different inversion methods.

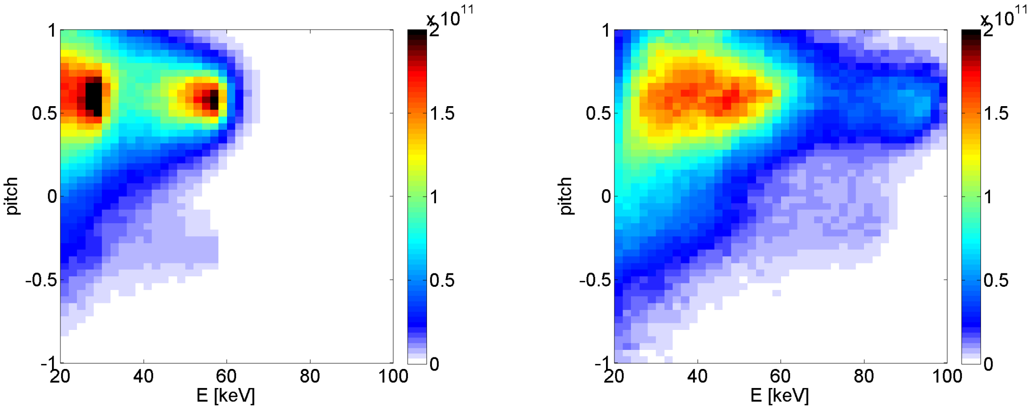

(a) One-beam distribution. (b) Three-beam distribution.

Figure 5.2.2: Simulated fast-ion velocity distribution functions in units of [ions/keV/cm^3].

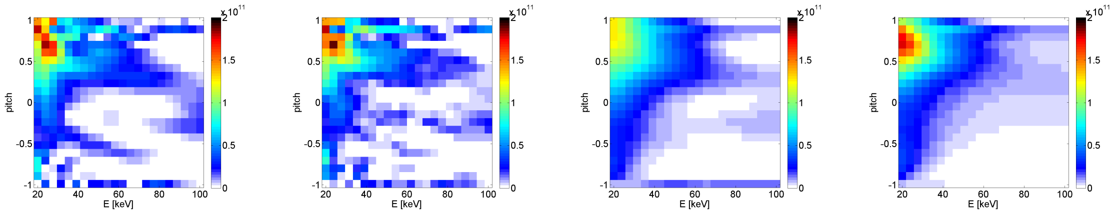

(a) One beam, SVD (b) One beam, T0 (c) One beam, T1 (d) One beam, MFI

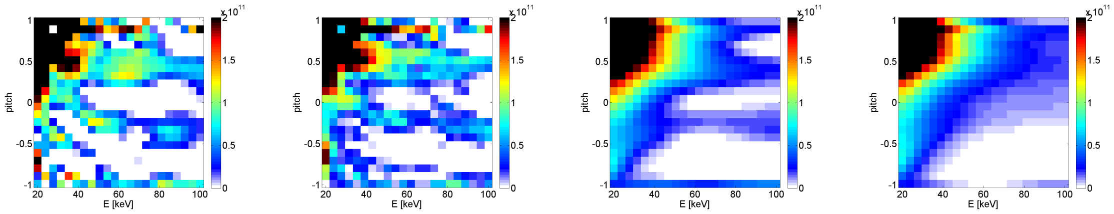

(e) Three beams, SVD (f) Three beams, T0 (g) Three beams, T1 (h) Three beams, MFI

Figure 5.2.3: Tomographies of the one-beam phase and three-beam phase in ASDEX Upgrade discharge #30950 in units of [ions/keV/cm^3].

5.3 Investigating sawtooth crashes using velocity-space tomography

In 2009, using the collective Thomson scattering diagnostic at TEXTOR, it was observed that sawtooth crashes affect some parts of velocity-space more than others [2, 75]. Using the flexibility of the CTS receiver, the viewing angle could be changed thus enabling a variation of the the velocity-space sensitivity of the detector, as given by the velocity-space weight functions. When a viewing angle close to 90° was used, the reduction in the fast-ion part of the CTS spectrum was less pronounced compared to the reduction observed when a more oblique angle around 40° was used. Using the velocity-space weight functions it was possible to identify the regions of velocity-space measured by the diagnostic in the two cases. It was found that when the diagnostic mainly measured ions with pitch close to 1, a reduction of about 50% was observed and when it mainly measured ions with pitch close to 0, a reduction of less than 20% was observed. This behaviour was afterwards observed at DIII-D [14]. At ASDEX Upgrade, a series of dedicated experiments were carried out with the aim of investigating the effect on the fast ions by sawtooth crashes and other MHD instabilities. Results from these investigations are presented here using the developed method of velocity-space tomography to help analysing the measurements.

5.3.1 ASDEX Upgrade discharge #30815

Paper IV investigates the effect on the fast ion caused by a sawtooth crash in ASDEX Upgrade in discharge #30815. As a part of this analysis, tomographies were calculated using time coherent averaged measurements taken just before and just after a sawtooth crash. Using the time coherent averaging, the signal-to-noise ratio could be increased. In paper IV, truncated SVD was used as inversion method since the other methods were not yet fully developed. In addition, the relative change was calculated to see whether some parts of velocity space were affected more than others.

Figure 5.3.1 shows the time coherent averaged FIDA spectra before (red) and after (blue) the crash. Only four FIDA views were measuring during this discharge. The shaded regions indicate the parts of the spectra which cannot be used due to beam and impurity emission. The sawtooth crash is especially evident in the upshifted part of the spectra in figures 5.3.1a and 5.3.1c and the downshifted part of the spectrum in figure 5.3.1b.

The tomographies of the central fast-ion distribution functions before and after the sawtooth crash included in the paper are shown in figure 5.3.2. The shaded region for energies below 15 keV cannot be recreated since there is no weight function coverage in this region.

Figure 5.3.3 shows simulations of the fast-ion distribution function from TRANSP/NUBEAM. The Kadomtsev sawtooth model implemented in TRANSP is used in the simulation of the distribution after the crash shown in figure 5.3.3b. Comparing figures 5.3.2 and 5.3.3 it is evident that the largest values in the tomographies are about twice as large as those in the simulation. This can be explained by the fact that some of the halo contribution is included in the tomographies and therefore the true comparison should be with the sum

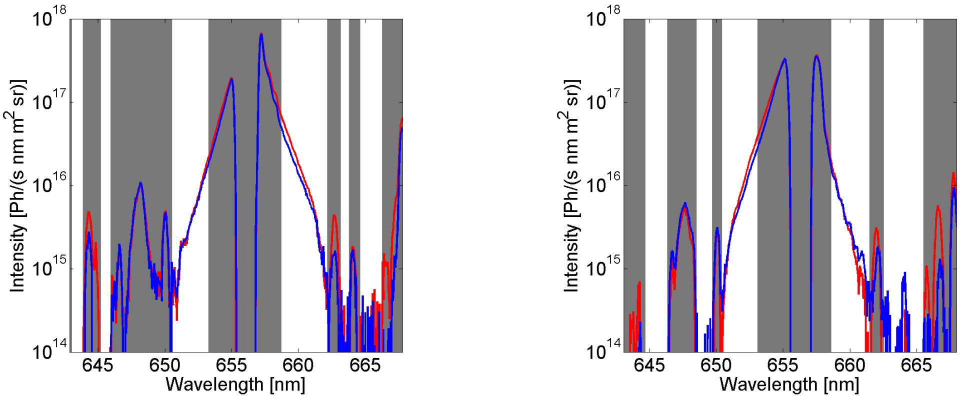

(a) $\phi = 137°$ (b) $\phi = 14°$

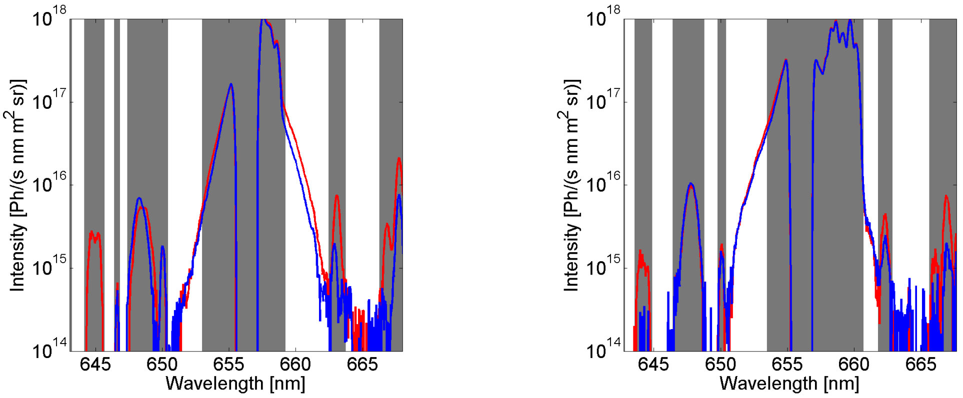

(c) $\phi = 103°$ (d) $\phi = 73°$

Figure 5.3.1: Time coherent averaged FIDA spectra before (red) and after (blue) a sawtooth crash.

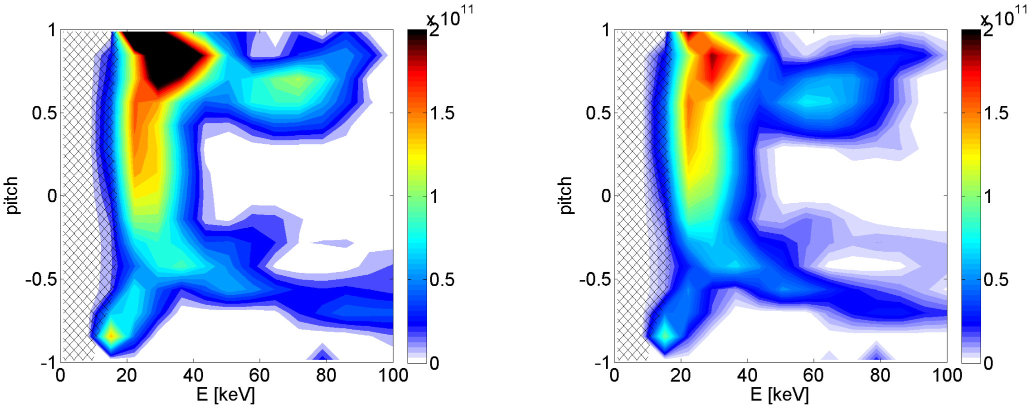

(a) Before (b) After

Figure 5.3.2: Tomography before and after the sawtooth crash in discharge #30815 in units [ions/keV/cm^3]. Calculated using SVD with a truncation level of $k = 36$.

of a TRANSP distribution and a Maxwellian with the correct temperature and density. A Maxwellian distribution in (E, p)-coordinates in units of [ions/m^3/eV] is defined as

$$f_{Maxwellian} = q\frac{n}{\sqrt{\pi}}\left(\frac{1}{k_BT}\right)^{3/2}\sqrt{E}\exp\left(-\frac{E}{k_BT}\right), \tag{5.3.1}$$

where q is the unit charge, n is the thermal ion density and T is the temperature. The derivation of equation (5.3.1) can be found in appendix B. The tomographies recreate the pitch of the full-energy peak very well, but the energy of the peak is too high. Another discrepancy is seen for negative pitch and energies above 40 keV where the TRANSP simulation predicts that no ions exist. This feature is likely an artefact caused by the inversion.

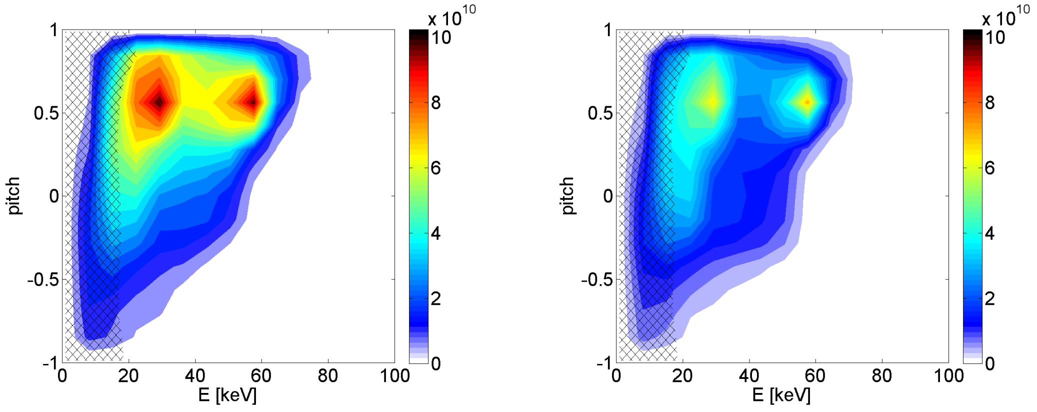

(a) Before (b) After

Figure 5.3.3: Simulation of the fast-ion distribution function before and after the sawtooth crash from TRANSP/NUBEAM in units of [ions/keV/cm^3].

The relative change is calculated as

$$\Delta\mathbf{F} = \frac{\mathbf{F}_{before} - \mathbf{F}_{after}}{\mathbf{F}_{before}}. \tag{5.3.2}$$

$\Delta\mathbf{F} = 1$ represents the situation where all ions present in the particular location in velocity-space are removed after the sawtooth crash and $\Delta\mathbf{F} = 0$ is the situation where the fast-ion distribution is left unchanged by the sawtooth crash. A negative $\Delta\mathbf{F}$ means that more ions exist in this part of velocity-space after the crash than previous to it. Figure 5.3.4 shows the relative change calculated for 29 keV and 36 keV. For both energies it is seen that the relative change is larger for $p > 0.5$ compared to pitches between -0.5 and 0.5.

The fast-ion density can be estimated by integrating the tomographies with respect to energy and pitch. However, as shown in paper III, the inferred density depends on the regularization strength, as more regularization lowers the inferred fast-ion density. The densities before and after the crash as a function of truncation index are shown in figure 5.3.5. Increasing the level of regularization means truncating the SVD sum earlier. The

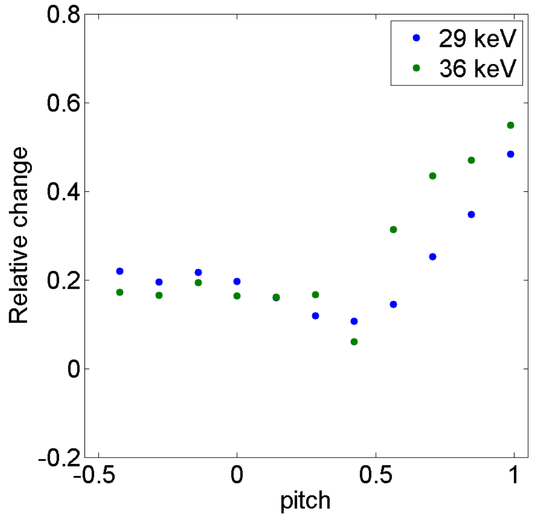

Figure 5.3.4: Relative change as a function of pitch for ions with energies around 29 keV and 36 keV.

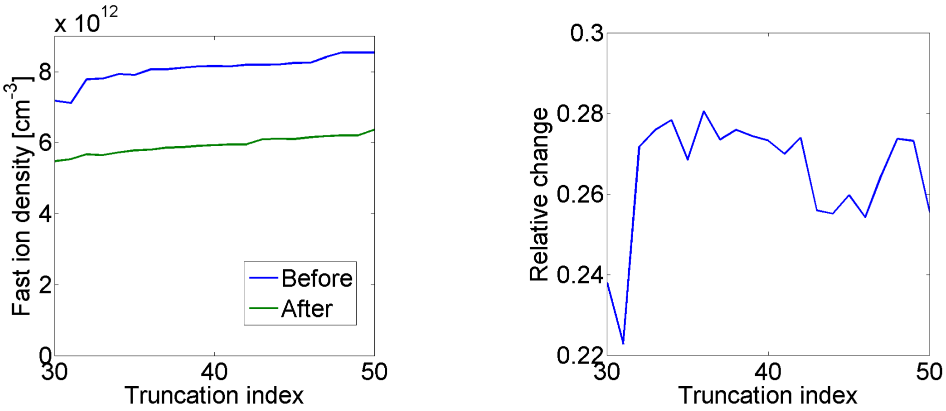

(a) Inferred densities (b) Relative change

Figure 5.3.5: Fast-ion densities calculated by integrating the tomographies as a function of the SVD truncation index.

predicted behaviour that the densities decrease with increasing regularization is clearly seen in figure 5.3.5a. Figure 5.3.5b shows the relative change in density. For the truncation index range shown here, it is found to be almost constant, despite the change in the individual densities. It is often the case that changes in amplitudes can be measured with greater confidence than the amplitudes themselves. The relative change is between 26% and 28% for this sawtooth crash.

To check these results, tomographies are calculated using the inversion methods described in chapter 4, choosing the regularizing strength using the L-curve method. The results are shown in figure 5.3.6. The top row consists of the tomographies of the distribution function before the sawtooth crash. The bottom row consists of the tomographies of the distribution function after the crash.

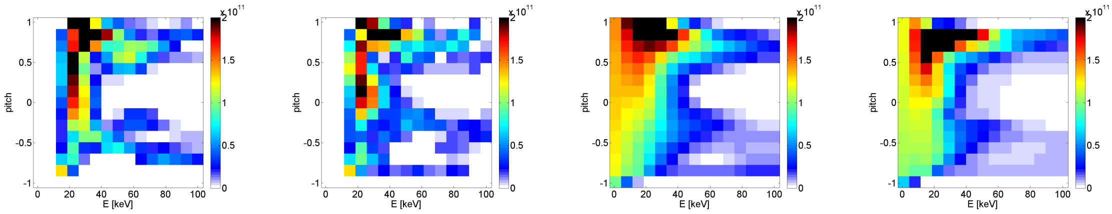

(a) Before, SVD (b) Before, T0 (c) Before, T1 (d) Before, MFI

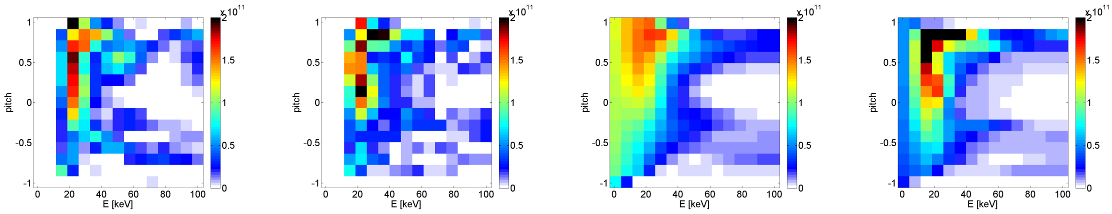

(e) After, SVD (f) After, T0 (g) After, T1 (h) After, MFI

Figure 5.3.6: Tomographies before and after the sawtooth crash in discharge #30815, calculated using the different inversion methods with L-curve method in units of [ions/keV/cm^3].

The drop in the fast-ion density in the plasma core across the sawtooth crash is seen in the reconstructions using all four inversion methods. As expected, the inversions using first order Tikhonov and minimum Fisher information is significantly smoother compared to truncated singular value decomposition and zeroth order Tikhonov. Figure 5.3.7 shows $\Delta\mathbf{F}$ as a function of pitch at an energy of 30 keV for the four different inversion methods. All four inversion methods agree that ions with pitch close to 1 are redistributed more compared to ions with pitch values close to 0. However, using the L-curve method for choosing the regularization strength, the relative change obtained with SVD and T0 are not as pronounced as that for T1 and MFI.

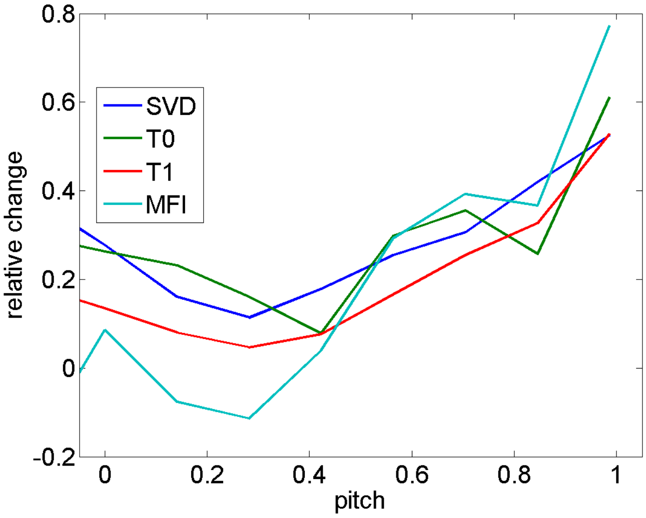

Figure 5.3.7: Relative change calculated using SVD, T0, T1 and MFI as a function of pitch for ions with an energy of 30 keV.

5.3.2 ASDEX Upgrade discharge #31557

ASDEX Upgrade discharge #31557 contains several sawtooth crashes. One of these is analysed in paper III. All five FIDA views were measuring in this discharge. The measured FIDA spectra from before (red) and after (blue) the sawtooth crash occurring at $t = 2.255$ s are shown in figure 5.3.8. The spectra shown in figure 5.3.8 are not as noisy

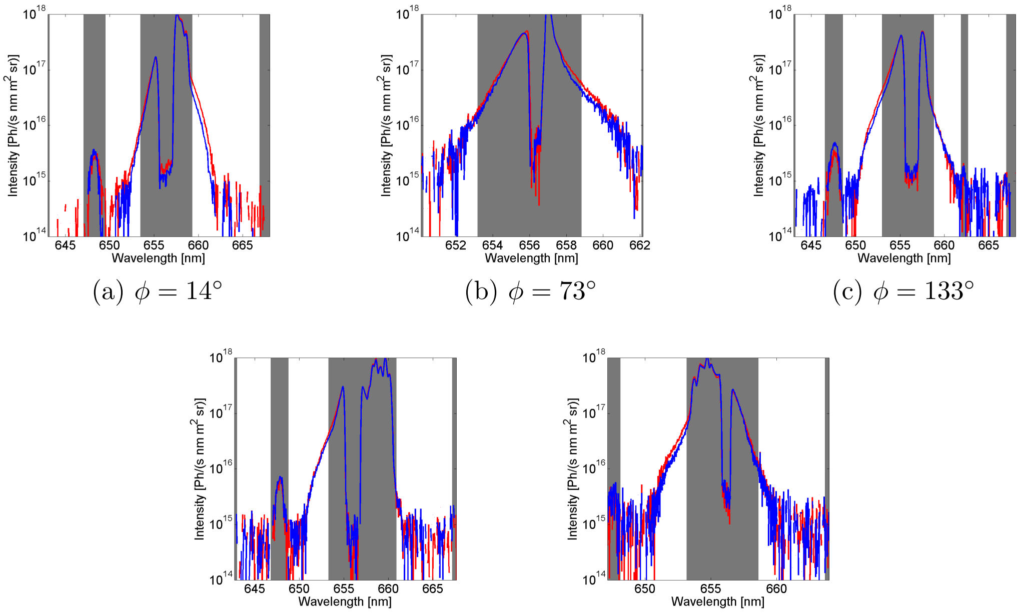

(a) $\phi = 14°$ (b) $\phi = 73°$ (c) $\phi = 133°$

(d) $\phi = 103°$ (e) $\phi = 153°$

Figure 5.3.8: FIDA spectra before (red) and after (blue) a sawtooth crash. The shaded parts indicate the wavelength ranges which are not suitable for use in the tomography analysis.

as those from discharge #30815 shown in figure 5.3.1 since a background subtraction was possible in discharge #31557. This is achieved by briefly turning off the Q3 NBI beam. The measured signal obtained during this off-phase can be used as a measurement of the background signal including the impurity radiation, which is independent of the injection of energetic neutral atoms from the NBI. The tomographies before and after the sawtooth crash are shown in figure 5.3.9 alongside TRANSP simulations of the velocity distribution. The top row shows the distribution before the crash, the bottom row shows the distribution after the crash. The asymmetry in pitch towards positive pitch are seen in all the tomographies. The overall shape of the distribution function is recreated very well by the first order Tikhonov and minimum Fisher information regularization methods. However, they are not able to resolve the full energy peak at 60 keV. Truncated singular value decomposition and zeroth order Tikhonov regularization produce a peak at roughly the predicted position. However, this is obscured by the amount of jitter in these tomographies.

As described in section 4.5, it is possible to estimate the uncertainty of a tomographic inversion. The different contributions to the uncertainty of the tomographies of the ve-

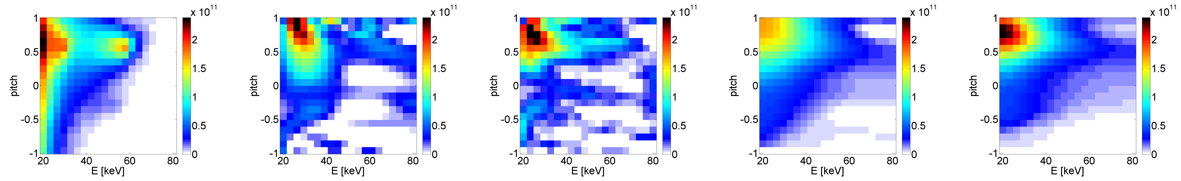

(a) Before, simulation (b) Before, SVD (c) Before, T0 (d) Before, T1 (e) Before, MFI

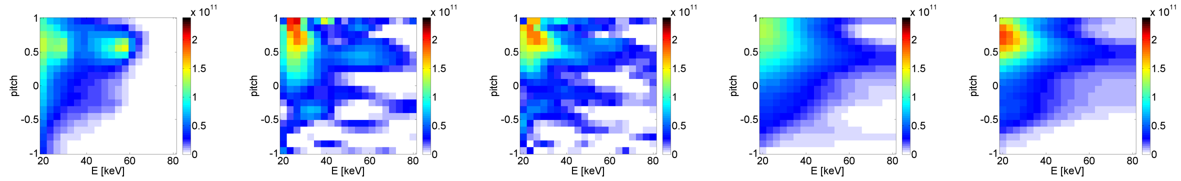

(f) After, simulation (g) After, SVD (h) After, T0 (i) After, T1 (j) After, MFI

Figure 5.3.9: Tomographies before and after the sawtooth crash in discharge #31557 in units of [ions/keV/cm^3], calculated using the different inversion methods and choosing the regularizing strength using the L-curve method. Also shown are the simulated velocity distribution funcitons. The Kadomtsev model implemented in TRANSP is used to simulate the redistribution of ions due to the sawtooth crash.

locity distribution before the sawtooth crash are shown in figure 5.3.10 as a function of energy and pitch.

The top row of figure 5.3.10 shows the noise in the measurements including the forward model error propagated through the transfer matrix to the tomographies according to equation (4.5.3). Note that the colorbar scales are not the same for the different inversion methods. The uncertainty from the measurement noise is relatively flat. Furthermore, it is almost a factor 10 lower in magnitude than the tomographies themselves. This is a clear example of the effect of regularization. The error introduced by the regularization methods, $\mathbf{e}_{reg}$, is shown in the middle row of figure 5.3.10. $\mathbf{e}_{reg}$ can be positive as well as negative. Negative regions correspond to parts of velocity space where this amount of regularization will tend to place too many ions. Positive regions correspond to regions where too few ions are placed. As mentioned in section 4.5, $\mathbf{e}_{reg}$ is based on an estimate of the true distribution function. Here, the simulated distribution function shown in figure 5.3.9a is used. The full energy peak can be seen in $\mathbf{e}_{reg}$ for all four inversion methods. The maximum absolute values of $\mathbf{e}_{reg}$ are between a factor of five to ten larger than those of $\mathbf{e}_{data}$. Thus, for these tomographies the uncertainties are dominated by the regularization uncertainty. The total uncertatinties are shown in the bottom row of figure 5.3.10. Using $\mathbf{e}_{tot}$, it is possible to estimate which parts of velocity space can be trusted.

The top row of figure 5.3.11 shows the relative change calculated using equation (5.3.2) and the tomographies from figure 5.3.9. The shaded parts correspond to regions where the distribution before the crash is zero. The uncertainty of the relative change, $\mathbf{e}_{\Delta\mathbf{F}}$ can be estimated by [76]

$$\mathbf{e}_{\Delta\mathbf{F}} \simeq |\Delta\mathbf{F}| \sqrt{\frac{\mathbf{e}^2_{tot,before} + \mathbf{e}^2_{tot,after}}{(\mathbf{F}_{before} - \mathbf{F}_{after})^2} + \frac{\mathbf{e}^2_{tot,before}}{\mathbf{F}^2_{before}}}\,. \tag{5.3.3}$$

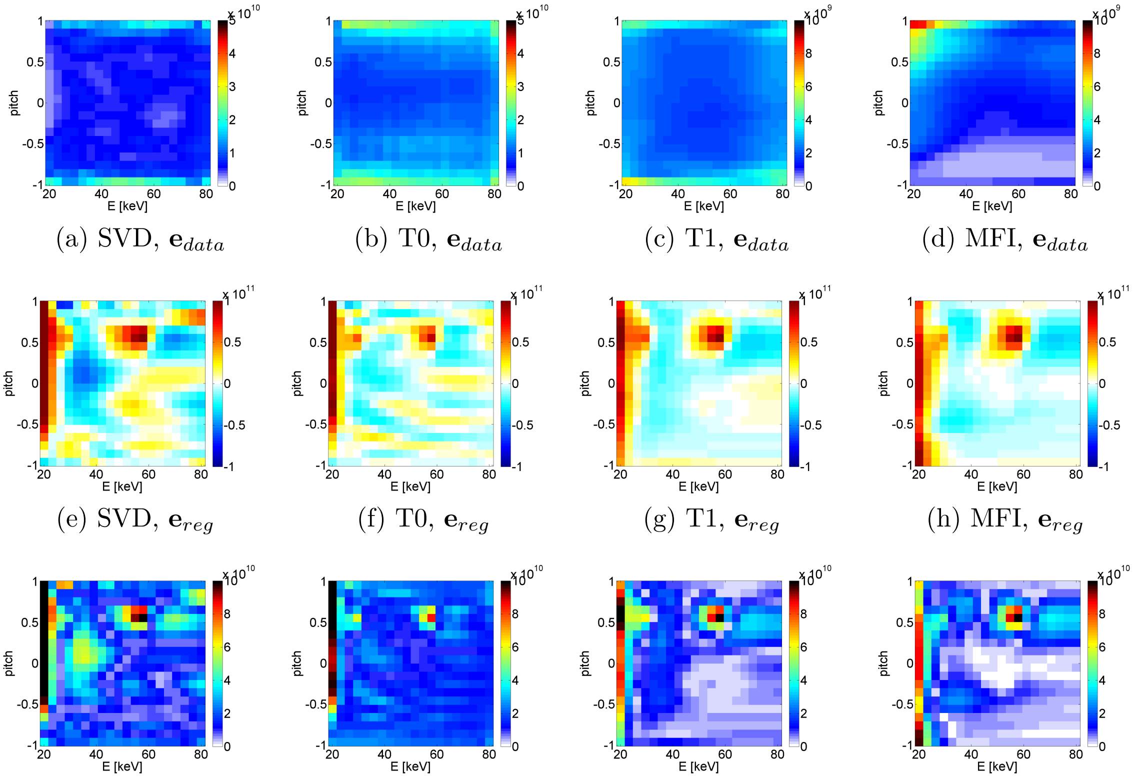

(a) SVD, $\mathbf{e}_{data}$ (b) T0, $\mathbf{e}_{data}$ (c) T1, $\mathbf{e}_{data}$ (d) MFI, $\mathbf{e}_{data}$

(e) SVD, $\mathbf{e}_{reg}$ (f) T0, $\mathbf{e}_{reg}$ (g) T1, $\mathbf{e}_{reg}$ (h) MFI, $\mathbf{e}_{reg}$

(i) SVD, $\mathbf{e}_{tot}$ (j) T0, $\mathbf{e}_{tot}$ (k) T1, $\mathbf{e}_{tot}$ (l) MFI, $\mathbf{e}_{tot}$

Figure 5.3.10: Uncertainties of the tomographies of the distribution before the sawtooth crash in units of [ions/keV/cm^3].

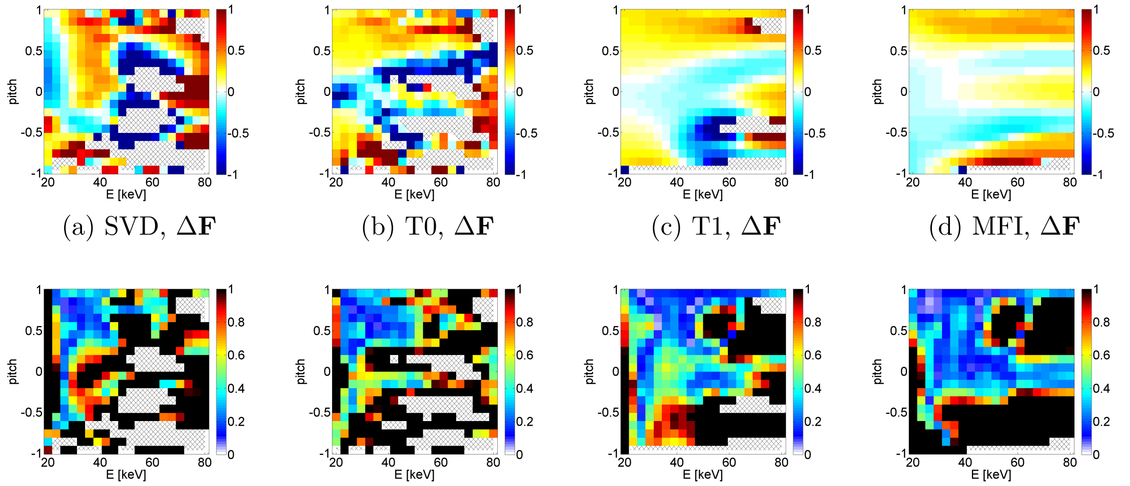

(a) SVD, $\mathbf{\Delta F}$ (b) T0, $\mathbf{\Delta F}$ (c) T1, $\mathbf{\Delta F}$ (d) MFI, $\mathbf{\Delta F}$

(e) SVD, $e_{\mathbf{\Delta F}}$ (f) T0, $e_{\mathbf{\Delta F}}$ (g) T1, $e_{\mathbf{\Delta F}}$ (h) MFI, $e_{\mathbf{\Delta F}}$

Figure 5.3.11: Relative change caused by the sawtooth crash in discharge #31557, shown together with the uncertainty of the relative change.

The bottom row of figure 5.3.11 shows $\mathbf{e}_{\Delta \mathbf{F}}$ for the different inversion methods as a function of energy and pitch. By comparing the top and bottom row of figure 5.3.11 it is possible to identify the parts of velocity space where the calculated relative change can be trusted. For SVD and zeroth order Tikhonov regularization, this is mainly ions with energies below 50 keV and positive pitch. For first order Tikhonov and minimum Fisher information regularization, a larger part of the relative change has a small uncertainty, and can therefore be trusted. The behaviour that ions with pitch values close to one are redistributed more than ions with pitch close to zero is observed for this discharge as well.

5.4 Combining CTS and FIDA

Using velocity-space tomography it becomes possible to combine measurements taken with entirely different fast-ion diagnostics. The results of the first ever combination using actual fast-ion measurements are presented here, in the form of a combination of FIDA and CTS data. Figure 5.4.1 shows the inferred 1D velocity distribution functions from the CTS measurements before and after a sawtooth crash in ASDEX Upgrade discharge #30382. A drop over the sawtooth crash is evident in $g(u)$.

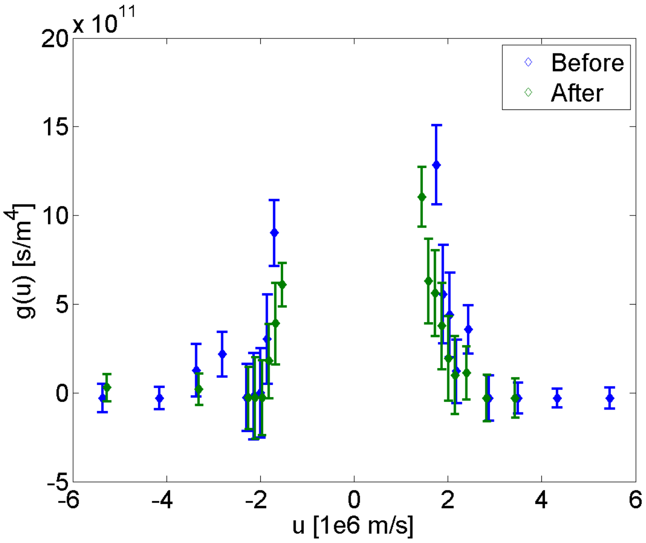

Figure 5.4.1: $g(u)$ spectra inferred from measured CTS spectra before and after a sawtooth crash in discharge #30382.

Figure 5.4.2 shows FIDA spectra measured during the same sawtooth crash. The shaded regions in figure 5.4.2 show the parts of the spectra which are not used in this analysis, either because these parts of the spectra are dominated by the beam-emission or impurity-lines or because the corresponding weight functions are covering regions below 10 keV or only regions above 100 keV. In this particular discharge, the NBI was not modulated, which means that a subtraction of background noise and impurity lines in the FIDA spectra is not possible. This limits the amount of usable FIDA data, especially for large Doppler shifts. On the other hand this L-mode discharge had a very low density and high temperature which significantly improves the FIDA signal-to-noise ratio.

When combining measurements from different diagnostics, the normalization of the data and transfer matrix with the measured uncertainties becomes crucial [52]. Finding a consistent way to handle the uncertainties proved to be the biggest issue for the combination of CTS and FIDA data. The reason being that the CTS uncertainties take into account uncertainties in the measured plasma parameters used in the fit of $g(u)$. These are not automatically included in the FIDA uncertainties. They only include the photon noise and a flat contribution from the emitted bremsstrahlung.

The forward model uncertainties in the FIDA weight functions are calculated as explained in section 4.5. The sum of a simulated NBI distribution function and a thermal Maxwellian

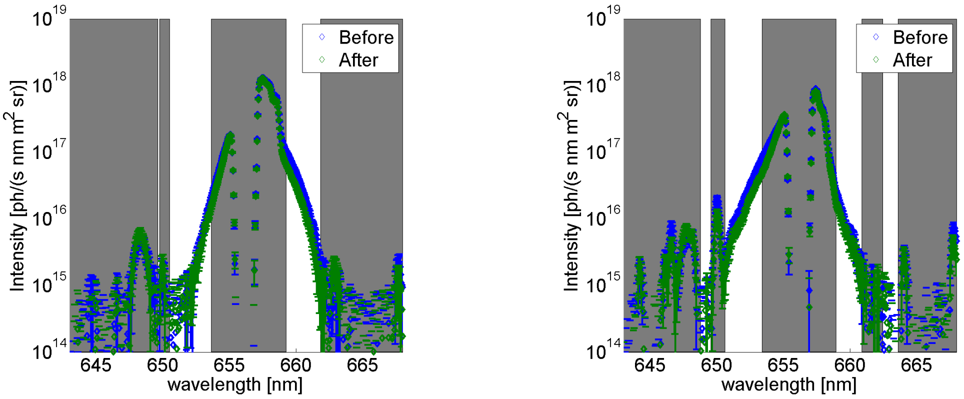

(a) View 1 (b) View 2

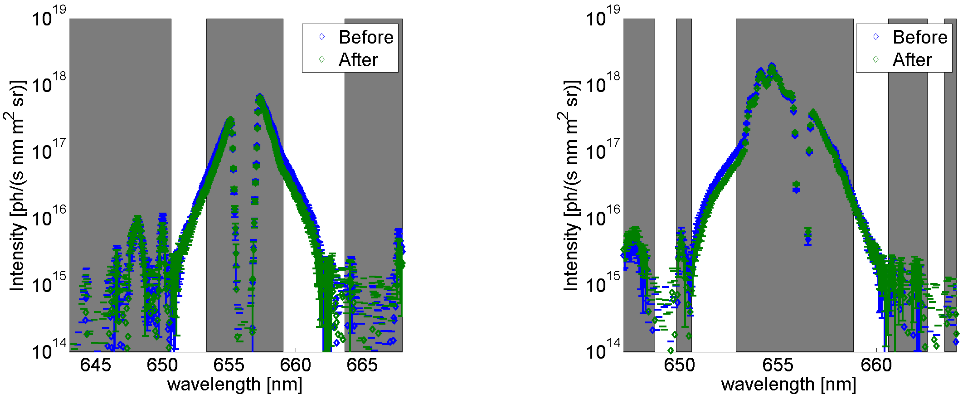

(c) View 3 (d) View 4

Figure 5.4.2: Measured FIDA spectra before and after the sawtooth crash in discharge #30382.

is used as the best estimate of the true distribution function. Figure 5.4.3 shows the uncertainties in the usable parts of the four FIDA spectra. $\mathbf{e}_p$ is the uncertainty from the photon noise and $\mathbf{e}_m$ is the forward model uncertainty.

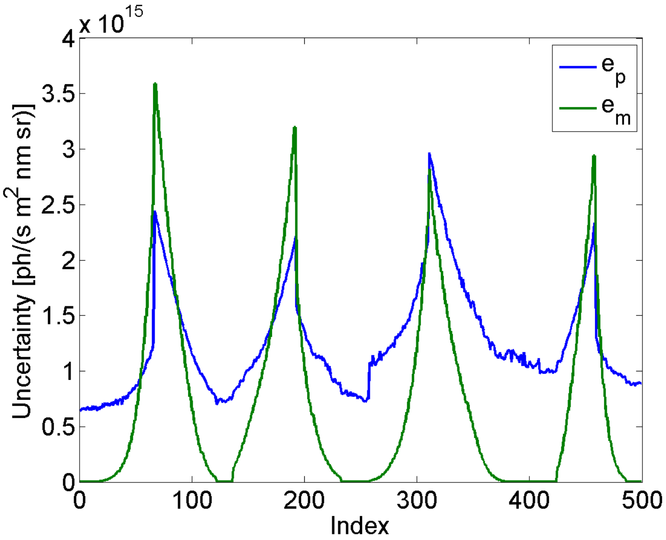

Figure 5.4.3: FIDA spectra uncertainties in discharge #30382.

The photon noise uncertainty scales with the FIDA intensity. The four peaks in figure 5.4.3 represent the parts of the spectra with the smallest Doppler-shifts where the FIDA intensity is largest. The forward model uncertainty is equal to or larger than the photon noise for the data points for smallest Doppler-shifts. However, it is smaller for larger Doppler-shifts where the noise from bremsstrahlung dominates the uncertainty. Figure 5.4.4 shows the measurements normalized with the uncertainty, as explained in the beginning of chapter 5, before and after the sawtooth crash in this discharge. The fifth peak for

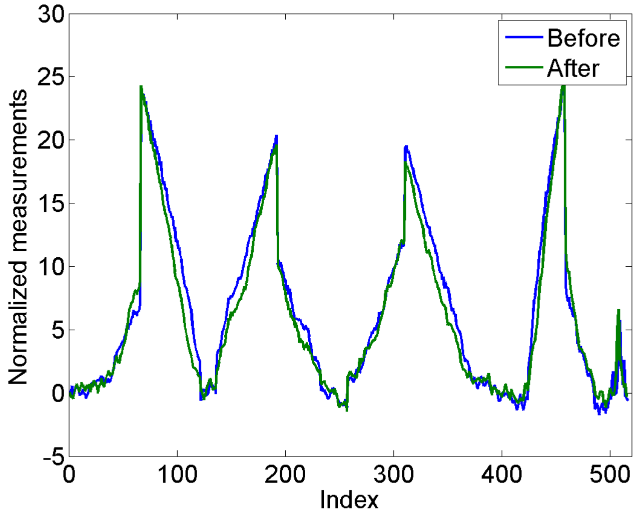

Figure 5.4.4: Normalized measurements in discharge #30382.

indices above 500 consists of the normalized CTS measurements. The normalized CTS measurements are about a factor four smaller than the normalized FIDA measurements.

Figure 5.4.5 shows tomographies calculated before and after the sawtooth crash using only FIDA data and a combination of FIDA and CTS data with the minimum Fisher information method. The addition of CTS does not change the tomographies much.

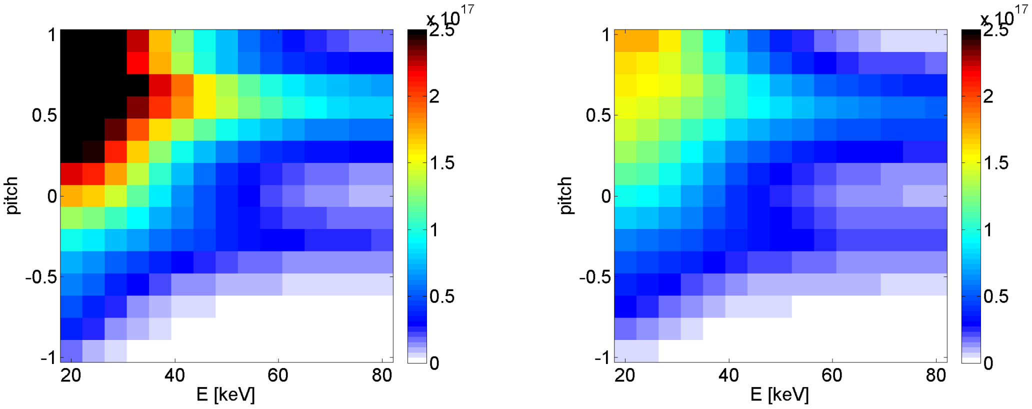

(a) Before, FIDA only (b) After, FIDA only

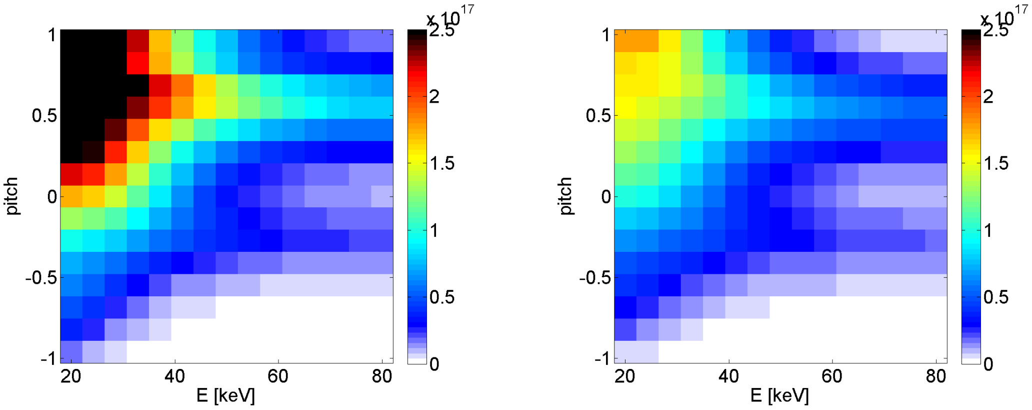

(c) Before, FIDA+CTS (d) After, FIDA+CTS

Figure 5.4.5: A comparison between FIDA and FIDA+CTS tomographies in units [ions/m^3/keV].

This is expected since the normalized CTS measurements in figure 5.4.4 are a factor four smaller compared to the FIDA measurements and there are in total 487 usable data points from the FIDA measurements and 18 from CTS in this discharge.

The uncertainties of the FIDA+CTS distribution before the sawtooth crash are shown in figure 5.4.6. As was the case for the tomographies of discharge #31557, the regularization error dominates the uncertainties.

The relative change, $\Delta\mathbf{F}$ and the associated uncertainty are shown in figure 5.4.7 Velocity-space tomography allows a benchmarking of CTS and FIDA measurements without relying on TRANSP as a common reference frame. Using the result of the FIDA-only tomography, a synthetic $g(u)$-spectrum can be calculated and compared with the actual

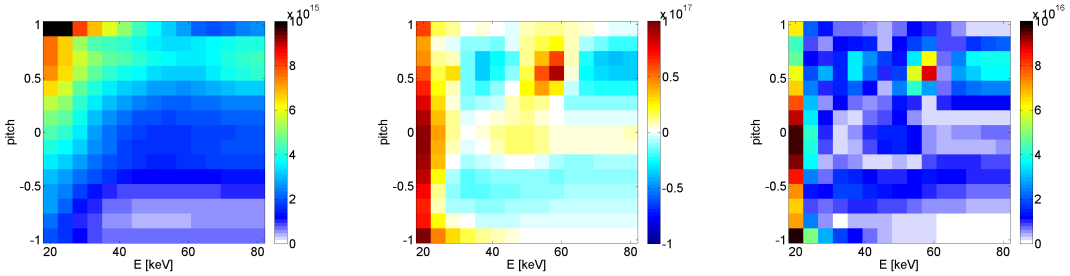

(a) $\mathbf{e}_{data}$ (b) $\mathbf{e}_{reg}$ (c) $\mathbf{e}_{tot}$

Figure 5.4.6: Uncertainties of the FIDA+CTS tomographies in units [ions/m^3/keV].

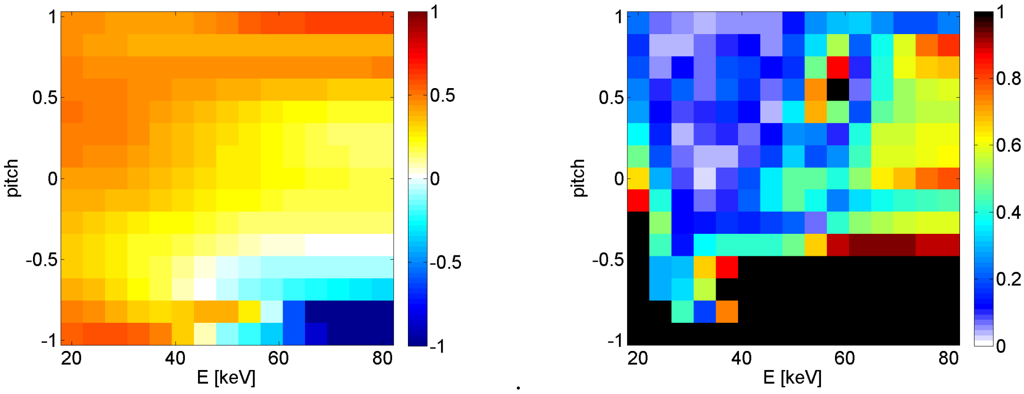

(a) $\Delta\mathbf{F}$ (b) $\mathbf{e}_{\Delta\mathbf{F}}$

Figure 5.4.7: Relative change of the fast-ion velocity-space distribution function across the sawtooth crash and its associated uncertainty.

measurements. Thus, the FIDA-implied (synthetic) CTS spectrum can be compared with the actual CTS measurements. Using the distributions shown in figures 5.4.5a and 5.4.5b, the FIDA-implied $g(u)$ are calculated using the CTS weight functions. The spectra are shown together with the CTS measurements in figure 5.4.8. The synthetic CTS spectra based on the FIDA-only tomographies lie slightly above the measured CTS measurements. A possible explanation is that the FIDA measurement volume is slightly more central compared to the CTS measurement volume where the bulk ion temperature and density are higher.

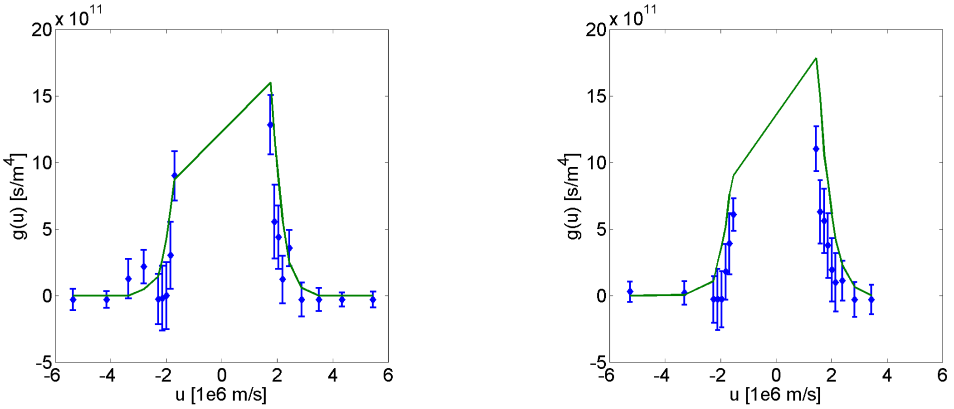

(a) Before

(b) After

Figure 5.4.8: FIDA implied CTS spectra. The data points are the CTS measurements and the lines are the synthetic spectra from the FIDA tomographies.

Chapter 6

Conclusions

During this project, I have expanded and improved the method of velocity-space tomography and applied it to study sawtooth crashes, as an example of how the velocity-space tomography method can be applied in situations where the physics is not well understood.

I have developed NES velocity-space sensitivity functions, so-called fast-ion weight functions, for the often dominating neutron contribution from reactions between a fast ion and a thermal ion. They connect the measured neutron energies to the fast-ion velocity distribution function. Assuming a stationary thermal ion, I have derived an analytic expression of the probability part of the weight function. This provides insight into the behaviour of the velocity-space sensitivity as the dependence on the different variables is revealed. Further, it becomes possible to investigate limiting cases. For example, it was found that the lowest possible energy obtainable by a neutron from a D-D reaction is $\frac{Q}{2}$, (see section 2 in paper I). The formalism developed for deriving the NES weight functions has since been used to derive one-step reaction gamma-ray spectroscopy weight functions [77] and lays the groundwork for the more complicated two-step reaction GRS weight functions [6].

It is possible to calculate instrument specific weight functions if the instrumental response function is known. This can be beneficial since it allows a direct connection between the velocity-space distribution function and the measurements. I have derived the general expression of how this is done and implemented it for the different neutron spectrometers at JET.

In order to improve the quality of the tomographies I have implemented and compared several different inversion methods. In general it is possible to improve the quality quite substantially from that of the previously used truncated singular value decomposition by using alternative inversion methods. Inversion methods which penalize steep gradients significantly reduce the jitter in the tomographies. Furthermore, the choice of the regularization strength by the L-curve method and the quantification of the uncertainty in the tomographies enable us to identify the features in a tomography which can be trusted.

Several tomographies have been calculated using real measurements from the ASDEX Upgrade tokamak. It is possible to distinguish between a fast-ion distribution function from a single NBI heating beam and from several beams. Further, several sawtooth crashes have been analysed. It is consistently found that ions with pitch values close to

±1 are redistributed more than ions with pitch close to 0. This is consistent with previous observations in several machines. This conclusion is seen with all the different inversion methods in the regions where they produce reliable results according to the calculated uncertainties.

Finally, the first-ever tomography of a fast-ion velocity-space distribution function has been calculated using a combination of measurements from different types of diagnostics. This is done using the CTS and FIDA diagnostics at the ASDEX Upgrade tokamak.

Chapter 7

Outlook

Using inversion methods which penalize steep gradients in the distribution function, the achievable quality of the tomographies of the fast-ion velocity distribution function has improved. As the understanding of the uncertainties, possible shortcomings and pitfalls has increased, the usability of this method in analysing experimental data has increased significantly. I expect this method to be used routinely in the future using FIDA measurements at ASDEX Upgrade, because of the high number of FIDA diagnostics installed in this machine. Other machines which could potentially implement this method using their existing diagnostic capabilities are: DIII-D (four FIDA views), NSTX (two FIDA views), MAST (two FIDA views) and LHD (two FIDA views).

With the newly developed gamma-ray spectroscopy weight functions [6] and the NES weight functions developed here, it might be possible to calculate a velocity-space tomography of the central fast-ion distribution function at JET combining the gamma-ray spectroscopic set-up with NES measurements from the different neutron diagnostics in a discharge with peaked profiles. Such a combination works for experimental CTS and FIDA measurements as demonstrated here.

ITER will also be equipped with several fast-ion diagnostics. A CTS system with several radially displaced measurement volumes is going to be installed as well as neutron spectrometers and a set of gamma-ray spectrometers. This could enable a tomographic inversion of the entire 4D fast-ion phase-space distribution. The four dimensions being $v_\parallel, v_\perp, R$ and z assuming toroidal symmetry.

With the inclusion of gamma-ray spectroscopy, weight functions for all major core fast-ion diagnostics have been developed. Thus, the next theoretical task could very well be the formulation of the 4D phase-space transfer matrix. In the case of no correlation between different measurement volumes in position space, the transfer matrix is simply a block diagonal matrix. In block diagonal matrices the different blocks are decoupled, and hence an independent tomography problem for each spatial position can be solved. This can already be achieved with the methods presented here. However, as soon as the measurement volumes begin to overlap, correlations between the different measurement volumes must be determined. In this case, the different blocks become coupled, and a single transfer matrix consisting of all spatial positions must be inverted.

Using the improved velocity-space tomography method, it becomes possible to investigate the physics of the interplay between fast ions and dynamical events in the plasma. Examples are the effect on fast ions by Alfvén eigenmodes and fishbones which are believed to affect ions selectively in velocity-space.

Bibliography

[1] W W Heidbrink, Y Luo, K H Burrell, R W Harvey, R I Pinsker, and E Ruskov. Measurements of fast-ion acceleration at cyclotron harmonics using Balmer-alpha spectroscopy. *Plasma Physics and Controlled Fusion*, 49(9):1457–1475, September 2007.

[2] S.K. Nielsen, M. Salewski, H. Bindslev, a. Bürger, V. Furtula, M. Kantor, S.B. Korsholm, H.R. Koslowski, a. Krämer-Flecken, F. Leipold, F. Meo, P.K. Michelsen, D. Moseev, J.W. Oosterbeek, M. Stejner, and E. Westerhof. Dynamics of fast ions during sawtooth oscillations in the TEXTOR tokamak measured by collective Thomson scattering. *Nuclear Fusion*, 51(6):063014, June 2011.

[3] M. Salewski, S.K. Nielsen, H. Bindslev, V. Furtula, N.N. Gorelenkov, S.B. Korsholm, F. Leipold, F Meo, P.K. Michelsen, D. Moseev, and M. Stejner. On velocity space interrogation regions of fast-ion collective Thomson scattering at ITER. *Nuclear Fusion*, 51(8):083014, August 2011.

[4] M Salewski, B Geiger, D Moseev, W W Heidbrink, a S Jacobsen, S B Korsholm, F Leipold, J Madsen, S K Nielsen, J Rasmussen, M Stejner, and M Weiland. On velocity-space sensitivity of fast-ion D-alpha spectroscopy. *Plasma Physics and Controlled Fusion*, 56(10):105005, October 2014.

[5] A.S. Jacobsen, M. Salewski, J. Eriksson, G. Ericsson, S.B. Korsholm, F. Leipold, S.K. Nielsen, J. Rasmussen, and M. Stejner. Velocity-space sensitivity of neutron spectrometry measurements. *Nuclear Fusion*, 55(5):053013, May 2015.

[6] M. Salewski, M. Nocente, G. Gorini, A.S. Jacobsen, V.G. Kiptily, S.B. Korsholm, F. Leipold, J. Madsen, D. Moseev, S.K. Nielsen, J. Rasmussen, M. Stejner, and M Tardocchi. Velocity-space observation regions of high-resolution two-step reaction gamma-ray spectroscopy. *Nuclear Fusion*, 55(9):093029, September 2015.

[7] B. Geiger. *Fast-ion transport studies using FIDA spectroscopy at the ASDEX Upgrade tokamak.* PhD thesis, Ludwig-Maximilians-Universität München, 2013.

[8] S.E. Sharapov, B. Alper, H.L. Berk, D.N. Borba, B.N. Breizman, C.D. Challis, I.G.J. Classen, E.M. Edlund, J. Eriksson, A. Fasoli, E.D. Fredrickson, G.Y. Fu, M. Garcia-Munoz, T. Gassner, K. Ghantous, V. Goloborodko, N.N. Gorelenkov, M.P. Gryaznevich, S. Hacquin, W.W. Heidbrink, C. Hellesen, V.G. Kiptily, G.J Kramer, P. Lauber, M.K Lilley, M. Lisak, F. Nabais, R. Nazikian, R. Nyqvist, M. Osakabe,

C. Perez von Thun, S.D. Pinches, M. Podesta, M. Porkolab, K. Shinohara, K. Schoepf, Y. Todo, K. Toi, M.A. Van Zeeland, I. Voitsekhovich, R.B. White, and V. Yavorskij. Energetic particle instabilities in fusion plasmas. *Nuclear Fusion*, 53(10):104022, 2013.

[9] W W Heidbrink, J R Ferron, C T Holcomb, M a Van Zeeland, X Chen, C M Collins, a Garofalo, X Gong, B a Grierson, M Podestà, L Stagner, and Y Zhu. Confinement degradation by Alfvén-eigenmode induced fast-ion transport in steady-state scenario discharges. *Plasma Physics and Controlled Fusion*, 56(9):095030, 2014.

[10] N.N. Gorelenkov, S.D. Pinches, and K Toi. Energetic particle physics in fusion research in preparation for burning plasma experiments. *Nuclear Fusion*, 2014.

[11] J. Wesson. *Tokamaks.* Oxford Science Publications, second edition edition, 1997.

[12] Fabien Jaulmes, Egbert Westerhof, and Hugo J De Blank. Redistribution of fast ions during sawtooth reconnection. 104013.

[13] A Sykes and JA Wesson. Relaxation instability in tokamaks. *Physical Review Letters*, 37(3):140–143, 1976.

[14] C M Muscatello, W W Heidbrink, Ya I Kolesnichenko, V V Lutsenko, M a Van Zeeland, and Yu V Yakovenko. Velocity-space studies of fast-ion transport at a sawtooth crash in neutral-beam heated plasmas. *Plasma Physics and Controlled Fusion*, 54(2):025006, February 2012.

[15] B. Geiger, M. Weiland, A.S. Jacobsen, D. Rittich, R. Dux, R. Fischer, C. Hopf, M. Maraschek, R.M. McDermot, S.K. Nielsen, T. Odstrcil, M. Reich, F. Ryter, M. Salewski, P.A. Schneider, and G. Tardini. Fast-ion transport and neutral beam current drive in ASDEX Upgrade. *Nuclear Fusion*, 55:083001, 2015.

[16] Henrik Bindslev. A quantitative study of scattering from electromagnetic fluctuations in plasmas. *Journal of Atmospheric and Terrestrial Physics*, 58(95):983–989, 1996.

[17] M Stejner, S K Nielsen, H Bindslev, S B Korsholm, and M Salewski. Principles of fuel ion ratio measurements in fusion plasmas by collective Thomson scattering. *Plasma Physics and Controlled Fusion*, 53(6):065020, June 2011.

[18] M Stejner, S K Nielsen, A S Jacobsen, S B Korsholm, F Leipold, R M McDermott, P K Michelsen, J Rasmussen, M Salewski, M Schubert, J Stober, and D H Wagner. Plasma rotation and ion temperature measurements by collective Thomson scattering at ASDEX Upgrade. *Plasma Physics and Controlled Fusion*, 57(6):062001, June 2015.

[19] S K Nielsen, M Stejner, J Rasmussen, A S Jacobsen, S B Korsholm, F Leipold, M Maraschek, F Meo, P K Michelsen, D Moseev, M Salewski, M Schubert, J Stober, W Suttrop, G Tardini, and D Wagner. Measurements of the fast-ion distribution function at ASDEX upgrade by collective Thomson scattering (CTS) using active and passive views. *Plasma Physics and Controlled Fusion*, 57(3):035009, March 2015.

[20] D Moseev, F Meo, S B Korsholm, T Koskela, M Albergante, O Asunta, H Bindslev, a Bürger, V Furtula, M Yu Kantor, F Leipold, P K Michelsen, S K Nielsen, M Salewski, O Schmitz, M Stejner, and E Westerhof. Comparison of measured and simulated fast ion velocity distributions in the TEXTOR tokamak. *Plasma Physics and Controlled Fusion*, 53(10):105004, October 2011.

[21] EE Salpeter. Electron density fluctuations in a plasma. *Physical Review*, 120, 1960.

[22] S. K. Nielsen, H. Bindslev, L. Porte, J. a. Hoekzema, S. B. Korsholm, F. Leipold, F. Meo, P. K. Michelsen, S. Michelsen, J. W. Oosterbeek, E. L. Tsakadze, G. Van Wassenhove, E. Westerhof, and P. Woskov. Temporal evolution of confined fast-ion velocity distributions measured by collective Thomson scattering in TEXTOR. *Physical Review E*, 77(1):016407, January 2008.

[23] W W Heidbrink. Fast-ion Dα measurements of the fast-ion distribution (invited). *The Review of scientific instruments*, 81(10):10D727, October 2010.

[24] T. Ito, M. Osakabe, K. Ida, M. Yoshinuma, M. Kobayashi, M. Goto, S. Murakami, M. Isobe, S. Kobayashi, K. Toi, K. Ogawa, Y. Takeiri, and S. Okamura. Fast ion charge exchange spectroscopy adapted for tangential viewing geometry in LHD. *Review of Scientific Instruments*, 81(10):1–5, 2010.

[25] B Geiger, R Dux, R M McDermott, S Potzel, M Reich, F Ryter, M Weiland, D Wünderlich, and M Garcia-Munoz. Multi-view fast-ion D-alpha spectroscopy diagnostic at ASDEX Upgrade. *The Review of scientific instruments*, 84(11):113502, November 2013.

[26] B. Geiger, M. Garcia-Munoz, R. Dux, F. Ryter, G. Tardini, L. Barrera Orte, I.G.J. Classen, E. Fable, R. Fischer, V. Igochine, and R.M. McDermott. Fast-ion transport in the presence of magnetic reconnection induced by sawtooth oscillations in ASDEX Upgrade. *Nuclear Fusion*, 54(2):022005, February 2014.

[27] M. Weiland, B. Geiger, Jacobsen A.S., M. Reich, M. Salewski, and T. Odstrcil. Velocity-space resolved fast-ion measurements from five FIDA views at the ASDEX Upgrade tokamak. 2015. submitted.

[28] W W Heidbrink, Y Luo, C M Muscatello, Y Zhu, and K H Burrell. A new fast-ion D(alpha) diagnostic for DIII-D. *The Review of scientific instruments*, 79(10):10E520, October 2008.

[29] W.W. Heidbrink, M.a. Van Zeeland, B.a. Grierson, C.M. Muscatello, J.M. Park, C.C. Petty, R. Prater, and Y.B. Zhu. Initial measurements of the DIII-D off-axis neutral beams. *Nuclear Fusion*, 52(9):094005, September 2012.

[30] a Bortolon, W W Heidbrink, and M Podestà. A tangentially viewing fast ion D-alpha diagnostic for NSTX. *The Review of scientific instruments*, 81(10):10D728, October 2010.

[31] C a Michael, N Conway, B Crowley, O Jones, W W Heidbrink, S Pinches, E Braeken, R Akers, C Challis, M Turnyanskiy, a Patel, D Muir, R Gaffka, and S Bailey. Dual view FIDA measurements on MAST. *Plasma Physics and Controlled Fusion*, 55(9):095007, September 2013.

[32] O M Jones, C a Michael, K G McClements, N J Conway, B Crowley, R J Akers, R J Lake, and S D Pinches. Fast-ion deuterium alpha spectroscopic observations of the effects of fishbones in the Mega-Ampere Spherical Tokamak. *Plasma Physics and Controlled Fusion*, 55(8):085009, August 2013.

[33] G. Gorini and J. Kallne. High count rate time-of-flight spectrometer for DD fusion neutrons. *Review of Scientific Instruments*, 63(10):4548–4550, 1992.

[34] G Tardini, a Zimbal, B Esposito, F Gagnon-Moisan, D Marocco, R Neu, H Schuhmacher, and the Asdex Upgrade Team. First neutron spectrometry measurements in the ASDEX Upgrade tokamak. *Journal of Instrumentation*, 7(03):C03004–C03004, March 2012.

[35] C Hellesen, M Albergante, E Andersson Sundén, L Ballabio, S Conroy, G Ericsson, M Gatu Johnsson, L Giacomelli, G Gorini, a Hjalmarsson, I Jenkins, J Källne, E Ronchi, H Sjöstrand, M Tardocchi, I Voitsekhovitch, and M Weiszflog. Neutron spectroscopy measurements and modeling of neutral beam heating fast ion dynamics. *Plasma Physics and Controlled Fusion*, 52(8):085013, August 2010.

[36] H Brysk. Fusion neutron energies and spectra. *Plasma Physics*, 15:611–617, 1973.

[37] M. Salewski, F. Meo, M. Stejner, O. Asunta, H. Bindslev, V. Furtula, S.B. Korsholm, T. Kurki-Suonio, F. Leipold, F. Leuterer, P.K. Michelsen, D. Moseev, S.K. Nielsen, J. Stober, G. Tardini, D. Wagner, and P. Woskov. Comparison of fast ion collective Thomson scattering measurements at ASDEX Upgrade with numerical simulations. *Nuclear Fusion*, 50(3):035012, March 2010.

[38] W. W. Heidbrink, R. E. Bell, Y. Luo, and W. Solomon. Fast-ion D-alpha diagnostic for NSTX. *Review of Scientific Instruments*, 77(10):10F120, 2006.

[39] Y Luo, W W Heidbrink, K H Burrell, D H Kaplan, and P Gohil. Measurement of the D alpha spectrum produced by fast ions in DIII-D. *The Review of scientific instruments*, 78(3):033505, March 2007.

[40] M Podesta, W W Heidbrink, R E Bell, and R Feder. The NSTX fast-ion D-alpha diagnostic. *The Review of scientific instruments*, 79(10):10E521, October 2008.

[41] M a Van Zeeland, W W Heidbrink, and J H Yu. Fast ion D α imaging in the DIII-D tokamak. *Plasma Physics and Controlled Fusion*, 51(5):1–19, May 2009.

[42] M.a. Van Zeeland, J.H. Yu, W.W. Heidbrink, N.H. Brooks, K.H. Burrell, M.S. Chu, a.W. Hyatt, C. Muscatello, R. Nazikian, N.a. Pablant, D.C. Pace, W.M. Solomon, and M.R. Wade. Imaging key aspects of fast ion physics in the DIII-D tokamak. *Nuclear Fusion*, 50(8):084002, August 2010.

[43] W W Heidbrink, G R McKee, D R Smith, and A Bortolon. 'Beam-emission spectroscopy' diagnostics also measure edge fast-ion light. *Plasma Physics and Controlled Fusion*, 53(8):085007, August 2011.

[44] M. Podesta, W. W. Heidbrink, D. Liu, E. Ruskov, R. E. Bell, D. S. Darrow, E. D. Fredrickson, N. N. Gorelenkov, G. J. Kramer, B. P. LeBlanc, S. S. Medley, a. L. Roquemore, N. a. Crocker, S. Kubota, and H. Yuh. Experimental studies on fast-ion transport by Alfven wave avalanches on the National Spherical Torus Experiment. *Physics of Plasmas*, 16(5):056104, 2009.

[45] M. Garcia-Munoz, I.G.J. Classen, B. Geiger, W.W. Heidbrink, M.a. Van Zeeland, S. Äkäslompolo, R. Bilato, V. Bobkov, M. Brambilla, G.D. Conway, S. Da Graça, V. Igochine, Ph. Lauber, N. Luhmann, M. Maraschek, F. Meo, H. Park, M. Schneller, and G. Tardini. Fast-ion transport induced by Alfvén eigenmodes in the ASDEX Upgrade tokamak. *Nuclear Fusion*, 51(10):103013, October 2011.

[46] B Geiger, M Garcia-Munoz, W W Heidbrink, R M McDermott, G Tardini, R Dux, R Fischer, and V Igochine. Fast-ion D-alpha measurements at ASDEX Upgrade. *Plasma Physics and Controlled Fusion*, 53(6):065010, June 2011.

[47] D. C. Pace, M. E. Austin, E. M. Bass, R. V. Budny, W. W. Heidbrink, J. C. Hillesheim, C. T. Holcomb, M. Gorelenkova, B. a. Grierson, D. C. McCune, G. R. McKee, C. M. Muscatello, J. M. Park, C. C. Petty, T. L. Rhodes, G. M. Staebler, T. Suzuki, M. a. Van Zeeland, R. E. Waltz, G. Wang, a. E. White, Z. Yan, X. Yuan, and Y. B. Zhu. Energetic ion transport by microturbulence is insignificant in tokamaks. *Physics of Plasmas*, 20(5):056108, 2013.

[48] a. S. Jacobsen, M. Salewski, J. Eriksson, G. Ericsson, a. Hjalmarsson, S. B. Korsholm, F. Leipold, S. K. Nielsen, J. Rasmussen, and M. Stejner. Velocity-space sensitivity of the time-of-flight neutron spectrometer at JETa). *Review of Scientific Instruments*, 85(11):11E103, November 2014.

[49] B Geiger, M. Weiland, A. Mlynek, M. Reich, A. Bock, M. Dunne, R. Dux, E. Fable, R. Fischer, M. Garcia-Munoz, J. Hobirk, C. Hopf, S. Nielsen, T. Odstrcil, C. Rapson, D. Rittich, F. Ryter, M. Salewski, P.A. Schneider, G. Tardini, and M. Willensdorfer. Quantification of the impact of large and small-scale instabilities on the fast-ion confinement in ASDEX Upgrade. *Plasma Physics and Controlled Fusion*, 57:014018, 2015.

[50] J. Rasmussen. Consistency between real and synthetic fast-ion measurements at ASDEX Upgrade. *submitted*, 2015.

[51] M. Salewski, B. Geiger, S.K. Nielsen, H. Bindslev, M. García-Muñoz, W.W. Heidbrink, S.B. Korsholm, F. Leipold, F. Meo, P.K. Michelsen, D. Moseev, M. Stejner, and G. Tardini. Tomography of fast-ion velocity-space distributions from synthetic CTS and FIDA measurements. *Nuclear Fusion*, 52(10):103008, October 2012.

[52] M. Salewski, B. Geiger, S.K. Nielsen, H. Bindslev, M. García-Muñoz, W.W. Heidbrink, S.B. Korsholm, F. Leipold, J. Madsen, F. Meo, P.K. Michelsen, D. Moseev, M. Stejner, and G. Tardini. Combination of fast-ion diagnostics in velocity-space tomographies. *Nuclear Fusion*, 53(6):063019, June 2013.

[53] M. Salewski, B. Geiger, a.S. Jacobsen, M. García-Muñoz, W.W. Heidbrink, S.B. Korsholm, F. Leipold, J. Madsen, D. Moseev, S.K. Nielsen, J. Rasmussen, M. Stejner, G. Tardini, and M. Weiland. Measurement of a 2D fast-ion velocity distribution function by tomographic inversion of fast-ion D-alpha spectra. *Nuclear Fusion*, 54(2):023005, February 2014.

[54] J. Egedal and H. Bindslev. Reconstruction of gyrotropic phase-space distributions from one-dimensional projections. *Physics of Plasmas*, 11(5):2191, 2004.

[55] M Salewski, B Geiger, W W Heidbrink, A S Jacobsen, S B Korsholm, F Leipold, J Madsen, D Moseev, S K Nielsen, J Rasmussen, L Stagner, D Steeghs, M Stejner, G Tardini, and M Weiland. Doppler tomography in fusion plasmas and astrophysics. *Plasma Physics and Controlled Fusion*, 57(1):014021, January 2015.

[56] P.C. Hansen. *Rank-deficient and discrete ill-posed problems: numerical aspects of linear inversion.* SIAM, 1998.

[57] P.C. Hansen. *Discrete Inverse Problems: Insight and Algorithms.* SIAM, 2010.

[58] J Källne, L Ballabio, J Frenje, S Conroy, G Ericsson, M Tardocchi, E Traneus, and G Gorini. Observation of the alpha particle "Knock-On" neutron emission from magnetically confined DT fusion plasmas. *Physical review letters*, 85(6):1246–9, August 2000.

[59] C. Hellesen, M. Gatu Johnson, E. Anderson Sundén, S. Conroy, G. Ericsson, E Ronchi, H. Sjöstrand, M. Weiszflog, G. Gorini, M. Tardocchi, T. Johnson, V.G. Kiptily, S.D. Pinches, and S.E. Sharapov. Neutron emission generated by fast deuterons accelerated with ion cyclotron heating at JET. *Nuclear Fusion*, 50(2):022001, February 2010.

[60] M. Gatu Johnson, L. Giacomelli, a. Hjalmarsson, J. Källne, M. Weiszflog, E. Andersson Sundén, S. Conroy, G. Ericsson, C. Hellesen, E. Ronchi, H. Sjöstrand, G. Gorini, M. Tardocchi, a. Combo, N. Cruz, J. Sousa, and S. Popovichev. The 2.5-MeV neutron time-of-flight spectrometer TOFOR for experiments at JET. *Nuclear Instruments and Methods in Physics Research Section A: Accelerators, Spectrometers, Detectors and Associated Equipment*, 591(2):417–430, June 2008.

[61] J Eriksson, C Hellesen, E Andersson Sundén, M Cecconello, S Conroy, G Ericsson, M Gatu Johnson, S D Pinches, S E Sharapov, and M Weiszflog. Finite Larmor radii effects in fast ion measurements with neutron emission spectrometry. *Plasma Physics and Controlled Fusion*, 55(1):015008, January 2013.

[62] J. Eriksson, M. Nocente, F. Binda, C. Cazzaniga, S. Conroy, G. Ericsson, L. Giacomelli, G. Gorini, C. Hellesen, T. Hellsten, A. Hjalmarsson, A.S. Jacobsen, T. Johnson, V. Kiptily, T. Koskela, M. Mantsinen, M. Salewski, M. Schneider, S. Sharapov, M. Skiba, M. Tardocchi, and M. Weiszflog. Dual sightline measurements of MeV range deuterons with neutron and gamma-ray spectroscopy at JET. 2015. submitted.

[63] N. P. Hawkes, J. M. Adams, D. S. Bond, S. Croft, O. N. Jarvis, and N. Watkins. Measurements of the proton light output function of the organic liquid scintillator NE213 in several detectors. *Nuclear Instruments and Methods in Physics Research, Section A: Accelerators, Spectrometers, Detectors and Associated Equipment*, 476(1-2):190–194, 2002.

[64] F. Binda, G. Ericsson, J. Eriksson, C. Hellesen, S. Conroy, and E. Andersson Sundén. Forward fitting of experimental data from a NE213 neutron detector installed with the magnetic proton recoil upgraded spectrometer at JETa). *Review of Scientific Instruments*, 85(11):11E123, 2014.

[65] C Cazzaniga, E Andersson Sundén, F Binda, G Croci, G Ericsson, L Giacomelli, G Gorini, E Griesmayer, G Grosso, G Kaveney, M Nocente, E Perelli Cippo, M Rebai, B Syme, and M Tardocchi. Single crystal diamond detector measurements of deuterium-deuterium and deuterium- tritium neutrons in Joint European Torus fusion plasmas Single crystal diamond detector measurements of deuterium-deuterium and deuterium-tritium neutrons in Joint European. 3643(May):0–8, 2014.

[66] G. Strang. *Linear algebra and its applications.* Thomson Learning, 1988.

[67] M Anton, H Weisen, M J Dutch, W von der Linden, F Buhlmann, R Chavan, B Marletaz, P Marmillod, and P Paris. X-ray tomography on the TCV tokamak. *Plasma Physics and Controlled Fusion*, 38(11):1849–1878, November 1996.

[68] R.C. Aster, B. Borchers, and H.T. Clifford. *Parameter estimation and inverse problems.*

[69] Per Christian Hansen. Analysis of Discrete Ill-Posed Problems by Means of the L-Curve, 1992.

[70] P.C. Hansen. The L-Curve and its Use in the Numerical Treatment of Inverse Problems. In *Computational Inverse Problems in Electrocardiology*, pages 119–142. WIT Press, 2001.

[71] Per Christian Hansen, Toke Koldborg Jensen, and Giuseppe Rodriguez. An adaptive pruning algorithm for the discrete L-curve criterion. *Journal of Computational and Applied Mathematics*, 198(2):483–492, 2007.

[72] W. W. Heidbrink. A Code that Simulates Fast-Ion D_alpha and Neutral Particle Measurements. *Communications in Computational Physics*, 10(3):716–741, 2011.

[73] Clive D. Rodgers. Characterization and error analysis of profiles retrieved from remote sounding measurements. *Journal of Geophysical Research*, 95(D5):5587, 1990.

[74] A. Doicu, T. Trautmann, and Schreier. *Numerical Regularization for Atmospheric Inverse Problems.*

[75] S K Nielsen, H Bindslev, M Salewski, a Bürger, E Delabie, V Furtula, M Kantor, S B Korsholm, F Leipold, F Meo, P K Michelsen, D Moseev, J W Oosterbeek, M Stejner, E Westerhof, and P Woskov. Fast-ion redistribution due to sawtooth crash in the TEXTOR tokamak measured by collective Thomson scattering. *Plasma Physics and Controlled Fusion*, 52(9):092001, September 2010.

[76] J.R. Taylor. *An Introduction to Error Analysis.* University Science Books, 1982.

[77] M. Salewski. Fast-ion energy resolution by one-step reaction gamma-ray spectroscopy. in preparation.

Appendices

Appendix A

NES weight functions derived in the center-of-mass frame

Brysk published a paper in 1973 where he derives the energy of a neutron resulting from a fusion reaction [36]. However, he calculates the conservation of energy and momentum in the center-of-mass frame. His result has since been adopted by the neutron spectroscopy community. According to Brysk, the energy of a neutron, E_n, resulting from a fusion process is,

$$E_n = \frac{1}{2}m_n v_{cm}^2 + \frac{m_{He}}{m_{He}+m_n}\left(Q+K\right) + v_{cm}\cos\left(\theta\right)\sqrt{\frac{2m_{He}m_n}{m_{He}+m_n}\left(Q+K\right)}\,, \qquad \text{(A.0.1)}$$

where v_{cm} is the center-of-mass velocity and Q is the total energy released in the fusion reaction. K is the relative kinetic energy of the reactants, defined as $K = \frac{1}{2}\frac{m_1 m_2}{m_1+m_2}v^2$, where $\mathbf{v} = \mathbf{v}_2 - \mathbf{v}_1$ and subscripts 1 and 2 relates to reactant 1 and 2 respectively. θ is the angle between the center-of-mass velocity and the velocity of the neutron in the center-of-mass frame. The exercise is now to recover the weight function from equation (A.0.1).

As in section 3.1 it is assumed that two deuterium ions undergoes fusion and that one of the deuterium ions is a fast ion and the other is a thermal ion with a velocity so much lower that it can be assumed stationary. Furthermore it is assumed that $m_{He} = 3m_n$ and $m_f = 2m_n$. This is done to simplify the derivations. Under these simplifications, the center-of-mass velocity can be written as,

$$\mathbf{v}_{cm} = \frac{m_1\mathbf{v}_1 + m_2\mathbf{v}_2}{m_1+m_2} = \frac{\mathbf{v}_f}{2}\,. \qquad \text{(A.0.2)}$$

In a similar manner the relative kinetic energy can be written as,

$$K = \frac{1}{2}\frac{m_f^2}{2m_f}v_f^2 = \frac{1}{4}m_f v_f^2 = \frac{1}{2}m_n v_f^2\,. \qquad \text{(A.0.3)}$$

Inserting all this in equation (A.0.1) one gets,

$$\begin{aligned} E_n &= \frac{1}{8}m_n v_f^2 + \frac{3}{4}\left(Q + \frac{1}{2}m_n v_f^2\right) + \frac{v_f}{2}\cos\left(\theta\right)\sqrt{\frac{3}{2}m_n\left(Q + \frac{1}{2}m_n v_f^2\right)} \\ \Rightarrow \frac{1}{2}m_n v_n^2 &= \frac{3}{4}Q + \frac{1}{2}m_n v_f^2 + \frac{1}{2}v_f\cos\left(\theta\right)\sqrt{\frac{3}{2}m_n\left(Q + \frac{1}{2}m_n v_f^2\right)}\,. \qquad \text{(A.0.4)} \end{aligned}$$

The neutron velocity in the center-of-mass frame is defined as,

$$\mathbf{u}_n = \mathbf{v}_n - \mathbf{v}_{cm} \, . \tag{A.0.5}$$

Since θ is the angle between the center-of-mass velocity and the neutron velocity in the center-of-mass frame, $\cos(\theta)$ can be written as,

$$\begin{aligned} \cos(\theta) &= \frac{\mathbf{v}_{cm} \cdot \mathbf{u}_n}{|\mathbf{v}_{cm}| \, |\mathbf{u}_n|} \\ &= \frac{\frac{1}{2}\mathbf{v}_f \cdot \left(\mathbf{v}_n - \frac{1}{2}\mathbf{v}_D\right)}{\frac{1}{2} v_f \, |\mathbf{u}_n|} \, . \end{aligned} \tag{A.0.6}$$

$|\mathbf{u}_n|$ can be written as,

$$\begin{aligned} |\mathbf{u}_n| &= \sqrt{\left(\mathbf{v}_n - \frac{1}{2}\mathbf{v}_f\right) \cdot \left(\mathbf{v}_n - \frac{1}{2}\mathbf{v}_f\right)} \\ &= \sqrt{v_n^2 + \frac{1}{4}v_f^2 - \mathbf{v}_f \cdot \mathbf{v}_n} \, . \end{aligned} \tag{A.0.7}$$

Inserting equation (A.0.6) in equation (A.0.4) one gets,

$$\begin{aligned} \frac{1}{2}m_n v_n^2 &= \frac{3}{4}Q + \frac{1}{2}m_n v_f^2 \\ &\quad + \frac{1}{2}v_f \left(\frac{\frac{1}{2}\mathbf{v}_f \cdot \mathbf{v}_n - \frac{1}{4}v_f^2}{\frac{1}{2}v_f \sqrt{v_n^2 + \frac{1}{4}v_f^2 - \mathbf{v}_f \cdot \mathbf{v}_n}} \right) \sqrt{\frac{3}{2}m_n \left(Q + \frac{1}{2}m_n v_f^2\right)} \\ \Rightarrow \frac{1}{2}m_n v_n^2 &= \frac{3}{4}Q + \frac{1}{2}m_n v_f^2 \\ &\quad + \frac{\frac{1}{2}\mathbf{v}_f \cdot \mathbf{v}_n - \frac{1}{4}v_f^2}{\sqrt{v_n^2 + \frac{1}{4}v_f^2 - \mathbf{v}_f \cdot \mathbf{v}_n}} \sqrt{\frac{3}{2}m_n \left(Q + \frac{1}{2}m_n v_f^2\right)} \, . \end{aligned} \tag{A.0.8}$$

Equation (A.0.8) contains only known quantities and the exercise is now to show that equation (3.1.9) is obtained if $\mathbf{v}_f \cdot \mathbf{v}_n$ is isolated in equation (A.0.8). However, this is a quadratic equation in $\mathbf{v}_f \cdot \mathbf{v}_n$ and it therefore takes a bit more work compared with deriving the weight function directly from first principles as was done in section 3.1. Multiplying with 2 and rewriting equation (A.0.8) one gets,

$$m_n v_n^2 - \frac{3}{2}Q - m_n v_f^2 = \left(\mathbf{v}_f \cdot \mathbf{v}_n - \frac{1}{2}v_f^2\right) \sqrt{\frac{\frac{3}{2}m_n Q + \frac{3}{4}m_n^2 v_f^2}{v_n^2 + \frac{1}{4}v_f^2 - \mathbf{v}_f \cdot \mathbf{v}_n}} \, . \tag{A.0.9}$$

Squaring equation (A.0.9) one gets,

$$\begin{aligned} &\left(m_n v_n^2 - \frac{3}{2}Q - m_n v_f^2\right)^2 = \left(\mathbf{v}_f \cdot \mathbf{v}_n - \frac{1}{2}v_f^2\right)^2 \frac{\frac{3}{2}m_n Q + \frac{3}{4}m_n^2 v_f^2}{v_n^2 + \frac{1}{4}v_f^2 - \mathbf{v}_f \cdot \mathbf{v}_n} \\ &\Rightarrow \quad m_n^2 v_n^4 + \frac{9}{4}Q^2 + m_n^2 v_f^4 - 3m_n v_n^2 Q - 2m_n^2 v_n^2 v_f^2 + 3m_n v_f^2 Q \\ &\qquad = 3\left((\mathbf{v}_f \cdot \mathbf{v}_n)^2 + \frac{1}{4}v_f^4 - v_f^2 \mathbf{v}_f \cdot \mathbf{v}_n\right) \frac{\frac{1}{2}m_n Q + \frac{1}{4}m_n^2 v_f^2}{v_n^2 + \frac{1}{4}v_f^2 - \mathbf{v}_f \cdot \mathbf{v}_n} \, . \end{aligned} \tag{A.0.10}$$

To reduce equation (A.0.10) a new variable is introduced, $X = \mathbf{v}_f \cdot \mathbf{v}_n$. Introducing this and rewriting some more gives,

$$\begin{aligned}
&\left(m_n^2v_n^4+\frac{9}{4}Q^2+m_n^2v_f^4-3m_nv_n^2Q-2m_n^2v_n^2v_f^2+3m_nv_f^2Q\right)\left(v_n^2+\frac{1}{4}v_f^2-X\right)\\
&=3\left(X^2+\frac{1}{4}v_f^4-v_f^2X\right)\left(\frac{1}{2}m_nQ+\frac{1}{4}m_n^2v_f^2\right)
\end{aligned}$$

$$\begin{aligned}
\Rightarrow\quad & m_n^2v_n^6+\frac{9}{4}Q^2v_n^2+m_n^2v_n^2v_f^4-3m_nv_n^4Q-2m_n^2v_n^4v_f^2+3m_nv_n^2v_f^2Q\\
&+\frac{1}{4}m_n^2v_n^4v_f^2+\frac{9}{16}v_f^2Q^2+\frac{1}{4}m_n^2v_f^6-\frac{3}{4}m_nv_n^2v_f^2Q-\frac{1}{2}m_n^2v_n^2v_f^4+\frac{3}{4}m_nv_f^4Q\\
&-\left(m_n^2v_n^4+\frac{9}{4}Q^2+m_n^2v_f^4-3m_nv_n^2Q-2m_n^2v_n^2v_f^2+3m_nv_f^2Q\right)X\\
&=3\left(\frac{1}{2}m_nQ+\frac{1}{4}m_n^2v_f^2\right)X^2+\frac{3}{8}m_nv_f^4Q-\frac{3}{2}m_nv_f^2QX+\frac{3}{16}m_n^2v_f^6-\frac{3}{4}m_n^2v_f^4X
\end{aligned}$$

$$\begin{aligned}
\Rightarrow\quad & \left(\frac{3}{2}m_nQ+\frac{3}{4}m_n^2v_f^2\right)X^2+\Big(-\frac{3}{2}m_nv_f^2Q-\frac{3}{4}m_n^2v_f^4\\
&+m_n^2v_n^4+\frac{9}{4}Q^2+m_n^2v_f^4-3m_nv_n^2Q-2m_n^2v_n^2v_f^2+3m_nv_f^2Q\Big)X\\
&=m_n^2v_n^6+\frac{9}{4}Q^2v_n^2+m_n^2v_n^2v_f^4-3m_nv_n^4Q-2m_n^2v_n^4v_f^2+3m_nv_n^2v_f^2Q\\
&+\frac{1}{4}m_n^2v_n^4v_f^2+\frac{9}{16}v_f^2Q^2+\frac{1}{4}m_n^2v_f^6-\frac{3}{4}m_nv_n^2v_f^2Q-\frac{1}{2}m_n^2v_n^2v_f^4+\frac{3}{4}m_nv_f^4Q\\
&-\frac{3}{8}m_nv_f^4Q-\frac{3}{16}m_n^2v_f^6
\end{aligned}$$

$$\begin{aligned}
\Rightarrow\quad & \left(\frac{3}{2}m_nQ+\frac{3}{4}m_n^2v_f^2\right)X^2+\Big(\frac{3}{2}m_nv_f^2Q+\frac{1}{4}m_n^2v_f^4+m_n^2v_n^4+\frac{9}{4}Q^2\\
&-3m_nv_n^2Q-2m_n^2v_n^2v_f^2\Big)X\\
&=m_n^2v_n^6+\frac{1}{16}m_n^2v_f^6-\frac{7}{4}m_n^2v_n^4v_f^2-3m_nv_n^4Q+\frac{1}{2}m_n^2v_n^2v_f^4+\frac{9}{4}m_nv_n^2v_f^2Q\\
&+\frac{9}{4}v_n^2Q^2+\frac{9}{16}v_f^2Q^2+\frac{3}{8}m_nv_f^4Q\,. \qquad \text{(A.0.11)}
\end{aligned}$$

Equation (A.0.11) is a quadratic equation in X on the standard form $AX^2+BX+C=0$ with A, B and C being,

$$A = \frac{3}{2}m_nQ+\frac{3}{4}m_n^2v_f^2 \qquad \text{(A.0.12)}$$

$$B = \frac{3}{2}m_nv_f^2Q+\frac{1}{4}m_n^2v_f^4+m_n^2v_n^4+\frac{9}{4}Q^2-3m_nv_n^2Q-2m_n^2v_n^2v_f^2 \qquad \text{(A.0.13)}$$

$$\begin{aligned}
C = &-m_n^2v_n^6-\frac{1}{16}m_n^2v_f^6+\frac{7}{4}m_n^2v_n^4v_f^2+3m_nv_n^4Q-\frac{1}{2}m_n^2v_n^2v_f^4\\
&-\frac{9}{4}m_nv_n^2v_f^2Q-\frac{9}{4}v_n^2Q^2-\frac{9}{16}v_f^2Q^2-\frac{3}{8}m_nv_f^4Q\,. \qquad \text{(A.0.14)}
\end{aligned}$$

To solve the quadratic equation, the discriminant, $\Delta = B^2 - 4AC$, must be found. First B^2 is calculated,

$$\begin{aligned}
B^2 \;&=\; \frac{9}{4}m_n^2v_f^4Q^2 + \frac{3}{4}m_n^3v_f^6Q + 3m_n^3v_n^4v_f^2Q + \frac{27}{4}m_nv_f^2Q^3 - 9m_n^2v_n^2v_f^2Q^2 \\
&\quad -6m_n^3v_n^2v_f^4Q + \frac{1}{16}m_n^4v_f^8 + \frac{1}{2}m_n^4v_n^4v_f^4 + \frac{9}{8}m_n^2v_f^4Q^2 - \frac{3}{2}m_n^3v_n^2v_f^4Q \\
&\quad -m_n^4v_n^2v_f^6 + m_n^4v_n^8 + \frac{9}{2}m_n^2v_n^4Q^2 - 6m_n^3v_n^6Q - 4m_n^4v_n^6v_f^2 + \frac{81}{16}Q^4 \\
&\quad -\frac{27}{2}m_nv_n^2Q^3 - 9m_n^2v_n^2v_f^2Q^2 + 9m_n^2v_n^4Q^2 + 12m_n^3v_n^4v_f^2Q + 4m_n^4v_n^4v_f^4
\end{aligned}$$

$$\begin{aligned}
\Rightarrow B^2 \;&=\; \frac{27}{8}m_n^2v_f^4Q^2 + \frac{3}{4}m_n^3v_f^6Q + 15m_n^3v_n^4v_f^2Q + \frac{27}{4}m_nv_f^2Q^3 - 18m_n^2v_n^2v_f^2Q^2 \\
&\quad -\frac{15}{2}m_n^3v_n^2v_f^4Q + \frac{1}{16}m_n^4v_f^8 + \frac{9}{2}m_n^4v_n^4v_f^4 - m_n^4v_n^2v_f^6 + m_n^4v_n^8 \\
&\quad +\frac{27}{2}m_n^2v_n^4Q^2 - 6m_n^3v_n^6Q - 4m_n^4v_n^6v_f^2 + \frac{81}{16}Q^4 - \frac{27}{2}m_nv_n^2Q^3\,. \qquad \text{(A.0.15)}
\end{aligned}$$

$4AC$ is now found,

$$\begin{aligned}
4AC \;&=\; -6m_n^3v_n^6Q - \frac{3}{8}m_n^3v_f^6Q + \frac{21}{2}m_n^3v_n^4v_f^2Q + 18m_n^2v_n^4Q^2 - 3m_n^3v_n^2v_f^4Q \\
&\quad -\frac{27}{2}m_n^2v_n^2v_f^2Q^2 - \frac{27}{2}m_nv_n^2Q^3 - \frac{27}{8}m_nv_f^2Q^3 - \frac{9}{4}m_n^2v_f^4Q^2 \\
&\quad -3m_n^4v_n^6v_f^2 - \frac{3}{16}m_n^4v_f^8 + \frac{21}{4}m_n^4v_n^4v_f^4 + 9m_n^3v_n^4v_f^2Q - \frac{3}{2}m_n^4v_n^2v_f^6 \\
&\quad -\frac{27}{4}m_n^3v_n^2v_f^4Q - \frac{27}{4}m_n^2v_n^2v_f^2Q^2 - \frac{27}{16}m_n^2v_f^4Q^2 - \frac{9}{8}m_n^3v_f^6Q
\end{aligned}$$

$$\begin{aligned}
\Rightarrow 4AC \;&=\; -6m_n^3v_n^6Q - \frac{3}{2}m_n^3v_f^6Q + \frac{39}{2}m_n^3v_n^4v_f^2Q + 18m_n^2v_n^4Q^2 - \frac{39}{4}m_n^3v_n^2v_f^4Q \\
&\quad -\frac{81}{4}m_n^2v_n^2v_f^2Q^2 - \frac{27}{2}m_nv_n^2Q^3 - \frac{27}{8}m_nv_f^2Q^3 - \frac{63}{16}m_n^2v_f^4Q^2 \\
&\quad -3m_n^4v_n^6v_f^2 - \frac{3}{16}m_n^4v_f^8 + \frac{21}{4}m_n^4v_n^4v_f^4 - \frac{3}{2}m_n^4v_n^2v_f^6\,. \qquad \text{(A.0.16)}
\end{aligned}$$

From equations (A.0.15) and (A.0.16) the discriminant can be calculated,

$$\begin{aligned}
\Delta \;&=\; \frac{117}{16}m_n^2v_f^4Q^2 - \frac{9}{2}m_n^3v_n^4v_f^2Q + \frac{9}{4}m_n^2v_n^2v_f^2Q^2 + \frac{9}{4}m_n^3v_n^2v_f^4Q \\
&\quad -\frac{3}{4}m_n^4v_n^4v_f^4 - \frac{9}{2}m_n^2v_n^4Q^2 + \frac{9}{4}m_n^3v_f^6Q + \frac{81}{8}m_nv_f^2Q^3 + \frac{1}{4}m_n^4v_f^8 \\
&\quad +\frac{1}{2}m_n^4v_n^2v_f^6 + m_n^4v_n^8 - m_n^4v_n^6v_f^2 + \frac{81}{16}Q^4
\end{aligned}$$

$$\begin{aligned}
\Rightarrow \Delta \;&=\; \frac{1}{16}\Big(117m_n^2v_f^4Q^2 - 72m_n^3v_n^4v_f^2Q + 36m_n^2v_n^2v_f^2Q^2 + 36m_n^3v_n^2v_f^4Q \\
&\quad -12m_n^4v_n^4v_f^4 - 72m_n^2v_n^4Q^2 + 36m_n^3v_f^6Q + 162m_nv_f^2Q^3 + 4m_n^4v_f^8 \\
&\quad +8m_n^4v_n^2v_f^6 + 16m_n^4v_n^8 - 16m_n^4v_n^6v_f^2 + 81Q^4\Big)\,. \qquad \text{(A.0.17)}
\end{aligned}$$

The terms in the parenthesis in equation (A.0.17) can be factorised into

$$\left(3Q + 2m_n v_f^2 - 2m_n v_n^2\right)^2 \left(3Q + m_n v_f^2 + 2m_n v_n^2\right)^2 . \tag{A.0.18}$$

This is most easily realised by expanding equation (A.0.18) and comparing it with equation (A.0.17).

$$\begin{aligned}
&\left(3Q + 2m_n v_f^2 - 2m_n v_n^2\right)^2 \left(3Q + m_n v_f^2 + 2m_n v_n^2\right)^2 \\
=\;& \left(9Q^2 + 4m_n^2 v_f^4 + 4m_n^2 v_n^4 + 12m_n v_f^2 Q - 12m_n v_n^2 Q - 8m_n^2 v_n^2 v_f^2\right) \\
&\cdot \left(9Q^2 + m_n^2 v_f^4 + 4m_n^2 v_n^4 + 6m_n v_f^2 Q + 12m_n v_n^2 Q + 4m_n^2 v_n^2 v_f^2\right)
\end{aligned}$$

$$\begin{aligned}
=\;& 81Q^4 + 9m_n^2 v_f^4 Q^2 + 36m_n^2 v_n^4 Q^2 + 54m_n v_f^2 Q^3 + 108m_n v_n^2 Q^3 + 36m_n^2 v_n^2 v_f^2 Q^2 \\
&+36m_n^2 v_f^4 Q^2 + 4m_n^4 v_f^8 + 16m_n^4 v_n^4 v_f^4 + 24m_n^3 v_f^6 Q + 48m_n^3 v_n^2 v_f^4 Q + 16m_n^4 v_n^2 v_f^6 \\
&+36m_n^2 v_n^4 Q^2 + 4m_n^4 v_n^4 v_f^4 + 16m_n^4 v_n^8 + 24m_n^3 v_n^4 v_f^2 Q + 48m_n^3 v_n^6 Q + 16m_n^4 v_n^6 v_f^2 \\
&+108m_n v_f^2 Q^3 + 12m_n^3 v_f^6 Q + 48m_n^3 v_n^4 v_f^2 Q + 72m_n^2 v_f^4 Q^2 + 144m_n^2 v_n^2 v_f^2 Q^2 + 48m_n^3 v_n^2 v_f^4 Q \\
&-108m_n v_n^2 Q^3 - 12m_n^3 v_n^2 v_f^4 Q - 48m_n^3 v_n^6 Q - 72m_n^2 v_n^2 v_f^2 Q^2 - 144m_n^2 v_n^4 Q^2 - 48m_n^3 v_n^4 v_f^2 Q \\
&-72m_n^2 v_n^2 v_f^2 Q^2 - 8m_n^4 v_n^2 v_f^6 - 32m_n^4 v_n^6 v_f^2 - 48m_n^3 v_n^2 v_f^4 Q - 96m_n^3 v_n^4 v_f^2 Q - 32m_n^4 v_n^4 v_f^4
\end{aligned}$$

$$\begin{aligned}
=\;& 81Q^4 + (9+36+72)m_n^2 v_f^4 Q^2 + (36+36-144)m_n^2 v_n^4 Q^2 + (36+72+72-144)m_n^2 v_n^2 v_f^2 Q^2 \\
&+(54+108)m_n v_f^2 Q^3 + (108-108)m_n v_n^2 Q^3 + 4m_n^4 v_f^8 + (4+16-32)m_n^4 v_n^4 v_f^4 \\
&+(24+12)m_n^3 v_f^6 Q + (48-12+48-48)m_n^3 v_n^2 v_f^4 Q + (16-8)m_n^4 v_n^2 v_f^6 + 16m_n^4 v_n^8 \\
&+(24+48-48-96)m_n^3 v_n^4 v_f^2 Q + (48-48)m_n^3 v_n^6 Q + (16-32)m_n^4 v_n^6 v_f^2
\end{aligned}$$

$$\begin{aligned}
=\;& 81Q^4 + 117m_n^2 v_f^4 Q^2 - 72m_n^2 v_n^4 Q^2 + 36m_n^2 v_n^2 v_f^2 Q^2 + 162m_n v_f^2 Q^3 \\
&+4m_n^4 v_f^8 - 12m_n^4 v_n^4 v_f^4 + 36m_n^3 v_f^6 Q + 36m_n^3 v_n^2 v_f^4 Q + 8m_n^4 v_n^2 v_f^6 \\
&+16m_n^4 v_n^8 - 72m_n^3 v_n^4 v_f^2 Q - 16m_n^4 v_n^6 v_f^2 .
\end{aligned} \tag{A.0.19}$$

Equation (A.0.19) is identical to the terms in the parenthesis in equation (A.0.17) and thus it is concluded that the discriminant can be written as,

$$\Delta = \frac{1}{16}\left(\left(3Q + 2m_n v_f^2 - 2m_n v_n^2\right)^2 \left(3Q + m_n v_f^2 + 2m_n v_n^2\right)^2\right) . \tag{A.0.20}$$

$\sqrt{\Delta}$ is needed to calculate the weight function, and it is therefore found.

$$\begin{aligned}
\sqrt{\Delta} &= \frac{1}{4}\left(3Q + 2m_n v_f^2 - 2m_n v_n^2\right)\left(3Q + m_n v_f^2 + 2m_n v_n^2\right) \\
\Rightarrow \sqrt{\Delta} &= \frac{1}{4}\left(9Q^2 + 3m_n v_f^2 Q + 6m_n v_n^2 Q + 6m_n v_f^2 Q + 2m_n^2 v_f^4\right. \\
&\quad \left. +4m_n^2 v_n^2 v_f^2 - 6m_n v_n^2 Q - 2m_n^2 v_n^2 v_f^2 - 4m_n^2 v_n^4\right) \\
\Rightarrow \sqrt{\Delta} &= \frac{1}{4}\left(9Q^2 + 9m_n v_f^2 Q + 2m_n^2 v_n^2 v_f^2 + 2m_n^2 v_f^4 - 4m_n^2 v_n^4\right)
\end{aligned} \tag{A.0.21}$$

Now X can be calculated.

$$X = \frac{-B \pm \sqrt{\Delta}}{2A} \tag{A.0.22}$$

The "-" solution gives,

$$\begin{aligned}
X &= \frac{1}{3m_nQ + \frac{3}{2}m_n^2v_f^2}\Big(-\frac{3}{2}m_nv_f^2Q - \frac{1}{4}m_n^2v_f^4 - m_n^2v_n^4 - \frac{9}{4}Q^2 + 3m_nv_n^2Q \\
&\quad + 2m_n^2v_n^2v_f^2 - \frac{9}{4}Q^2 - \frac{9}{4}m_nv_f^2Q - \frac{1}{2}m_n^2v_n^2v_f^2 - \frac{1}{2}m_n^2v_f^4 + m_n^2v_n^4\Big) \\
\Rightarrow X &= \frac{1}{3m_nQ + \frac{3}{2}m_n^2v_f^2}\Big(-\frac{9}{2}Q^2 - \frac{15}{4}m_nv_f^2Q + \frac{3}{2}m_n^2v_n^2v_f^2 - \frac{3}{4}m_n^2v_f^4 + 3m_nv_n^2Q\Big) \\
\Rightarrow X &= \frac{1}{6\left(Q + \frac{1}{2}m_nv_f^2\right)}\left(-9\frac{Q^2}{m_n} - \frac{15}{2}v_f^2Q + 3m_nv_n^2v_f^2 - \frac{3}{2}m_nv_f^4 + 6v_n^2Q\right) \\
\Rightarrow X &= \frac{1}{6\left(Q + \frac{1}{2}m_nv_f^2\right)}\left(-9\frac{Q}{m_n}\left(Q + \frac{1}{2}m_nv_f^2\right) - 3v_f^2Q + +3m_nv_n^2v_f^2 - \frac{3}{2}m_nv_f^4 + 6v_n^2Q\right) \\
\Rightarrow X &= \frac{1}{6\left(Q + \frac{1}{2}m_nv_f^2\right)}\left(-9\frac{Q}{m_n}\left(Q + \frac{1}{2}m_nv_f^2\right) - 3v_f^2\left(Q + \frac{1}{2}m_nv_f^2\right) + 6v_n^2\left(Q + \frac{1}{2}m_nv_f^2\right)\right) \\
\Rightarrow X &= -\frac{3}{2}\frac{Q}{m_n} - \frac{1}{2}v_f^2 + v_n^2\,. \qquad \text{(A.0.23)}
\end{aligned}$$

Inserting $X = \mathbf{v}_f \cdot \mathbf{v}_n$ in equation (A.0.23) gives,

$$\mathbf{v}_f \cdot \hat{\mathbf{v}}_n = v_n - \frac{1}{2}\frac{v_f^2}{v_n} - \frac{3}{2}\frac{Q}{m_nv_n}\,, \tag{A.0.24}$$

which is identical to equation (3.1.9).

Appendix B

Maxwellian in (E, p) coordinates

A Maxwellian distribution in velocity-space is given as

$$f^v = n\left(\frac{m}{2\pi k_B T}\right)^{3/2} \exp\left(-\frac{m\mathbf{v}^2}{2k_B T}\right) , \tag{B.0.1}$$

The 2D distribution is obtained by integrating out the gyro-motion. The Jacobian determinant for this change of variables is $v_\perp$. The 2D distribution is

$$\begin{aligned} f^v_{2D} &= n\left(\frac{m}{2\pi k_B T}\right)^{3/2} v_\perp \exp\left(-\frac{mv_\parallel^2}{2k_B T}\right) \int_0^{2\pi} \exp\left(-\frac{mv_\perp^2\left(\cos(\gamma)^2+\sin(\gamma)^2\right)}{2k_B T}\right) \mathrm{d}\gamma \\ &= 2\pi n\left(\frac{m}{2\pi k_B T}\right)^{3/2} v_\perp \exp\left(-\frac{mv_\parallel^2}{2k_B T}\right) \exp\left(-\frac{mv_\perp^2}{2k_B T}\right) . \end{aligned} \tag{B.0.2}$$

To calculate the expressions in (E,p)-coordinates, the following relations are needed:

$$v_\parallel = p\sqrt{\frac{2E}{m}} \tag{B.0.3}$$

$$v_\perp = \sqrt{1-p^2}\sqrt{\frac{2E}{m}} \tag{B.0.4}$$

Inserting equations (B.0.3) and (B.0.4) in equation (B.0.2) gives

$$\begin{aligned} f^{E,p}_{2D} &= 2\pi n\left(\frac{m}{2\pi k_B T}\right)^{3/2} \sqrt{1-p^2}\sqrt{\frac{2E}{m}} \exp\left(-\frac{p^2 E}{k_B T}\right) \exp\left(-\frac{\left(1-p^2\right) E}{k_B T}\right) \\ &= 2\pi n\left(\frac{m}{2\pi k_B T}\right)^{3/2} \sqrt{1-p^2}\sqrt{\frac{2E}{m}} \exp\left(-\frac{E}{k_B T}\right) . \end{aligned} \tag{B.0.5}$$

To get $f^{E,p}_{2D}$ in units of [ions/energy], the Jacobian determinant for that transformation is needed, see equation (2.4.8). The Jacobian determinant is

$$\frac{v}{mv_\perp} = \frac{1}{m\sqrt{1-p^2}} . \tag{B.0.6}$$

$f^{E,p}_{2D}$ in units if [ions/eV] is

$$f^{E,p}_{2D} = q\frac{n}{\sqrt{\pi}}\left(\frac{1}{k_B T}\right)^{3/2} \sqrt{E} \exp\left(-\frac{E}{k_B T}\right) \tag{B.0.7}$$

Paper I

IOP Publishing | International Atomic Energy Agency Nuclear Fusion

Nucl. Fusion **55** (2015) 053013 (13pp) doi:10.1088/0029-5515/55/5/053013

Velocity-space sensitivity of neutron spectrometry measurements

A.S. Jacobsen[1], M. Salewski[1], J. Eriksson[2], G. Ericsson[2], S.B. Korsholm[1], F. Leipold[1], S.K. Nielsen[1], J. Rasmussen[1], M. Stejner[1] and JET EFDA Contributors[a]

JET-EFDA, Culham Science Centre, Abingdon, OX14 3DB, UK
[1] Technical University of Denmark, Department of Physics, DK-2800 Kgs. Lyngby, Denmark
[2] Department of Physics and Astronomy, Uppsala University, Sweden

E-mail: ajsen@fysik.dtu.dk

Received 24 October 2014, revised 5 February 2015
Accepted for publication 11 March 2015
Published 15 April 2015

Abstract

Neutron emission spectrometry (NES) measures the energies of neutrons produced in fusion reactions. Here we present velocity-space weight functions for NES and neutron yield measurements. Weight functions show the sensitivity as well as the accessible regions in velocity space for a given range of the neutron energy spectrum. Combined with a calculated fast-ion distribution function, they determine the part of the distribution function producing detectable neutrons in a given neutron energy range. Furthermore, we construct a forward model based on weight functions capable of rapidly calculating neutron energy spectra. This forward model can be inverted and could thereby be used to directly measure the fast-ion phase-space distribution functions, possibly in combination with other fast-ion diagnostics. The presented methods and results can be applied to neutron energy spectra measured by any kind of neutron spectrometer and to any neutron yield measurement.

Keywords: neutron emission spectrometry, velocity-space sensitivity, fast ions, energetic particles, plasma diagnostics

(Some figures may appear in colour only in the online journal)

1. Introduction

Fast ions in fusion devices play an important role. They are created by ionization of injected energetic neutral particles, by acceleration of ions using ion cyclotron resonance heating or by fusion processes. It is envisaged that the fast ions born in the fusion process will deliver a large part of the heating in an eventual fusion power plant. For this to work, it is critical that the fast ions are sufficiently confined. It has been found that fast ions can be redistributed or expelled by magnetohydrodynamic (MHD) modes. Furthermore, it has been observed that the ions can have an influence on the stability of such modes [1–3]. Therefore, the study of the behaviour of the fast ions and their interplay with MHD modes in present-day fusion devices is important.

One method to diagnose fast ions in fusion plasmas is by analysing the neutrons created in fusion reactions. The energies of the neutrons depend on the energy released in the fusion reactions as well as the velocities of the reacting ions. Neutron emission spectrometers measure neutron energy spectra and are hence sensitive to the velocity distribution functions of these ions. One such spectrometer is the time-of-flight spectrometer TOFOR at JET which measures 2.45 MeV neutrons from deuterium plasmas [4–11]. TOFOR consists of two sets of detectors placed at a known distance from each other. By measuring the time it takes the neutrons to travel from the first to the second set of detectors, it is possible to infer information about the neutron energy spectrum. Here we present a general method to relate neutron energy spectra and neutron yield measurements to velocity space. Furthermore, we apply our method to neutron energy spectra measured by TOFOR. TOFOR is chosen as an example because of its excellent energy resolution. However, the weight function method is general and can be applied to energy spectra from any spectrometer.

Neutron spectrometers are installed or planned on a number of machines: time-of-flight spectrometers at EAST [12] and LHD [13], and compact spectrometers at EAST [14], ASDEX Upgrade [15], JET [16] and FTU [17]. Neutron yield detectors are installed at NSTX [18], DIII-D [19], Alcator C-Mod [20], EAST [21], LHD [22], JT-60U [23], MAST [18], JET [24] and planned for Wendelstein 7-X [25] . Furthermore, both neutron spectrometers and yield detectors are planned for ITER [26].

---

[a] See the appendix of Romanelli F. *et al* 2012 *Proc. 24th IAEA Fusion Energy Conf.* 2012 (San Diego, CA, 2012) http://iopscience.iop.org/0029-5515/53/10/104002/article

In calculations of neutron energy spectra, it is convenient to consider three different contributions to the spectra: neutrons from reactions involving two thermal ions, neutrons originating from reactions involving two fast ions and neutrons originating from reactions involving a fast and thermal ion. Here, we study the latter which often dominates the spectrum, especially for high neutron energies [4]. Neutrons created in a D–D reaction will have energies around 2.45 MeV. However, the neutron energy spectrum can be broadened significantly if one or both ions have high energies. If an ensemble of fast ions concentrated in a small region in velocity space reacts with thermal ions, the neutron spectra will have a characteristic double-hump shape due to the gyro-motion of the ions [7, 8, 27, 28].

Here we develop weight functions for neutron emission spectrometry (NES) and neutron yield measurements analogous to those for fast-ion D_α (FIDA) spectroscopy [29–31] and collective Thomson scattering (CTS) [32]. Weight functions show the velocity-space sensitivity for a given energy range of a measured spectrum. So far, weight functions have been applied in four different ways for FIDA and CTS measurements. The simplest application is as an illustration of the region of velocity space that is accessible by a given part of a measured spectrum and the sensitivity within this region [29–49]. For a given fast-ion distribution function, the product of the weight function and the distribution function shows which ions contribute most to the measurements in the given measurement range [29, 30, 42–49]. By integrating the product of the weight functions and a given distribution function, it is possible to calculate a synthetic spectrum which can then be compared with the measured one. This replaces the traditional forward modelling that is often based on time-consuming Monte-Carlo calculations [50–52]. Finally, weight functions are the basic ingredients in the pursuit to extract fast-ion distribution functions directly from measurements using tomographic inversion in velocity space [32, 50–53].

This paper is organized as follows. In section 2 we derive analytic weight functions for NES and neutron yield measurements. In section 3 we calculate weight functions numerically using an existing forward model. We investigate the effect of various bulk ion temperatures on the velocity-space sensitivity of NES measurements in section 4. Weight functions are used to illustrate the region in velocity space measured by a given part of a neutron spectrum from TOFOR in section 5, and in section 6 we formulate a forward model based on weight functions. In section 7 we discuss perspectives, and conclusions are summarized in section 8.

2. Analytic expressions for neutron spectrometry weight functions

A fusion process between a fast and a thermal deuterium ion can create a neutron and a helium-3 ion according to the following reaction:

$$\mathrm{D} + \mathrm{D} \rightarrow {}^{3}\mathrm{He} + \mathrm{n}. \tag{1}$$

The neutrons, being uncharged, leave the plasma and can be detected using neutron spectrometers. The energies of the detected neutrons depend on the velocities of the reacting ions. Here we show which part of velocity space can generate neutrons with energies in particular energy ranges using weight functions. Weight functions are defined as functions relating a given measurement to the fast-ion phase-space distribution function, $f(v_\parallel, v_\perp, \mathbf{r})$:

$$s\left(v_{n,1}, v_{n,2}, \phi\right) = \iiint w\left(v_{n,1}, v_{n,2}, \phi, v_\parallel, v_\perp, \mathbf{r}\right) \times f\left(v_\parallel, v_\perp, \mathbf{r}\right) \mathrm{d}v_\parallel \mathrm{d}v_\perp \mathrm{d}\mathbf{r}, \tag{2}$$

where $s(v_{n,1}, v_{n,2}, \phi)$ is the detection rate of neutrons with velocities between $v_{n,1}$ and $v_{n,2}$ measured by a detector at an angle ϕ between its line-of-sight and the magnetic field. $w(v_{n,1}, v_{n,2}, \phi, v_\parallel, v_\perp, \mathbf{r})$ is the weight function in units of $[\frac{\mathrm{N}_n}{\mathrm{s}\,\mathrm{N}_f}]$, i.e. number of detected neutrons in a given energy or velocity range per second per fast ion. $f(v_\parallel, v_\perp, \mathbf{r})$ is in units of $[\frac{\mathrm{N}_f\,\mathrm{s}^2}{\mathrm{m}^5}]$. $v_\parallel$ and $v_\perp$ denote the ion velocity parallel and perpendicular to the magnetic field, respectively, and $\mathbf{r}$ denotes the spatial coordinates. $v_\parallel$ is defined positive in the direction of the magnetic field. The spatial integral is over the conical measurement volume oriented along the line-of-sight. The velocity-space integrals are over the entire velocity space. The fast-ion phase-space distribution function and the weight functions have a spatial dependence since the plasma parameters may vary significantly along the line-of-sight. Equation (2) can also be expressed as a function of energy and pitch of the fast ions

$$s\left(v_{n,1}, v_{n,2}, \phi\right) = \iiint w\left(v_{n,1}, v_{n,2}, \phi, E, p, \mathbf{r}\right) \times f\left(E, p, \mathbf{r}\right) \mathrm{d}E\,\mathrm{d}p\,\mathrm{d}\mathbf{r}, \tag{3}$$

where E is the fast-ion energy and p is the pitch defined as $p = \frac{v_\parallel}{v}$. It is here assumed that the co-current direction is in the same toroidal direction as the magnetic field.

In the following, weight functions will be derived in $(v_\parallel, v_\perp)$-space as the mathematical expressions take a simpler form in these coordinates. However, the most important expressions will be given in the more commonly used (E, p)-space as well. Weight functions can be written as a product of two factors:

$$w\left(v_{n,1}, v_{n,2}, \phi, v_\parallel, v_\perp, \mathbf{r}\right) = R\left(\phi, v_\parallel, v_\perp, \mathbf{r}\right) \times \mathrm{prob}\left(v_{n,1} < v_n < v_{n,2} \middle| \phi, v_\parallel, v_\perp\right). \tag{4}$$

$\mathrm{prob}(v_{n,1} < v_n < v_{n,2}|\phi, v_\parallel, v_\perp)$ is the probability that a neutron has a velocity between $v_{n,1}$ and $v_{n,2}$ (or likewise a kinetic energy between $E_{n,1}$ and $E_{n,2}$), given it was created in a fusion reaction between a thermal ion and a fast ion with velocity $(v_\parallel, v_\perp)$ and observed at an angle ϕ. The conditioning symbol '|' means given. This factor contains the spectral information that determines which part of velocity space a given interval in the neutron energy spectrum is susceptible to. $R(\phi, v_\parallel, v_\perp, \mathbf{r})$ is the rate of detected neutrons per fast ion as a function of velocity and position.

Before we derive analytic expressions for the probability part, we illustrate the properties of the rate function $R(\phi, v_\parallel, v_\perp, \mathbf{r})$. The rate function gives the total number of neutrons detected per second per fast ion irrespective of the neutron energies. It depends on the relative velocity, $\mathbf{v}_{\mathrm{rel}}$ between the fast and thermal ions and can be calculated

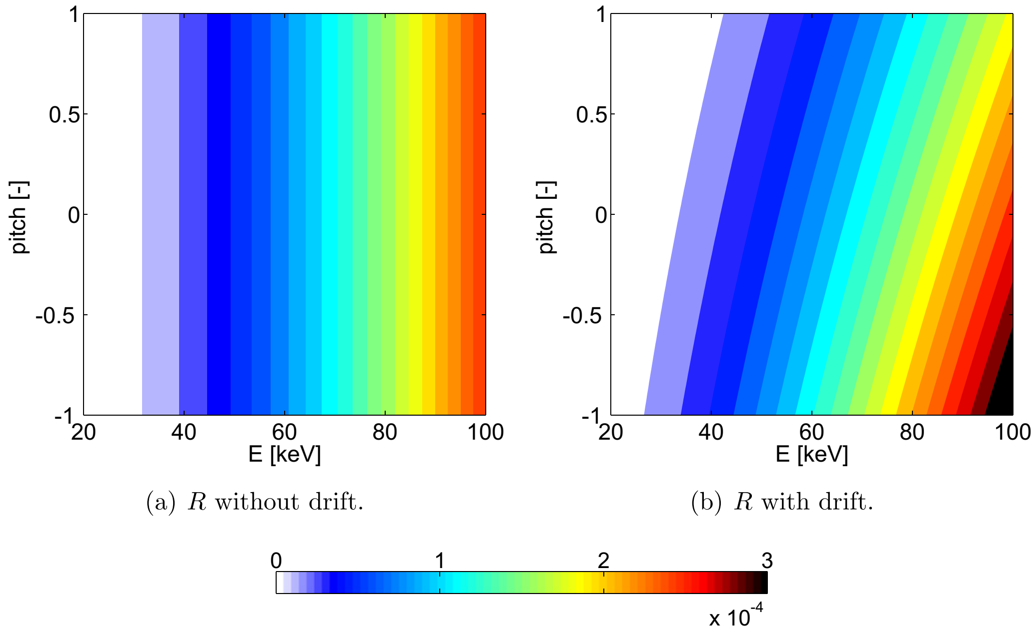

(a) R without drift.

(b) R with drift.

Figure 1. Rate functions with and without a drift of the thermal ions in units of $[\frac{N_n}{N_{fs}}]$. The co-current drift velocity is 2.1×10^5 m s^{-1}. The thermal ion density is 5×10^{19} m^{-3}.

according to

$$R\left(\phi, v_\parallel, v_\perp, \mathbf{r}\right) = \frac{\Omega\left(\mathbf{r}\right)}{4\pi}\iint f_t\left(v_{t,\parallel}, v_{t,\perp}, \mathbf{r}\right)\sigma\left(\phi, v_{\mathrm{rel}}\right) v_{\mathrm{rel}}\,\mathrm{d}v_{t,\parallel}\mathrm{d}v_{t,\perp}, \qquad (5)$$

where Ω is the solid angle of the detector as seen from the plasma as a function of position, f_t is the thermal ion distribution function, $v_{t,\parallel}$ and $v_{t,\perp}$ are the thermal ion velocities parallel and perpendicular to the magnetic field, σ is the fusion cross section and $v_{\mathrm{rel}} = |\mathbf{v}_{\mathrm{rel}}|$ is the magnitude of the relative velocity. The integral is over the thermal ion velocity and is calculated by numerically sampling over a Maxwellian distribution.

Here we illustrate some basic properties of R by assuming that the velocities of the fast ions are significantly larger than the velocities of the thermal ions. Furthermore, we neglect the ϕ-dependence of the cross section and the finite solid angle. This allows us to approximate the thermal-ion distribution function by a δ-function located at origo. In this case, the relative velocity becomes the velocity of the fast ions and equation (5) reduces to

$$R\left(v_\parallel, v_\perp, \mathbf{r}\right) = n_t\left(\mathbf{r}\right)\sigma\left(\sqrt{v_\parallel^2 + v_\perp^2}\right)\sqrt{v_\parallel^2 + v_\perp^2}\,, \qquad (6)$$

where n_t is the thermal ion density. In this case R does not depend on pitch as shown in figure 1(a). Here, σ is approximated by [54]

$$\sigma = \frac{S}{E_{\mathrm{cm}}\left(\exp\left(\frac{B_G}{\sqrt{E_{\mathrm{cm}}}}\right) - 1\right)}, \qquad (7)$$

where E_{cm} is the energy in the centre-of-mass frame, B_G is a constant and S is a fifth-order polynomial in E_{cm}. A thermal ion density of 5×10^{19} m^{-3} is used. Plasma rotation has an effect on R [29] which can be taken into account by modelling the rotating thermal distribution as a drifting Maxwellian. Here, for simplicity we model the rotating thermal distribution as a δ-function located at a non-zero parallel velocity and no perpendicular velocity. Thereby the rate function becomes

$$R\left(v_\parallel, v_\perp, \mathbf{r}\right) = n_t\left(\mathbf{r}\right)\sigma\left(\sqrt{\left(v_\parallel - v_d\right)^2 + v_\perp^2}\right) \times\sqrt{\left(v_\parallel - v_d\right)^2 + v_\perp^2}\,, \qquad (8)$$

where v_d is the drift velocity parallel to the magnetic field. This introduces an asymmetry in pitch, as we show in figure 1(b). Here a co-current drift velocity of $v_d = 2.1 \times 10^5$ m s^{-1} is used. In this situation, the neutron rate is largest for fast ions with negative pitch, as they move in the direction opposite to the thermal drift and thus have a larger relative velocity.

The rate function, R, is the weight function for neutron yield measurements [29], which count any neutron irrespective of energy. This follows from equation (4) for $v_{n,1} \to 0$ and $v_{n,2} \to c$, where c is the speed of light, as the probability function becomes unity for very large neutron energy ranges, i.e. the probability that a detected neutron has a velocity between 0 and c must be 1. Neutron yield measurements are most sensitive in the velocity-space regions with the largest amplitudes of R, where most neutrons are produced per ion per second.

Now we derive analytic expressions for the probability part of the weight functions. The probability that a detected neutron has a velocity in a given interval, $v_{n,1} < v_n < v_{n,2}$ is the integral of the probability density function of the neutron velocity integrated over this interval:

$$\mathrm{prob}\left(v_{n,1} < v_n < v_{n,2}\left|\phi, v_\parallel, v_\perp\right.\right) = \int_{v_{n,1}}^{v_{n,2}} \mathrm{pdf}_{v_n}\,\mathrm{d}v_n. \qquad (9)$$

We assume that the energy and the momentum of the thermal ions are negligible compared with the energy and the momentum of the fast ions, respectively. Thus, given the parallel and perpendicular velocities of the fast ion and the angle, ϕ, to the detector, the neutron velocity only depends on the gyro-angle, γ, of the fast ion before the reaction [55]. The neutron velocity probability density function can therefore be expressed as a function of the gyro-angle probability density function:

$$\mathrm{pdf}_{v_n} = \mathrm{pdf}_{\gamma} \left| \frac{\mathrm{d}\gamma}{\mathrm{d}v_n} \right| . \tag{10}$$

The gyro-angle distribution is assumed uniform, i.e. it is assumed that an ion is equally likely to have any given gyro-angle. Thus, the gyro-angle probability distribution function is uniform:

$$\mathrm{pdf}_{\gamma} = \frac{1}{2\pi}, \tag{11}$$

and the problem reduces to expressing the relation between the gyro-angle of the fast ion and the neutron velocity in known quantities. Conservation of energy during a fusion process between a fast ion and a stationary thermal ion in the lab frame of reference dictates

$$\tfrac{1}{2} m_f v_f^2 + Q = \tfrac{1}{2} m_{\mathrm{He}} v_{\mathrm{He}}^2 + \tfrac{1}{2} m_n v_n^2, \tag{12}$$

where m_f, m_{He} and m_n and v_f, v_{He} and v_n are the masses and velocities of the fast ion, the helium ion and the neutron, respectively, and Q is the energy released in the fusion process. For a D–D reaction, $Q = 3.27$ MeV. Conservation of momentum dictates

$$m_f \mathbf{v}_f = m_{\mathrm{He}} \mathbf{v}_{\mathrm{He}} + m_n \mathbf{v}_n. \tag{13}$$

Isolating $\mathbf{v}_{\mathrm{He}}$ and squaring gives

$$\begin{aligned} v_{\mathrm{He}}^2 &= \frac{1}{m_{\mathrm{He}}^2} \left(m_f \mathbf{v}_f - m_n \mathbf{v}_n \right)^2 \\ &= \frac{1}{m_{\mathrm{He}}^2} \left(m_f^2 v_f^2 + m_n^2 v_n^2 - 2 m_f m_n \mathbf{v}_f \cdot \mathbf{v}_n \right). \end{aligned} \tag{14}$$

To calculate the dot product $\mathbf{v}_f \cdot \mathbf{v}_n$, we write

$$\mathbf{v}_n = \hat{\mathbf{v}}_n v_n, \tag{15}$$

where $\hat{\mathbf{v}}_n$ is the unit vector in the direction towards the spectrometer along the line-of-sight. The projection of the fast-ion velocity in the direction towards the neutron spectrometer, u, can then be expressed as

$$u = \mathbf{v}_f \cdot \hat{\mathbf{v}}_n. \tag{16}$$

Inserting equations (14), (15) and (16) in equation (12) and isolating u gives

$$u = \frac{1}{2} \frac{(m_{\mathrm{He}} + m_n)}{m_f} v_n - \frac{1}{2} \frac{\left(m_{\mathrm{He}} - m_f \right)}{m_n} \frac{v_f^2}{v_n} - \frac{m_{\mathrm{He}}}{m_f m_n} \frac{Q}{v_n}. \tag{17}$$

Only neutrons moving along the line-of-sight towards the neutron spectrometer are detected. We define a $(v_\parallel, v_{\perp,1}, v_{\perp,2})$-coordinate system similar to the one defined in reference [32]. The $v_{\perp,1}$-axis is oriented such that the line-of-sight of the spectrometer lies in the $(v_\parallel, v_{\perp,1})$-plane. The fast-ion velocity can be written as

$$\mathbf{v}_f = v_\parallel \hat{\mathbf{v}}_\parallel + v_\perp \cos(\gamma) \hat{\mathbf{v}}_{\perp,1} + v_\perp \sin(\gamma) \hat{\mathbf{v}}_{\perp,2}, \tag{18}$$

where $\hat{\mathbf{v}}_\parallel$, $\hat{\mathbf{v}}_{\perp,1}$ and $\hat{\mathbf{v}}_{\perp,2}$ are the three unit vectors. In this coordinate system $\hat{\mathbf{v}}_n$ becomes

$$\hat{\mathbf{v}}_n = \cos(\phi) \hat{\mathbf{v}}_\parallel + \sin(\phi) \hat{\mathbf{v}}_{\perp,1}. \tag{19}$$

The projected fast-ion velocity, u, can be expressed in terms of the parallel and perpendicular ion velocities [32]:

$$u = \mathbf{v}_f \cdot \hat{\mathbf{v}}_n = v_\parallel \cos(\phi) + v_\perp \sin(\phi) \cos(\gamma). \tag{20}$$

If, for a given u, equation (20) is fulfilled for γ, then so it is for $2\pi - \gamma$ as well. Combining equations (17) and (20) and isolating γ gives

$$\begin{aligned} \gamma &= \arccos\left(\frac{u - v_\parallel \cos(\phi)}{v_\perp \sin(\phi)} \right) \\ &= \arccos\left(\frac{1}{v_\perp \sin(\phi)} \left(\frac{1}{2} \frac{(m_{\mathrm{He}} + m_n)}{m_f} v_n \right.\right. \\ &\quad - \frac{1}{2} \frac{\left(m_{\mathrm{He}} - m_f \right)}{m_n} \frac{\left(v_\parallel^2 + v_\perp^2 \right)}{v_n} \\ &\quad \left.\left. - \frac{m_{\mathrm{He}}}{m_f m_n} \frac{Q}{v_n} - v_\parallel \cos(\phi) \right) \right). \end{aligned} \tag{21}$$

To find pdf_{v_n} from equation (10), we differentiate γ with respect to the neutron velocity

$$\begin{aligned} \frac{\mathrm{d}\gamma}{\mathrm{d}v_n} &= -\frac{1}{\sin(\gamma)} \left(\frac{1}{v_\perp \sin(\phi)} \left(\frac{1}{2} \frac{(m_{\mathrm{He}} + m_n)}{m_f} \right.\right. \\ &\quad \left.\left. + \frac{1}{2} \frac{\left(m_{\mathrm{He}} - m_f \right)}{m_n} \frac{\left(v_\parallel^2 + v_\perp^2 \right)}{v_n^2} + \frac{m_{\mathrm{He}}}{m_f m_n} \frac{Q}{v_n^2} \right) \right). \end{aligned} \tag{22}$$

Combining equations (9)–(11) and changing the integration variable to γ gives

$$\begin{aligned} \mathrm{prob}\left(v_{n,1} < v_n < v_{n,2} \middle| \phi, v_\parallel, v_\perp \right) &= \int_{\gamma(v_{n,1})}^{\gamma(v_{n,2})} \frac{1}{2\pi} \frac{\left| \frac{\mathrm{d}\gamma}{\mathrm{d}v_n} \right|}{\frac{\mathrm{d}\gamma}{\mathrm{d}v_n}} \mathrm{d}\gamma \\ + \int_{2\pi - \gamma(v_{n,1})}^{2\pi - \gamma(v_{n,2})} \frac{1}{2\pi} \frac{\left| \frac{\mathrm{d}\gamma}{\mathrm{d}v_n} \right|}{\frac{\mathrm{d}\gamma}{\mathrm{d}v_n}} \mathrm{d}\gamma. \end{aligned} \tag{23}$$

The second integral in equation (23) arises since equation (20) is fulfilled for both γ and $2\pi - \gamma$ as mentioned earlier. As ϕ is only defined between 0° and 180°, the terms in the parenthesis in equation (22) are always positive, and thus the signs of the integrands in equation (23) depend only on γ. For $0 < \gamma < \pi$ the integrand is negative, and for $\pi < \gamma < 2\pi$, the integrand is positive. The probability can now be calculated

$$\begin{aligned} &\mathrm{prob}\left(v_{n,1} < v_n < v_{n,2} \middle| \phi, v_\parallel, v_\perp \right) \\ &\quad = \frac{1}{2\pi} \left(\int_{\gamma(v_{n,1})}^{\gamma(v_{n,2})} (-1)\, \mathrm{d}\gamma + \int_{2\pi - \gamma(v_{n,1})}^{2\pi - \gamma(v_{n,2})} \mathrm{d}\gamma \right) \\ &\quad = \frac{\gamma(v_{n,1}) - \gamma(v_{n,2})}{\pi}, \end{aligned} \tag{24}$$

where the γ values are given by equation (21). Thus, the probability function is the fraction of the gyro-orbit that leads to neutrons with energies within the given neutron energy range. These results are valid for $\phi \neq 0°$ or $180°$. For $\phi = 0°$ or $180°$, the projected fast-ion velocity becomes $u = \pm v_\parallel$, and a given $(v_\parallel, v_\perp)$-coordinate will give a single neutron velocity using equation (17) since v_n cannot be negative. In this specific case, the probability functions become semicircular arcs in $(v_\parallel, v_\perp)$-space with an amplitude of one. The probability function can also be expressed in terms of the neutron energy, E_n:

$$\mathrm{prob}\left(E_{n,1} < E_n < E_{n,2} \left| \phi, v_\parallel, v_\perp\right.\right) = \frac{\gamma\left(E_{n,1}\right) - \gamma\left(E_{n,2}\right)}{\pi}. \tag{25}$$

$\gamma(E_n)$ is found by inserting $v_n = \sqrt{\frac{2E_n}{m_n}}$ in equation (21). In energy-pitch coordinates, the probability becomes

$$\mathrm{prob}\left(E_{n,1} < E_n < E_{n,2} \right| \phi, E, p\left.\right) = \frac{\gamma\left(E_{n,1}\right) - \gamma\left(E_{n,2}\right)}{\pi}. \tag{26}$$

The γ values are then calculated from

$$\gamma = \arccos\left(\frac{1}{\sqrt{1-p^2}}\frac{1}{\sin(\phi)}\left(\frac{1}{2}\frac{(m_{\mathrm{He}}+m_n)}{\sqrt{m_f m_n}}\sqrt{\frac{E_n}{E}} - \frac{1}{2}\frac{\left(m_{\mathrm{He}}-m_f\right)}{\sqrt{m_f m_n}}\sqrt{\frac{E}{E_n}} - \frac{1}{2}\frac{m_{\mathrm{He}}}{\sqrt{m_f m_n}}\frac{Q}{\sqrt{E E_n}} - p\cos(\phi)\right)\right). \tag{27}$$

For the special case $m_{\mathrm{He}} = 3m_n$ and $m_f = 2m_n$, which we treat here, equations (17), (21) and (27) reduce considerably. Equation (17) becomes

$$u = v_n - \frac{1}{2}\frac{v_f^2}{v_n} - \frac{3}{2}\frac{Q}{m_n v_n}. \tag{28}$$

Equation (21) becomes

$$\gamma = \arccos\left(\frac{1}{v_\perp \sin(\phi)}\left(v_n - \frac{1}{2}\frac{\left(v_\parallel^2 + v_\perp^2\right)}{v_n} - \frac{3}{2}\frac{Q}{m_n v_n} - v_\parallel \cos(\phi)\right)\right) \tag{29}$$

and equation (27) becomes

$$\gamma = \arccos\left(\frac{1}{\sqrt{1-p^2}\sin(\phi)}\left(\sqrt{2\frac{E_n}{E}} - \frac{1}{2}\sqrt{\frac{E}{2E_n}} - \frac{3}{2}\frac{Q}{\sqrt{2EE_n}} - p\cos(\phi)\right)\right). \tag{30}$$

Examples of probabilities calculated for D–D neutrons using equation (25) for projection angles $\phi = 90°$, 45° and 10° for different neutron energies are plotted in figure 2 in $(v_\parallel, v_\perp)$-space. They are calculated for a neutron energy interval of $\Delta E_n = E_{n,2} - E_{n,1} = 0.03\,\mathrm{MeV}$. The coloured regions are observable for the given neutron energy range and projection angle ϕ whereas the white regions cannot contribute to the signal and are unobservable regions. The probability functions corresponding to different neutron energy ranges cover different regions in velocity space. We have chosen to show these examples of the weight functions for very large $(v_\parallel, v_\perp)$-values in order to reveal the shape of the observable region. Fast ions at JET typically have lower energies. Figure 2 shows that the weight functions for higher neutron energies cover larger velocity-space regions. The observable regions for a given neutron energy do not necessarily include the regions for lower neutron energies as demonstrated by figures 2(g) and (i). The probability for the neutrons to be in a particular energy range is largest for ions close to the edges of the probability functions. This is analogous to weight functions for CTS and FIDA [31, 32].

The limiting edges separating the observable region in velocity space from the unobservable region, i.e. the edges of the weight functions, can be found by inserting $\cos(\gamma) = \pm 1$ in equation (21), as in this case the projected velocities and therefore the neutron energies are at their extreme values. In this case, equation (21) can be rewritten in the form $(v_\parallel - v_{\parallel,0})^2 + (v_\perp - v_{\perp,0})^2 = r^2$ which is the equation of a circle centred at $(v_{\parallel,0}, v_{\perp,0})$ with radius r. Rewriting equation (21) with $\cos(\gamma) = -1$ gives

$$v_{\parallel,0} = -\frac{m_n v_n}{m_{\mathrm{He}} - m_f}\cos(\phi), \tag{31}$$

$$v_{\perp,0} = \frac{m_n v_n}{m_{\mathrm{He}} - m_f}\sin(\phi), \tag{32}$$

$$r = \sqrt{2\frac{m_{\mathrm{He}}\left(m_{\mathrm{He}} + m_n - m_f\right)}{m_f\left(m_{\mathrm{He}} - m_f\right)^2}E_n - 2\frac{m_{\mathrm{He}}}{m_f\left(m_{\mathrm{He}} - m_f\right)}Q}. \tag{33}$$

The centre of the circle lies on a straight line through the origin with angle $180° - \phi$ to the $v_\parallel$-axis since $\frac{v_{\perp,0}}{v_{\parallel,0}} = -\tan(\phi)$. The distance from the centre of the circle to the origin is $\frac{m_n}{m_{\mathrm{He}} - m_f}v_n$. Thus, the larger the neutron energy, the further the centre of the weight function moves away from the origin. Rewriting equation (21) with $\cos(\gamma) = 1$ gives

$$v'_{\parallel,0} = v_{\parallel,0}, \tag{34}$$

$$v'_{\perp,0} = -v_{\perp,0}, \tag{35}$$

$$r' = r, \tag{36}$$

where $(v'_{\parallel,0}, v'_{\perp,0})$ and r' are the centre coordinates and radius of a second circle. Thus the second circle is a mirror image of the first, mirrored across the $v_\parallel$-axis. The weight functions are bounded by the parts of the circles with positive $v_\perp$-coordinates. This differs from weight functions for FIDA and CTS which have characteristic triangular shapes in $(v_\parallel, v_\perp)$-coordinates [31, 32]. Letting $r \to 0$ in equation (33) gives a lower limit for the neutron energy E_n. For D–D neutrons this limit is found to be $E_n = \frac{Q}{2}$. Figure 2 further shows the dependence of the weight functions on the projection angle ϕ. The weight functions occupy a smaller region of velocity space for ϕ-angles far from 90°, a behaviour also seen for CTS and FIDA weight functions. For a perpendicular view ($\phi = 90°$), the weight functions are symmetric with respect to $v_\parallel$ as figures 2(a), (b) and (c) show. This is also evident from equation (31) as $v_{\parallel,0} = 0$ for $\phi = 90°$. For $0° < \phi < 90°$ the weight functions are shifted towards negative parallel velocities, whereas for $90° < \phi < 180°$ they are shifted towards positive parallel velocities.

Figure 3 shows examples of the probability functions calculated in (E, p)-space. We again calculate the probability functions up to high ion energies to show large portions of the weight functions. As for $(v_\parallel, v_\perp)$-coordinates, we find that for smaller ϕ angles, the weight functions cover a smaller region of (E, p)-space, and the symmetry in pitch for $\phi = 90°$ is evident. However, the shape of the weight functions in (E, p)-space is more complicated than in $(v_\parallel, v_\perp)$-space. The probability functions have finite values down to $E = 0\,\mathrm{MeV}$ for $E_n \simeq 2.45\,\mathrm{MeV}$. However, this does not mean that the

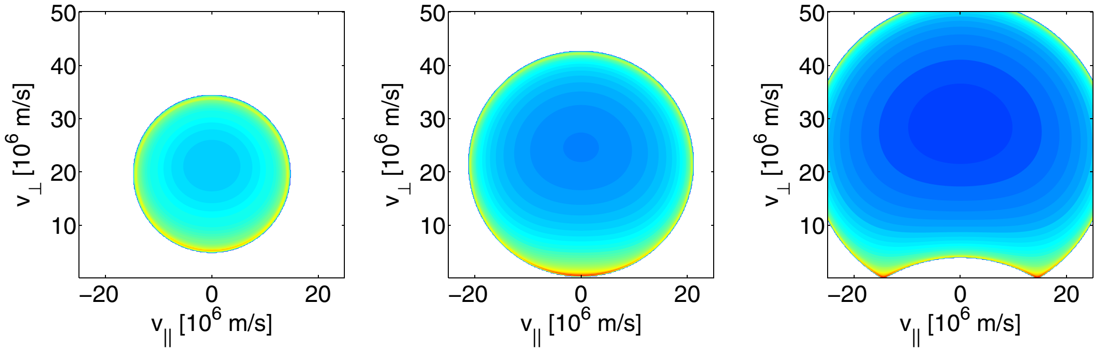

(a) $E_n = 2$ MeV, $\phi = 90°$ (b) $E_n = 2.4$ MeV, $\phi = 90°$ (c) $E_n = 3$ MeV, $\phi = 90°$

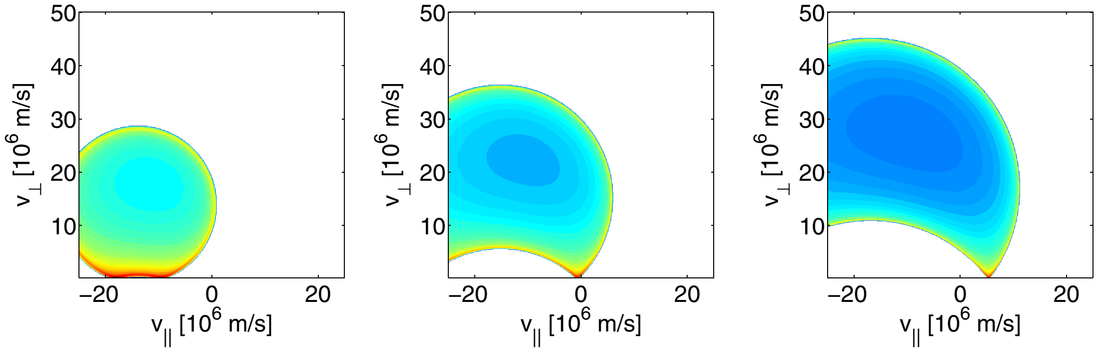

(d) $E_n = 2$ MeV, $\phi = 45°$ (e) $E_n = 2.4$ MeV, $\phi = 45°$ (f) $E_n = 3$ MeV, $\phi = 45°$

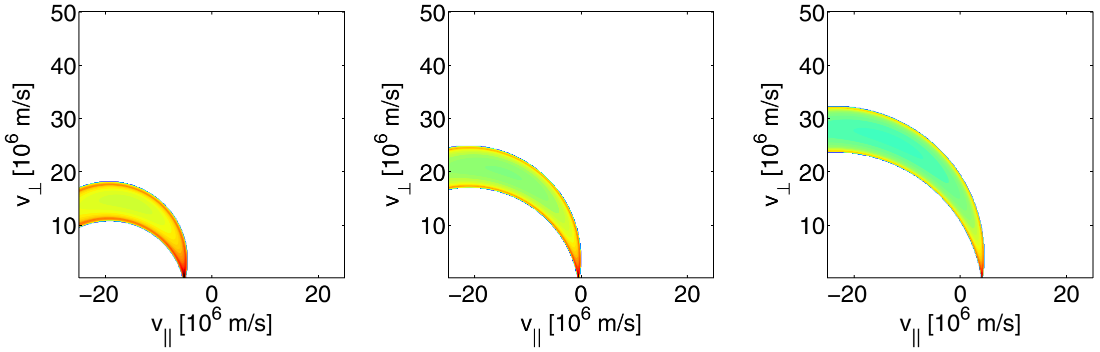

(g) $E_n = 2$ MeV, $\phi = 10°$ (h) $E_n = 2.4$ MeV, $\phi = 10°$ (i) $E_n = 3$ MeV, $\phi = 10°$

Figure 2. The probability part of neutron spectrometry weight functions calculated in $(v_{\parallel}, v_{\perp})$-space for $\Delta E_n = 0.03$ MeV centred at E_n.

full weight functions have significant values at very low ion energies, as the rate function goes rapidly to zero for such low ion energies.

3. Numerical calculation of neutron spectrometry weight functions

Weight functions can be computed numerically using a forward model capable of calculating a neutron energy spectrum for a given arbitrary fast-ion velocity distribution and a given thermal ion velocity distribution function. The forward model used here has previously been used for neutron spectrometry analysis in e.g. [9, 56]. We define a point-like velocity distribution function for the fast ions and calculate the corresponding energy spectrum. This distribution function can be written as a product of δ-functions

$$f(E, p, \mathbf{r}) = N_f \delta(E_0 - E)\,\delta(p_0 - p)\,\delta(\mathbf{r}_0 - \mathbf{r}), \qquad (37)$$

where N_f is the number of fast ions. Inserting equation (37) in equation (3) and integrating gives the amplitude of the weight function at $(E_0, p_0, \mathbf{r}_0)$ for the given neutron energy range and projection angle:

$$w\left(E_{n,1}, E_{n,2}, \phi, E_0, p_0, \mathbf{r}_0\right) = \frac{s\left(E_{n,1}, E_{n,2}, \phi\right)}{N_f}. \qquad (38)$$

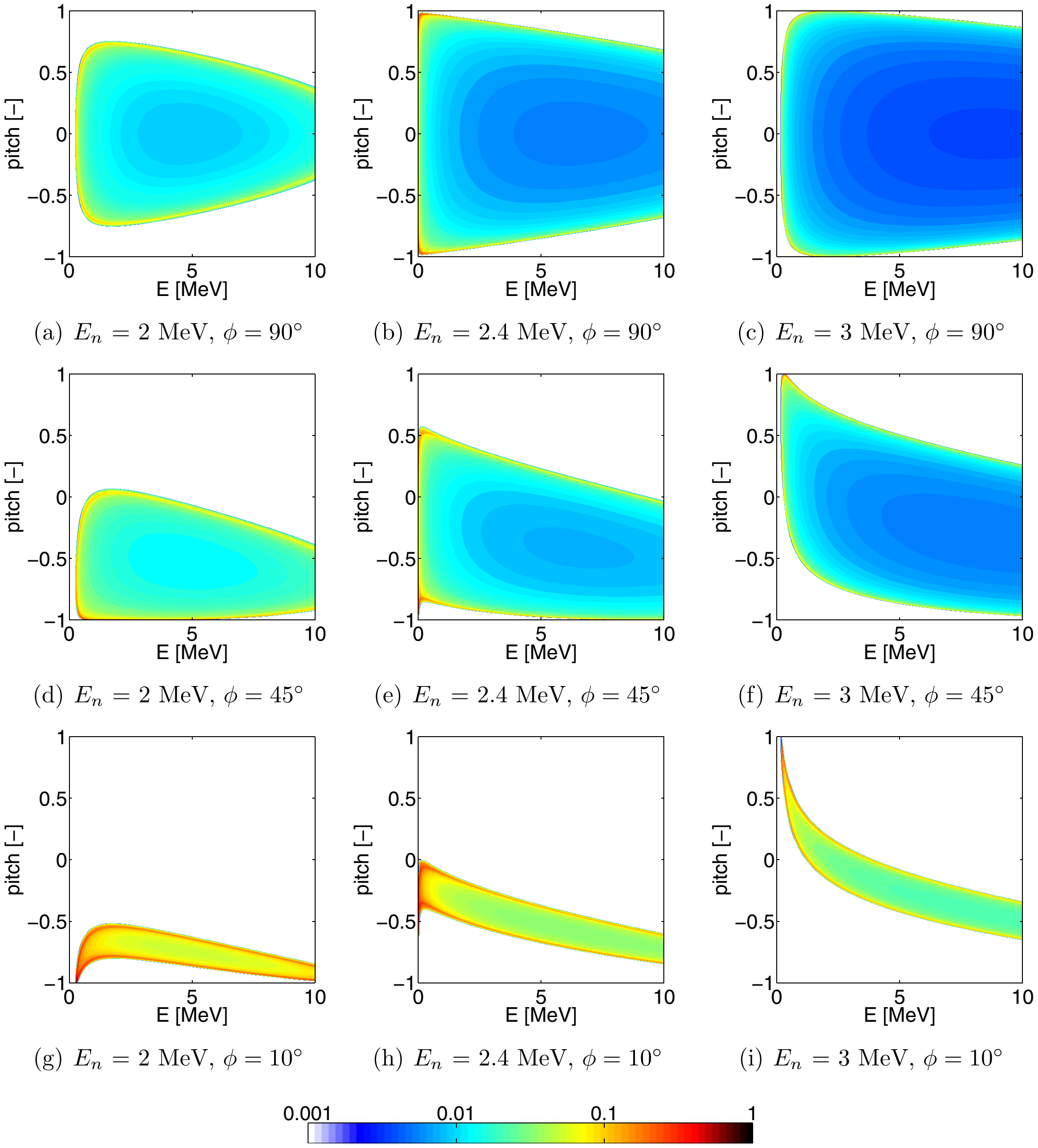

(a) $E_n = 2$ MeV, $\phi = 90°$ (b) $E_n = 2.4$ MeV, $\phi = 90°$ (c) $E_n = 3$ MeV, $\phi = 90°$

(d) $E_n = 2$ MeV, $\phi = 45°$ (e) $E_n = 2.4$ MeV, $\phi = 45°$ (f) $E_n = 3$ MeV, $\phi = 45°$

(g) $E_n = 2$ MeV, $\phi = 10°$ (h) $E_n = 2.4$ MeV, $\phi = 10°$ (i) $E_n = 3$ MeV, $\phi = 10°$

Figure 3. The probability part of neutron spectrometry weight functions calculated in (E, p)-space for $\Delta E_n = 0.03$ MeV centred at E_n.

The probability part can now be calculated according to

$$\mathrm{prop}\left(E_{n,1} < E_n < E_{n,2} \middle| \phi, E_0, p_0\right) = \frac{w\left(E_{n,1}, E_{n,2}, \phi, E_0, p_0, \mathbf{r}_0\right)}{R\left(\phi, E_0, p_0, \mathbf{r}_0\right)}, \tag{39}$$

where the rate part can be calculated using equation (5) or directly from the spectrum as

$$R\left(\phi, E_0, p_0, \mathbf{r}_0\right) = \frac{s\left(E_{n,1} \to 0, E_{n,2} \to \infty, \phi\right)}{N_f}. \tag{40}$$

This is repeated on a numerical grid of velocity-space positions of the point-like distribution. Figure 4 compares examples of the probability part of the weight functions calculated using the analytical approach derived in section 2 and the numerical approach calculated using equation (39). The analytic and numeric results agree very well, in shape as well as in amplitudes. The numerically calculated weight functions are less smooth than the analytic ones since the forward model uses a Monte-Carlo approach. Furthermore, the numerical weight functions have a coarser velocity-space resolution because the computation of analytic weight functions requires much less computational time.

4. Effect of temperature on the velocity-space sensitivity of NES

Our approach to calculate analytic weight functions assumed stationary thermal ions corresponding to zero temperature of the thermal-ion distribution. We can readily investigate the effect of a non-zero temperature on the velocity-space sensitivity of NES using numerical weight functions. The effect of increasing the temperature of the Maxwellian thermal

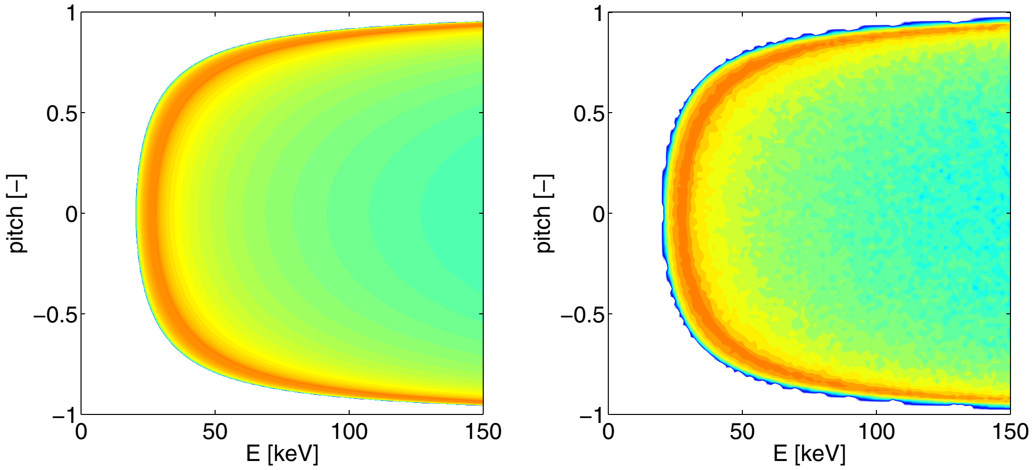

(a) $\phi = 90°$, analytical (b) $\phi = 90°$, numerical

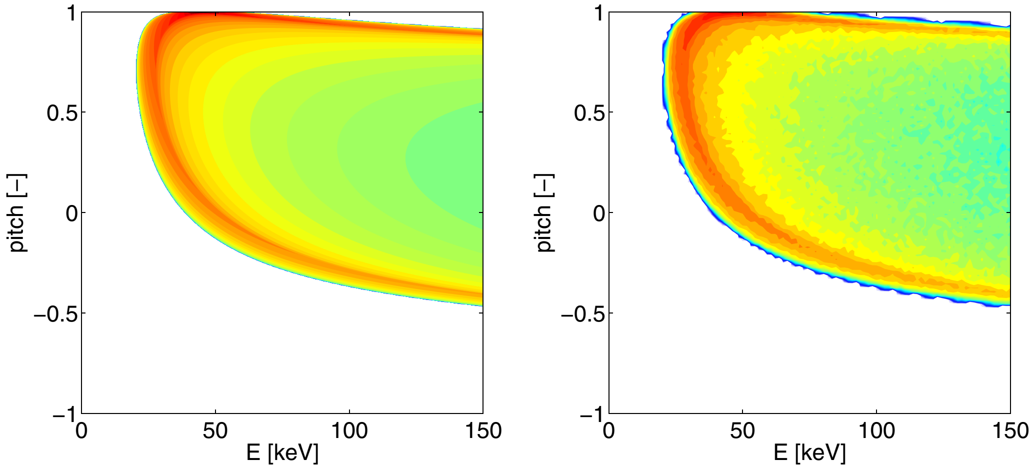

(c) $\phi = 45°$, analytical (d) $\phi = 45°$, numerical

Figure 4. Comparison of the probability part of neutron spectrometry weight functions calculated numerically and analytically, for $E_n = 2.6\,\mathrm{MeV}$ and $\Delta E_n = 0.03\,\mathrm{MeV}$.

distribution is shown in figure 5. The sharp features of the zero temperature probability function are becoming blurred for a finite temperature of the thermal distribution. The larger the temperature, the more blurred the probability functions become. The largest amplitudes close to the edge of the probability function are reduced and broadened already for a temperature of 1 keV. These trends become more pronounced with increasing temperatures. The dotted lines in figure 5 show the edge of the weight function in the $T = 0\,\mathrm{keV}$ case calculated using equations (31)–(33) and transformed to (E, p)-space.

5. Weight functions used to show interrogation regions

For the remainder of this paper, we will consider the complete weight functions consisting of the probability part and the neutron rate part according to equation (4). We will be using numerical weight functions calculated using appropriate angle-dependent cross-sections and plasma parameters. As mentioned earlier, a weight function shows the velocity-space sensitivity of the measurement for a given neutron energy range and in particular which regions are accessible by the measurements. Figure 6(*a*) shows a time-of-flight spectrum from TOFOR measured during an 8 s steady period from $t = 17 - 25\,\mathrm{s}$ in JET discharge #68138, together with a synthetic time-of-flight spectrum from a calculated energy spectrum. The synthetic time-of-flight spectrum matches the measurements well, except at large time-of-flight values where scattered neutrons contribute to the measured spectrum. The corresponding synthetic neutron energy spectrum is shown in figure 6(*b*). The average rate of neutrons, $s(E_{n,1}, E_{n,2}, \phi)$ from equation (2), can be obtained by dividing the spectrum by the measurement time, here 8 s. A shaded bar has been inserted in figure 6(*b*). The weight function for the energies corresponding to the shaded interval is shown in figure 6(*c*), i.e. the neutrons with energies in the shaded region of figure 6(*b*)

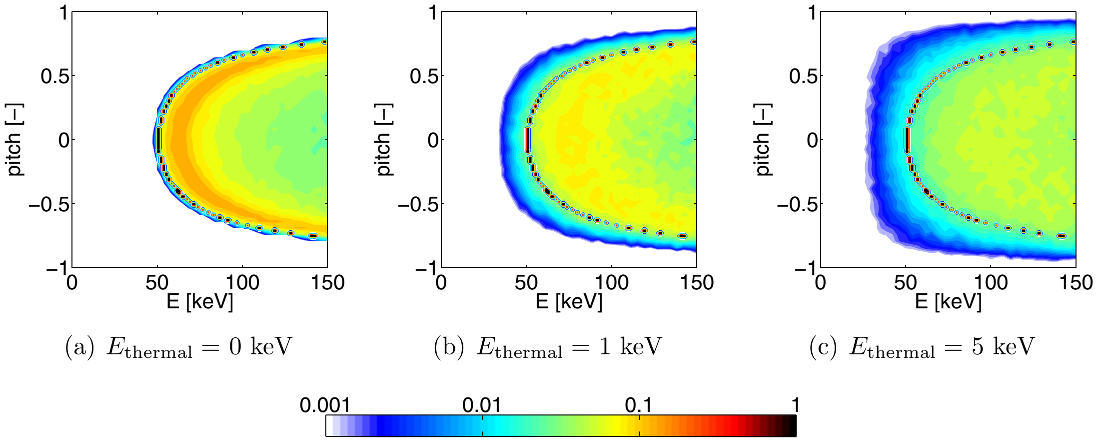

(a) $E_{\mathrm{thermal}} = 0$ keV (b) $E_{\mathrm{thermal}} = 1$ keV (c) $E_{\mathrm{thermal}} = 5$ keV

Figure 5. Probability part of neutron spectrometry weight functions with $\phi = 90°$, $E_n = 2.2\,\mathrm{MeV}$ and $\Delta E_n = 0.03\,\mathrm{MeV}$ calculated for various thermal ion temperatures. The dotted lines show the edge of the $T = 0\,\mathrm{keV}$ weight function.

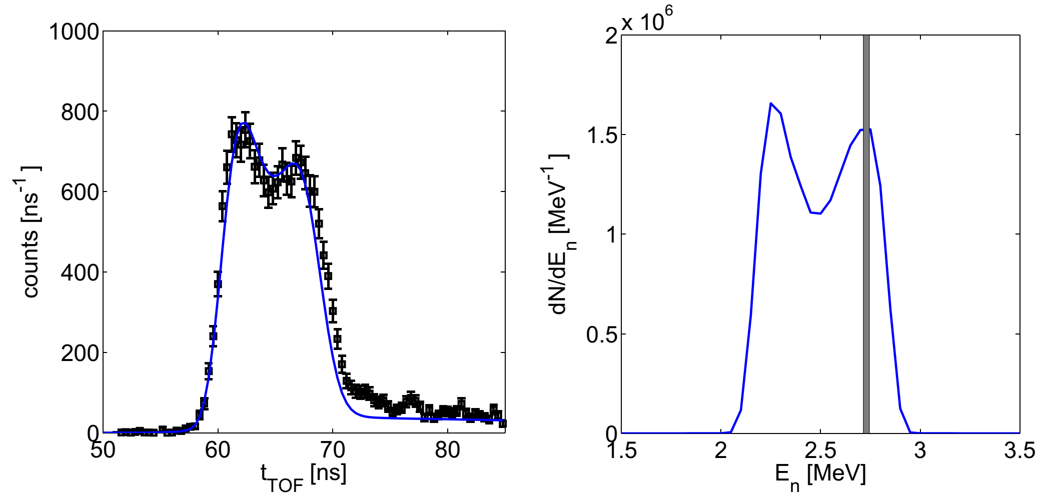

(a) Time-of-flight spectrum. (b) Simulated neutron energy spectrum.

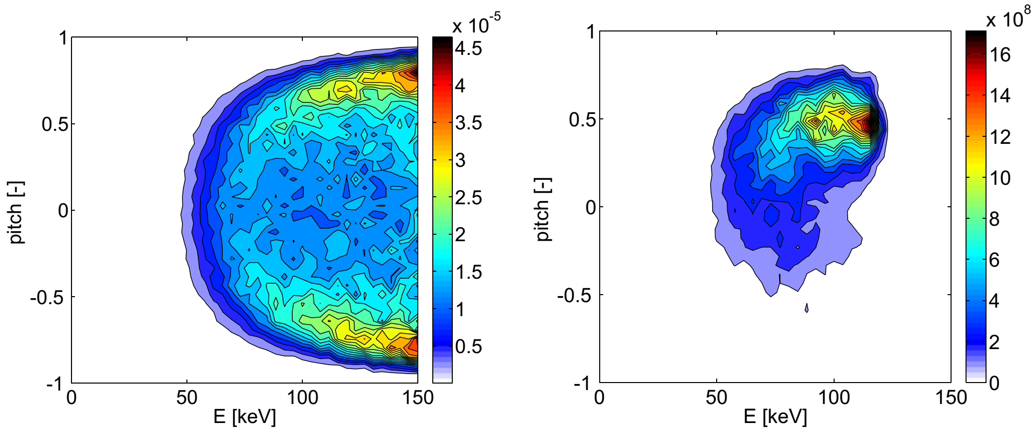

(c) w. (d) $f \times w$.

Figure 6. Example of applying the weight function approach to neutron measurements at JET from discharge #68138. (*a*) Measured time-of-flight spectrum and a synthetic spectrum. (*b*) Corresponding simulated neutron energy spectrum. (*c*) Weight function in units of [neutrons per second per fast ion] for $E_n = 2.73 \pm 0.015\,\mathrm{MeV}$ and a bulk ion temperature of 2.3 keV. (*d*) Product of the weight function and a simulated fast ion distribution function integrated over a central volume in units of [neutrons per second per keV], illustrating the measured part of the distribution.

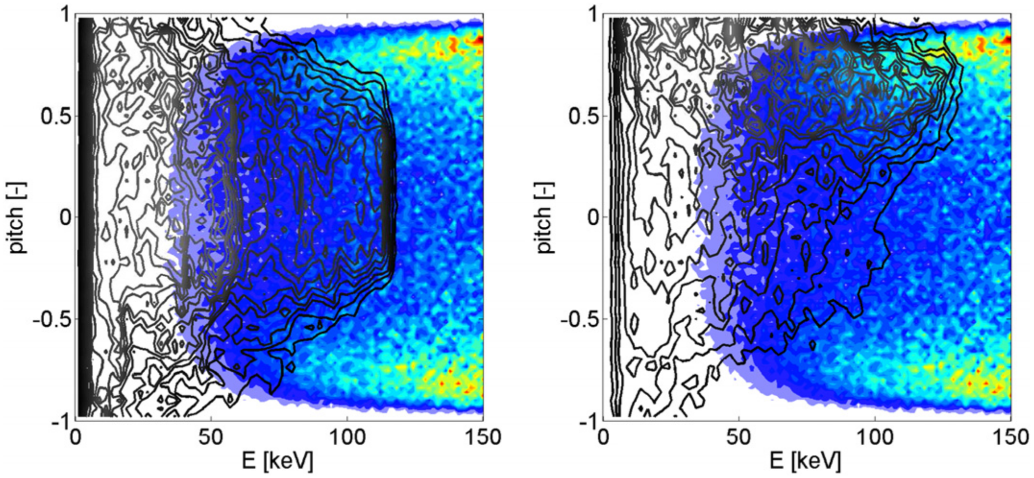

(a) f and w, radial NBI. (b) f and w, tangential NBI.

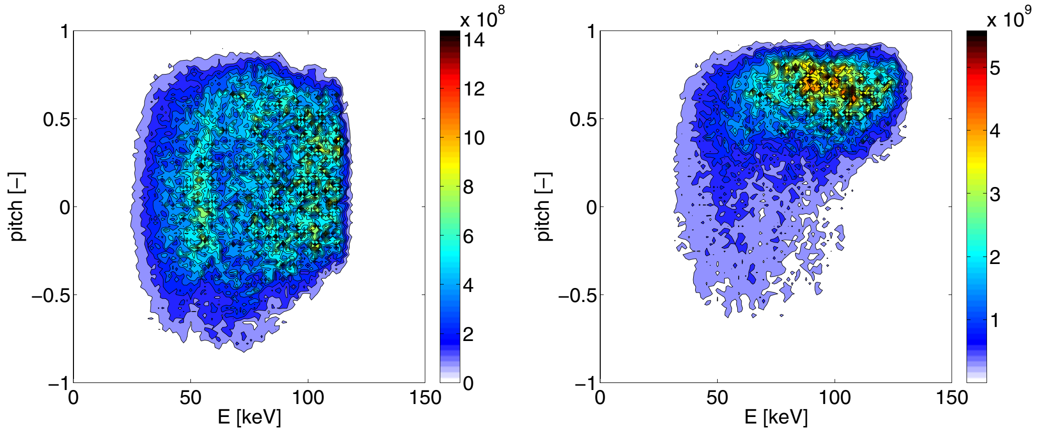

(c) $f \times w$, radial NBI. (d) $f \times w$, tangential NBI.

Figure 7. (a), (b) By plotting a calculated distribution function (black lines) together with a calculated weight function (coloured region), it is possible to visualize the region in velocity space which is accessible by a given part of the neutron energy spectrum. (c) and (d) show the product of f and w, which illustrates where most neutrons come from, given the calculated distribution function. These examples are for a numerical weight function calculated for $E_n = 2.3 \pm 0.015$ MeV and $\phi = 90^\circ$. The distribution functions are calculated for JET discharge #69242 using TRANSP together with the NUBEAM module.

can only arise from reactions involving fast ions with velocities located in the coloured region of figure 6(c). This weight function is calculated using a background ion temperature of 2.3 keV. To estimate which regions in velocity space generate most neutrons for a given velocity-space distribution function, one plots the product of a weight function and the distribution function, i.e. the integrand of equations (2) or (3). The integrand shows the number density of detected neutrons with energies in a given energy range per second in velocity space for the particular distribution function. The fast-ion distribution function has been calculated using TRANSP with the NUBEAM module [57] for JET discharge #68138. The fast ions have been simulated in the entire TOFOR measurement volume. Here the velocity distribution of the ions in the centre of JET is considered, as these will often produce most of the detected neutrons. The product of the weight function and the central fast-ion velocity distribution function is shown in figure 6(d). It is also possible to formulate instrument-specific weight functions directly connecting the time-of-flight measurement of TOFOR with velocity space [58]. Here we discuss weight functions in terms of neutron energy as this quantity is independent of the particular spectrometer.

In figure 7 we illustrate using weight functions that, even though the measured neutron energies are the same, the ions generating most of the detected neutrons can reside in very different velocity-space regions. The weight function is calculated for $E_n = 2.3 \pm 0.015$ MeV, $\phi = 90^\circ$ and $E_{\text{thermal}} = 2$ keV. Figure 7(a) shows a beam-ion distribution function originating from an off-axis radial injection, while figure 7(b) shows a distribution function from an on-axis tangential injection. Both are from JET discharge #69242. The products of the weight function and the distribution functions are shown in figures 7(c) and (d). In the case of a radial injection, the range of neutron energies between 2.285 and 2.315 MeV measures fast ions with energies higher than 40 keV and pitch values between −0.75 and 0.75 as seen in figure 7(c). For a tangential injection, most detected neutrons in this energy range are produced in reactions involving passing ions with $p > 0.5$ as seen in figure 7(d).

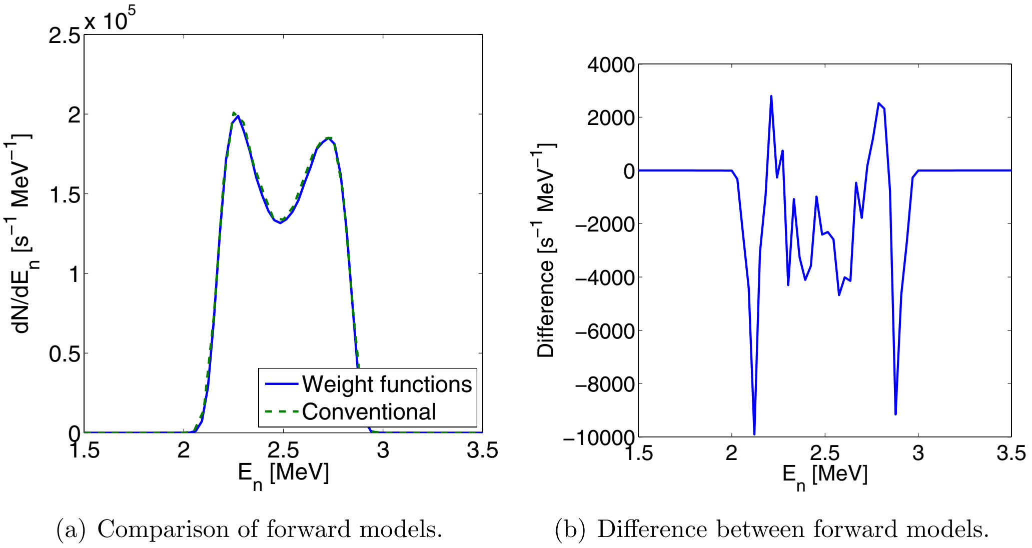

(a) Comparison of forward models. (b) Difference between forward models.

Figure 8. (*a*) Comparison of a spectrum computed using a fast forward-model based on weight functions, and a spectrum calculated using the conventional forward model calculated using a Monte Carlo approach. (*b*) The spectrum calculated using the weight function approach minus the spectrum calculated using the conventional forward model.

6. Weight functions used in a forward model

Weight functions can be used to calculate a spectrum given a fast-ion distribution function, $f(E, p, \mathbf{r})$, using equation (3). This is done by evaluating equation (3) for every neutron energy interval of relevance. Both the fast-ion distribution function and the weight function have a spatial dependence as the ion temperatures and densities can vary throughout the acceptance cone of the neutron detector. Figure 8(*a*) shows neutron energy spectra calculated with a conventional forward model and using weight functions. Figure 8(*b*) shows the difference between the two spectra. The two methods produce spectra that are almost identical. The spectrum computed using weight functions is calculated by splitting the entire TOFOR viewing cone up in 10 volumes. In each volume, the ion temperatures and densities are assumed constant and a fast-ion distribution function is simulated for each. The conventional forward model splits up the volume in the sightline of TOFOR in volumes of 1 cm^3. This gives a total of 128 000 volumes, each weighted by the appropriate solid angle to the detector. The weight function method is significantly faster than the traditional forward model since the spectra can be calculated by matrix multiplication. This is advantageous if synthetic spectra for many different fast-ion distribution functions are to be calculated, or if a fast preliminary analysis is to be done right after a discharge. Furthermore, the weight function approach provides information on the measurable region in velocity space as explained in section 5.

7. Discussion

Recent studies at ASDEX Upgrade have investigated the potential of combining measurements taken simultaneously using several fast-ion D_α or CTS views, and even combining measurements from the two different types of diagnostics [50, 51]. This is made possible by the use of weight functions in the form of equation (2) in tomographic inversion algorithms to directly measure the fast-ion distribution function. NES weight functions as we formulated here allow us to combine NES measurements with CTS and FIDA measurements to measure the fast-ion distribution function. However, so far only localized measurements in small measurement volumes such as those for CTS or FIDA can be combined whereas the measurement volume of NES is a cone oriented along the line-of-sight. The larger measurement volume makes a combination cumbersome but not impossible. Assuming that most detectable neutrons have been produced near the plasma centre and assuming that the contribution from reactions involving a fast and a thermal ion dominates, NES measurements could be combined with CTS or FIDA measurements from central measurement volumes at ASDEX Upgrade. No further development of the NES weight functions are needed under these assumptions. Otherwise, the inference of the fast-ion distribution function must account for the spatial dependencies.

The examples shown in this paper have been calculated using values of the $\text{d(d,n)}^3\text{He}$ reaction. However, the derivation in section 2 is also valid, under the assumptions given, for neutrons from the $\text{d(t,n)}^4\text{He}$ reaction, or any other reaction, as long as the appropriate values of m_f, m_{He} and Q are used.

8. Conclusions

We have calculated velocity-space weight functions for neutron spectrometers and neutron yield counters both analytically and numerically, considering the often dominant contribution from reactions involving a fast and a thermal ion. These show the velocity-space sensitivity of NES measurements in given energy ranges of detected neutrons. The accessible region in $(v_\parallel, v_\perp)$-space is bounded by circles or circular arcs in the limit where the velocities of the thermal ions are zero. The closer a fast ion is to the edge of the circle, the more likely it is to generate a detectable neutron in the given energy range. The larger the energy of the detected neutron, the larger the observation region becomes for a given observation angle. Finite temperatures of the thermal ions blur the weight functions. The weight functions can be used to investigate the region in velocity space accessible by a given part of a neutron spectrum. Given a fast-ion distribution function, the weight functions can be used to calculate the part of the distribution function that generates most neutrons in the given energy range. Furthermore, they can be used in a forward model based on matrix multiplication that is significantly faster than traditional forward models based on Monte-Carlo sampling.

Acknowledgments

This project has received funding from the Euratom research and training programme 2014–2018 and from the European Unions Horizon 2020 research and innovation programme under grant agreement number 633053. This work was supported by EURATOM and carried out within the framework of the European Fusion Development Agreement. The views and opinions expressed herein do not necessarily reflect those of the European Commission.

References

[1] Heidbrink W.W. and Sadler G.J. 1994 The behaviour of fast ions in tokamak experiments *Nucl. Fusion* **34** 535–615

[2] Pinches S.D. *et al* and JET-EFDA Contributors 2004 The role of energetic particles in fusion plasmas *Plasma Phys. Control. Fusion* **46** B187–200

[3] Gorelenkov N.N., Pinches S.D. and Toi K. 2014 Energetic particle physics in fusion research in preparation for burning plasma experiments *Nucl. Fusion* **54** 125001

[4] Gatu Johnson M. *et al* 2008 The 2.5-MeV neutron time-of-flight spectrometer TOFOR for experiments at JET *Nucl. Instrum. Methods Phys. Res.* A **591** 417–30

[5] Gatu Johnson M. *et al* 2010 Neutron emission from beryllium reactions in JET deuterium plasmas with 3 He minority *Nucl. Fusion* **50** 045005

[6] Gatu Johnson M. *et al* 2010 Modelling and TOFOR measurements of scattered neutrons at JET *Plasma Phys. Control. Fusion* **52** 085002

[7] Hellesen C. *et al* 2010 Neutron emission generated by fast deuterons accelerated with ion cyclotron heating at JET *Nucl. Fusion* **50** 022001

[8] Hellesen C. *et al* 2010 Measurements of fast ions and their interactions with MHD activity using neutron emission spectroscopy *Nucl. Fusion* **50** 084006

[9] Hellesen C. *et al* 2010 Neutron spectroscopy measurements and modeling of neutral beam heating fast ion dynamics *Plasma Phys. Control. Fusion* **52** 085013

[10] Hellesen C. *et al* 2013 Fast-ion distributions from third harmonic ICRF heating studied with neutron emission spectroscopy *Nucl. Fusion* **53** 113009

[11] Eriksson J., Hellesen C., Andersson Sundén E., Cecconello M., Conroy S., Ericsson G., Gatu Johnson M., Pinches S.D., Sharapov S.E. and Weiszflog M. 2013 Finite Larmor radii effects in fast ion measurements with neutron emission spectrometry *Plasma Phys. Control. Fusion* **55** 015008

[12] Zhang X. *et al* 2014 Diagnosing NB plasmas on the EAST tokamak with new time-of-flight neutron spectrometer *Nucl. Fusion* **54** 104008

[13] Tomita H., Iwai H., Iguchi T., Isobe M., Kawarabayashi J. and Konno C. 2010 Development of neutron spectrometer toward deuterium plasma diagnostics in LHD *Rev. Sci. Instrum.* **81** 10D309

[14] Yuan X. *et al* 2013 Neutron energy spectrum measurements with a compact liquid scintillation detector on EAST *J. Instrum.* **8** P07016

[15] Giacomelli L., Zimbal A., Tittelmeier K., Schuhmacher H., Tardini G. and Neu R. 2011 The compact neutron spectrometer at ASDEX Upgrade *Rev. Sci. Instrum.* **82** 123504

[16] Belli F. *et al* 2012 Conceptual design, development and preliminary tests of a compact neutron spectrometer for the JET experiment *IEEE Trans. Nucl. Sci.* **59** 2512–9

[17] Kaschuck Yu.A., Esposito B., Trykov L.A. and Semenov V.P. 2002 Fast neutron spectrometry with organic scintillators applied to magnetic fusion experiments *Nucl. Instrum. Methods Phys. Res.* A **476** 511–5

[18] Cecconello M. *et al* 2014 The 2.5 MeV neutron flux monitor for MAST *Nucl. Instrum. Methods Phys. Res.* A **753** 72–83

[19] Heidbrink W.W., Taylor P.L. and Phillips J.A. 1997 Measurements of the neutron source strength at DIII-D *Rev. Sci. Instrum.* **68** 536

[20] Fiore C.L. and Boivin R.L. 1995 Performance of the neutron diagnostic system for Alcator C-Mod *Rev. Sci. Instrum.* **66** 945

[21] Guoqiang Z. and Liqun H. 2011 Measurement of neutron flux at the initial phase of discharge in EAST *Plasma Sci. Technol.* **13** 162–6

[22] Isobe M. *et al* 2010 Fusion product diagnostics planned for Large Helical Device deuterium experiment *Rev. Sci. Instrum.* **81** 10D310

[23] Hayashi T., Nishitani T. and Ishikawa M. 2004 First measurement of time-resolved neutron yield on JT-60U using a microfission chamber *Rev. Sci. Instrum.* **75** 3575–7

[24] Syme D.B., Popovichev S., Conroy S., Lengar I. and Snoj L. 2012 Fusion yield measurements on JET and their calibration *Nucl. Eng. Des.* **246** 185–90

[25] Schneider W., Wiegel B., Grünauer F., Burhenn R., Koch S., Schuhmacher H. and Zimbal A. 2012 Neutron diagnostics at the Wendelstein 7-X stellarator *J. Instrum.* **7** C03025

[26] Donné A.J.H. *et al* 2007 Progress in the ITER physics basis. Chapter 7: diagnostics *Nucl. Fusion* **47** S337–84

[27] Heidbrink W.W. 1984 Fusion reaction spectra produced by anisotropic 3He ions during ICRF *Nucl. Fusion* **24** 636–9

[28] Tardocchi M., Conroy S., Ericsson G., Gorini G., Henriksson H. and Källne J. 2002 Neutron emission spectroscopy of radio frequency heated (D)T plasmas *Nucl. Fusion* **42** 1273–88

[29] Heidbrink W.W., Luo Y., Burrell K.H., Harvey R.W., Pinsker R.I. and Ruskov E. 2007 Measurements of fast-ion acceleration at cyclotron harmonics using Balmer-alpha spectroscopy *Plasma Phys. Control. Fusion* **49** 1457–75

[30] Heidbrink W.W. 2010 Fast-ion Dα measurements of the fast-ion distribution (invited) *Rev. Sci. Instrum.* **81** 10D727

[31] Salewski M. *et al* 2014 On velocity-space sensitivity of fast-ion D-alpha spectroscopy *Plasma Phys. Control. Fusion* **56** 105005

[32] Salewski M. *et al* 2011 On velocity space interrogation regions of fast-ion collective Thomson scattering at ITER *Nucl. Fusion* **51** 083014

[33] Heidbrink W.W., Bell R.E., Luo Y. and Solomon W. 2006 Fast-ion D-alpha diagnostic for NSTX *Rev. Sci. Instrum.* **77** 10F120

[34] Geiger B. *et al* 2014 Fast-ion transport in the presence of magnetic reconnection induced by sawtooth oscillations in ASDEX Upgrade *Nucl. Fusion* **54** 022005

[35] Luo Y., Heidbrink W.W., Burrell K.H., Kaplan D.H. and Gohil P. 2007 Measurement of the D alpha spectrum produced by fast ions in DIII-D *Rev. Sci. Instrum.* **78** 033505

[36] Podestà M., Heidbrink W.W., Bell R.E. and Feder R. 2008 The NSTX fast-ion D-alpha diagnostic *Rev. Sci. Instrum.* **79** 10E521

[37] Van Zeeland M.A., Heidbrink W.W. and Yu J.H. 2009 Fast ion D α imaging in the DIII-D tokamak *Plasma Phys. Control. Fusion* **51** 055001

[38] Van Zeeland M.A. *et al* 2010 Imaging key aspects of fast ion physics in the DIII-D tokamak *Nucl. Fusion* **50** 084002

[39] Bortolon A., Heidbrink W.W. and Podestà M. 2010 A tangentially viewing fast ion D-alpha diagnostic for NSTX *Rev. Sci. Instrum.* **81** 10D728

[40] Heidbrink W.W., McKee G.R., Smith D.R. and Bortolon A. 2011 Beam-emission spectroscopy diagnostics also measure edge fast-ion light *Plasma Phys. Control. Fusion* **53** 085007

[41] Michael C.A. *et al* 2013 Dual view FIDA measurements on MAST *Plasma Phys. Control. Fusion* **55** 095007

[42] Podesta M. *et al* 2009 Experimental studies on fast-ion transport by AlfveÌ'n wave avalanches on the National Spherical Torus Experiment *Phys. Plasmas* **16** 056104

[43] García-Muñoz M. *et al* 2011 Fast-ion transport induced by Alfvén eigenmodes in the ASDEX Upgrade tokamak *Nucl. Fusion* **51** 103013

[44] Geiger B., García-Muñoz M., Heidbrink W.W., McDermott R.M., Tardini G., Dux R., Fischer R. and Igochine V. 2011 Fast-ion D-alpha measurements at ASDEX Upgrade *Plasma Phys. Control. Fusion* **53** 065010

[45] Geiger B., Dux R., McDermott R.M., Potzel S., Reich M., Ryter F., Weiland M., Wünderlich D. and García-Muñoz M. 2013 Multi-view fast-ion D-alpha spectroscopy diagnostic at ASDEX Upgrade *Rev. Sci. Instrum.* **84** 113502

[46] Muscatello C.M., Heidbrink W.W., Kolesnichenko Ya.I., Lutsenko V.V., Van Zeeland M.A. and Yakovenko Yu.V. 2012 Velocity-space studies of fast-ion transport at a sawtooth crash in neutral-beam heated plasmas *Plasma Phys. Control. Fusion* **54** 025006

[47] Pace D.C. *et al* 2013 Energetic ion transport by microturbulence is insignificant in tokamaks *Phys. Plasmas* **20** 056108

[48] Heidbrink W.W., Luo Y., Muscatello C.M., Zhu Y. and Burrell K.H. 2008 A new fast-ion Dα diagnostic for DIII-D *Rev. Sci. Instrum.* **79** 10E520

[49] Geiger B. *et al* 2015 Quantification of the impact of large and small-scale instabilities on the fast-ion confinement in ASDEX Upgrade *Plasma Phys. Control. Fusion* **57** 014018

[50] Salewski M. *et al* 2012 Tomography of fast-ion velocity-space distributions from synthetic CTS and FIDA measurements *Nucl. Fusion* **52** 103008

[51] Salewski M. *et al* 2013 Combination of fast-ion diagnostics in velocity-space tomographies *Nucl. Fusion* **53** 063019

[52] Salewski M. *et al* 2014 Measurement of a 2D fast-ion velocity distribution function by tomographic inversion of fast-ion D-alpha spectra *Nucl. Fusion* **54** 023005

[53] Salewski M. *et al* 2015 Doppler tomography in fusion plasmas and astrophysics *Plasma Phys. Control. Fusion* **57** 014021

[54] Bosch H.-S. and Hale G.M. 1992 Improved formulas for fusion cross-sections and thermal reactivities *Nucl. Fusion* **32** 611–31

[55] Brysk H. 1973 Fusion neutron energies and spectra *Plasma Phys.* **15** 611–17

[56] Källne J., Ballabio L., Frenje J., Conroy S., Ericsson G., Tardocchi M., Traneus E. and Gorini G. 2000 Observation of the alpha particle ‘Knock-On’ neutron emission from magnetically confined DT fusion plasmas *Phys. Rev. Lett.* **85** 1246–9

[57] Pankin A., McCune D., Andre R., Bateman G. and Kritz A. 2004 The tokamak Monte Carlo fast ion module NUBEAM in the National Transport Code Collaboration library *Comput. Phys. Commun.* **159** 157–84

[58] Jacobsen A.S., Salewski M., Eriksson J., Ericsson G., Hjalmarsson A., Korsholm S.B., Leipold F., Nielsen S.K., Rasmussen J. and Stejner M. 2014 Velocity-space sensitivity of the time-of-flight neutron spectrometer at JETa) *Rev. Sci. Instrum.* **85** 11E103

Paper II

REVIEW OF SCIENTIFIC INSTRUMENTS **85**, 11E103 (2014)

Velocity-space sensitivity of the time-of-flight neutron spectrometer at JET[a)]

A. S. Jacobsen,[1,b)] M. Salewski,[1] J. Eriksson,[2] G. Ericsson,[2] A. Hjalmarsson,[2]
S. B. Korsholm,[1] F. Leipold,[1] S. K. Nielsen,[1] J. Rasmussen,[1] M. Stejner,[1]
and JET-EFDA Contributors[c)]
JET-EFDA, Culham Science Centre, Abingdon OX14 3 DB, United Kingdom
[1]*Association Euratom - DTU, Technical University of Denmark, Department of Physics, Kgs. Lyngby, Denmark*
[2]*Association Euratom - VR, Uppsala University, Department of Physics and Astronomy, Uppsala, Sweden*

(Presented 3 June 2014; received 1 June 2014; accepted 14 June 2014; published online 8 July 2014)

The velocity-space sensitivities of fast-ion diagnostics are often described by so-called weight functions. Recently, we formulated weight functions showing the velocity-space sensitivity of the often dominant beam-target part of neutron energy spectra. These weight functions for neutron emission spectrometry (NES) are independent of the particular NES diagnostic. Here we apply these NES weight functions to the time-of-flight spectrometer TOFOR at JET. By taking the instrumental response function of TOFOR into account, we calculate time-of-flight NES weight functions that enable us to directly determine the velocity-space sensitivity of a given part of a measured time-of-flight spectrum from TOFOR. [http://dx.doi.org/10.1063/1.4885477]

I. INTRODUCTION

The detection and analysis of fast ions in fusion devices are important since fusion-born alpha-particles are foreseen to contribute a large part of the heating in an eventual fusion power plant. Fast ions can be diagnosed using a variety of different diagnostics. One such diagnostic is neutron emission spectrometry (NES) in which the energy spectrum of neutrons produced in fusion reactions is measured. The energies of these neutrons depend on the energy released in the fusion reaction and on the energies of the reacting ions. Thus, by analysing the neutron energy spectrum, information on velocities of fast ions in the plasma can be gained. We recently derived weight functions describing the velocity-space sensitivities of the often dominant beam-target part of neutron energy spectra. In particular, they show the observable regions in velocity space and, for a given fast-ion velocity distribution function, the regions where most neutrons are generated. Here we apply these previously derived general expressions for neutron energy spectra to the time-of-flight spectrometer TOFOR at JET by taking the instrumental response function of TOFOR into account.

In Sec. II, the TOFOR instrument is described. The NES weight functions are introduced in Sec. III, and in Sec. IV we calculate time-of-flight NES weight functions for TOFOR and show examples of their applications. The results are summarized in Sec. V.

II. NEUTRON TIME-OF-FLIGHT SPECTROMETER TOFOR

TOFOR[1] is a time-of-flight spectrometer. It measures the time it takes for neutrons to travel between two sets of plastic scintillator detectors. The time-of-flight depends on the incident neutron energy; 2.45 MeV neutrons from the D-D reaction result in flight times centered around 65 ns. TOFOR is located in the roof laboratory 19 m above JET and has a vertical view of the plasma so that the line-of-sight of TOFOR is perpendicular to the magnetic field. The viewing cone of TOFOR covers a large portion of the plasma cross-section, including the plasma center.

III. NES WEIGHT FUNCTIONS

Weight functions determine the velocity-space sensitivity of a given diagnostic. Weight functions have previously been calculated for fast-ion D_α spectroscopy (FIDA)[2,3] and collective Thomson scattering (CTS).[4] Furthermore, weight functions were recently developed for the beam-target part of neutron energy spectra measured using NES.[5] NES weight functions relate a measurement in a given neutron energy range to the fast-ion distribution function:

$$s(E_{n,1}, E_{n,2}, \phi) = \iiint w(E_{n,1}, E_{n,2}, \phi, E, p, \mathbf{r}) f(E, p, \mathbf{r}) \mathrm{d}E\, \mathrm{d}p\, \mathrm{d}\mathbf{r}, \quad (1)$$

where $s(E_{n,1}, E_{n,2}, \phi)$ is the rate of neutrons with energies between $E_{n,1}$ and $E_{n,2}$ measured with an instrument with a line-of-sight at a projection angle, ϕ, to the magnetic field. $w(E_{n,1}, E_{n,2}, \phi, E, p, \mathbf{r})$ is the weight function calculated for specific neutron energies and projection angle ϕ as a function of energy, E, and pitch, $p = \frac{v_\parallel}{v}$, of the fast ions. The weight function has a spatial dependence since it depends on the bulk ion temperature and density, which can vary

---

[a)] Contributed paper, published as part of the Proceedings of the 20th Topical Conference on High-Temperature Plasma Diagnostics, Atlanta, Georgia, USA, June 2014.

[b)] Author to whom correspondence should be addressed. Electronic mail: Ajsen@fysik.dtu.dk

[c)] See the appendix of F. Romanelli *et al.*, Proceedings of the 24th IAEA Fusion Energy Conference 2012, San Diego, USA.

0034-6748/2014/85(11)/11E103/3/$30.00

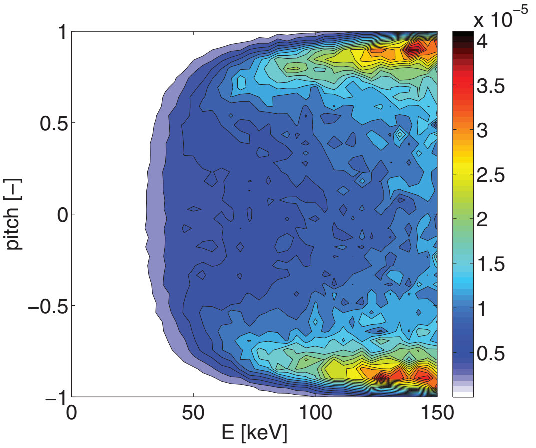

FIG. 1. NES weight function in units of [neutrons per second per fast ion] for a neutron energy of 2.6 MeV ± 0.015 MeV, calculated using a Monte Carlo approach.

significantly along the line-of-sight. $f(E, p, \mathbf{r})$ is the fast-ion distribution function. NES weight functions are general and relate the fast-ion distribution function to a given neutron energy spectrum, irrespective of the specific instrument or technology used to acquire it. An example of a NES weight function is shown in Figure 1 for a neutron energy of 2.6 MeV ± 0.015 MeV. The coloured region of the figure illustrates the part of (E, p)-space accessible to the specific neutron energy range, and the white region are inaccessible for this neutron energy range. A thermal ion temperature of 2.3 keV has been used in these calculations.

IV. TIME-OF-FLIGHT NES WEIGHT FUNCTIONS

TOFOR measures time-of-flight spectra from which the neutron energy spectra must be inferred. It is therefore useful to derive weight functions directly relating the time-of-flight spectra to velocity-space. This transformation requires knowledge of the particular instrumental response function. The instrumental response function of TOFOR describes the time-of-flight signal produced for an incoming beam of neutrons. It is dominated by the flight-time of neutrons that scatter only once in both sets of detectors. However, multiple-scattering events as well as the finite sizes of the detectors broaden the spectra. Thus, a mono-energetic flux of neutrons will produce a distribution of flight times. The response of TOFOR to incident neutrons of various energies has been modeled in detail with Monte Carlo calculations, taking the full 3D geometry of the instrument into account.[1] The resulting response function is shown in Figure 2. It transforms energy spectra to time-of-flight spectra so as to compare these with measurements by TOFOR.

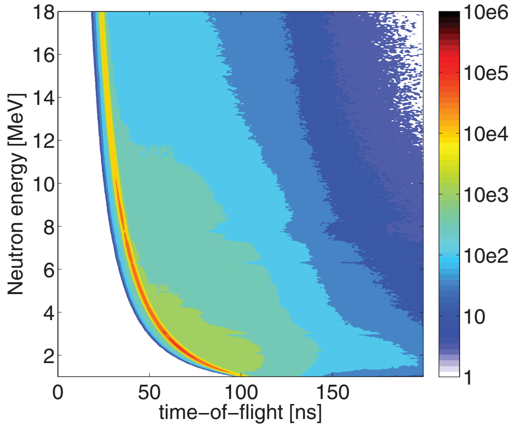

FIG. 2. TOFOR response function.

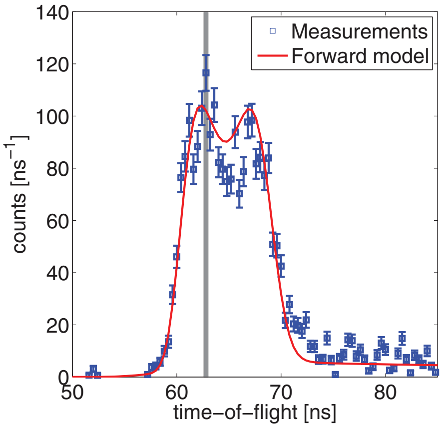

FIG. 3. Measured time-of-flight spectrum from JET discharge #68138 compared with a calculated spectrum from a forward model. We show the velocity-space sensitivity of the shaded region in Figure 4.

Figure 3 shows a typical time-of-flight spectrum measured during JET discharge #68138 as well as a spectrum calculated using a forward model. A double-hump resulting from the gyromotion of the fast ions appears in the spectrum at a flight-time of about 65 ns corresponding to a neutron energy of 2.45 MeV. The synthetic spectrum is calculated using fast-ion velocity distribution functions in the grid cells in the viewing cone simulated using TRANSP/NUBEAM.[6] The synthetic spectrum agrees reasonably well with the measured spectrum.

Figure 4 shows an example of a time-of-flight NES weight function for the time-of-flight range illustrated by the

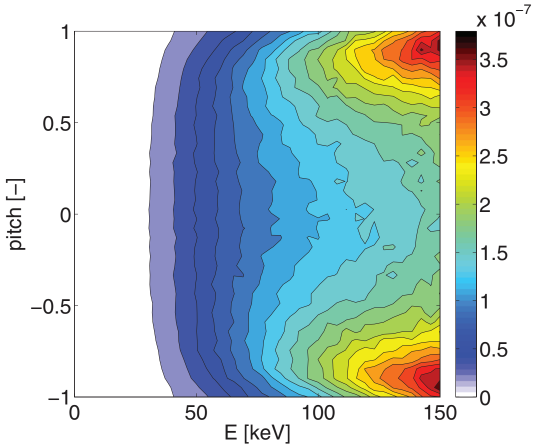

FIG. 4. Time-of-flight weight function in units of [neutrons per second per fast ion] for a flight-time of 62.8 ± 0.2 ns. This flight-time range is illustrated in Figure 3.

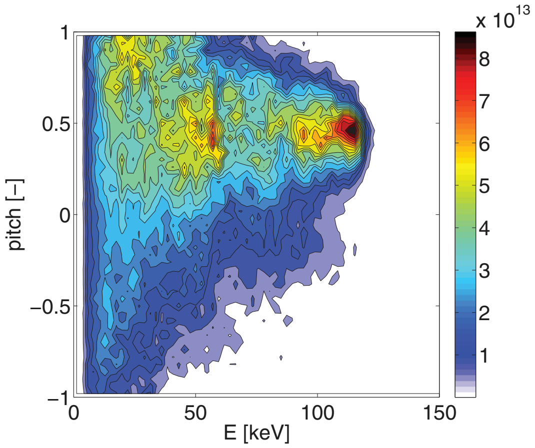

FIG. 5. Central fast-ion distribution function in units of [fast ions per keV] calculated using TRANSP/NUBEAM.

shaded region in Figure 3. Time-of-flight NES weight functions are calculated from general NES weight functions and the TOFOR response functions according to

$$w_{\mathrm{tof},ijl} = R_{n,kl} w_{\mathrm{E_n},ijk}, \tag{2}$$

where R_n is the response function, i, j, k, and l are indices of fast ion energy and pitch, neutron energy, and time-of-flight, respectively. Repeated indices imply summation.

Figure 5 shows a central fast-ion distribution function from JET discharge #68138 simulated using TRANSP/NUBEAM. TOFOR measures neutrons originating from the entire viewing cone. However, the majority will often come from the plasma center where both the thermal and fast ion densities are largest.

Figure 6 shows the product of the weight function in Figure 4 and the central fast-ion distribution function in Figure 5. This shows the part of the given central distribution function producing most of the detected neutrons. Since the measured spectrum agrees well with the synthetic spectrum (Figure 3), the simulated fast-ion velocity distribution function should be a good model for the fast ion population in the plasma. Hence the predicted regions of maximum beam-target neutron production shown in Figure 6 should be accurate. The main part of the signal in this flight-time range is caused by the ions with energies around 100 keV and pitches of about 0.5.

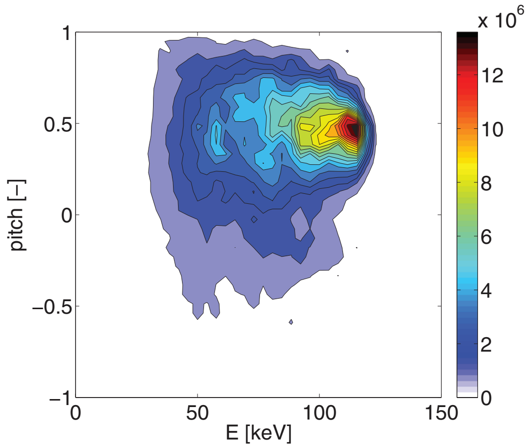

FIG. 6. Product of time-of-flight NES weight function from Figure 4 and the fast-ion distribution function from Figure 5.

V. CONCLUSIONS

We have developed time-of-flight NES weight functions that illustrate the regions in velocity or energy-pitch space accessible to a given part of a measured time-of-flight spectrum from TOFOR taking the response function into account. This allows us to directly determine the velocity-space sensitivity of given flight-time ranges in a TOFOR spectrum. This has several potential applications: as shown in Figure 4, we can directly determine the velocity-space sensitivity and observable regions of a given part of a measured spectrum. Given a fast-ion distribution function, we can determine which part of the distribution function contributes most to the spectrum as shown in Figure 6. Furthermore, they can be used in an efficient forward model by solving equation (1) for a given distribution function. Finally, weight functions on the form presented here can potentially enable us to use the NES diagnostic in velocity-space tomography to infer the fast-ion distribution function.[7,8]

ACKNOWLEDGMENTS

This work, supported by the European Communities under the contract of Association between Euratom and DTU, was supported by EURATOM and carried out within the framework of the European Fusion Development Agreement. The views and opinions expressed herein do not necessarily reflect those of the European Commission.

[1] M. Gatu Johnson *et al.*, Nucl. Instrum. Methods Phys. Res., Sect. A **591**, 417 (2008).
[2] W. W. Heidbrink, Y. Luo, K. H. Burrell, R. W. Harvey, R. I. Pinsker, and E. Ruskov, Plasma Phys. Controlled Fusion **49**, 1457 (2007).
[3] M. Salewski *et al.*, “On velocity-space sensitivity of fast-ion D-alpha spectroscopy” (unpublished).
[4] M. Salewski *et al.*, Nucl. Fusion **51**, 083014 (2011).
[5] A. S. Jacobsen, M. Salewski, J. Eriksson, G. Ericsson, S. B. Korsholm, F. Leipold, S. K. Nielsen, J. Rasmussen, and M. Stejner, “Velocity-space sensitivity of neutron spectrometry measurements” (unpublished).
[6] A. Pankin, D. McCune, R. Andre, G. Bateman, and A. Kritz, Comput. Phys. Commun. **159**, 157 (2004).
[7] M. Salewski *et al.*, Nucl. Fusion **53**, 063019 (2013).
[8] M. Salewski *et al.*, Nucl. Fusion **54**, 023005 (2014).

Paper III

Inversion methods for fast-ion velocity-space tomography in fusion plasmas

A. S. Jacobsen[1], L. Stagner[2], M. Salewski[1], B. Geiger[3], W. W. Heidbrink[2], S. B. Korsholm[1], F. Leipold[1], S. K. Nielsen[1], J. Rasmussen[1], M. Stejner[1], H. Thomsen[4], M. Weiland[3], and the ASDEX Upgrade team[3]

[1] Technical University of Denmark, Department of Physics, DK-2800 Kgs. Lyngby, Denmark

[2] University of California Irvine, Irvine, CA, USA

[3] Max-Planck-Institute for Plasma Physics, Boltzmannstr. 2, 85748 Garching, Germany

[4] Max-Planck-Institute for Plasma Physics, Wendelsteinstrasse 1, 17491 Greifswald, Germany

E-mail: `ajsen@fysik.dtu.dk`

E-mail: `lstagner@uci.edu`

Abstract. Velocity-space tomography has been used to infer 2D fast-ion velocity distribution functions. Here we compare the performance of five different tomographic inversion methods: Truncated singular value decomposition, maximum entropy, minimum Fisher information and zeroth- and first-order Tikhonov regularization. The inversion methods are applied to fast-ion D_α measurements taken just before and just after a sawtooth crash in the ASDEX Upgrade tokamak as well as to synthetic measurements from different test distributions. We find that the methods regularizing by penalizing steep gradients perform best. We assess the uncertainty of the calculated inversions taking into account photon noise, uncertainties in the forward model as well as uncertainties introduced by the regularization which allows us to distinguish regions of high and low confidence in the tomographies. In high confidence regions, all methods agree that ions with pitch values close to zero, as well as ions with large pitch values, are ejected from the plasma center by the sawtooth crash, and that this ejection depletes the ion population with large pitch values more strongly.

1. Introduction

Traditional fast-ion diagnostics and analysis procedures provide only incomplete information about the 2D fast-ion velocity distribution function. Usually, only a 1D function of the velocity distribution function can be measured. Here we use fast-ion D_α (FIDA) spectroscopy measurements that measure the intensity of Doppler-shifted D_α light as function of wavelength [1, 2]. Using velocity-space tomography it is possible to combine data from several such measurements to infer the 2D fast-ion velocity distribution function [3–10]. With this approach it should even be possible to combine measurements from different diagnostics which is beneficial as they are sensitive to different regions of velocity-space [6]. This velocity-space sensitivity is quantified by velocity-space sensitivity functions, also called weight functions, which have been developed for FIDA [11,12], collective Thomson scattering (CTS) [4], fast-ion loss detectors (FILD) [13], neutron emission spectrometry (NES) [14,15] and gamma-ray spectroscopy (GRS) [16]. The weight functions, w, relate a measurement, s, to the fast-ion velocity distribution function, f:

$$s = \int\int w f \,\mathrm{d}E\,\mathrm{d}p\,, \tag{1}$$

where E is the fast-ion energy and p is the pitch defined as $p = \frac{v_\parallel}{v}$. Here $v_\parallel$ is the ion velocity parallel to the magnetic field and v is the ion speed. p is defined positive in the co-current direction. Examples of FIDA weight functions are shown in figure 1. The shapes of the weight functions are determined by the angle, ϕ, between the line-of-sight of the diagnostic and the magnetic field in the measurement volume, as well as the wavelength range in which the signal is detected.

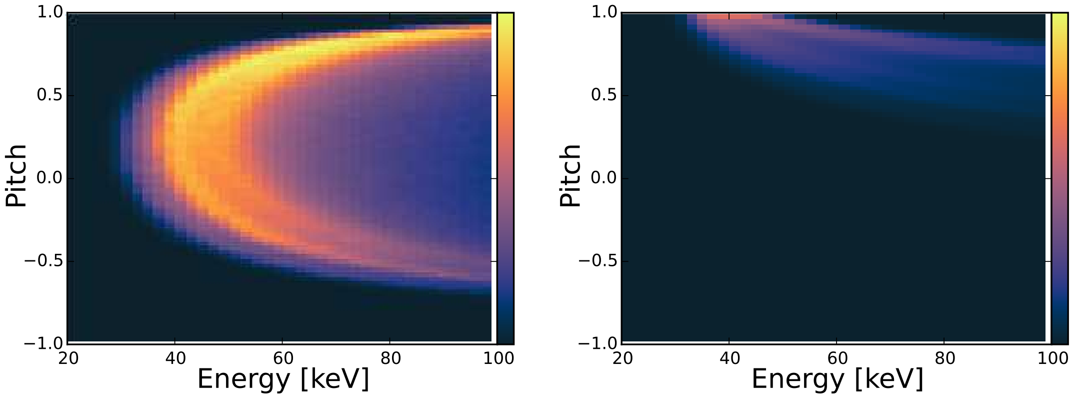

(a) $\phi = 80°$ (b) $\phi = 10°$

Figure 1. Examples of FIDA weight functions calculated for ASDEX Upgrade discharge #31557 for two different ϕ-angles.

By discretizing equation (1) a linear system of equations is obtained:

$$S = WF\,. \tag{2}$$

S and W are normalized by the measurement uncertainties as described in [6]. S and F are vectors of length m and n, respectively, and W is an $m \times n$ matrix dubbed the transfer matrix. Calculating F from equation (2) is a mathematically ill-posed inverse problem. An ill-posed problem is one for which a unique solution might not exist. Furthermore, any solution might be extremely sensitive to small changes in the data. The sensitivity with respect to the data is suppressed by regularizing the problem. Many different inversion methods have been developed and applied in many scientific fields. Here we compare five inversion methods to measure fast-ion velocity distribution functions by tomographic inversion: truncated singular value decomposition, maximum entropy, zeroth- and first-order Tikhonov regularization and minimum Fisher information. These methods have previously been compared for position-space tomography in fusion plasmas [17, 18]. Here we test these methods for velocity-space tomography. In our comparison we use a transfer matrix describing FIDA measurements taken simultaneously in five views at ASDEX Upgrade in discharge #31557. This large number of FIDA views makes ASDEX Upgrade particularly suitable for tomographic inversions of fast-ion velocity distribution functions. This diagnostic set-up (i.e. this transfer matrix) is used, firstly, with synthetic measurements to calculate inversions for known velocity distribution functions and, secondly, with real five-view FIDA measurements taken just before and just after a sawtooth crash. The synthetic measurements enable us to quantify the performance of the different methods for assumed measurement uncertainties since the true solution is known. The real measurements allow us to investigate the redistribution of fast ions due to a sawtooth crash resolved in 2D velocity space for ion energies above 20 keV.

The paper is organised as follows. The FIDA diagnostic set-up is described in section 2. Section 3 explains the different inversion methods. In section 4 we quantify the performance of the inversion methods by inverting synthetic data based on known test functions. In section 5 the methods are used to investigate the effect of a sawtooth crash on the central fast-ion population. The results are discussed in section 6 and conclusions are summarized in section 7.

2. ASDEX Upgrade FIDA system

A FIDA diagnostic set-up measures Doppler-shifted deuterium Balmer-alpha light from the plasma. It is extensively used to diagnose fast ions at ASDEX Upgrade [19, 20], DIII-D [21, 22], NSTX [23], MAST [24, 25] and LHD [26]. The newly upgraded set-up at ASDEX Upgrade now consists of five different views, each with several lines of sight measuring at different radial locations. We use one line of sight from each view, each intersecting the beam path of neutral beam injector (NBI) Q3 in the plasma centre as shown in figure 2. The grey line is the Q3 NBI beam and each coloured line is a single FIDA line-of-sight. These originate from different positions in the plasma wall and intersect the NBI beam at approximately the same position. The measurement volume is placed slightly on the low-field side. Each view has a different angle between its line of sight and the magnetic field. Thereby, they probe different regions in velocity space as described by their weight functions [12]. In the plasma centre, the respective angles are 14°, 73°, 103°, 133° and 153°. A description of the upgraded FIDA system is found in [10].

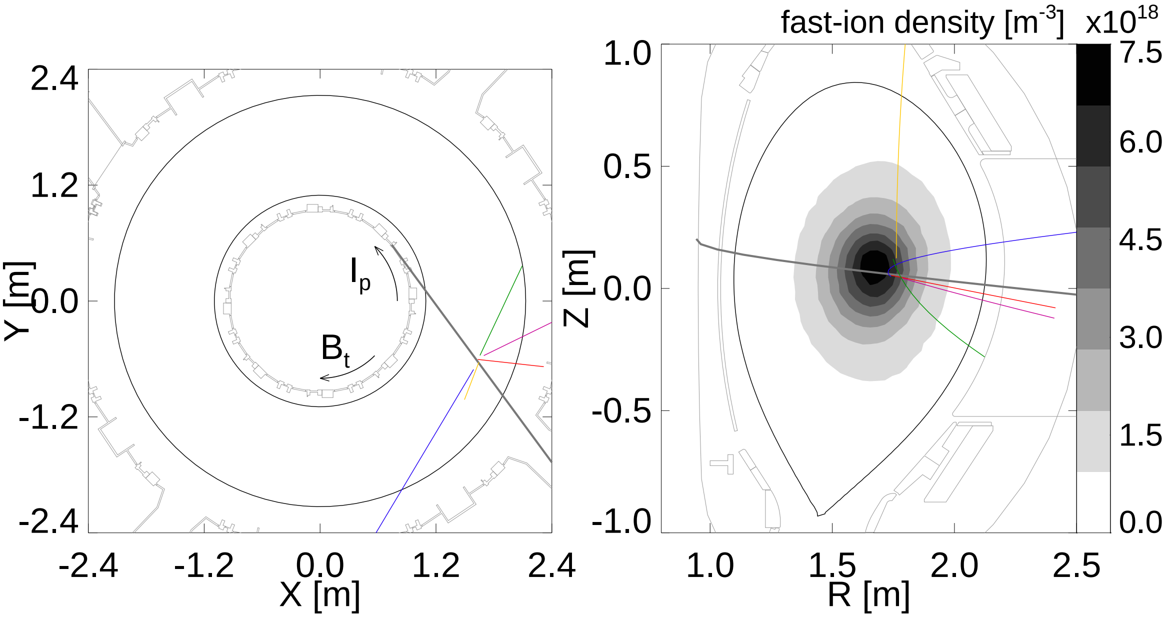

Figure 2. Sketch of the geometry of the FIDA diagnostic set-up. a) Top view of the ASDEX Upgrade tokamak showing the NBI beam in grey and the FIDA lines-of-sight in colours. Only the lines-of-sight used here are shown. b) Poloidal cross-section showing that the FIDA measurement volume used here is slightly on the low-field side of the ASDEX Upgrade tokamak.

3. Inversion methods

3.1. Singular value decomposition

Truncated singular value decomposition (SVD) has been used previously to calculate velocity-space tomographies in fusion plasmas [5–9]. The $m \times n$ transfer matrix, W, can as any matrix be written as the product of three matrices:

$$W = U \Sigma V^T \,, \tag{3}$$

where the columns of the $m \times m$ matrix U are the eigenvectors of the matrix WW^T and the columns of the $n \times n$ matrix V are the eigenvectors of the matrix $W^T W$ [27]. U as well as V are orthogonal matrices. Σ is a diagonal $m \times n$ rectangular matrix. The values in the diagonal are called the singular values. They are the square roots of the non-zero eigenvalues of both WW^T and $W^T W$ [28]. The values in the diagonal of Σ are ordered in a decreasing manner.

Given equation (1) the solution, F_{SVD}, is found as

$$F_{SVD} = W^+ S \,, \tag{4}$$

where W^+ is called the *pseudoinverse* of W [28]. W^+ can be calculated using the SVD factorization:

$$W^{+} = V\Sigma^{+}U^{T}\,, \tag{5}$$

where Σ^{+} is a rectangular diagonal matrix with the reciprocals of the diagonal elements of Σ on the diagonal. Equation (3) can be written as a sum

$$W = \sum_{j=1}^{r} u_j \sigma_j \left(v_j^T\right)\,, \tag{6}$$

where r is the number of non-zero singular values, u_j and v_j are the j'th columns of U and V, respectively, and σ_j is the j'th singular value. v_j^T indicates the transpose of the j'th column of V. F_{SVD} can likewise be expressed as a sum:

$$F_{SVD} = \sum_{j=1}^{r} \frac{\left(u_j^T S\right)}{\sigma_j} v_j\,. \tag{7}$$

Experimental data always contain some form of noise. Here we define

$$S = S_{exact} + e\,, \tag{8}$$

where S_{exact} is the idealized measurement without noise and e is the noise. Inserting equation (8) in equation (7) we get

$$F_{SVD} = \sum_{j=1}^{r} \frac{\left(u_j^T S_{exact}\right)}{\sigma_j} v_j + \sum_{j=1}^{r} \frac{\left(u_j^T e\right)}{\sigma_j} v_j = F_{exact} + \sum_{j=1}^{r} \frac{\left(u_j^T e\right)}{\sigma_j} v_j\,, \tag{9}$$

where F_{exact} is the exact solution we seek and the last sum describes the effect of the noise. For very small singular values, the SVD solution can be completely dominated by the noise. To reduce its influence, a possibility is to truncate the sum after k terms. However, this makes it impossible to reconstruct F_{exact} completely. This method is called truncated SVD. Truncated SVD introduces the problem of choosing the optimum truncation level, k. Here we use the L-curve method to choose k [29]. The L-curve method chooses k such that the solution both minimizes the residual norm and the norm of the regularizing term.

3.2. Tikhonov regularization

The inverse problem posed in equation (2) can be formulated as a least squares problem, i.e. find the solution F which minimizes the norm of the residual:

$$\text{minimize}\left\{||WF - S||^2\right\}\,. \tag{10}$$

Well-posed problems can be solved using the normal equations:

$$F = \left(W^T W\right)^{-1} W^T S\,. \tag{11}$$

However, for ill-posed problems a small change in S can have a significant impact on F. In Tikhonov regularization, the ill-posed least squares problem is replaced by a closely related well-posed least squares problem

$$\text{minimize}\left\{||WF - S||^2 + \alpha||LF||^2\right\}\,, \tag{12}$$

where L is a regularization matrix of size $n \times n$ and α is a non-negative number determining the weight of the regularization term. As for truncated SVD, we determine the value of α using the L-curve method [30]. The Tikhonov solution, F_α, becomes

$$F_\alpha = \left(W^T W + \alpha L^T L\right)^{-1} W^T S\,. \tag{13}$$

The choice of regularization matrix determines the nature of the regularization. Common choices of L penalize the magnitude of f or its derivative to different orders. Therefore, Tikhonov regularization is also sometimes called linear regularization. The simplest regularization matrix is

$$L = I\,, \tag{14}$$

where I is the $n \times n$ identity matrix so that $L^T L = I$ and equation (13) becomes

$$F_\alpha = \left(W^T W + \alpha I\right)^{-1} W^T S\,. \tag{15}$$

This penalizes large absolute values of f and is called 0'th order regularization.

1'st order regularization penalizes large gradients. In 2D velocity space $\left(v_\parallel, v_\perp\right)$, the penalty operator is

$$L^T L = \nabla_{v_\parallel}^T \nabla_{v_\parallel} + \nabla_{v_\perp}^T \nabla_{v_\perp}\,. \tag{16}$$

Here $\nabla_{v_\parallel}$ and $\nabla_{v_\perp}$ are matrix representations of finite difference operators. In (E, p)-coordinates, the velocity-space gradient is

$$\nabla F = \sqrt{2mE}\,(\nabla_E F)\,\hat{e}_E + \sqrt{\frac{m}{2E}}\sqrt{1-p^2}\,(\nabla_p F)\,\hat{e}_p\,. \tag{17}$$

The derivation of equation 17 is included in Appendix A. In (E, p)-coordinates the penalty operator becomes

$$L^T L = 2mE\,\nabla_E^T \nabla_E + \frac{m}{2E}\left(1-p^2\right)\,\nabla_p^T \nabla_p\,. \tag{18}$$

3.3. Minimum Fisher information regularization

The principle of minimum Fisher information has been used to compute inversions in soft X-ray tomography in tokamak plasmas [17]. In reference [17] the minimum Fisher information principle is effectively built in as a Tikhonov penalty function. It can therefore be seen as a variant or extension of the general Tikhonov regularization method. The minimum Fisher information method penalizes large gradients divided by the function values. The normalization with the distribution itself means that the smoothing effect is strongest where the distribution has low values.

The minimum Fisher information method is implemented here as an iterative algorithm [17]. First a solution $F^{(1)}$ is found using Tikhonov regularization with a first-order linear penalty function. In the subsequent iterations, the penalty function in $\left(v_\parallel, v_\perp\right)$-coordinates becomes

$$L^T L = \nabla_{v_\parallel}^T M^{(n)} \nabla_{v_\parallel} + \nabla_{v_\perp} M^{(n)} \nabla_{v_\perp}\,, \tag{19}$$

where

$$M_{i,j}^{(n)} = \frac{1}{F_i^{(n-1)}}\,\delta_{i,j} \qquad \text{if} \qquad F_i^{(n-1)} > 0 \tag{20}$$

$$M_{i,j}^{(n)} = M_{max}^{(n)}\,\delta_{i,j} \qquad \text{if} \qquad F_i^{(n-1)} \leq 0\,. \tag{21}$$

$M_{max}^{(n)}$ is the largest $M^{(n)}$ for $F_i > 0$. In (E, p)-coordinates the penalty function becomes

$$L^T L = 2mE\nabla_E^T M^{(n)} \nabla_E + \frac{m}{2E}\left(1 - p^2\right) \nabla_p^T M^{(n)} \nabla_p\,. \tag{22}$$

In each iteration, the corresponding Tikhonov solution with the appropriate minimum Fisher information penalty function is found. We find that the solution converges after only a few iterations.

3.4. Maximum entropy regularization

The last inversion method we have implemented is maximum entropy regularization. In the case of maximum entropy regularization it is assumed that the object that is to be reconstructed from data is positive $f(E, p) \geq 0$. The other inversion methods can produce unphysical negative results. When they do, we set those parts of the solution to zero. The specific formulation of maximum entropy regularization adopted here can be found in references [17,31]. Maximum entropy regularization can be formulated as a minimization problem of the form

$$\text{minimize}\left\{\frac{1}{2}||WF - S||^2 + \alpha H\right\}\,. \tag{23}$$

where α is a free parameter controlling the strength of our assumptions similar to the free parameter introduced in Tikhonov and minimum Fisher information regularization. We determine the optimal value of α using the L-curve method [30]. H is the Shannon information entropy given by

$$H = -\sum_{i=1}^{N} (F_i - m_i - F_i \ln(F_i/m_i))\,. \tag{24}$$

The entropy H is minimized when $F_i = m_i$. Thus m_i is called the default model as it is the value F_i will take when there is no information or data influencing it. While the default model is usually set to be constant in phase-space to prevent biasing of the solution, we may choose to set the default model to be given by a theoretical model. For this work, the default model is set to be constant. The solution of this minimization problem, called the maximum entropy solution, is found using a general non-linear optimization library [32–34].

4. Tomographies using synthetic measurements

In this section we calculate tomographies using synthetic data obtained using equation (1) and known distribution functions. Inversions of synthetic spectra calculated from known distribution functions enable us to compare the performance of the inversion methods by quantitative figures of merit since we know the true solution.

4.1. Test velocity-distribution functions

Three different velocity distributions will be investigated in this analysis. A Gaussian distribution, a bi-Maxwellian distribution and a simulated NBI-distribution from TRANSP/NUBEAM [35]. The three distributions are shown in figure 3. We choose these three distribution functions as they pose different challenges to the inversion methods. The Gaussian distribution is highly localized and requires good resolution properties of the method. A Gaussian distribution may further represent a source of fast particles typical for the peaks at the injection energies for neutral beam heating. The bi-Maxwellian is a wide function covering the entire pitch range. Here the challenge is to recreate the large-scale undulation. Lastly, we study a distribution function typical for neutral beam injection as simulated by TRANSP. This is an important test case as it should be very similar to the distribution functions in experiments with NBI heating. The challenge here is the structural complexity on both small and large scales. The NBI distribution used in this study is typical for a DIII-D discharge rather than for ASDEX Upgrade which does not have counter-injection beams.

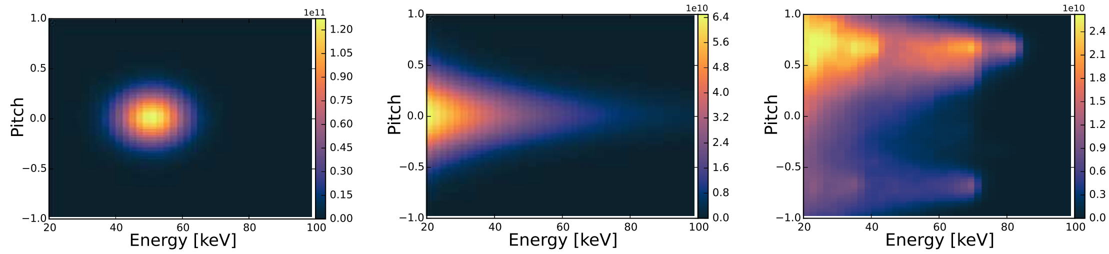

(a) Gaussian. (b) Bi-Maxwellian. (c) NBI.

Figure 3. Test velocity distributions functions as a function of energy and pitch of the ions. The functions are given in units of [ions/keV/cm^3]

4.2. Modelling of measurement noise

The photon noise of FIDA light scales approximately with the square root of the signal. However, in the absence of FIDA light the photon noise is dominated by bremsstrahlung setting a lower limit on the noise level. These two effects are modelled as

$$S_{noisy} = S_{exact} + k \left\langle \sqrt{S_{exact}} \right\rangle \mathcal{N}\left(0, \max\left(e_{min}, \sqrt{S_{exact}}\right)\right) , \tag{25}$$

where S_{noisy} is the noisy spectrum, S_{exact} is the exact noise-free spectrum, e_{min} is the bremsstrahlung level and k is a scaling constant that allows us to vary the noise level. $\mathcal{N}\left(0, \max\left(e_{min}, \sqrt{S_{exact}}\right)\right)$ denotes a Gaussian distribution with a mean of zero and a standard deviation of the maximum of $\sqrt{S_{exact}}$ and the bremsstrahlung level e_{min}. By varying the noise level we can investigate how robust the methods are against noise. Figure 4 shows example of the standard deviation of the synthetic spectra calculated using the NBI test distribution for $k = 0.1$, $k = 0.5$ and $k = 0.9$. When calculating the synthetic spectra, wavelengths blocked by impurity emission in ASDEX Upgrade discharge #31557 are included as the impurity emission is discharge-specific and here we wish to compare the inversion methods for a generic discharge.

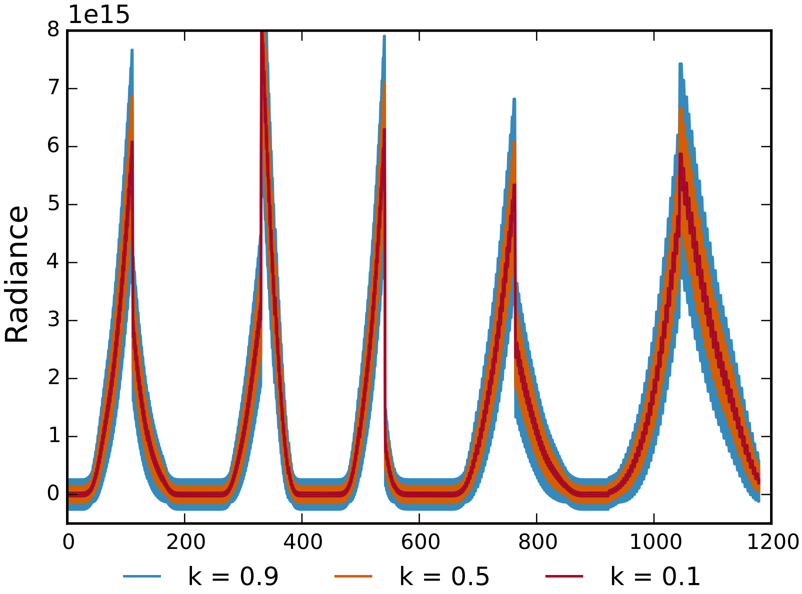

Figure 4. Examples of the average noise levels in the synhtetic spectra calculated usign the NBI test distribution and equation (25) for $k = 0.1$, 0.5 and 0.9. The width of the spectra corresponds to the standard deviation of the noise for the given k-value.

4.3. Variance and bias of the solution

Using equation (25) noisy spectra can be calculated. In order to determine how the noise propagates from the spectra to the tomographies, 25 noisy spectra are calculated for every value of k. A tomography is calculated for each spectrum. Thereby, an ensemble of tomographies is obtained for each k-value. The propagation of the uncertainties from the measurements to the tomographies is found by calculating the variance of the ensemble of tomographies for each velocity-space coordinate. This variance corresponds to the propagation of the uncertainties through the regularized inverse of the transfer matrix as explained in [6].

A forward model can itself contain uncertainties. The forward model here is given by the FIDA weight functions. These are calculated numerically based on profiles of several nuisance parameters. The weight functions are most sensitive to the ion temperature and rotation velocity, the electron temperature and density and the effective charge Z_{eff}. Hence we consider the impact of these parameters on the tomographic inversion results for the different regularization methods. The uncertainties in the bulk plasma parameters lead to uncertainties in the weight functions, δW. Assuming a Gaussian error distribution of the bulk plasma parameters, we calculate the uncertainty in the forward model (i.e. in the weight functions) by sampling a population of weight functions calculated varying one nuisance plasma parameter at a time and keeping the other parameters fixed. The total variance of the weight function is then obtained by summing up the variances obtained from each plasma parameter. The corresponding error, e_m, from the forward model error is

$$e_m = \delta W F_{true} \, . \tag{26}$$

e_m depends on the (often unknown) true distribution function. However, if an estimate of F_{true} can be obtained, e_m can be estimated. The combined uncertainty due to uncertainty in the forward model and measurement uncertainty is then

$$e_{data} = \sqrt{e_{ph}^2 + e_m^2} \, . \tag{27}$$

where e_{ph} is the photon noise. F_{true} is approximated by the sum of a Maxwellian for the bulk ions and a TRANSP/NUBEAM simulation to estimate the NBI ions. The Maxwellian is calculated using measured ion temperature and density. The forward model error is included in the analysis using real measurements but not for the synthetic measurements.

As mentioned above, uncertainties in the measurements propagate through to the tomography. However, this effect is suppressed by the regularization methods as the tomographies would otherwise be completely dominated by the noise in the measurements. The regularization itself introduces an error in the tomography though. Here we calculate this as the bias of the tomography. It is given as the difference of the mean of the ensemble of calculated tomographies for a given k and the true test distribution:

$$\text{bias} = F_\mu - F_{true} \, , \tag{28}$$

where F_μ is the mean of the calculated tomographies. Thus the bias also depends on F_{true}.

We define a measure of the total uncertainty in the tomography as the mean squared error, MSE, given by

$$\text{MSE} = \text{variance} + \text{bias}^2 \, . \tag{29}$$

4.4. Figures of merit

We define two different figures of merit. The first is the total mean squared error. This is a measure of the total uncertainty in the obtained tomography. It is calculated by summing the MSE of every pixel. For this figure of merit the smallest values correspond to the best performance of the inversion method.

The second figure of merit is the ratio of the inferred fast-ion density to the true fast-ion density which is calculated as the integral of the tomography normalized by the integral of the true distribution,

$$\frac{\int\int F_{tomography} \, \mathrm{d}E \mathrm{d}p}{\int\int F_{true} \, \mathrm{d}E \mathrm{d}p} \, . \tag{30}$$

Optimally, this figure of merit is one.

4.5. Inversion results

Figure 5 shows tomographies of the Gaussian distribution shown in figure 3(a) calculated with the different inversion methods for various noise levels. All methods reconstruct the position of the Gaussian distribution well. The characteristic widths of the Gaussians are approximately right but tend to be slightly larger than in the original test distribution. Measurement noise enhances this trend. We further observe the appearance of jitter in the inversions throughout velocity space. The minimum Fisher information regularization stands out from the other methods in that it resembles the original function the most and exhibits the least jitter. This suggests superior resolution performance of the method. The minimum Fisher information regularization is furthermore most robust against measurement noise. Of the other methods, the maximum entropy regularization performs best. It is not as smooth, but it is able to localize the large values of the Gaussian distribution very well in velocity space.

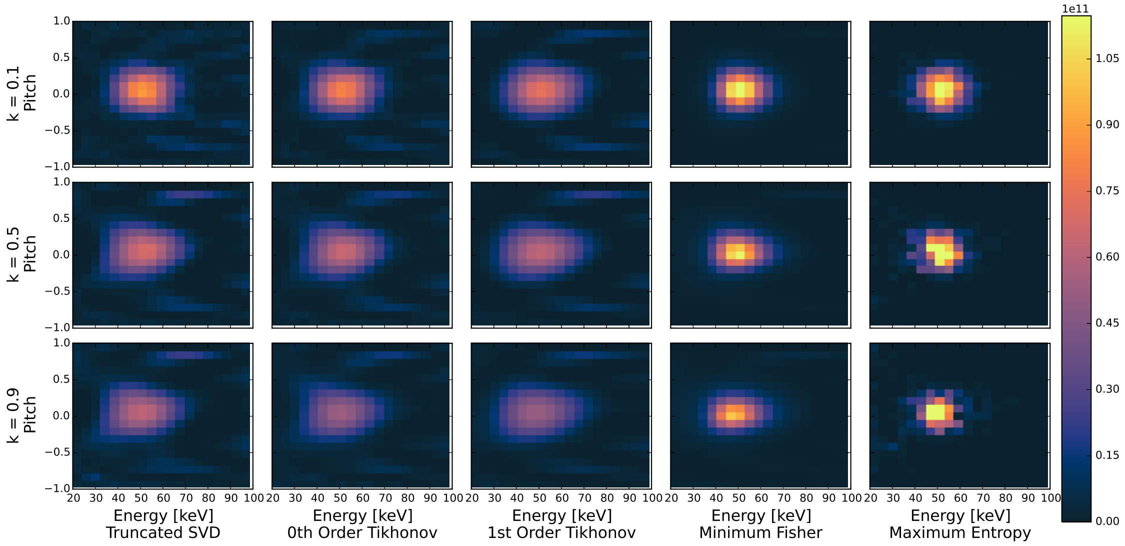

Figure 5. Tomographies of the Gaussian distribution from figure 3(a) in units of [ions/keV/cm^3] based on synthetic measurements using various inversion methods and noise levels. The noise level k is defined in equation (25).

Figure 6 shows the reconstructions of the bi-Maxwellian distribution function. The large-scale shape of the distribution is reproduced by all five inversion methods. The pitch angle symmetry with respect to $p = 0$ is reproduced well and the larger perpendicular temperature compared with the parallel temperature is reflected in the large fast-ion densities for pitches close to zero. The 1'st order Tikhonov and the minimum Fisher information reproduce the symmetry and the large fast-ion densities for pitches close to zero particularly well. Additionally, penalizing large gradients, as in these two methods, produces smooth functions which resemble the smooth bi-Maxellian function well. Further, the jitter appearing throughout velocity space for larger noise levels is significantly smaller.

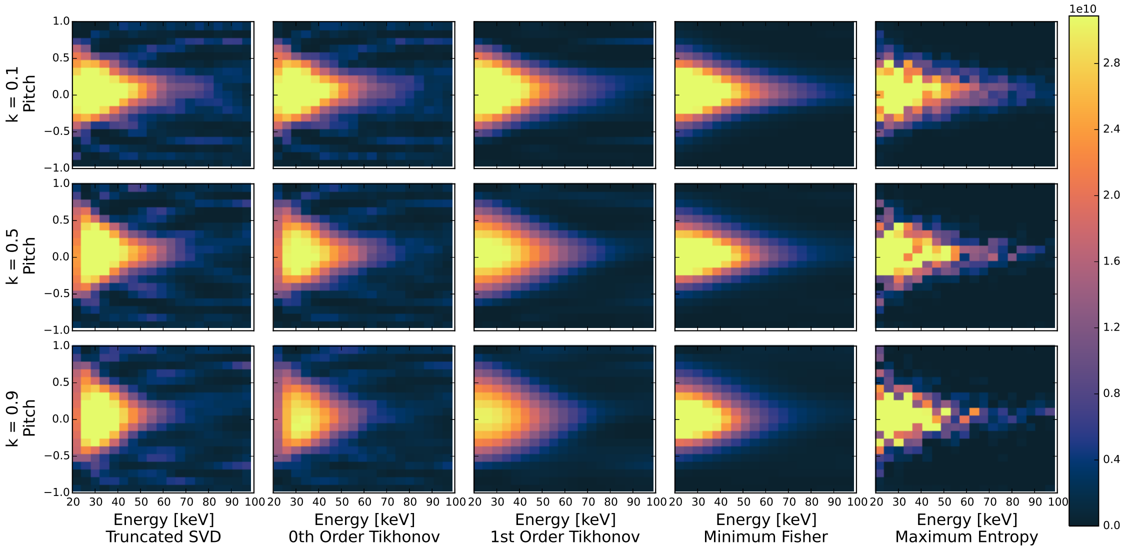

Figure 6. Tomographies of the bi-Maxwellian from figure 3(b) in units of [ions/keV/cm^3] based on synthetic measurements using various inversion methods and noise levels. The noise level k is defined in equation (25).

Figure 7 shows reconstructions of the NBI distribution function for various noise levels and inversion methods. This fast-ion distribution function is typical for neutral beam injection with two co-current beams with injection energies at 80 keV and 70 keV and one counter-current beam with an injection energy of 70 keV. Therefore, this distribution function is a more difficult test case than previously presented reconstructions of distribution functions which are more typical for a single NBI beam. The overall shape of the NBI distribution function with bias towards positive pitches is well reproduced by all five inversion methods. The protrusion at pitches of about 0.7 originates from the co-current beam injection, and the weaker protrusion at pitches of -0.7 from the counter-current beam injection. All reconstructions show that the full energy beam injection peak for co-current injection (positive pitch) is at larger energies than that for counter-current injection (negative pitch). As observed for the Gaussian and bi-Maxwellian distributions, the 1'st order Tikhonov and the minimum Fisher information regularization result in smooth tomographies with very little jitter compared with the SVD, 0'th order Tikhonov and maximum entropy. The small amplitudes of the jitter makes the overall shape of the function with protrusions at positive and negative pitches stand out most clearly for the 1'st order Tikhonov and the minimum Fisher information regularization. The local maxima due to the beam injection peaks at full, half and third energies can be seen in the SVD and 0'th order Tikhonov in the case of low noise ($k = 0.1$). For larger noise levels, none of the methods are able to resolve more than one peak.

Figure 8 shows the behaviour of the performance parameters as a function of noise level for the tomographies of the three test functions. Figures 8(a), 8(c) and 8(e) show the total mean squared error. The mean squared error increases for larger noise levels

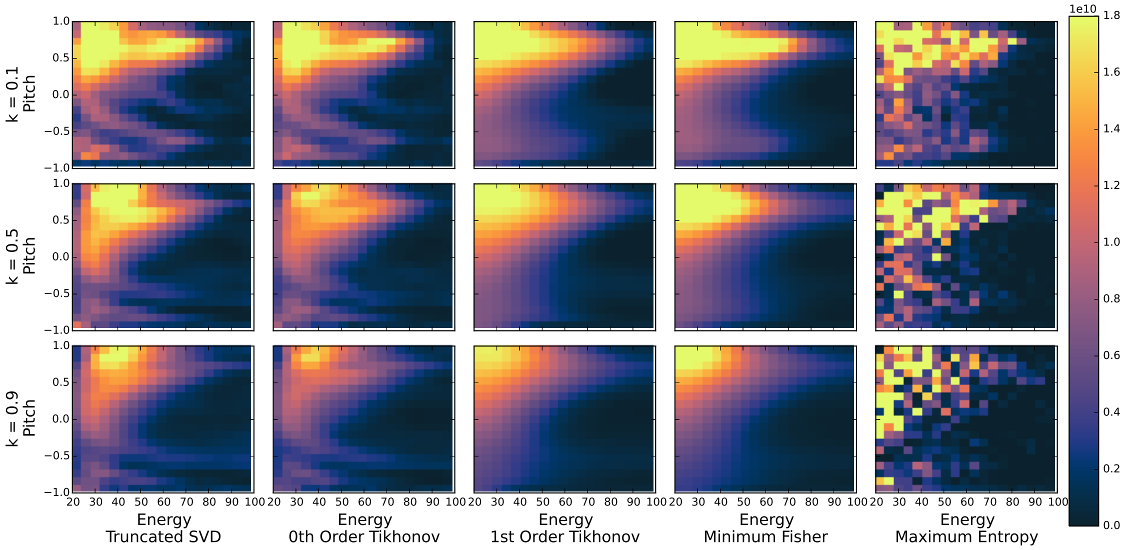

Figure 7. Tomographies of the beam distribution from figure 3(c) in units of [ions/keV/cm^3] based on synthetic measurements using various inversion methods and noise levels. The noise level k is defined in equation (25).

for all inversion methods and test distributions. The minimum Fisher information regularization method has the lowest mean squared error for all test distributions whereas the maximum entropy method has the highest. Figures 8(b), 8(d) and 8(f) show the density ratios calculated using equation (30). The general trend is that the methods produce a lower density ratio for large error levels. Thus, for very large noise levels the absolute values of an inferred density obtained from a reconstruction might be unreliable. For the Gaussian test distribution, the minimum Fisher information and maximum entropy methods are very good at recreating the correct density. The other three methods overestimate the amount of ions present. This is also the case for the bi-Maxwellian distribution but not to the same extent. For the NBI test distribution the spread in densities is smaller than for the other cases.

The uncertainties of the tomographies of the beam distribution as defined in section 4.3 are shown in figure 9 for a noise level of $k = 0.5$ in equation (25). Here we disregard the model uncertainty for simplicity. The top row shows the square root of the variance of the tomographies. Compared with the values of the tomographies in figure 7, the uncertainties are about one order of magnitude smaller, and smallest for first order Tikhonov and minimum Fisher information regularization. The middle row shows the bias. Negative values denote regions where too few ions are placed, positive values denote regions where too many ions are placed. The beam peaks are seen in the bias, especially for first order Tikhonov and minimum Fisher information regularization as these two are only able to resolve the spiky nature of the peaks for low noise levels. The last row shows the square root of the mean squared error. It is seen that for all but maximum entropy, the main contribution to the uncertainty is the bias.

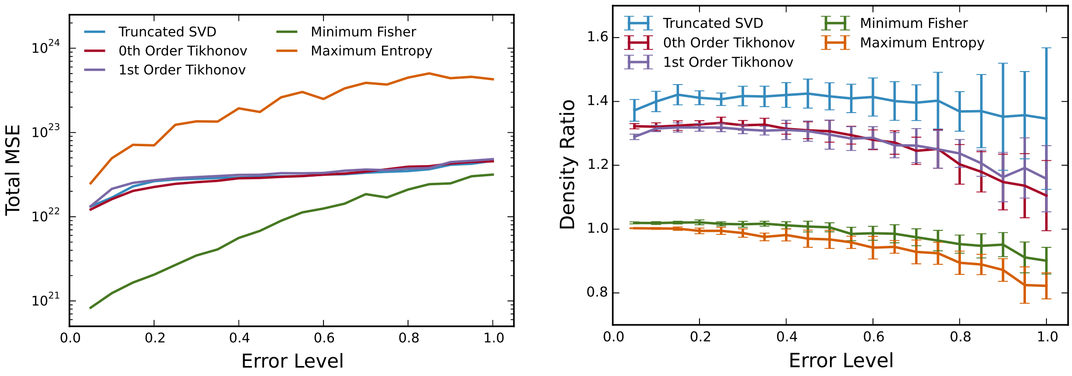

(a) Total MSE, Gaussian (b) Density ratio, Gaussian

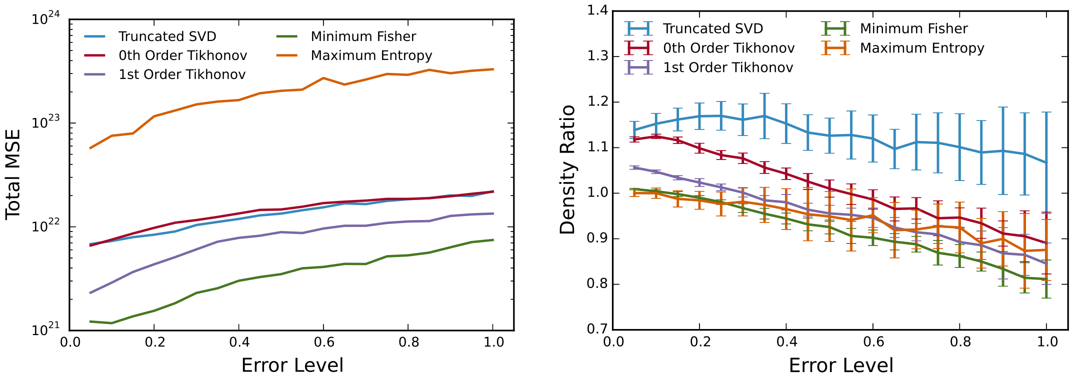

(c) Total MSE, bi-Maxwellian (d) Density ratio, bi-Maxwellian

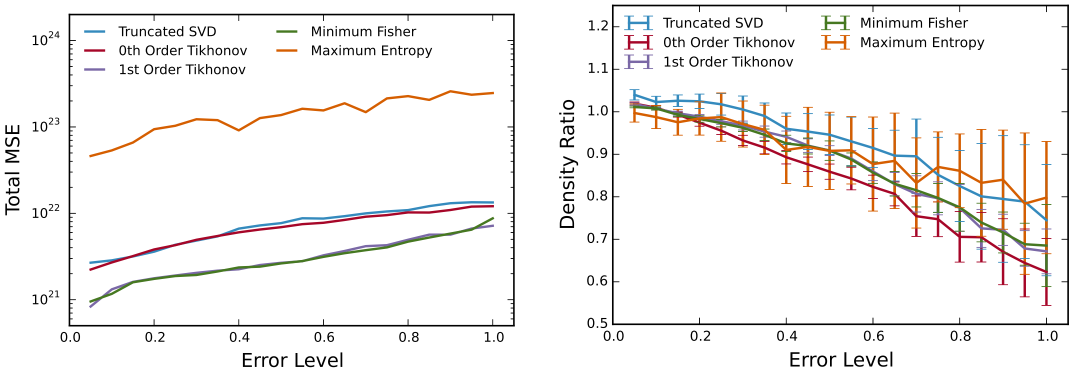

(e) Total MSE, NBI (f) Density ratio, NBI

Figure 8. Figures of merit of the reconstructions of the test distributions. The left column shows the total mean squared error. The right column shows the density ratio.

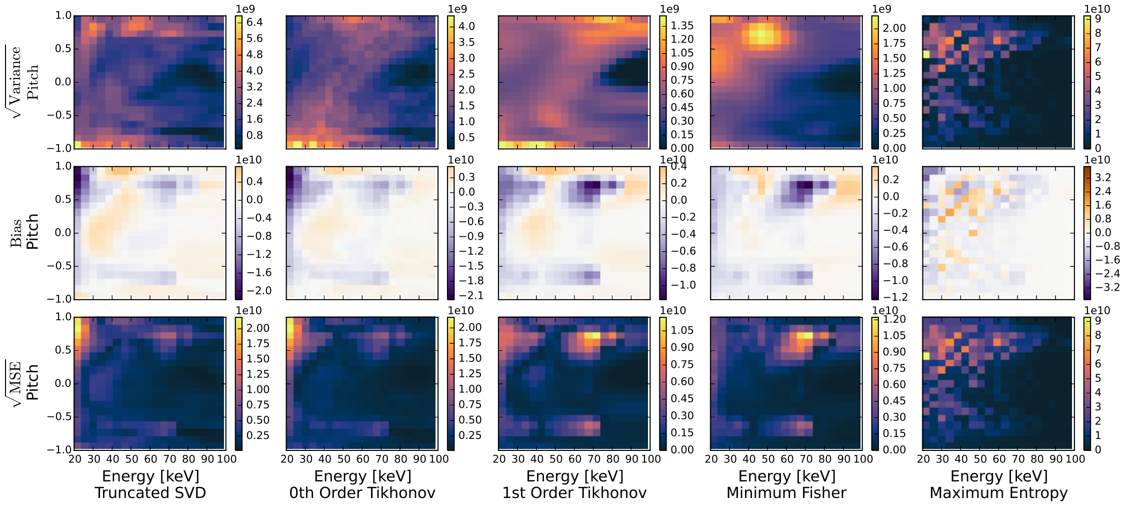

Figure 9. Uncertainties for the tomographies of the beam distribution in units of [ions/keV/cm^3]. All uncertainties are calculated for a noise level of $k = 0.5$.

4.6. Tomographies using two to four views

ASDEX Upgrade is currently the only machine with five FIDA views whereas FIDA systems on other machines have fewer views. To test the influence of the number of views on the performance of the different inversion methods, we repeat the analysis using two, three and four views. Tomographies of the NBI distribution function calculated for $k = 0.5$ are shown in figure 10. Even using only two views, it is possible to recreate the overall shape of the NBI test distribution. Adding additional views improve the quality of the tomographies of all inversion methods, in agreement with the findings for

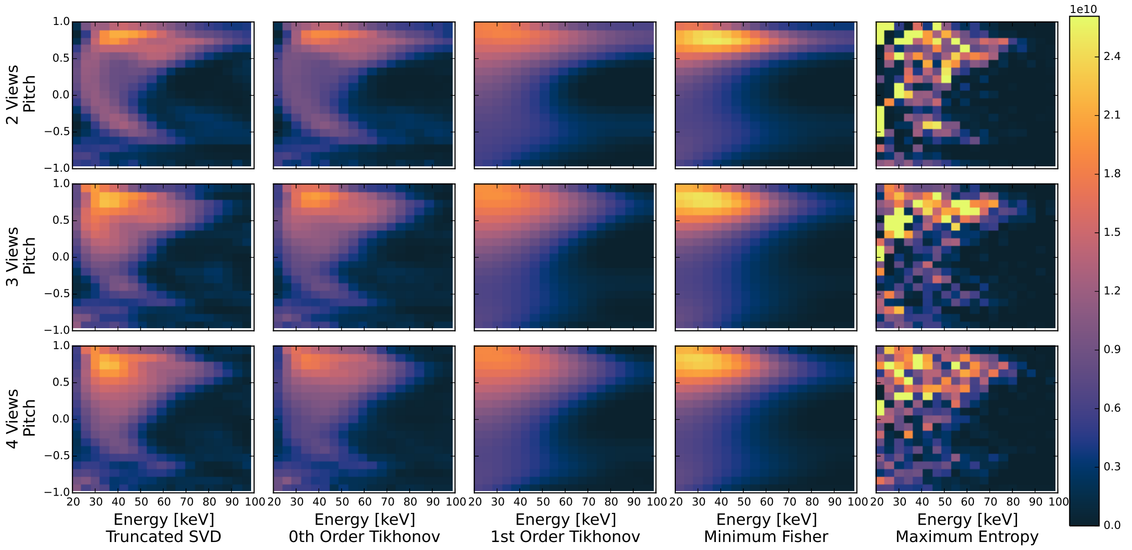

Figure 10. Tomographies of the NBI distribution using two, three and four FIDA views. All are calculated for $k = 0.5$.

truncated SVD in [5]. Furthermore, it is evident that the best results are obtained using the minimum Fisher information regularization method for any number of views.

5. Tomographies of a measured sawtooth crash

A sawtooth crash is a periodic plasma instability which can occur when the central safety factor drops below one. It changes the magnetic field topology and has been observed to redistribute particles and energy from the center of the plasma. It has furthermore been observed on several machines that passing fast ions are redistributed more strongly compared to trapped ions [9,36,37]. Figure 11 shows tomographies based on experimental data. They are calculated using the different inversion methods applied to FIDA spectra measured just before and after a sawtooth crash in ASDEX Upgrade discharge #31557 at 2.25 s. Figure 12 shows the uncertainties of the tomographies of the pre-crash distribution. Again it seen that the bias dominates the uncertainty. We stress again that the bias depends on the unknown true solution, for which we here use the TRANSP model.

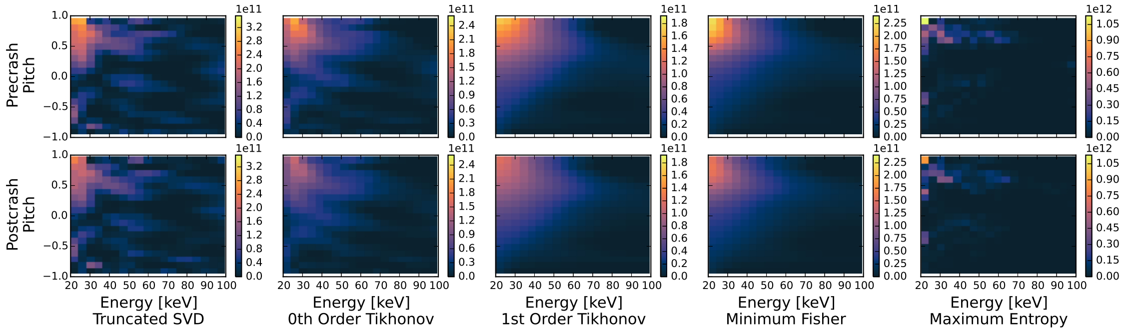

Figure 11. Tomographies before and after a sawtooth crash calculated using the different regularization methods.

Common for all regularization methods, the inferred fast ion density drops significantly during the sawtooth crash. By comparing the absolute values of the tomographies with the uncertainties, we can identify the velocity-space regions where we can be confident in the tomography. In particular the minimum Fisher information and the first-order Tikhonov are reliable in large regions. For the SVD and zeroth order Tikhonov we observe that large regions at negative pitch are unreliable for this discharge and regularization level.

To further investigate the velocity-space dependence of the change in the fast-ion distribution function, we calculate the relative change:

$$(\Delta F)_{rel} = \frac{F_{after} - F_{before}}{F_{before}} \,. \tag{31}$$

The relative change is calculated for every regularization method and plotted in figure 13. The top row shows the relative change as a function of energy and pitch. The bottom row shows the uncertainties of the relative change. The velocity-space dependence of

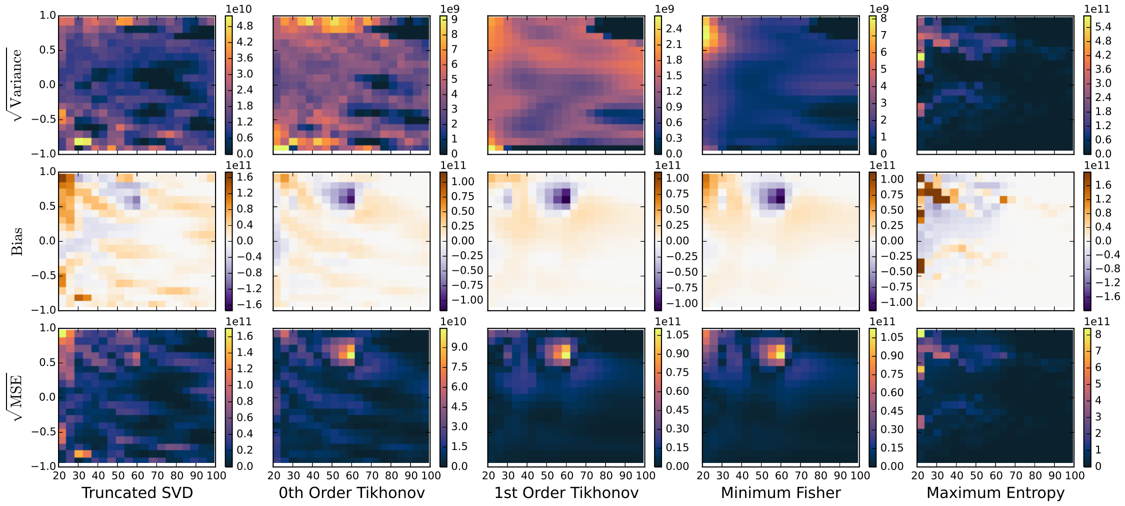

Figure 12. Measures of uncertainties using the different regularization methods.

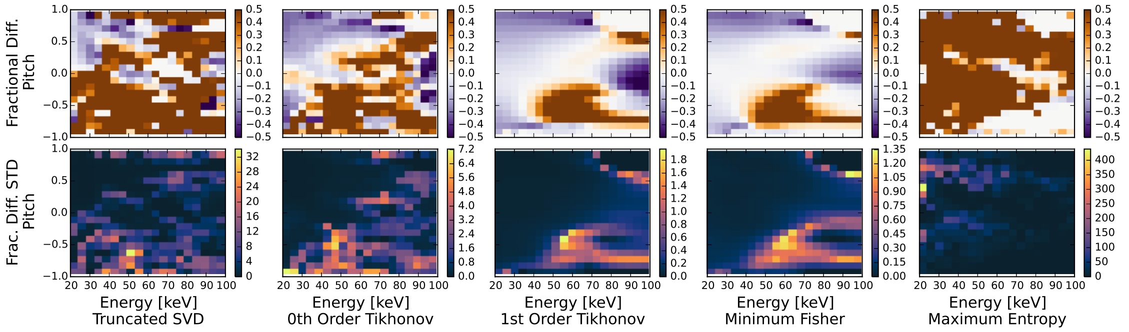

Figure 13. Relative change of the fast-ion velocity distribution function.

the relative change is especially clear in the first order Tikhonov and the minimum Fisher information figures as the amount of jitter in these tomographies is significantly smaller compared to the other methods. Both first order Tikhonov and minimum Fisher information suggest that ions with large pitch values are redistributed more compared to ions with pitch close to zero. This trend is also confirmed by the singular value decomposition and zeroth order Tikhonov in the regions where the tomographies are reliable. The unreliable regions are here shown as those with large standard deviation compared with amplitudes of the tomographies. Similar trends were observed previously using singular value decomposition [9] and a variant of a first-order Tikhonov [10] where different regularization levels were chosen rather than set by the L-curve method. Figure 14 shows the ratio of the post-crash distribution to the pre-crash distribution integrated over energy as a function of pitch for all five inversion methods. Thus it is a measure of the pitch dependence of the change in the fast ion distribution function. For pitch values close to zero all five inversion methods predict a redistribution level of between 10% and 20%. For pitch values above 0.4 the redistribution level increases to between 30% and 40% as seen by all five inversion methods. For negative pitch values where very few ions are present it is not possible to determine the amount of redistribution.

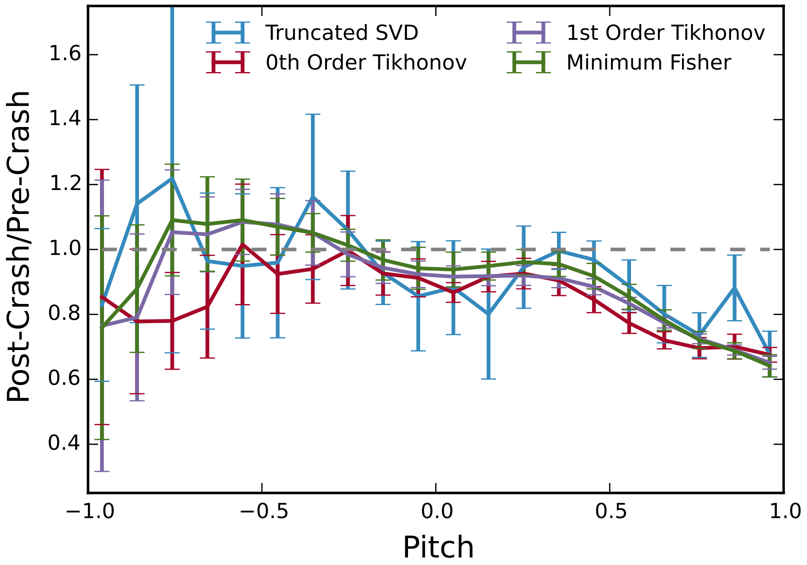

Figure 14. Ratio of the fast-ion velocity-space distribution functions befor and after the crash integrated over energy shown as a function of pitch.

6. Discussion

Both the bias and the forward model uncertainty require an estimate of the true fast-ion velocity distribution function. For actual measurements, where F_{true} is unknown, the total mean squared error will be biased by the estimate of F_{true}. However, the uncertainty will have approximately the correct magnitude if a good estimate of F_{true} can be calculated. Furthermore, it is useful to gain insight into whether the uncertainties obtained are dominated by the uncertainties in the measurements or by the regularization itself.

It is seen that when the noise level is not too large, the first order Tikhonov and minimum Fisher information regularization methods can reconstruct the overall shape of the true distribution function very well. However, they lack capability to resolve very fine and detailed features. It is seen that the absolute values of a derived quantity such as the fast-ion density depend on the noise level in the data. However, we find that the ratio of such quantities is less sensitive to the specific noise level and amount of regularization. Hence we can make statements about changes in such quantities with greater confidence than about the absolute values themselves since systematic errors introduced by the inversion methods will tend to cancel. For example, the bias in the tomographies tends to be similar before and after a sawtooth crash, and hence it partly cancels in the relative change.

7. Conclusion

We have compared the performance of five different inversion methods for velocity-space tomography. In order to estimate the confidence in the presented analysis, uncertainties of the tomographies are defined and calculated taking into account the photon noise, uncertainties in the forward model as well as uncertainty introduced by the inversion methods themselves. It is found that for the regularization level used here, the bias introduced by the inversion methods is the major contribution. The performance is tested using synthetic data calculated using a realistic transfer-matrix from the five-view FIDA-system at ASDEX Upgrade. It is found that the first order Tikhonov and minimum Fisher information regularization methods which penalize steep gradients perform best for realistic test functions. The uncertainty analysis allows us to identify confidence regions in velocity space, and regions where the tomographies are not reliable for the given data and regularization level. Furthermore, the various methods are applied to actual FIDA measurements obtained in ASDEX Upgrade discharge #31557 just before and just after a sawtooth crash. Using velocity-space tomography it is possible to investigate the velocity-space dependence of the fast-ion redistribution in regions where we are confident in the tomography. We find that sawtooth crashes at ASDEX Upgrade affect ions with large pitch values more than ions with pitch close to zero.

Acknowledgement

This work has been carried out within the framework of the EUROfusion Consortium and has received funding from the Euratom research and training programme 2014-2018 under grant agreement No 633053. The views and opinions expressed herein do not necessarily reflect those of the European Commission. The source code for the inversion methods is available upon request to lstagner@uci.edu.

References

[1] W W Heidbrink, K H Burrell, Y Luo, N A Pablant, and E Ruskov. Hydrogenic fast-ion diagnostic using Balmer-alpha light. *Plasma Physics and Controlled Fusion*, 46(12):1855–1875, December 2004.

[2] W W Heidbrink. Fast-ion Dα measurements of the fast-ion distribution (invited). *The Review of scientific instruments*, 81(10):10D727, October 2010.

[3] J. Egedal and H. Bindslev. Reconstruction of gyrotropic phase-space distributions from one-dimensional projections. *Physics of Plasmas*, 11(5):2191, 2004.

[4] M. Salewski, S.K. Nielsen, H. Bindslev, V. Furtula, N.N. Gorelenkov, S.B. Korsholm, F. Leipold, F Meo, P.K. Michelsen, D. Moseev, and M. Stejner. On velocity space interrogation regions of fast-ion collective Thomson scattering at ITER. *Nuclear Fusion*, 51(8):083014, August 2011.

[5] M. Salewski, B. Geiger, S.K. Nielsen, H. Bindslev, M. García-Muñoz, W.W. Heidbrink, S.B. Korsholm, F. Leipold, F. Meo, P.K. Michelsen, D. Moseev, M. Stejner, and G. Tardini. Tomography of fast-ion velocity-space distributions from synthetic CTS and FIDA measurements. *Nuclear Fusion*, 52(10):103008, October 2012.

[6] M. Salewski, B. Geiger, S.K. Nielsen, H. Bindslev, M. García-Muñoz, W.W. Heidbrink, S.B. Korsholm, F. Leipold, J. Madsen, F. Meo, P.K. Michelsen, D. Moseev, M. Stejner, and G. Tardini. Combination of fast-ion diagnostics in velocity-space tomographies. *Nuclear Fusion*, 53(6):063019, June 2013.

[7] M. Salewski, B. Geiger, A.S. Jacobsen, M. García-Muñoz, W.W. Heidbrink, S.B. Korsholm, F. Leipold, J. Madsen, D. Moseev, S.K. Nielsen, J. Rasmussen, M. Stejner, G. Tardini, and M. Weiland. Measurement of a 2D fast-ion velocity distribution function by tomographic inversion of fast-ion D-alpha spectra. *Nuclear Fusion*, 54(2):023005, February 2014.

[8] M Salewski, B Geiger, W W Heidbrink, A S Jacobsen, S B Korsholm, F Leipold, J Madsen, D Moseev, S K Nielsen, J Rasmussen, L Stagner, D Steeghs, M Stejner, G Tardini, and M Weiland. Doppler tomography in fusion plasmas and astrophysics. *Plasma Physics and Controlled Fusion*, 57(1):014021, January 2015.

[9] B. Geiger, M. Weiland, A.S. Jacobsen, D. Rittich, R. Dux, R. Fischer, C. Hopf, M. Maraschek, R.M. McDermot, S.K. Nielsen, T. Odstrcil, M. Reich, F. Ryter, M. Salewski, P.A. Schneider, and G. Tardini. Fast-ion transport and neutral beam current drive in ASDEX Upgrade. *Nuclear Fusion*, 55:083001, 2015.

[10] M. Weiland, B. Geiger, A.S. Jacobsen, M. Reich, M. Salewski, and T. Odstrcil. Velocity-space resolved fast-ion measurements from five FIDA views at the tokamak ASDEX Upgrade. submitted.

[11] W W Heidbrink, Y Luo, K H Burrell, R W Harvey, R I Pinsker, and E Ruskov. Measurements of fast-ion acceleration at cyclotron harmonics using Balmer-alpha spectroscopy. *Plasma Physics and Controlled Fusion*, 49(9):1457–1475, September 2007.

[12] M Salewski, B Geiger, D Moseev, W W Heidbrink, A S Jacobsen, S B Korsholm, F Leipold, J Madsen, S K Nielsen, J Rasmussen, M Stejner, and M Weiland. On velocity-space sensitivity of fast-ion D-alpha spectroscopy. *Plasma Physics and Controlled Fusion*, 56(10):105005, October 2014.

[13] W W Heidbrink, J R Ferron, C T Holcomb, M A Van Zeeland, X Chen, C M Collins, a Garofalo, X Gong, B a Grierson, M Podestà, L Stagner, and Y Zhu. Confinement degradation by Alfvén-eigenmode induced fast-ion transport in steady-state scenario discharges. *Plasma Physics and Controlled Fusion*, 56(9):095030, 2014.

[14] A. S. Jacobsen, M. Salewski, J. Eriksson, G. Ericsson, A. Hjalmarsson, S. B. Korsholm, F. Leipold, S. K. Nielsen, J. Rasmussen, and M. Stejner. Velocity-space sensitivity of the time-of-flight neutron spectrometer at JETa). *Review of Scientific Instruments*, 85(11):11E103, November 2014.

[15] A.S. Jacobsen, M. Salewski, J. Eriksson, G. Ericsson, S.B. Korsholm, F. Leipold, S.K. Nielsen, J. Rasmussen, and M. Stejner. Velocity-space sensitivity of neutron spectrometry measurements. *Nuclear Fusion*, 55(5):053013, May 2015.

[16] M. Salewski, M. Nocente, G. Gorini, A.S. Jacobsen, V.G. Kiptily, S.B. Korsholm, F. Leipold, J. Madsen, D. Moseev, S.K. Nielsen, J. Rasmussen, M. Stejner, and M Tardocchi. Velocity-space observation regions of high-resolution two-step reaction gamma-ray spectroscopy. *Nuclear Fusion*, 55(9):093029, September 2015.

[17] M Anton, H Weisen, M J Dutch, W von der Linden, F Buhlmann, R Chavan, B Marletaz, P Marmillod, and P Paris. X-ray tomography on the TCV tokamak. *Plasma Physics and Controlled Fusion*, 38(11):1849–1878, November 1996.

[18] T. Craciunescu, G. Bonheure, V. Kiptily, A. Murari, I. Tiseanu, and V. Zoita. A comparison of four reconstruction methods for JET neutron and gamma tomography. *Nuclear Instruments and Methods in Physics Research Section A: Accelerators, Spectrometers, Detectors and Associated Equipment*, 605(3):374–383, July 2009.

[19] B Geiger, R Dux, R M McDermott, S Potzel, M Reich, F Ryter, M Weiland, D Wünderlich, and M Garcia-Munoz. Multi-view fast-ion D-alpha spectroscopy diagnostic at ASDEX Upgrade. *The Review of scientific instruments*, 84(11):113502, November 2013.

[20] B. Geiger, M. Garcia-Munoz, R. Dux, F. Ryter, G. Tardini, L. Barrera Orte, I.G.J. Classen, E. Fable, R. Fischer, V. Igochine, and R.M. McDermott. Fast-ion transport in the presence of magnetic reconnection induced by sawtooth oscillations in ASDEX Upgrade. *Nuclear Fusion*, 54(2):022005, February 2014.

[21] W.W. Heidbrink, M.A. Van Zeeland, B.A. Grierson, C.M. Muscatello, J.M. Park, C.C. Petty, R. Prater, and Y.B. Zhu. Initial measurements of the DIII-D off-axis neutral beams. *Nuclear Fusion*, 52(9):094005, September 2012.

[22] D. C. Pace, M. E. Austin, E. M. Bass, R. V. Budny, W. W. Heidbrink, J. C. Hillesheim, C. T. Holcomb, M. Gorelenkova, B. A. Grierson, D. C. McCune, G. R. McKee, C. M. Muscatello, J. M. Park, C. C. Petty, T. L. Rhodes, G. M. Staebler, T. Suzuki, M. A. Van Zeeland, R. E. Waltz, G. Wang, A. E. White, Z. Yan, X. Yuan, and Y. B. Zhu. Energetic ion transport by microturbulence is insignificant in tokamaks. *Physics of Plasmas*, 20(5):056108, 2013.

[23] A Bortolon, W W Heidbrink, and M Podestà. A tangentially viewing fast ion D-alpha diagnostic for NSTX. *The Review of scientific instruments*, 81(10):10D728, October 2010.

[24] C A Michael, N Conway, B Crowley, O Jones, W W Heidbrink, S Pinches, E Braeken, R Akers, C Challis, M Turnyanskiy, A Patel, D Muir, R Gaffka, and S Bailey. Dual view FIDA measurements on MAST. *Plasma Physics and Controlled Fusion*, 55(9):095007, September 2013.

[25] O M Jones, C A Michael, K G McClements, N J Conway, B Crowley, R J Akers, R J Lake, and S D Pinches. Fast-ion deuterium alpha spectroscopic observations of the effects of fishbones in the Mega-Ampere Spherical Tokamak. *Plasma Physics and Controlled Fusion*, 55(8):085009, August 2013.

[26] T. Ito, M. Osakabe, K. Ida, M. Yoshinuma, M. Kobayashi, M. Goto, S. Murakami, M. Isobe, S. Kobayashi, K. Toi, K. Ogawa, Y. Takeiri, and S. Okamura. Fast ion charge exchange spectroscopy adapted for tangential viewing geometry in LHD. *Review of Scientific Instruments*, 81(10):1–5, 2010.

[27] W.H. Press, S.A. Teukolsky, W.T. Vetterling, and B.P. Flannery. *Numerical recipies: The art of scientific computing*. Cambridge university press, 2007.

[28] G. Strang. *Linear algebra and its applications*. Thomson Learning, 1988.

[29] Per Christian Hansen, Toke Koldborg Jensen, and Giuseppe Rodriguez. An adaptive pruning algorithm for the discrete L-curve criterion. *Journal of Computational and Applied Mathematics*, 198(2):483–492, 2007.

[30] P.C. Hansen. *Rank-deficient and discrete ill-posed problems: numerical aspects of linear inversion*. SIAM, 1998.

[31] SF Gull and J Skilling. Maximum entropy method in image processing. *Communications, Radar and Signal Processing, IEE Proceedings F*, 131(6):646–659, 1984.

[32] Adom Giffin and Ariel Caticha. Updating probabilities with data and moments. In *Bayesian Inference and Maximum Entropy Methods in Science and Engineering*, volume 954, pages 74–84, 2007.

[33] Andreas Wächter and Lorenz T Biegler. On the implementation of an interior-point filter line-search algorithm for large-scale nonlinear programming. *Mathematical programming*, 106(1):25–57, 2006.

[34] Miles Lubin and Iain Dunning. Computing in operations research using julia. *INFORMS Journal on Computing*, 27(2):238–248, 2015.

[35] Alexei Pankin, Douglas McCune, Robert Andre, Glenn Bateman, and Arnold Kritz. The tokamak Monte Carlo fast ion module NUBEAM in the National Transport Code Collaboration library. *Computer Physics Communications*, 159(3):157–184, June 2004.

[36] S.K. Nielsen, M. Salewski, H. Bindslev, A. Bürger, V. Furtula, M. Kantor, S.B. Korsholm, H.R. Koslowski, A. Krämer-Flecken, F. Leipold, F. Meo, P.K. Michelsen, D. Moseev, J.W. Oosterbeek, M. Stejner, and E. Westerhof. Dynamics of fast ions during sawtooth oscillations in the TEXTOR tokamak measured by collective Thomson scattering. *Nuclear Fusion*, 51(6):063014,

June 2011.

[37] C M Muscatello, W W Heidbrink, Ya I Kolesnichenko, V V Lutsenko, M A Van Zeeland, and Yu V Yakovenko. Velocity-space studies of fast-ion transport at a sawtooth crash in neutral-beam heated plasmas. *Plasma Physics and Controlled Fusion*, 54(2):025006, February 2012.

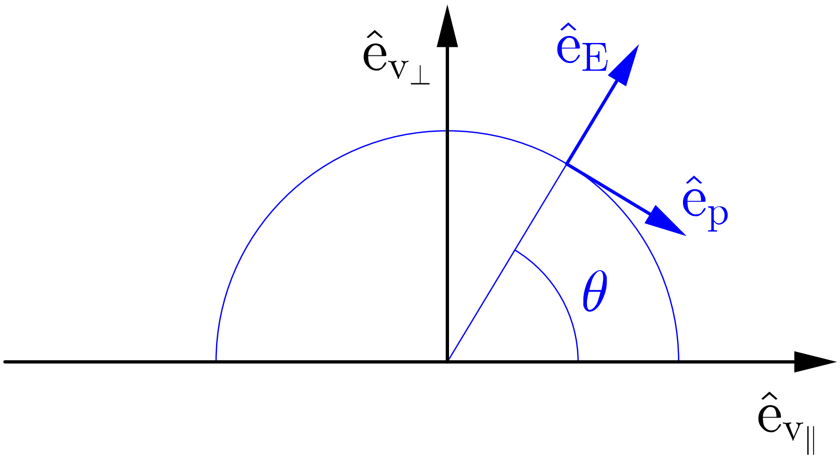

Figure A1. The relations between the unit vectors $\hat{e}_{v_\parallel}, \hat{e}_{v_\perp}, \hat{e}_E$ and $\hat{e}_p$.

Appendix A. Derivation of velocity-gradient in (E, p)-coordinates

To calculate the velocity-space gradient in (E, p)-coordinates, the gradient is transformed from $\left(v_\parallel, v_\perp\right)$-coordinates to (E, p)-coordinates. 1'st order regularization in $\left(v_\parallel, v_\perp\right)$-coordinates can be achieved by setting

$$L^T L = \nabla_{v_\parallel}^T \nabla_{v_\parallel} + \nabla_{v_\perp}^T \nabla_{v_\perp}\,, \tag{A.1}$$

where $\nabla_{v_\parallel}$ and $\nabla_{v_\perp}$ are finite difference matrix representations of the first-order differential operators. These have to be transformed to (E,p)-coordinates. It is apparent that the velocity-space gradient in (E, p)-coordinates has similarities to the real-space gradient in polar coordinates. The relations between the unit vectors $\hat{e}_{v_\parallel}, \hat{e}_{v_\perp}, \hat{e}_E$ and $\hat{e}_p$ are illustrated graphically in figure A1. The velocity-space gradient of f is

$$\nabla f = \left(\nabla_{v_\parallel} f\right)\,\hat{e}_{v_\parallel} + \left(\nabla_{v_\perp} f\right)\,\hat{e}_{v_\perp} = a\left(\nabla_E f\right)\,\hat{e}_E + b\left(\nabla_p f\right)\,\hat{e}_p\,, \tag{A.2}$$

where a and b are unknowns that must be calculated from the Jacobian. ∇_E and ∇_p are velocity-gradients along $\hat{e}_E$ and $\hat{e}_p$ respectively. Writing $\hat{e}_E$ and $\hat{e}_p$ as functions of $\hat{e}_{v_\parallel}$ and $\hat{e}_{v_\perp}$ gives

$$\hat{e}_E = \cos(\theta)\,\hat{e}_{v_\parallel} + \sin(\theta)\,\hat{e}_{v_\perp} = p\,\hat{e}_{v_\parallel} + \sqrt{1-p^2}\,\hat{e}_{v_\perp}\,, \tag{A.3}$$

$$\hat{e}_p = \sin(\theta)\,\hat{e}_{v_\parallel} - \cos(\theta)\,\hat{e}_{v_\perp} = \sqrt{1-p^2}\,\hat{e}_{v_\parallel} - p\,\hat{e}_{v_\perp}\,, \tag{A.4}$$

where the relation $p = \cos(\theta)$ has been used. The gradient in energy is now found by dotting equation (A.2) with $\hat{e}_E$:

$$(\nabla f)\cdot\hat{e}_E \Rightarrow \left(\nabla_{v_\parallel} f\right) p + \left(\nabla_{v_\perp} f\right)\sqrt{1-p^2} = a\left(\nabla_E f\right)$$

$$= a\left(\left(\nabla_{v_\parallel} f\right)\frac{\partial v_\parallel}{\partial E} + \left(\nabla_{v_\perp} f\right)\frac{\partial v_\perp}{\partial E}\right), \tag{A.5}$$

To calculate the partial derivatives, the relations between $v_\parallel, v_\perp, E$ and p are needed:

$$v_\parallel = p\sqrt{\frac{2E}{m}} \tag{A.6}$$

$$v_\perp = \sqrt{1-p^2}\sqrt{\frac{2E}{m}}\,. \tag{A.7}$$

The partial derivatives are:

$$\frac{\partial v_\parallel}{\partial E} = \frac{p}{\sqrt{2mE}} \tag{A.8}$$

$$\frac{\partial v_\perp}{\partial E} = \frac{\sqrt{1-p^2}}{\sqrt{2mE}}\,. \tag{A.9}$$

Inserting equations (A.8) and (A.9) in equation (A.5) gives

$$\left(\nabla_{v_\parallel} f\right)p + \left(\nabla_{v_\perp} f\right)\sqrt{1-p^2} = a\left(\left(\nabla_{v_\parallel} f\right)\frac{p}{\sqrt{2mE}} + \left(\nabla_{v_\perp} f\right)\frac{\sqrt{1-p^2}}{\sqrt{2mE}}\right). \tag{A.10}$$

Equation (A.10) is fulfilled for

$$a = \sqrt{2mE}\,. \tag{A.11}$$

Similarly, b can be found by dotting equation (A.2) with $\hat{e}_p$:

$$\begin{aligned}(\nabla f)\cdot\hat{e}_p \Rightarrow \left(\nabla_{v_\parallel} f\right)\sqrt{1-p^2} - \left(\nabla_{v_\perp} f\right)p &= b\left(\nabla_p f\right)\\ &= b\left(\left(\nabla_{v_\parallel} f\right)\frac{\partial v_\parallel}{\partial p} + \left(\nabla_{v_\perp} f\right)\frac{\partial v_\perp}{\partial p}\right).\end{aligned} \tag{A.12}$$

The partial derivatives are:

$$\frac{\partial v_\parallel}{\partial p} = \sqrt{\frac{2E}{m}}\,, \tag{A.13}$$

$$\frac{\partial v_\perp}{\partial p} = -\frac{p}{\sqrt{1-p^2}}\sqrt{\frac{2E}{m}}\,. \tag{A.14}$$

Inserting equations (A.13) and (A.14) in equation (A.12) gives

$$\left(\nabla_{v_\parallel} f\right)\sqrt{1-p^2} - \left(\nabla_{v_\perp} f\right)p = b\left(\left(\nabla_{v_\parallel} f\right)\sqrt{\frac{2E}{m}} - \left(\nabla_{v_\perp} f\right)\frac{p}{\sqrt{1-p^2}}\sqrt{\frac{2E}{m}}\right). \tag{A.15}$$

Equation (A.15) is fulfilled for

$$b = \sqrt{\frac{m}{2E}}\sqrt{1-p^2}\,. \tag{A.16}$$

Thus, the velocity-space gradient in energy-pitch coordinates becomes

$$\nabla f = \sqrt{2mE}\left(\nabla_E f\right)\,\hat{e}_E + \sqrt{\frac{m}{2E}}\sqrt{1-p^2}\left(\nabla_p f\right)\,\hat{e}_p\,. \tag{A.17}$$

Paper IV

IOP Publishing | International Atomic Energy Agency Nuclear Fusion

Nucl. Fusion **55** (2015) 083001 (12pp) doi:10.1088/0029-5515/55/8/083001

Fast-ion transport and neutral beam current drive in ASDEX upgrade

B. Geiger[1], M. Weiland[1], A.S. Jacobsen[2], D. Rittich[1], R. Dux[1], R. Fischer[1], C. Hopf[1], M. Maraschek[1], R.M. McDermott[1], S.K. Nielsen[2], T. Odstrcil[1], M. Reich[1], F. Ryter[1], M. Salewski[2], P.A. Schneider[1], G. Tardini[1] and The ASDEX Upgrade Team[1]

[1] Max-Planck-Institute for Plasma Physics, Boltzmannstr. 2, 85748 Garching, Germany
[2] Technical University of Denmark, Department of Physics, Dk-2800 Kgs Lyngby, Denmark

E-mail: benedikt.geiger@ipp.mpg.de

Received 12 February 2015, revised 24 April 2015
Accepted for publication 19 May 2015
Published 30 June 2015

Abstract

The neutral beam current drive efficiency has been investigated in the ASDEX Upgrade tokamak by replacing on-axis neutral beams with tangential off-axis beams. A clear modification of the radial fast-ion profiles is observed with a fast-ion D-alpha diagnostic that measures centrally peaked profiles during on-axis injection and outwards shifted profiles during off-axis injection. Due to this change of the fast-ion population, a clear modification of the plasma current profile is predicted but not observed by a motional Stark effect diagnostic. The fast-ion transport caused by MHD activity has been studied in low collisionality discharges that exhibit strong $(1, 1)$ modes. In particular due to sawtooth crashes, significant radial redistribution of co-rotating fast-ions is observed which can very well be described by the Kadomtsev model. In addition, first tomographic reconstructions of the central 2D fast-ion velocity space in the presence of sawtooth crashes allow the investigation of the pitch dependence of the mode-imposed redistribution: a stronger redistribution of mainly co-rotating fast ions is observed than of those with smaller pitch values.

Keywords: current drive, FIDA, fast ion, sawtooth crash, off-axis NBI

(Some figures may appear in colour only in the online journal)

1. Introduction

In present day fusion devices fast ions are mainly generated by neutral beam injection (NBI). They heat plasmas through collisions with electrons and ions and, if injected with a sufficiently parallel velocity component, their associated current drive can be used to reach non-inductive conditions or to tailor the plasma current profile [1]. Well confined fast ions are, hence, essential to obtain good heating and current drive performances. In addition, detailed understanding of the fast-ion transport mechanisms is needed in view of future fusion devices, not only to guarantee good performance, but also to ensure the safety of the machine: fast helium ions will be produced in fusion reactions that could, if poorly confined, damage the first wall [2]. In toroidally axisymmetric devices such as tokamaks, the fast-ion transport induced by collisions and orbit effects, i.e. the neo-classical transport, is relatively small. However, enhanced fast-ion transport, caused by large- and small-scale instabilities (anomalous transport), could reduce the fast-ion confinement and must, therefore, be investigated. In particular, core localized MHD modes must be studied in detail because they spatially overlap with the fast-ion distribution functions which are typically peaked on-axis. One of the most severe types of core-perturbation in tokamak plasmas is induced by sawtooth crashes [3] which are caused by the fast reconnection of a mode with toroidal and poloidal mode numbers of one ($n = 1$ and $m = 1$). They appear periodically in the plasma center when the safety factor, q, is below one and cause a fast crash of the central pressure, followed by a recovery phase. The crashes strongly redistribute fast ions, as reported from D-T experiments at JET [4] and TFTR [5] and from deuterium plasmas at DIII-D [6], TEXTOR [7], MAST [8] and ASDEX

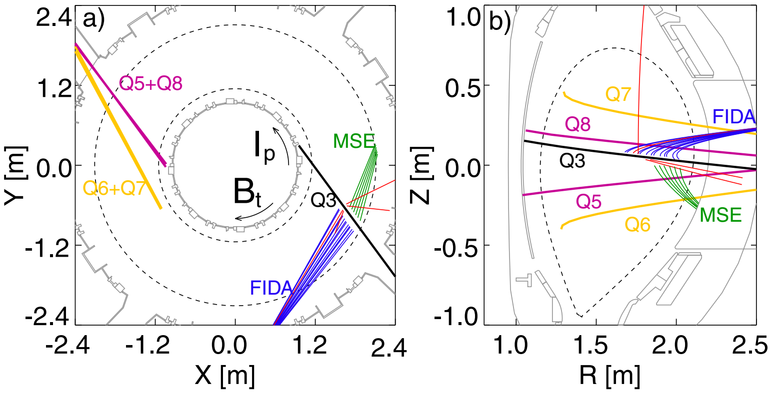

Figure 1. Top down and poloidal view of the ASDEX Upgrade tokamak. The geometry of the off-axis NBI sources is sketched in yellow and that of the on-axis sources applied during the experiments is illustrated in purple (93 keV) and black (60 keV). The toroidal lines of sight of the FIDA diagnostic are shown in blue and those used for a tomographic reconstruction of the central fast-ion velocity space distribution are indicated in red. The viewing geometry of the MSE diagnostic is plotted in green.

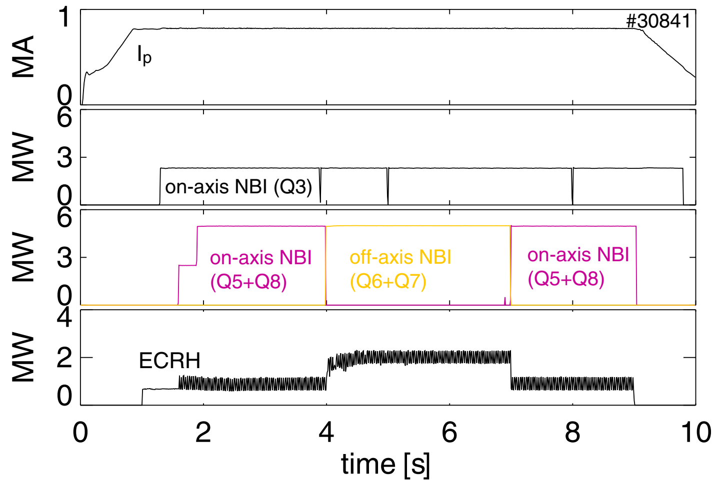

Figure 2. Time traces of discharge #30841 showing the evolution of the plasma current, the NBI heating power and the ECRH heating power.

Upgrade [9]. There are two mechanisms that are responsible for the strong redistribution. These are $\mathbf{E} \times \mathbf{B}$ drift effects and the motion of the fast particles along the evolving magnetic field lines. The details of these mechanisms are, however, not yet clear and need to be investigated in detail.

Of special interest is also the characterization of the off-axis neutral beam current drive (NBCD) efficiency, which is motivated by somewhat contradicting results in the past. On the one hand, previous experiments in ASDEX Upgrade showed that the evolution of the current profile did not follow neo-classical predictions when replacing on-axis NBI with off-axis NBI. In particular, the effect of off-axis NBCD on measurements of the current profile by a motional Stark effect diagnostic (MSE) was weaker than predicted by theory [10]. On the other hand, current-drive studies based on vertically shifted plasmas at DIII-D [11] agreed with modeling. Moreover, measured radial fast-ion profiles, which are expected to be linked to the beam driven current, exhibited good agreement with neo-classical predictions [12, 13].

This important aspect, as well as the fast-ion redistribution due to sawtooth crashes, has now been revisited in ASDEX Upgrade [14], motivated by new measurement capabilities. In particular, a fast-ion D-alpha (FIDA [15]) spectroscopy diagnostic is now available that measures radial profiles of co-rotating fast-ions and allows reconstructions of central 2D fast-ion velocity distribution functions by a tomographic inversion in velocity space.

This paper is structured as follows. In section 2, a study of off-axis fast-ion populations and the associated NBI current drive is presented. Radial fast-ion profiles and MSE measurements are compared with theoretical predictions. The effect of sawtooth crashes on the fast ions is discussed in section 3. Measured neutron rates and radial FIDA profiles of co-rotating ions are compared with theoretical predictions and the central fast-ion velocity space is analyzed using tomographic inversions. Finally, a short summary and conclusion are given.

2. Fast-ion current drive study

The ASDEX Upgrade tokamak is very well equipped for neutral beam current drive studies because it has a sensitive set of fast-ion diagnostics, an MSE diagnostic and flexible heating and current drive systems. Up to 5 MW of electron cyclotron resonance heating (ECRH) and current drive (ECCD) are available to maintain constant electron temperatures (feedback control of T_e) and to stabilize MHD instabilities [16, 17].

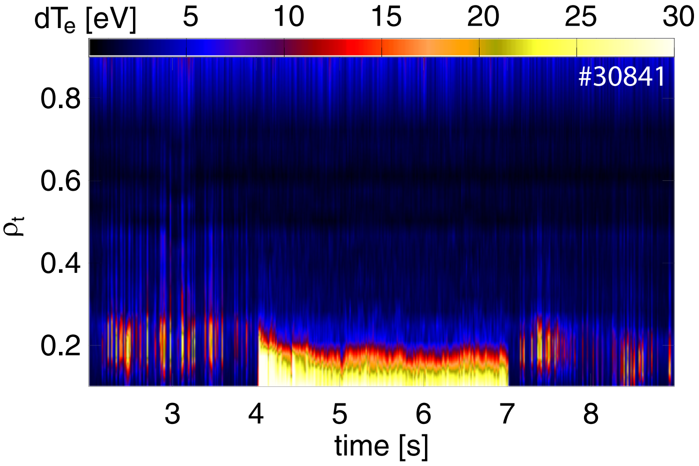

Figure 3. Evolution of the maximum T_e perturbation amplitude as a function of the toroidal flux label for frequencies between 5 kHz and 30 kHz. During on-axis NBI, fishbone modes are present and a continuous $(1, 1)$ mode is localized in the plasma core during off-axis NBI.

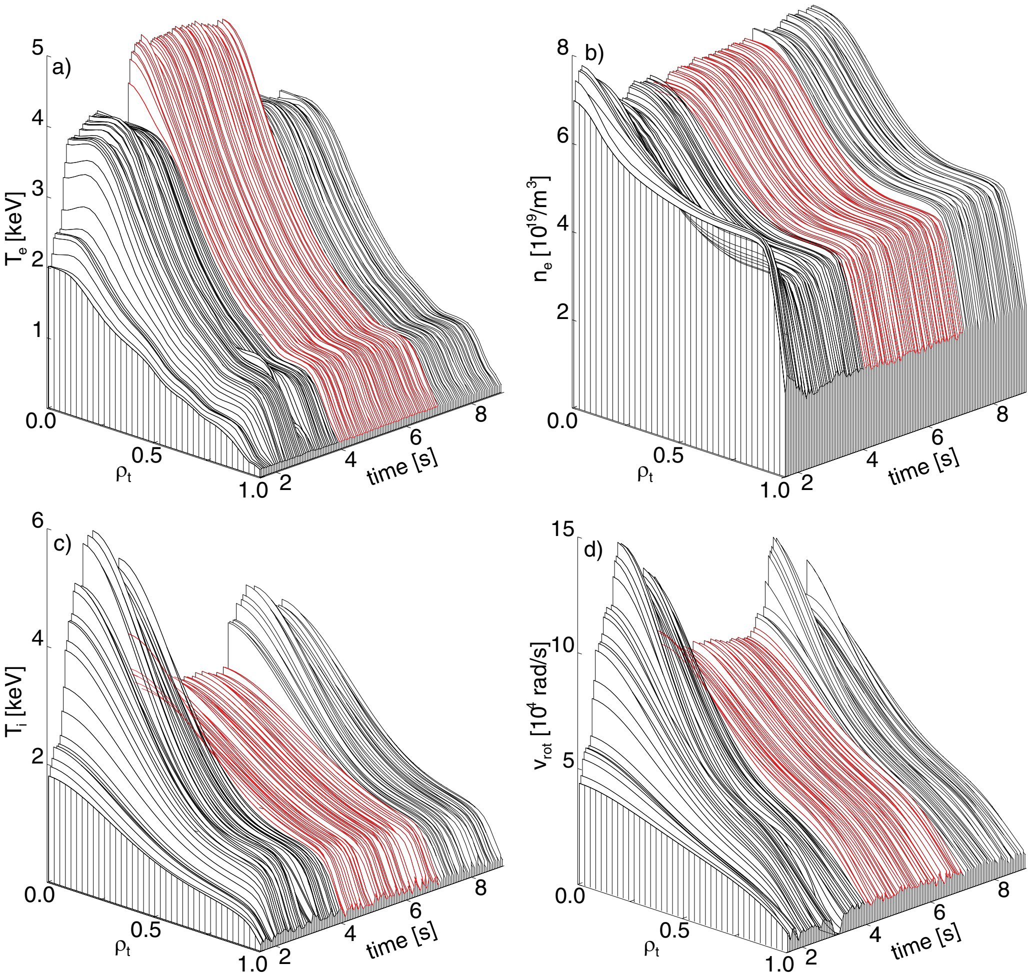

Figure 4. Bulk plasma profiles of discharge #30841 showing the electron temperature (*a*), the electron density (*b*), the ion temperature (*c*) and the toroidal plasma rotation frequency (*d*). The profiles acquired during off-axis NBI are plotted in red.

Moreover, eight neutral beam sources with each 2.5 MW of heating power are installed of which two beams have an off-axis geometry. In figure 1, the geometry of those NBI sources applied during this study is displayed. The off-axis beams, illustrated in yellow (Q6 + Q7), inject above and below the plasma center and have a tangential geometry.

The fast-ion current drive efficiency of the off-axis sources has been investigated in discharges with a toroidal magnetic field of -2.6 T and a feedback controlled plasma current of 0.8 MA. An overview plot of the heating scheme applied in a representative discharge (#30841) is shown in figure 2. Starting at 1.3 s, 2.5 MW of heating power from the 60 keV on-axis

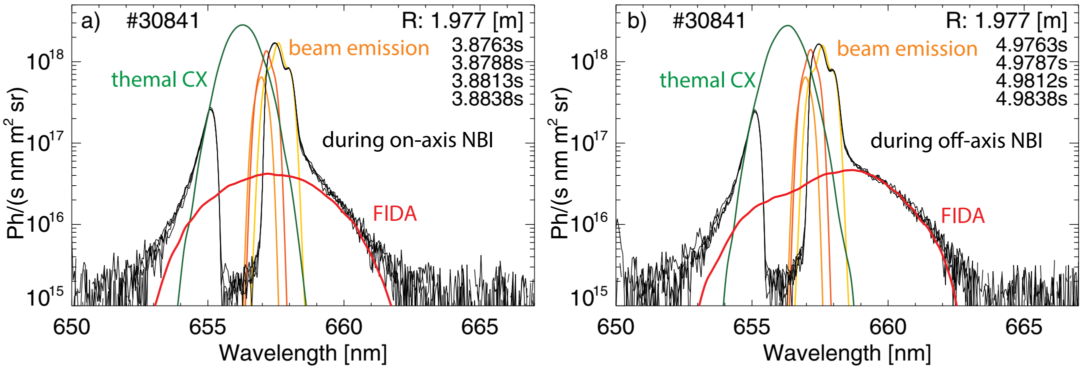

Figure 5. Measured spectra at $\rho_t \approx 0.55$ during on-axis (*a*) and off-axis (*b*) NBI heating. In color, synthetic spectra from FIDASIM are plotted.

source Q3 was applied because this source is needed for charge exchange recombination spectroscopy (CXRS) [18], MSE and FIDA measurements. From about 1.7 s on, additional 5 MW of heating power were injected by the two on-axis neutral beams which are indicated in purple in figure 1. Between 4 s and 7 s, these two radial sources were replaced by the tangential off-axis beams.

In addition to the NBI heating power, up to 2 MW of ECRH were applied to avoid sawtooth crashes (co-ECCD inside $q = 1$), to avoid the formation of a $(2, 1)$ magnetic island (modulated co-ECCD at the $q = 2$ surface) and to prevent the drop of the central electron temperature during off-axis NBI. These three aims were achieved in discharge #30841. The central electron temperature did not drop during the off-axis NBI phase, no sawtooth crashes and no $(2, 1)$ magnetic islands were observed. Only core localized $n = 1$, $m = 1$ modes in the frequency range between 10 kHz and 25 kHz were present. The positions of these modes were determined by studying the mode-induced electron temperature fluctuations that are measured by an electron cyclotron emission (ECE) diagnostic. In figure 3, the evolution of the amplitude of the dominant mode is plotted as a function of the normalized toroidal flux coordinate, ρ_t. During on-axis NBI, $(1, 1)$ modes, identified as fishbones [19], are located at $\rho_t \approx 0.2$ and during off-axis NBI, a continuous mode is localized at $\rho_t \approx 0.15$.

Figure 4 shows the evolution of electron and ion temperature profiles, as well as of profiles of the electron density and plasma rotation frequency. The electron density (inferred by integrated data analysis (IDA) [20]) remains constant during the experiment while the central ion temperature and rotation (both measured by CXRS diagnostics) drop during the off-axis NBI phase, which is well explained by reduced central heating and momentum input. The impurity density, measured by CXRS (on helium, boron and nitrogen), remained low and constant during the experiments and result in an effective charge number of about 1.3, which is agreement with the measured level of Bremsstrahlung. As mentioned above, we tried to keep the electron temperature constant during the experiment by adding ≈0.8 MW of feedback controlled central ECRH power between 4 s and 7 s. Constant electron temperatures are necessary for NBI current drive studies because the shape of the ohmic current profile depends strongly on T_e and significant changes would make the analysis of the off-axis neutral beam current drive efficiency very difficult. Here, the electron temperature is slightly too high in the plasma center during the off-axis phase. This is not ideal but can be taken into account by the forward modeling.

The fast-ion population during on-axis NBI and off-axis NBI has been studied by a FIDA spectroscopy diagnostic [21] which analyzes Doppler-shifted Balmer alpha radiation ($\lambda_0 = 656.1$ nm) from fast ions that undergo charge exchange reactions along the path of NBI Q3.

Example spectra measured by a line of sight that intersects NBI Q3 at $\rho_t \approx 0.55$ are shown in figure 5 during on-axis NBI and during off-axis NBI. The spectra, plotted on a semi-logarithmic scale, have been measured with a temporal resolution of 2.5 ms and passive radiation, acquired during a 10 ms long phase without operation of NBI Q3, has been subtracted. Between 655 and 657 nm, a filter blocks un-shifted Balmer alpha radiation from the plasma edge to avoid saturation effects. The spectral wing above 659 nm corresponds to the charge exchange radiation of fast-ions (FIDA radiation), which is more pronounced during off-axis NBI than during on-axis NBI. This is expected because off-axis NBI generates a larger fast-ion population at the measurement position ($\rho_t \approx 0.55$) than on-axis NBI. In addition to the measurement, simulated spectra are shown in color. The spectra have been calculated by the synthetic diagnostic FIDASIM [22] which needs to be supplied with theoretical fast-ion distribution functions. For the study presented here, the theoretical fast-ion distribution functions are predicted by the TRANSP code [23]. TRANSP needs information on kinetic profiles, the heating sources, the initial q-profile, information on the separatrix position, the toroidal magnetic field and the plasma current as inputs and uses a the Monte Carlo module NUBEAM [24] to simulate fast ions. The code is based on neo-classical theory, but one can also add a predefined diffusive like fast-ion transport. The simulated FIDA radiation, plotted in red in figures 5(*a*) and (*b*), agrees well with the red-shifted wing of the measured radiation. This already suggests that TRANSP consistently describes the fast-ion distribution function during on-axis NBI and off-axis NBI. In addition to the simulated FIDA radiation, the predicted beam emission (yellow/orange) and the thermal charge exchange component (green), i.e. the

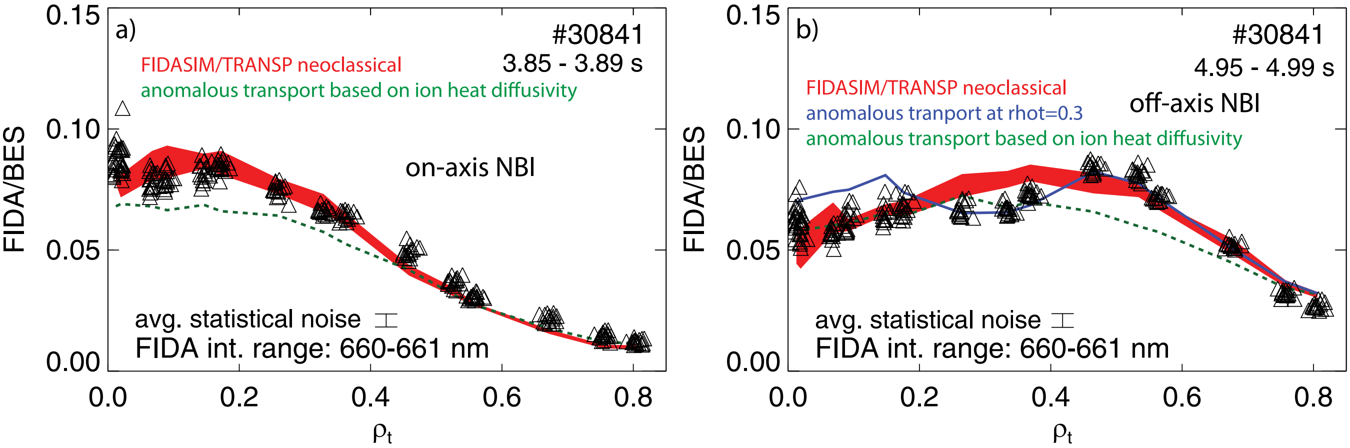

Figure 6. Radial FIDA/BES profiles during on-axis NBI (*a*) and off-axis NBI (*b*) compared with predictions by TRANSP+FIDASIM. In red, a sensitivity scan of neo-classical predictions is shown that is based on the variation of the kinetic profiles input to TRANSP (plus and minus one sigma of the measurement uncertainties of $T_e, T_i, n_e, Z_{\mathrm{eff}}, v_{\mathrm{tor}}$). In blue, the TRANSP+FIDASIM predictions is illustrated that represent a local anomalous fast-ion diffusivity during off-axis NBI at $\rho_t = 0.3$. The simulated FIDA/BES profiles in green correspond to anomalous transport based on the calculated ion-heat diffusivity (scaled by 0.1).

halo radiation, are shown. The good agreement between these components and the measurement is an important consistency check when comparing FIDA measurement and simulation.

Information on radial fast-ion profiles is obtained by analyzing the spectra from an array of lines of sight that intersect the NBI path at different positions. Depending on the viewing geometry relative to the magnetic field direction and on the observed wavelength range, different parts of the fast-ion velocity space can be sampled (see [13]). Here, we use toroidal lines of sight (shown in blue in figure 1) and focus on red shifted radiation between 660–661 nm. This corresponds to co-rotating fast-ions with energies above 30 keV which cover the part of the fast-ion velocity space distribution that contributes most to the fast-ion current. Radial profiles of the corresponding FIDA radiation are displayed in figure 6. Passive radiation, measured in phases without operation of NBI Q3, has been subtracted from the spectra before integrating. Moreover, the data has been normalized by the simultaneously measured beam emission (BES) which enables the neutral beam attenuation to be taken into account and to be independent of the intensity calibration.

The measured radial FIDA/BES profiles show a clear modification of the fast-ion population when switching from on-axis NBI (see figure 6(*a*)) to off-axis NBI (see figure 6(*b*)). Furthermore, the measured profiles are in good agreement with the prediction from TRANSP+FIDASIM. The profiles shown in red have been calculated by integrating the simulated spectra in wavelength and applying the normalization based on the simulated beam emission. The widths of the synthetic profiles correspond to ± one standard deviation of the uncertainties of predictions. The latter have been determined by a sensitivity scan using ten different TRANSP and FIDASIM runs per time point. For each run, one of the kinetic profiles ($T_e, T_i, n_e, Z_{\mathrm{eff}}, v_{\mathrm{tor}}$), input to TRANSP and FIDASIM, was increased or decreased by one standard deviation of the corresponding statistical measurement uncertainties. The resulting differences relative to the non-modified prediction have been summed up by applying a Gaussian error propagation.

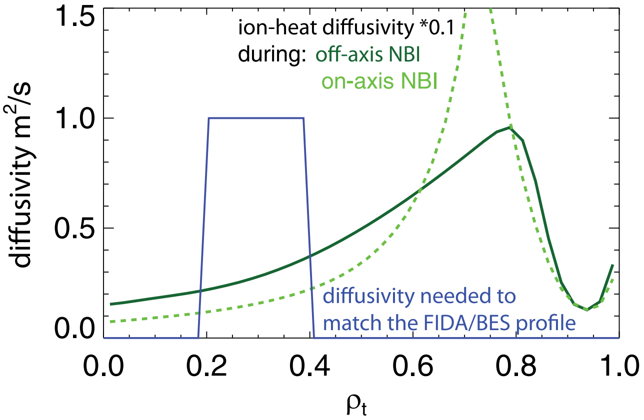

Figure 7. Radial profiles of the different anomalous fast-ion diffusion coefficient input to TRANSP.

During on-axis NBI (figure 6(*a*)), the simulated profiles agree very well with the simulation. Also during off-axis NBI, simulation and measurement roughly match. However, the prediction slightly overestimates the measured FIDA/BES signal between $\rho_t = 0.2 - 0.4$. By assuming an additional anomalous fast-ion diffusivity in TRANSP between 4s and 7s that is localized at $\rho_t \approx 0.3$ (see details in figure 7) the simulation agrees better with the experimental data, as plotted in blue in figure 6(*b*).

The origin of this localized anomalous fast-ion diffusivity, which is needed to explain the measurement, is not clear yet. The geometry of the NBI system has been checked with dedicated beam-into-gas experiments which makes a geometry induced discrepancy very unlikely. The continuous $(1, 1)$ mode present in discharge #30841 does not obviously cause an anomalous fast-ion diffusivity at $\rho_t = 0.3$ because it is located at $\rho_t = 0.15$. Anomalous fast-ion diffusivity induced by turbulence is also unlikely because, based on a power balance analysis, we would expect the strongest effect of turbulent transport further out. Figure 7 shows radial profiles of the TRANSP-calculated ion heat diffusivity ($D_{\mathrm{fast}} = 0.1 * \chi_{\mathrm{ion-heat}}$) during on-axis NBI and during

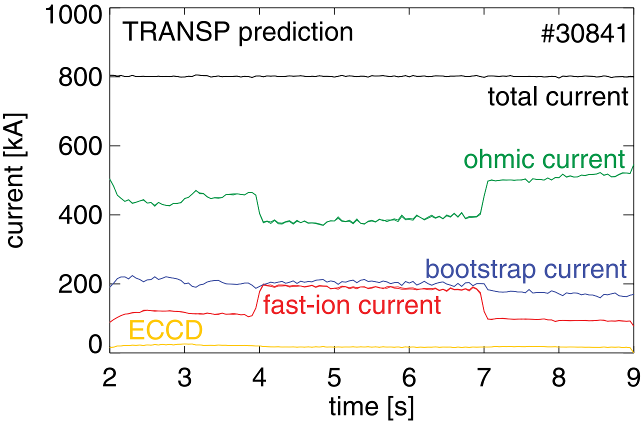

Figure 8. TRANSP predicted composition of the plasma current when assuming neo-classical fast-ion transport and when assuming a localized level of anomalous fast-ion diffusivity during off-axis NBI (there is almost no difference between the two cases).

off-axis NBI. The maximum of the heat diffusivity, which indicates the location of strong turbulent transport, is clearly not located at $\rho_t = 0.3$ but at $\rho_t = 0.7$. To test the possibility of turbulence induced fast-ion diffusivity, the scaled ion heat diffusivity has been input to a TRANSP+FIDASIM simulation. However, the resulting FIDA/BES profiles shown in figure 6 in green clearly do not agree with the measurement.

Therefore, we unfortunately cannot resolve the discrepancy between the FIDA measurement and the simulation. However, being able to simulate a fast-ion population that matches the experimental data, we can investigate the current drive efficiency of this fast-ion distribution function.

To calculate the current distribution, several options are available in TRANSP. For the study presented here, we applied the Sauter formula [25] to calculate the plasma resistivity and the bootstrap current, TORAY [26] to determine the current driven by ECCD and the Lin-Liu formula [27] to calculate the shielding of the positive current carried by the fast ions.

In figure 8, the TRANSP predicted evolution of the contributions to the plasma current are illustrated. In red, the fast-ion current is shown. It increases between 4 s and 7 s, well explained by the tangential injection geometry of the off-axis NBI sources. The increased fast-ion current is immediately balanced by a reduction of the feedback controlled ohmic current while the contributions of the bootstrap current and the current driven by ECCD remain constant. In addition to this neo-classical simulation, the current expected when applying the artificial fast-ion diffusion coefficient at $\rho_t = 0.3$ during off-axis NBI is shown. However, the second curve can hardly be seen because the current drive efficiency is almost unchanged. It should be noted that assuming anomalous transport in the simulation does not significantly change the total current driven by off-axis NBI because it mainly broadens the fast-ion profile. The reduced current drive efficiency of fast ions that are redistributed outwards (e.g. lost or slowed down more quickly) is balanced by an inward diffusion of fast ions where the increased slowing down time allows particles to contribute more to the plasma current.

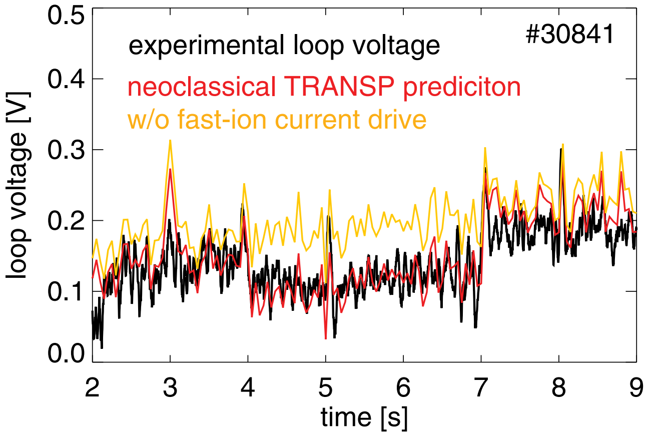

Figure 9. Measured loop voltage compared with predictions from TRANSP. The simulation plotted in red takes the current driven by the fast ions into account while the simulation given in yellow does not.

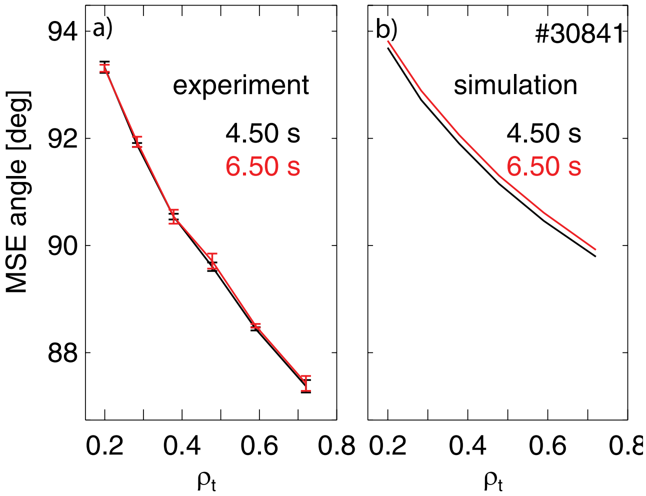

Figure 10. Measured (*a*) and TRANSP-predicted (*b*) MSE angles for time points shortly and 2.5 s after switching to off-axis NBI.

Experimentally, a reduced ohmic current is observed during off-axis NBI since the loop voltage, induced by the ohmic transformer coil to drive the current, drops. As shown in figure 9, the measured loop voltage is reduced by ≈50% between 4 and 7 s. This observation is in good agreement with the TRANSP predicted loop voltage, shown in red. In contrast, when assuming no current driven by the fast ions (simulation plotted in yellow) prediction and experiment disagree. This shows without ambiguity that the reduction of the loop voltage is mainly caused by an increased current-drive from the off-axis NBI. In addition, it should be noted that the good match between the predicted and measured loop-voltage also validates the kinetic profiles input to TRANSP.

In contrast to this good agreement with the neo-classical simulation, the comparison between measured and predicted MSE angles shows differences. Figure 10 compares radial profiles of the MSE measurement for two time points during the off-axis phase. The MSE diagnostic measures the projection of the polarization direction of the sigma component of

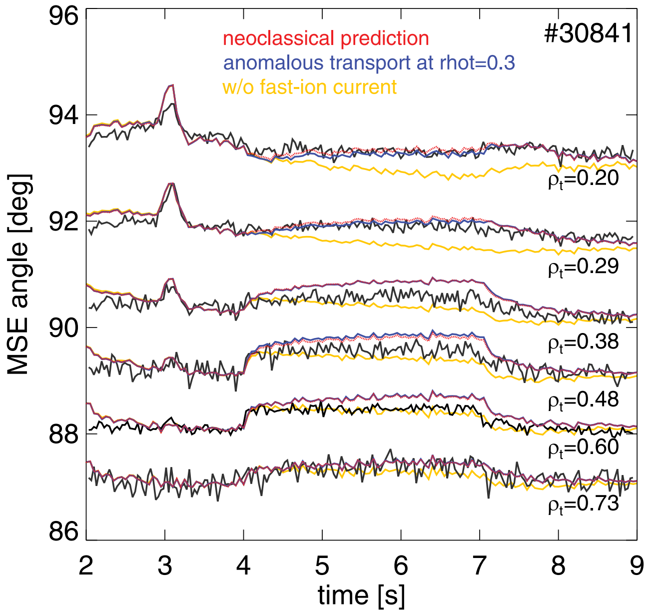

Figure 11. Temporal evolution of the measured and predicted MSE angles. In red, the neo-classical prediction by TRANSP is shown. The prediction in blue represents the application of a local anomalous fast-ion diffusivity during the off-axis NBI phase and the simulation in yellow represents no fast-ion driven current.

the beam emission of 60 keV neutrals of NBI Q3 on the plane perpendicular to its lines of sight (see geometry in figure 1). The polarization direction depends on the electric field vector encountered by the neutrals which are injected with the velocity $\mathbf{v}_n$. This electric field consists of the $\mathbf{v}_n \times \mathbf{B}$ Lorentz field and the radial electric field. The latter has been calculated based on the radial force balance [28] and on the assumption that the poloidal rotation velocity of deuterium is negligible (valid for neo-classical conditions). Here, it should be noted that our previous publication ([13]) neglected the diamagnetic term and applied the wrong sign for the radial electric field (a bug in TRANSP which has been resolved now). This overestimated the change of the predicted MSE angles by about 20% NBI but did not qualitatively modify the result.

The combination of the line of sight geometry of the MSE diagnostic and the radial injection geometry of NBI Q3 provides a good sensitivity of the MSE diagnostic on changes of the poloidal magnetic field and, hence, on changes of the plasma current profile. The predicted MSE profile, plotted in figure 10(*b*), shows a clear modification between 4.5 s and 6.5 s (shortly and 2.5 s after switching to off-axis NBI). This change is expected during the off-axis phase because the current profile and, thus, the poloidal magnetic field, are supposed to vary slowly on the resistive time scale of seconds. First, the current generated by off-axis NBI is completely compensated by a reduction of the local ohmic current. Then, the current profile should change according to the off-axis beam deposition on the resistive time scale. However, even after 2.5 s, the measured MSE profiles hardly exhibit any changes (see figure 10(*a*)).

Also when comparing the temporal evolution of the MSE data with the prediction by TRANSP, a disagreement is observed compared to the neo-classical simulation. Figure 11 shows time traces of the individual channels of the MSE diagnostic. A radial sweep of ≈2 cm of the plasma at ≈3 s proves the reliability of the diagnostic through the clear change in the measurement that is well reproduced by TRANSP. Moreover, the diagnostic resolves well a step in the measured MSE angles at 4 s directly after the application of off-axis NBI. This is explained by a change of the Shafranov shift induced by a variation in the fast-ion pressure profile. To be able to compare the time evolution with the TRANSP prediction, a channel dependent offset has been added to the simulation to match the experimental data between 3 and 4 s. As can be seen, the neo-classically predicted MSE angles in red change more than the measured ones. Also when assuming the level of anomalous fast-ion diffusivity at $\rho_t \approx 0.3$ which is needed to match the FIDA measurements during off-axis NBI, a very similar result to the neo-classical prediction is obtained (see the blue curve in figure 11). In contrast, the simulation changes substantially when switching off the fast-ion-driven current in the simulation. Without fast-ion current drive, the predicted evolution of the MSE angles strongly differs from the measured one. This proves that the NBI current drive efficiency is not zero. However, the profile of the driven current differs from the prediction.

One possible explanation for the disagreement of the experimental and predicted current profile could be an incomplete model of the shielding factor of the positive ion current. However, all options available in the TRANSP code to calculate the fast-ion driven current show very similar results (e.g. the application of a collisionality dependent shielding factor ([29]) does not significantly change the NBI current drive efficiency.). We also tested if the choice of the initial q-profile in a TRANSP simulation changes the conclusion but this is not the case. Further, a sensitivity scan similar to figure 6 has been conducted. However, the modifications are very small and cannot be displayed properly. Another possibility to explain the data would be that the fast-ions behave neo-classically in the observed part of the velocity space but experience strong anomalous transport in other regions. Further, the $(1, 1)$ mode activity during on-axis NBI could already broaden the plasma current distribution, which would make the effect of off-axis NBI less pronounced. These two possibilities need to be investigated in future experiments with q-profiles above one and, hence, without $(1, 1)$ modes and with extended capabilities to diagnose the fast-ion distribution functions.

3. Sawtooth-induced fast-ion transport

In the 2014 experimental campaign of ASDEX Upgrade, fast-ion transport experiments were performed with 1 MA of plasma current, a toroidal magnetic field of -2.6 T and 2.5 MW of heating power from one radially injecting on-axis NBI source (NBI Q3). The discharges feature low densities ($\approx 4 \times 10^{19}\,\mathrm{m}^{-3}$) and high ion temperatures (up to 6 keV) and exhibit strong sawtooth activity, indicated by periodic drops of the central electron temperature, ion temperature and rotation. The magnetic spectrogram in figure 12(*a*) shows the footprint of fishbone modes that appear prior to the sawtooth crashes. In addition, modes are visible after the crashes which

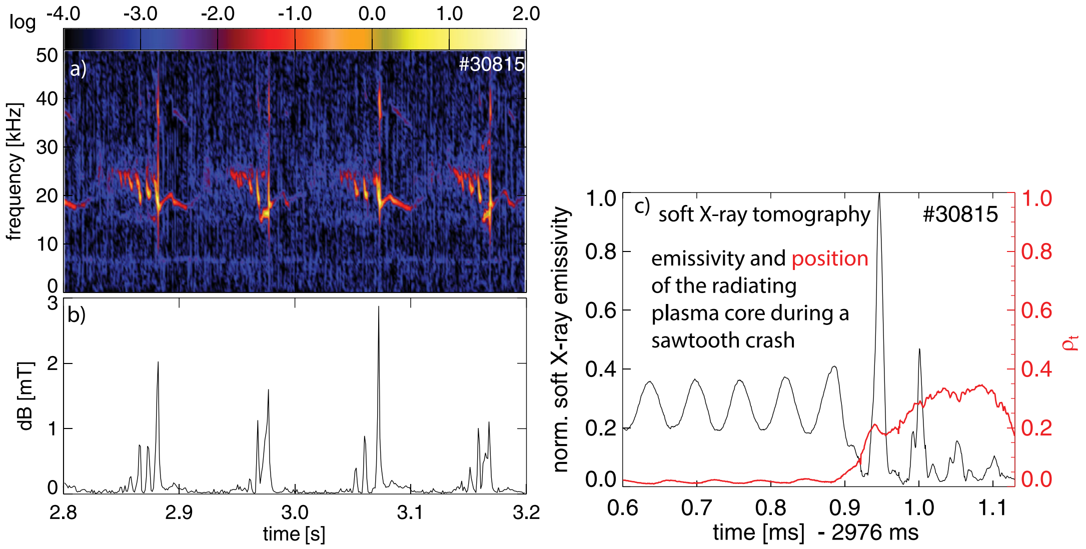

Figure 12. (*a*) Magnetic spectrogram and amplitude of the magnetic perturbation (*b*). (*c*) Emissivity and position of soft x-ray radiation during a sawtooth crash inferred by a tomographic reconstruction.

indicates an incomplete magnetic reconnection during the crashes which is a routine phenomenon observed in ASDEX Upgrade [30]. The crash times of the sawteeth are in the range of 0.1 ms which can be determined from tomographic reconstructions of soft x-ray measurements. Figure 12(*c*) shows the position of the radiating plasma center as a function of time for one sawtooth crash. During the crash phase, the movement of the plasma core reaches the $q = 1$ surface and the emissivity (mainly tungsten) drops. It should be noted that the emissivity is modulated before the crash due to the mode rotation and the accumulation of tungsten on the low-field side which is caused by centrifugal forces.

The effect of the crashes on the fast ions is illustrated in figure 13. Panel a shows the measured count rate of neutrons, mainly produced by fusion reactions between fast ions and the background plasma. It should be noted that the experimental neutron rate in arbitrary units has been measured by a novel neutron spectrometer [31] that has a very good signal to noise ratio when integrating the measurement in energy but does not provide absolute fluxes. Clearly, the neutron rate drops periodically at every sawtooth crash. The same behavior can be seen in the predicted neutron rates from TRANSP that are plotted in red. The TRANSP code models the effect of sawtooth crashes on the fast ions by applying the Kadomtsev model [32], which assumes full reconnection of the helical magnetic field due to the crash and redistributes fast particles according to the evolving field lines. TRANSP predicts an outwards fast-ion redistribution to a colder plasma region where fast ions are slowed down more quickly and hence contribute less to the neutron rate. The predicted relative change of the neutron rate in figure 13(*a*) agrees very well with the relative change in the experimental data. This suggests that the Kadomtsev model describes the sawtooth-induced fast-ion redistribution well. However, it should be noted that the neutron fluxes are dominated by specific parts of the fast-ion phase space [33] and no strong and global statement can be made here.

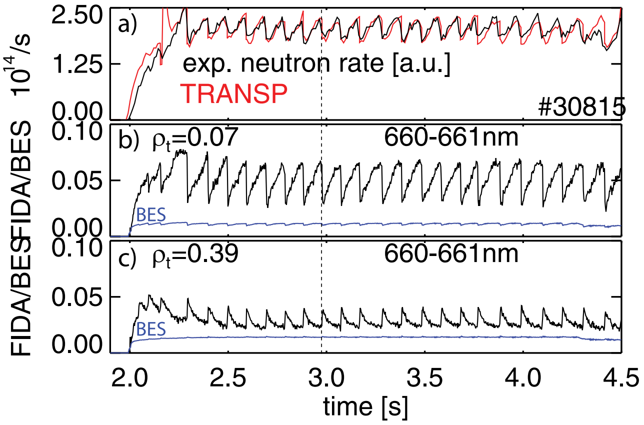

Figure 13. (*a*) Measured neutron rate in arbitrary units, scaled to roughly match the prediction from TRANSP (Kadomtsev model) given in red. (*b*) Temporal evolution of the measured FIDA/BES ratio at $\rho_t = 0.07$ showing a clear reduction of the fast-ion density when sawteeth appear. (*c*) FIDA/BES ratio measured at $\rho_t = 0.39$, indicating an increased fast-ion density after sawtooth crashes outside the sawtooth inversion radius. In blue. the evolution of the beam emission is given in 2×10^{19} photons s^{-1} sr^{-1} m^{-2} which has been used to normalize the FIDA data.

In figures 13(*b*) and (*c*) we show the evolution of the integrated (660–661 nm) and normalized FIDA radiation observed by two toroidal lines of sight. The beam emission used to normalize the data is plotted in blue in figures 13(*b*) and (*c*) and changes only weakly when sawtooth crashes appear. This shows that the probability of fast-ions to undergo charge exchange reactions and to emit FIDA radiation is not significantly modified. The strong drops of the central FIDA/BES ratio (figure 13(*b*)) and the increased signal outside the $q = 1$ surface (figure 13(*c*)) can, hence, be attributed to a radial fast-ion redistribution.

Figure 14 shows radial FIDA/BES profiles from the toroidal lines of sight before and after the sawtooth crash at ≈3 s as a function of ρ_t. A constant offset has been subtracted

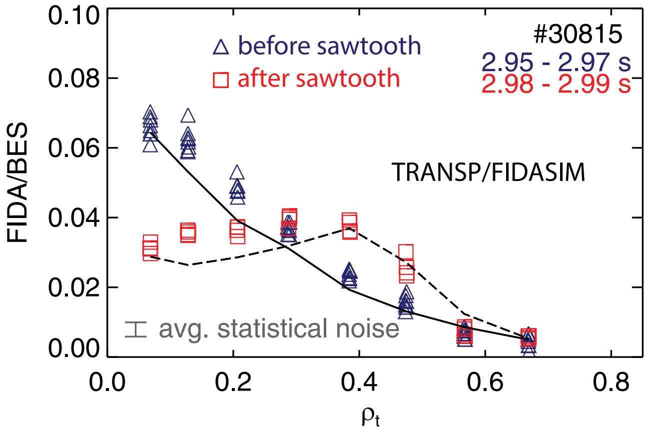

Figure 14. Radial FIDA/BES profiles (660–661 nm) acquired with a time resolution of 2.5 ms before (blue) and after (red) a sawtooth crash at ≈3 s. In black, synthetic profiles from TRANSP+FIDASIM are given. The error-bar plotted in the lower left part of the figure illustrates the average statistical uncertainties of the FIDA measurement.

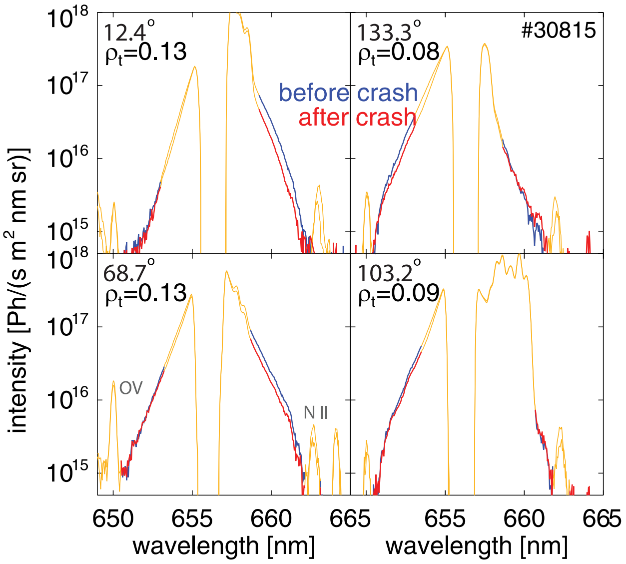

Figure 15. Time coherent averaged spectra containing FIDA radiation before (blue) and after (red) a sawtooth crash from four different viewing geometries on a semi logarithmic scale. The FIDA radiation can mainly be analyzed between 650 and 653 nm and between 659 and 662 nm where it is not superimposed by other spectral contributions, like the cold D-alpha radiation, the beam emission and impurity line emissions. The measured radiation plotted in yellow corresponds to the spectral regions that have been excluded from the tomographic reconstruction.

from each channel to account for passive radiation from the plasma edge. The simulated FIDA/BES profiles, illustrated by the black lines, have been calculated by FIDASIM and the predicted change of the profiles is in good agreement with the measurement. This indicates that the sawtooth crashes cause an internal fast-ion redistribution of co-rotating fast-ions (observed by toroidal lines of sight between 660 and 661 nm) that is dominated by the motion of fast particles along the evolving field line, as assumed in the Kadomtsev model.

In order to study the effect of sawtooth crashes on the central fast-ion velocity space distribution of fast ions, a tomographic inversion has been performed which has been demonstrated previously [34–36] and is applied here to measure 2D fast-ion velocity distribution functions as a function of energy and pitch (pitch $= v_{\|}/v_{\mathrm{tot}}$ where $v_{\|}$ is the fast-ion velocity anti-parallel to the magnetic field and v_{tot} is the total fast-ion velocity). The inversion is based on the analysis of FIDA spectra from four viewing geometries, shown in figure 1 in red. The four lines of sight intersect the path of NBI Q3 in the plasma center ($\rho_t < 0.09$) and have angles to the local magnetic field of 12.4 degrees, 133.3 degrees, 68.7 degrees and 103.2 degrees. Depending on this observation angle and a given wavelength, each view collects FIDA radiation of neutralized fast-ions from different regions in velocity space, described by FIDA weight functions [37]. As an example, the toroidal view (12.4 degree) is sensitive to co-rotating fast-ions when analyzing strongly red-shifted FIDA light while the poloidal view (68.7 degree) is sensitive to fast-ions with pitch values close to zero at the blue shifted side.

Coherently averaged spectra from the four views, just before and just after sawtooth crashes, are plotted in figure 15 (coherent averaging has been used between 2.3 s and 4.5 s in discharge #30815 to reduce the statistical uncertainties of the measurement). Not all wavelength regions can be analyzed because additional spectral components are present, in addition to the FIDA radiation. In particular, the cold D-alpha radiation at 656.1 nm (here blocked by a filter), the beam emission and strong impurity line emissions must be excluded from the analysis. Moreover, when performing tomographic inversions we use only FIDA light with Doppler shifts that correspond to fast ions with energies above 10 keV. In consequence, only the highlighted parts of the spectra (plotted in blue and red in figure 15) can be analyzed. Clearly, the measurement of the toroidal view (12.4 degree) shows a sawtooth-induced reduction of the FIDA radiation at red-shifted wavelengths while the poloidal view exhibits only a very weak variation at the blue shifted side. This already indicates that mainly co-rotating fast-ions are affected by the sawtooth crashes.

For a more detailed analysis that includes all accessible wavelength ranges and viewing geometries, a tomographic inversion has been applied that is based on a truncated singular value decomposition as in previous work [34–36]. In this method the forward model to calculate FIDA spectra is formulated in the form of a matrix equation composed of weight functions which have been calculated by FIDASIM. The Moore–Penrose pseudoinverse of this transfer matrix is then calculated by a truncated singular value decomposition. Here we discretized the (energy,pitch)-space uniformly using 15×15 grid points for pitches from -1 to 1 and energies from 0 to 100 keV and a truncation level of 38 has been applied. The inferred 2D fast-ion velocity distribution functions just before and just after the coherently averaged sawtooth crash are shown in figures 16(*a*) and (*b*), respectively. The influence of the sawtooth crashes on the kinetic profiles and, hence, on the charge exchange and photon emission probability of fast ions is contained in the weight functions and, therefore, is considered by the tomography. As indicated by the cross-hatched area, we do not provide information on the low energy region

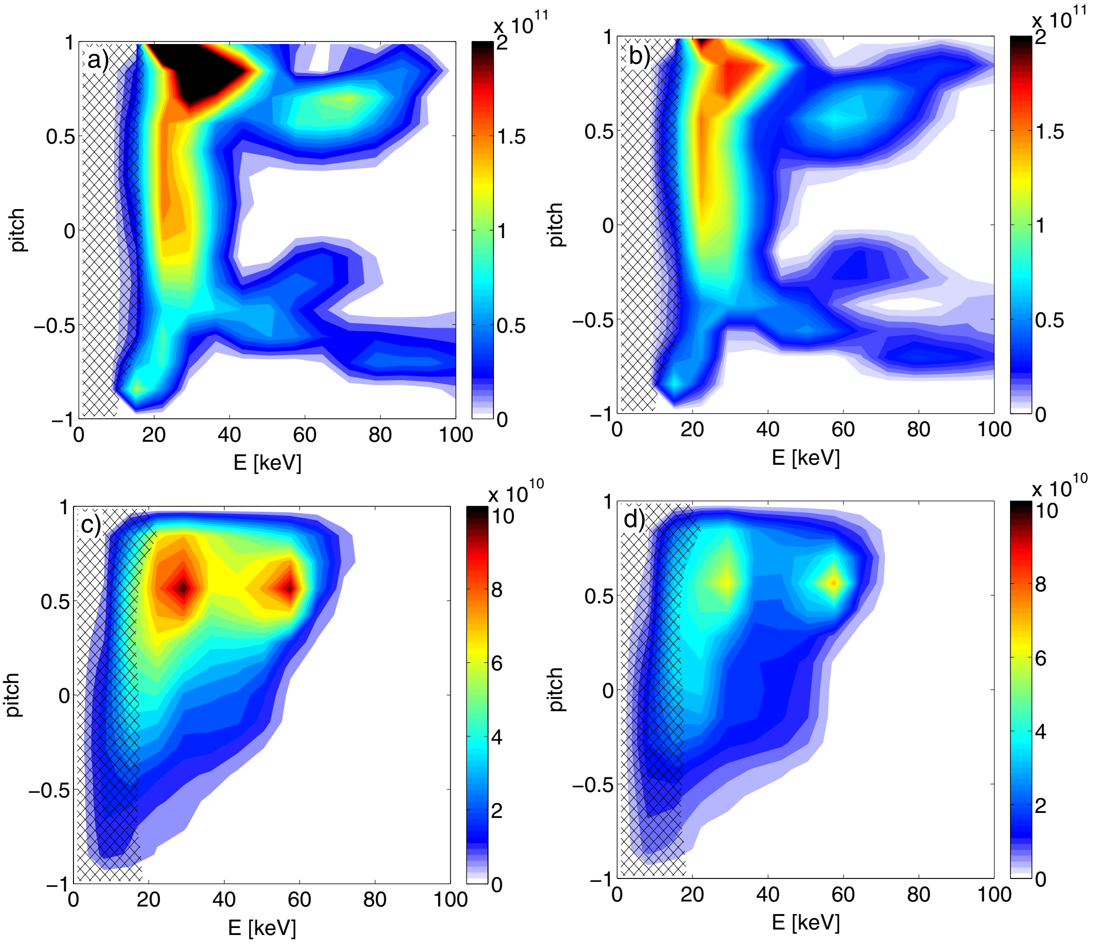

Figure 16. (*a*)+(*b*) Reconstructions of the fast-ion velocity-space distribution function in the plasma center (inside $q = 1$) before and after a sawtooth crash in units of [ions/(keV cm^3)]. (*b*)+(*c*) TRANSP predicted fast-ion velocity-space distribution function in the plasma center.

because of our restriction in the observable wavelength range to fast ions above 10 keV.

The overall shapes of the reconstructed fast-ion distribution functions agree well with the fast-ion distribution functions predicted by TRANSP, shown in figures 16(*c*) and (*d*). The simulations and the reconstructions before and after the crash show larger values for positive pitches than for negative pitches, explained by the co-current NBI injection geometry. Further, the beam injection peaks at full, half, and third injection energies (60 keV, 30 keV and 20 keV) partly appear in the reconstructions. However, there are also some discrepancies possibly explained as we do not necessarily expect the TRANSP simulation to match the reconstruction since the discharge is not MHD quiescent but has strong $(1, 1)$ activity also before the sawtooth crashes. Further, perfect subtraction of passive impurity radiation was not possible, which can also cause discrepancies: The reconstructions suggest slightly higher beam injection energy than expected from this 60 keV source. We also observe non-zero fast-ion phase-space densities at energies very much higher than 60 keV for positive as well as for negative pitches. These are likely artifacts of the reconstructions since similar features also appear in tomographic inversions of synthetic FIDA data for various truncation levels of the singular value decomposition. With the experimental FIDA data, these artifacts are even stronger because we cannot measure the absence of FIDA light at large wavelength shifts when these wavelength ranges contain impurity line emissions. It is also possible that we have misleadingly identified weak impurity radiation at large Doppler shifts as FIDA radiation which could also lead to such tails. Lastly, it should be noted that we cannot distinguish between fast ions generated by NBI and the high-energy tail of the thermal distribution. Hence the tomographic reconstruction shows the sum of the fast ions that have been injected and the ions of the thermal distribution that have more energy than 10 keV.

Despite these uncertainties, the tomographic reconstruction allows us to provide, for the first time, a direct measurement of the redistribution level of fast ions. By integrating the inferred velocity space distribution in energy and pitch, we find a fast-ion density before the crash of 8.1×10^{12} fast ions cm^{-3} and a fast-ion density of 5.9×10^{12} fast ions cm^{-3} after the sawtooth crash. This corresponds to a redistribution of about 30% of the central fast ion population. It should be emphasized that we present an estimate covering the entire velocity-space above 10 keV while previous studies [6, 9] reported on fast-ion densities only in specific parts of the velocity-space. In addition, the tomographic reconstruction permits us to study

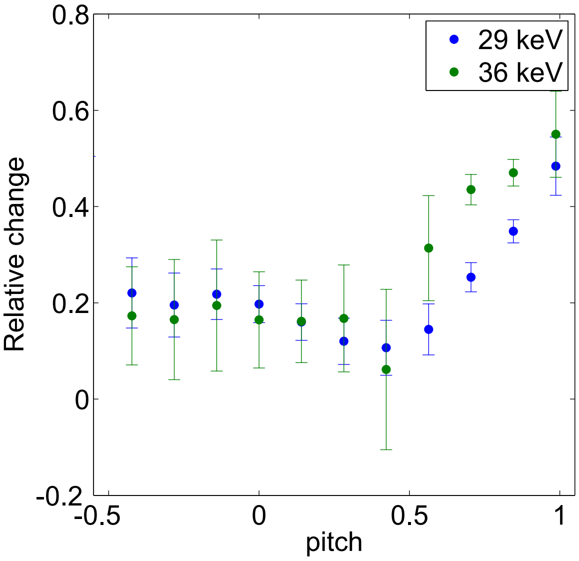

Figure 17. Relative change $(f_{\mathrm{before}} - f_{\mathrm{after}})/f_{\mathrm{before}}$ of the fast-ion density at 29 keV. and 36 keV as a function of the pitch value. The error-bars represent the photon noise in the FIDA spectra used for the tomographic reconstruction.

the pitch-angle dependence of the sawtooth-induced fast-ion redistribution.

Figure 16(*c*) shows the relative changes in the fast-ion distribution function over the average sawtooth crash at 29 keV and 36 keV for pitches ranging from -0.5 to 1. Here we focus on energies and pitches for which the amplitudes of the distribution functions are large and smooth. As can be seen, the relative change is strongly dependent on pitch. The changes are modest for small pitches up to 0.5 (5% to 25% of redistribution) and strong for co-rotating ions with pitches close to 1 (up to 60% redistribution). The errorbars provided here represent the photon noise in the analyzed spectra and have been calcualted by the square roots of the diagonal elements of the covariance matrix of the inversion. It should be noted that the errorbars do not consider uncertainties in the weight functions or in the reconstruction algorithm.

The reconstruction shows that, particles moving parallel to the evolving field lines are affected most by sawtooth crashes while fast ions with significant velocity components perpendicular to the magnetic field are less sensitive to the sawtooth instability. This result is in agreement with [6] and [7] and will be compared with MHD modeling results in future publications. Moreover, it should be noted that further improvements of the tomographic reconstruction are planned by using a fifth FIDA view, by modeling or avoiding impurity radiation and by combining the FIDA measurements with data from collective Thomson scattering [38].

4. Summary and conclusion

In NBI current drive experiments, the loop-voltage changes in agreement with the neo-classical prediction when replacing on-axis NBI by off-axis NBI. However, measurements of the MSE diagnostic do not agree with the predictions by TRANSP. The possibility to explain this discrepancy with an increased fast-ion transport has been studied by analyzing radial profiles from a FIDA diagnostic. Here, measurements during on-axis NBI are in good agreement with the neo-classical prediction and during off-axis, the measured profiles are only slightly flatter than expected. The level of anomalous fast-ion diffusivity need to match the slightly flatter profiles cannot explain the discrepancy between the MSE measurement and the modeling. Possibly, $(1, 1)$ MHD activity present in the discharges affects the plasma current distribution which is very difficult to consider in the simulation. Therefore, new experiments without $(1, 1)$ MHD activity are planned in the 2015 experimental campaign, in particular aiming at experiment with elevated q-profiles.

During sawtooth crashes, very strong fast-ion redistribution is measured by an array of toroidal FIDA views and good agreement with the Kadomtsev model is found. 2D fast-ion velocity distribution functions in the plasma center have been calculated based on 4-view FIDA measurements which are easier to interpret than the raw FIDA spectra. They show a clear drop of the central fast-ion density after sawtooth crashes and a stronger redistribution of purely passing fast ions than of those ions with pitch values in the vicinity of zero.

Acknowledgments

This work has been carried out within the framework of the EUROfusion Consortium and has received funding from the Euratom research and training programme 2014–2018 under grant agreement No 633053. The views and opinions expressed herein do not necessarily reflect those of the European Commission.

References

[1] Fisch N.J. 1987 *Rev. Mod. Phys.* **59** 175
[2] Editors I.P.B. *et al* 1999 *Nucl. Fusion* **39** 2137
[3] Von Goeler S.S *et al* 1974 *Phys. Rev. Lett.* **33** 1201
[4] Marcus F.B. *et al* 1991 *Plasma Phys. Control. Fusion* **33** 277
[5] Lovberg J.A. *et al* 1989 *Phys. Fluids B: Plasma Physics* **1** 874
[6] Muscatello C.M. *et al* 2012 *Plasma Phys. Control. Fusion* **54** 025006
[7] Nielsen S.K. *et al* 2010 *Plasma Phys. Control. Fusion* **52** 092001
[8] Cecconello M. *et al* 2015 *Plasma Phys. Control. Fusion* **57** 014006
[9] Geiger B. *et al* 2014 *Nucl. Fusion* **54** 022005
[10] Guenter S. *et al* 2007 *Nucl. Fusion* **47** 920
[11] Park J.M. *et al* 2009 *Phys. Plasmas* **16** 092508
[12] Pace D.C. *et al* 2013 *Phys. Plasmas* **20** 056108
[13] Geiger B. *et al* 2015 *Plasma Phys. Control. Fusion* **57** 014018
[14] Herrmann A. *et al* 2003 *Fusion Sci. Technol.* **44** 569
[15] Heidbrink W.W. *et al* 2004 *Plasma Phys. Control. Fusion* **46** 1855
[16] Zohm H. *et al* 2001 *Nucl. Fusion* **41** 197
[17] Mück A. *et al* 2005 *Plasma Phys. Control. Fusion* **47** 1633
[18] Isler R.C. 1994 *Plasma Phys. Control. Fusion* **36** 171
[19] Chen L. *et al* 1984 *Phys. Rev. Lett.* **52** 1122
[20] Fischer R. *et al* 2010 *Fusion Sci. Technol.* **58** 675

[21] Geiger B. *et al* 2013 *Rev. Sci. Instrum.* **84** 113502
[22] Heidbrink W. *et al* 2011 *Commun. Comput. Phys.* **10** 716
[23] Hawryluk R. *et al* 1980 *Phys. Plasmas Close Thermonucl. Cond.* **1** 19
[24] Pankin A. *et al* 2004 *Comput. Phys. Commun.* **159** 157
[25] Sauter O. *et al* 1999 *Phys. Plasmas* **6** 2834
[26] Westerhof E. 1989 *Rijnhuizen Report (Amsterdam, Netherlands)* no. 20064787 (https://inis.iaea.org/search/searchsinglerecord.aspx?recordsFor=SingleRecord&RN=20064787)
[27] Lin-Liu Y.R. *et al* 1997 *Phys. Plasmas* **4** 4179
[28] Ida K. 1998 *Plasma Phys. Control. Fusion* **40** 1429
[29] Honda M. *et al* 2012 *Nucl. Fusion* **52** 023021
[30] Igochine V. *et al* 2007 *Nucl. Fusion* **47** 23
[31] Tardini G. *et al* 2012 *J. Instrum.* **7** C03004
[32] Porcelli F. *et al* 1996 *Plasma Phys. Control. Fusion* **38** 2163
[33] Jacobsen A. *et al* 2015 *Nucl. Fusion* **55** 053013
[34] Salewski M. *et al* 2012 *Nucl. Fusion* **52** 103008
[35] Salewski M. *et al* 2013 *Nucl. Fusion* **53** 063019
[36] Salewski M. *et al* 2014 *Nucl. Fusion* **54** 023005
[37] Salewski M. *et al* 2014 *Plasma Phys. Control. Fusion* **56** 105005
[38] Nielsen S.K. *et al* 2015 *Plasma Phys. Control. Fusion* **57** 035009